Electrical Resistivity and Magnetic Properties in (La, Ag)-Mn-O, (Nd, Ag)-Mn-O and (Y, Ce)-Mn-O Based Manganites

A Thesis Submitted

By

Sandeep Kumar Srivastava

Roll No: 04612108

In Partial Fulfillment of the Requirements for the Award of the Degree of

Doctor of Philosophy in Physics

Department of Physics
Indian Institute of Technology Guwahati,
Guwahati-781039, INDIA

October, 2008

Statement

The work contained in the thesis entitled **"Electrical Resistivity and Magnetic Properties in (La, Ag)-Mn-O, (Nd, Ag)-Mn-O and (Y, Ce)-Mn-O Based Manganites"** has been carried out by me under the supervision of Dr. S. Ravi, Associate Professor, Department of Physics, Indian Institute of Technology Guwahati, Guwahati. This work has not been submitted elsewhere for the award of any degree.

20th October, 2008

(Sandeep Kumar Srivastava)
Department of Physics
Indian Institute of Technology Guwahati
Guwahati - 781039

Certificate

It is certified that the work contained in the thesis entitled **"Electrical Resistivity and Magnetic Properties in (La, Ag)-Mn-O, (Nd, Ag)-Mn-O and (Y, Ce)-Mn-O Based Manganites"** by Mr. Sandeep Kumar Srivastava, a Ph. D. student of the Department of Physics, Indian Institute of Technology Guwahati, Guwahati for the award of the degree of *Doctor of Philosophy* has been carried out under my supervision. This work has not been submitted elsewhere for the award of any degree.

20th October, 2008

(Dr. S. Ravi)
Associate Professor
Department of Physics
Indian Institute of Technology Guwahati
Guwahati – 781 039

Dedicated

to

My Parents

Acknowledgements

Looking back at the few years in IIT Guwahati, there are quite a few people I would like to express my gratitude for helping me along the long course to a Ph.D. thesis.

First of all, I wish to give my sincere thanks to my supervisor Dr S. Ravi for his support, for being so generous with his time, knowledge and plan for work. It has been a great experience working with him. I will never forget his cool and down to earth behavior. The way he guided me, and the way he proceeded with my thesis, it was a learning experience for me. Not only did I learn the subject from him that included diverse subjects like experimental techniques, CMR materials, magnetism and other advanced physics topics, but, numerous things in my personal life also. It was really incredible learning all these till the time of my thesis submission.

I would like to offer my thanks to the doctoral committee (DC) members, Dr P.K. Giri (Chairman), Prof. A. T. Khan and Dr A. Perumal for their frank comments and suggestions that helped to improve the quality of my work.

I will never fail to give my gratitude to my lab mates. They themselves have made the environment, interesting to work. So, in no particular order, I offer my thanks to former and present research group members for their assistance, advice and cooperation: Dr Manoranjan Kar, Dr Pramoda Nayak, Biswanath Samantaray and Sunita Mohanty. My special thanks to Dr Manoranjan Kar for his several help and advice during my Ph.D. I recall various help by Dr. Pramoda also. I will never forget the altruistic help extended by Biswanath at several occasions.

I am thankful to faculty members of my department, especially to the Head of department Prof. Alika Khare for her friendly behavior and help whenever it was needed. I would like to give my thanks to Prof. A. Srinivasan (former HOD) also, for extending experimental facility and his help.

I am thankful to central workshop, engineering section for their cooperation and, central instrumental facility (CIF), IIT-Guwahati, for enabling me to avail several sophisticated instruments to perform the experiments. I am thankful to Mr Kula Kamal Senapati and Mr Chandan Borgohain, Scientific officers, CIF for their help. I am also

thankful to HOC, Nanotechnology Prof. Arun Chattopadhyay for extending X-ray diffractometer facility.

I am grateful to Dr. P. D. Babu (UGC-DAE CSR, Mumbai) for magnetization measurements.

I am thankful to all research scholars of my department for pleasant memories had with them. I would like to thank Purabi, Anto, Manos, Veena, Meera, Gaurav, Rajendra, Debabrata, Arpita, Aneesh and Mrs & Mr Dutta (Poulumi & Biswanath). Here, I would also like to thank Mr Sidananda for his friendly discussion. I wish to thank office staff Mr. Pankaj and all technical assistant of my department for their help.

Away from the academia, I spent quality time during my stay at IIT Guwahati. I made many good friends, few best ones and special also. I am thankful to all my friends for the colorful and memorable times we had together. I will never fail to remember my friends Atul, Satish and Biswaranjan.

Special mention must go to Priyanka, for her support in the back drop of this journey- my heartiest thanks to her. This work would not have been completed without her support and warmth. Finally, none of this would have been possible without the constant support, love, and affection of my family members during the entire period of this work. My sincere gratitude to my parents, brother (Prinshu) and sisters (Priti and Priya). I am thankful to my other family members for their encouragement.

Last but not the least, I am grateful to Indian Institute of Technology Guwahati for giving the financial support to carry out the present thesis work.

Sandeep Kumar Srivastava

IIT Guwahati, INDIA, October 2008

Abstract

One group of fascinating compounds with many potential applications is the mixed valence perovskite manganites. The versatility of perovskite manganites for electronic applications is demonstrated by the fact that, these materials exhibit wide range of conductivity ranging from highly conducting metallic state to insulating state. The discovery of large negative magnetoresistivity in these materials has led to the expectation of potential applications in magnetic storage, magnetic sensor and magnetic switches. These materials have also potential applications as catalysts for automobile exhausts, oxygen sensors and magnetic refrigeration. The number of applications is so wide that Physicists, Chemists and Materials scientists have shown a keen interest in these materials.

There are several reports on La based divalent alkaline earth doped manganites and investigations on doping of Mn site with other magnetic and non-magnetic materials to understand the nature of magnetic interactions. The doping at Mn site in these mixed valent manganites by other transitions elements (T = Co, Cr, Cu, Fe, Ti, Ni, Ru etc.) or non-magnetic impurities like Al gives rise to change in Mn^{3+}/Mn^{4+} ratio, and the nearest neighbor environment. The magnetic and transport properties of such materials were found to be quite interesting. But there was lack of information on doping of these transition elements at Mn site of CMR materials based on mono-valent substitution in rare earth site. The mono-valent substitution based CMR materials with optimum Mn^{3+}/Mn^{4+} concentration with relatively small lattice distortion is already known viz. $La_{1-x}Ag_xMnO_3$, $La_{1-x}K_xMnO_3$, etc. Moreover the research work on electron doped manganites, where there is a possible double exchange interaction in Mn^{2+}-O-Mn^{3+} networks is limited.

In my research work, I have mainly chosen monovalent doped compounds. The monovalent doping has the advantage of creation of optimum concentration of Mn^{3+}/Mn^{4+} ions with relatively small level of doping. Thus, the lattice distortion can be kept minimum in the monovalent doped materials. I have planned to study the effect of substitution of transition metal ions (Co and Cr) and nonmagnetic Al ion at Mn site of $La_{0.85}Ag_{0.15}MnO_3$ compound to understand the nature of magnetic interactions. I have also studied the effect of the substitution of Cu at Mn site of La-Mn-O series to understand the nature of magnetic interactions. The monovalent Ag doped materials were prepared to explore the possible CMR

effect in Nd-Mn-O series. To understand the magnetic interactions in Mn^{2+}/Mn^{3+} networks, electron doped (Y, Ce)-Mn-O were prepared and studied.

I have prepared the following compounds for the present thesis work,

1. $La_{0.85}Ag_{0.15}Mn_{1-y}Co_yO_3$ (y=0-0.50)
2. $La_{0.85}Ag_{0.15}Mn_{1-y}Cr_yO_3$ (y=0-0.20)
3. $La_{0.85}Ag_{0.15}Mn_{1-y}Al_yO_3$ (y=0-0.20)
4. $LaMn_{1-y}Cu_yO_3$ (y=0-0.30)
5. $Nd_{1-x}Ag_xMnO_3$ (x=0-0.20)
6. $Y_{1-x}Ce_xMnO_3$ (x=0-0.15)

The above samples were characterized by using X-ray diffraction (XRD), Scanning electron micrographs (SEM), Energy-dispersive spectrum (EDS) and chemical titration. To understand the magnetic properties and different magnetic interactions involved, I have carried out temperature and frequency variations of ac susceptibility and, dc magnetization as a function of temperature and field. To explore the electronic transport properties, I have carried out temperature variations of electrical resistivity and magneto-resistivity.

The present thesis is divided into seven chapters, namely,

(1) Introduction (2) Experimental Techniques (3) Mn site doped (La, Ag)-Mn-O Series (4) Cu doped La-Mn-O Series (5) Hole doped (Nd, Ag)-Mn-O Series (6) Electron doped (Y, Ce)-Mn-O Series (7) Conclusions.

In chapter 1, different types of crystal structure of manganites are discussed. Various types of magnetic ordering, magnetic interaction and magnetic frustrations due to competing interactions are presented. Different conduction mechanism in electrical resistivity has been discussed briefly. The literature on divalent and monovalent doped mixed valent manganites and Mn site doped manganites have been reviewed with special emphasis on their crystal structure, electrical transport and magnetic properties

Chapter 2 is devoted to experimental techniques, where the method of material preparation and, physical measurements such as electrical resistivity, magneto-resistivity and ac susceptibility are discussed. The working principle of various sophisticated instruments such as X-Ray diffractometer, scanning electron microscope, vibrating sample magnetometer and SQUID magnetometer are presented.

In chapter 3, effect of Mn site doping in $(La_{0.85}Ag_{0.15})MnO_3$ by using transition elements (Co, Cr) and nonmagnetic element (Al) have been discussed.

$(La_{0.85}Ag_{0.15})Mn_{1-y}Co_yO_3$ compounds are found to be in single phase form upto y=0.50. Structural transition from rhombohedral to orthorhombic has been observed with

increasing doping. However, both Cr and Al doped samples $(La_{0.85}Ag_{0.15})$ $Mn_{1-y}M_yO_3$ (M= Cr, Al) could be prepared in single phase form upto 20% of doping. Both series are found to crystallize in rhombohedral structure.

From the magnetic measurements and analysis of Co doped samples, $(La_{0.85}Ag_{0.15})Mn_{1-y}Co_yO_3$, it is found that all Co doped compounds exhibit paramagnetic (PM)- ferromagnetic (FM) transitions along with low temperature competing magnetic interaction for $y \leq 0.20$ samples. The presence of competing interactions between Mn and Co networks is discussed and they give rise to spin glass like behavior. The ferromagnetic transition temperature was found to decrease with increase in doping upto y=0.20 and for further increase in doping, the T_c was found to increase. The possible reasons are discussed in detail.

The Cr doped materials exhibit PM-FM transition along with low temperature spin glass like behavior and these observations are discussed in detail. The Al doped samples are also found to exhibit paramagnetic to ferromagnetic transitions alongwith metal-insulator transitions. No low temperature anomaly has been observed in this series. The FM T_c is found to decrease systematically with increase in Al concentration due to the dilution of double exchange FM interaction. The measured magnetization of Cr doped samples is explained on the basis of FM and AFM interactions in various Mn-O-Mn and Mn-O-Cr networks. On the other hand in Al doped materials, it is explained on simple dilution of double exchange FM interaction.

Metal-Insulator (M-I) transitions and colossal magneto-resistivity have been observed up to 10 at% of Co doping. All other samples show semiconducting behavior. However, all Cr doped samples show semiconducting behavior along with colossal magneto-resistivity. The metal- insulator transition is found to hold on for all Al doped samples. The electrical conductivity in the metallic region for Al doped samples could be explained by electron-magnon scattering. The magneto-resistivity at low temperature is found to increase with the Al concentration.

In chapter 4, the effect of Cu doping at Mn site of $LaMnO_3$ has been discussed. All $LaMn_{1-x}Cu_xO_3$ compounds exhibit paramagnetic to ferromagnetic transitions. The analyses of temperature variations of linear and non-linear ac susceptibility, frequency variation of linear ac susceptibility and dc magnetization show that the present materials exhibit spin glass like behaviour at low temperature.

Chapter 5, deals with hole doped $Nd_{1-x}Ag_xMnO_3$ series. The study of their crystal structure, electrical resistivity, ac susceptibility and magnetization is presented. These materials are found to crystallize in Pbnm space group with increase in lattice parameters with doping. The magnetic properties were studied by measuring dc magnetization and ac susceptibility. Paramagnetic to ferromagnetic transition along with the signature of presence of competing anti-ferromagnetic interaction has been observed. The measured magnetization has been analyzed by using Brillouin function and by taking into account the ferromagnetic interaction. The measured magnetization has been explained on the basis of spin canting with ferromagnetic component along a unique axis and with anti-ferromagnetic interaction in a plane perpendicular to the unique axis. The analysis of frequency variation of ac susceptibility and harmonic susceptibility indicate the presence of spin glass like behavior below the ferromagnetic transition temperature.

Chapter 6, deals with electron doped $Y_{1-x}Ce_xMnO_3$ series. The samples were found to be crystallized in hexagonal structure. Temperature variations of ac susceptibility and magnetization measurements show that these Ce doped materials exhibit weak ferromagnetic transition. The observed ferromagnetic transition is attributed to the double exchange ferromagnetic interaction between Mn^{2+} and Mn^{3+} ions due to electron doping. The field variation of magnetization data could be analyzed based on bound magnetic polaron (BMP) model. The increase in saturation magnetization and decrease in bound magnetic polaron concentrations have been observed with increase in Ce doping.

The summary of conclusions drawn from the analysis of experimental data on four Mn site doped series, one monovalent hole doped series and one electron doped series have been presented in chapter 7. Except the doping of non-magnetic element, all other doping in place of Mn gives rise to competing magnetic interactions and reentrant spin glass like behavior. The results on (Nd, Ag)-Mn-O have been interpreted in terms of spin canting with ferromagnetic component along unique axis and antiferromagnetism in perpendicular plane. Weak double exchange ferromagnetic interaction in Mn^{2+}-O^{2-}-Mn^{3+} networks has been observed in electron doped (Y, Ce)-Mn-O series.

List of Abbreviations used in this Thesis

AFM Antiferromagnet (ic)

CMR Colossal Magnetoresistance

CO Charge-Ordered

DE Double Exchange

EDS Energy Dispersive Spectra

FC Field Cooled

FM Ferromagnet (ic)

FMI Ferromagnetic Insulator

FMM Ferromagnetic Metal

JT Jahn-Teller

PM Paramagnet (ic)

MR Magnetoresistance

SE Superexchange

SEM Scanning Electron Micrograph

VRH Variable Range Hopping

VSM Vibrating Sample Magnetometer

ZFC Zero-Field Cooled

Table of Contents

List of Figures

Chapter1:

Chapter 2:

Chapter 3:

$La_{0.85}Ag_{0.15}Mn_{1-y}Co_yO_3$ for y = 0.05- 0.50.

Figure 3.18: Temperature variations of linear out-phase ac susceptibility (χ''_1) of samples $La_{0.85}Ag_{0.15}Mn_{1-y}Co_yO_3$ for y = 0.05- 0.50.

Figure 3.19: χ''_1 versus temperature (T) measured at frequencies f = 333 Hz, 1333 Hz, 3333 Hz, 6333 Hz and 9333 Hz for the sample y=0.10 and 0.15 samples.

Figure 3.20: Plots of T_f versus frequency for the samples y= 0.15 and 0.20

Figure 3.21: Plots of ln(τ) versus ln[$(T_f-T_g)/T_g$] for the samples y= 0.15 and 0.20 .

Figure 3.22: χ'_3 versus T for the sample $La_{0.85}Ag_{0.15}Mn_{0.90}Co_{0.10}O_3$ and $La_{0.85}Ag_{0.15}Mn_{0.85}Co_{0.15}O_3$.

Figure 3.23: Temperature variations of electrical resistivity of $La_{0.85}Ag_{0.15}Mn_{1-y}Co_yO_3$. (a) y = 0.0, (b) y = 0.05, (c) y = 0.10 and (d) y = 0.15.

Figure 3.24: Temperature variations of electrical resistivity of $La_{0.85}Ag_{0.15}Mn_{1-y}Co_yO_3$.

Figure 3.25: Temperature variation of magneto resistivity ($(-\Delta\rho/\rho_0)$ for the y= 0.05, 0.10 and 0.15 samples.

Fig. 3.26: Resistivity versus $T^{-1/4}$ for the sample y = 0.20. The solid line shows the fit to Mott-VRH model.

Figure 3.27: Plots of ln[$\rho/T(\Omega cmK^{-1})$] versus (1/T) for y= 0.30 and 0.50 samples. Fit to ASPH model is shown as solid line.

Figure 3.28: XRD patterns of the samples $La_{0.85}Ag_{0.15}Mn_{1-y}Cr_yO_3$ (y = 0, 0.05, 0.10, 0.15 and 0.20).

Figure 3.29: XRD patterns for the samples y = 0.10 and 0.20. The circles represent experimental points and solid line represents Rietveld refined data. The bottom line shows the difference between experimental and refined data. The marked 2θ positions are the allowed Bragg peaks.

Figure 3.30: SEM image (magnification 8000) of $La_{0.85}Ag_{0.15}Mn_{0.85}Cr_{0.15}O_3$ sample.

Figure 3.31: Typical SEM-EDS spectrum for y=0.15 sample.

Figure 3.32: The temperature dependence of (ZFC) zero field cooled (Circles) and (FC) field cooled (square) magnetization for y=0.05, 0.10, 0.15, 0.20 samples.

Figure 3.33: Plot of ferromagnetic (FM) transition temperature, T_c as a function of doped Cr concentration, y.

Figure 3.34: $1/\chi_{dc}$ versus temperature for the samples (a) y=0.10 and (b) y=0.15. Solid lines represent fit to the Curie-Weiss law.

Chapter 4:

Chapter 5:

Chapter 6:

Chapter 7:

List of Table

Chapter 1:

Chapter 3:

Table 3.12: Parameters obtained from magnetization measurements of $La_{0.85}Ag_{0.15}Mn_{1-y}Cr_yO_3$. θ_C (Curie temperature), C (Curie constant), μ_{eff} (μ_B) have been found from inverse dc susceptibility fitting. μ_{th} is the theoretical paramagnetic moment.

Table 3.13: Parameters obtained from Brillouin function fitting to magnetization data. S_{eff} is the effective spin contribution towards FM interaction. M_S is the experimental saturation magnetization.

Table 3.14: Parameters obtained from frequency variation of ac susceptibility measurement. T_f, T_g are spin glass freezing temperature and spin glass temperature respectively. τ_0 is the characteristic time constant.

Table 3.15: Parameters obtained from the Rietveld analysis of XRD patterns for the samples $La_{0.85}Ag_{0.15}Mn_{1-y}Al_yO_3$ (y = 0.05, 0.10, 0.15 and 0.20). R_p, $R_{\omega p}$, R_{exp}, R_{Bragg}, R_F and χ^2 are the reliability factors. S_C is the crystallite size.

Table 3.16: Cationic ratio determined from EDS analysis of $La_{0.85}Ag_{0.15}Mn_{1-y}Al_yO_3$ series.

Table 3.17: Parameters obtained from magnetization measurements of $La_{0.85}Ag_{0.15}Mn_{1-y}Al_yO_3$. θ_C (Curie temperature), C (Curie constant) have been found from Curie-Weiss law fit of susceptibility.

Table 3.18: Parameters obtained from Brillouin function fitting to magnetization data. S_{eff} is the effective spin contribution towards FM interaction. M_S is the experimental saturation magnetization.

Table-3.19: Parameters obtained from electrical resistivity measurements and analysis. ρ_0 is the temperature-independent residual resistivity. ρ_2 and $\rho_{4.5}$ are respectively the coefficients of electron-electron and electron magnon scatterings.

Chapter 4:

Table 4.1: Parameters obtained from the XRD analysis of the samples $LaMn_{1-y}Cu_yO_3$ (y = 0.05, 0.10, 0.15, 0.20 and 0.30). S_C is the average crystallite size obtained from the line broadening of the XRD pattern.

Table 4.2: The cationic ratio determined from EDS analysis for $LaMn_{1-y}Cu_yO_3$ compounds.

Table 4.3: Parameters obtained from magnetization measurement of $LaMn_{1-y}Cu_yO_3$. T_C is ferromagnetic transition temperature. θ_C (Curie temperature), C (Curie constant), μ_{eff} (μ_B) have been found from inverse dc susceptibility fitting.

Table 4.4: Parameters obtained from Brillouin function fitting to magnetization data. S_{eff} is the effective spin contribution towards FM interaction. M_S is the experimental saturation magnetization.

Table 4.5: Parameters obtained from the measurement and analysis of frequency variation of linear susceptibility. T_f and T_g are freezing and spin glass transition temperature respectively. τ_0 is the characteristic time constant and $z\nu$ is the critical exponent.

Table 4.6: The spin glass freezing temperature peaks, T_f at two different field amplitudes.

Chapter 5:

Table 5.1: Parameters obtained from the Rietveld analysis of XRD patterns of $Nd_{1-x}Ag_xMnO_3$ (x= 0.05, 0.10, 0.15, 0.20). The numbers in brackets are estimated errors.

Table 5.2: The cationic ratio determined from EDS analysis for $Nd_{0.85}Ag_{0.15}MnO_3$ samples.

Table 5.3: Parameters obtained from the measurement and analysis of magnetization of $Nd_{1-x}Ag_x\ MnO_3$.

Table 5.4: Parameters obtained from Brillouin function fitting to magnetization data of $Nd_{1-x}Ag_xMnO_3$. S_{eff} is the effective spin contribution towards FM interaction. β is spin canting angle. M_s is the experimental saturation magnetization.

Table 5.5: Results obtained from resistivity analysis. Here, ρ_{0s} is the ES residual resistivity and T_{0s} is the ES characteristic temperature ε_r is the dielectric constant.

Chapter 6:

Table 6.1: Parameters obtained from the XRD analysis of the samples $Y_{1-x}Ce_xMnO_3$ (x = 0.0, 0.05, 0.10 and 0.15). R_p, $R_{\omega p}$, R_{exp}, R_{Bragg}, R_F and χ^2 are the reliability factors. S_C is the crystallite size.

Table 6.2: The cationic ratio determined from EDS analysis for $Y_{1-x}Ce_xMnO_3$ samples.

Table 6.3: Parameters obtained from ac susceptibility measurement and Hall-effect measurement.

Table 6.4: Parameters obtained from magnetization measurement of $Y_{1-x}Ce_x\ MnO_3$. T_C is the ferromagnetic transition temperature calculated from dM/dT. θ_C (Curie temperature), C (Curie constant), μ_{eff} (μ_B) have been found from the fit of dc susceptibility to Curie-Weiss law.

Table 6.5: Parameters obtained from analysis of M- H curve employing Bound Magnetic Polaron (BMP) model. M_0' is the spontaneous magnetization, χ_m is the susceptibility of the matrix and m_{eff} is effective spontaneous moments per BMP. N is number of BMPs.

Chapter 1: Introduction

One group of fascinating compounds with many potential applications in spintronics devices are the mixed valence perovskite manganites. The versatility of perovskite manganites for electronic applications is demonstrated by the fact that, these materials exhibit wide range of conductivity ranging from highly conducting metallic state to insulating state. The number of applications are so wide that Physicists, Chemists and Materials scientists have shown a keen interest in these materials. The discovery of large negative magneto-resistivity in 1993 in these materials has renewed the attention of researchers because of their potential applications in magnetic storage and retrieval, magnetic sensor and magnetic switches [1]. The phenomenon of appearance of large negative magneto-resistivity, in the vicinity of ferromagnetic transition temperature is called colossal magneto-resistivity (CMR) [2]. They are also potential candidates as catalysts for automobile exhausts, oxygen sensors and magnetic refrigeration.

The mixed valent manganites are described by a general chemical formula $R_{1-x}A_xMnO_3$, where R is a trivalent rare earth element and A is a divalent alkaline earth element or monovalent alkali element. Rare earth manganites usually form a perovskite structure. In parent compounds Mn ions are generally in Mn^{3+} state. The mixed valence oxides $(R^{3+}_{1-x}A^{2+}_x)(Mn^{3+}_{1-x}Mn^{4+}_x)O_3$ can be obtained by the substitution of mono-valent/divalent elements in place of R or by doping at Mn site. One can also get mixed valent manganites by self doping in parent compounds, i.e. by creating vacancy in Mn or R site [3-7]. Such a doping leads to the oxidation of some of Mn^{3+} ions into Mn^{4+} state, thereby having a mixture of Mn^{3+}-Mn^{4+}. The mixed valent Mn ions play a major role on CMR properties of manganite perovskites. These materials exhibit transition from paramagnetic insulator to ferromagnetic metallic state upon cooling with CMR behaviour. They are explained on the basis of Zener double exchange ferromagnetic (FM) interaction in Mn^{3+}-O^{2-}-Mn^{4+} networks [8]. In addition to the mixed valency, ionic size mismatch, Mn-O bond length, $\angle Mn-O-Mn$ bond angle, strong electron-phonon interaction, etc. play a considerable role on CMR behaviour [9, 10].

These materials continued to draw the attention of Physicist due to their interesting and challenging physical properties such as charge ordering, orbital ordering, magnetic phase separation, reentrant spin glass like behaviour etc. In this chapter, the crystal structure, magnetic and electrical transport properties of manganites are reviewed.

1.1. Crystal Structure

The crystal structure parameters such as atomic positions, inter-atomic distance, atomic bond angles, number of nearest neighbour elements, their nature and their co-ordination symmetry, unit cell dimensions, etc. play a crucial role in determining the magnetic, mechanical and electrical properties of any material. So, it is very important to understand the crystal structure of materials under study in order to explain the various physical properties.

The crystal structure of rare earth (R) manganites $RMnO_3$, originates from the ideal cubic perovskite structure as shown in Figure1.1. Here the R ion is situated at the body centered position and Mn ions are at the corner of the cubic cell. The O ions are in octahedral co-ordination with Mn ions. The regular arrangement of MnO_6 octahedra with vertex sharing can be seen in Figure 1.1. Here Mn-O-Mn bond angle is 180° and the unit cell dimensions are equivalent to Mn-Mn bond lengths. However, the actual crystal structure of both undoped and doped compounds of $RMnO_3$ series deviates from the ideal cubic structure due to some of the following reasons;

- The Jahn-Teller distortions due to the presence of Jahn Teller active Mn^{3+} ions and oxygen off stoichiometry or cation vacancy lead to the lattice distortion and reduced crystal symmetry in undoped $RMnO_3$.
- In doped $RMnO_3$ series, the ionic size mismatch at R site leads to the tilting of MnO_6 octahedra towards or away from the R ion, because of vertex sharing of MnO_6. The tilting of one MnO_6 octahedra produces tilting in the neighbouring octahedral, thereby leading to co-operative tilting of MnO_6 octahedra. Such tilting gives rise to change in crystal symmetry and space group.

The above change in crystal structure gives rise to change in Mn-O bond lengths and Mn-O-Mn bond angle, which play a major role on the magnetic and electrical properties of the materials.

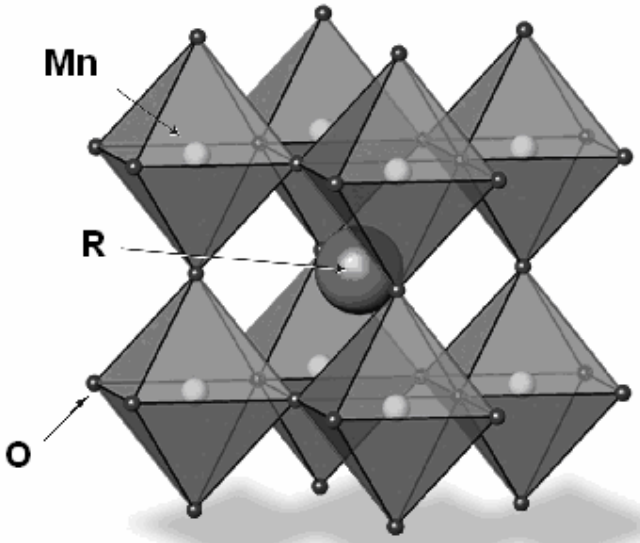

Figure 1.1: Structure of perovskite with simple cubic ABO_3 unit cell.

$RMnO_3$ compounds are prepared for a wide range of R ions with different ionic sizes. The stability and type of crystal structure depend upon size of R ions. It is quantitatively determined based on Goldschmidt tolerance factor, $t = (r_A + r_O)/[\sqrt{2}(r_B + r_O)]$. Here, t is a measure of lattice distortion from ideal cubic structure. r_A, r_B and r_O are the radii of the A site (R), B site, (Mn) and Oxygen ions respectively in ABO_3 structure. Stable perovskite structure is expected for $0.80 \leq t \leq 1.1$ [11]. Manganites based on R ions having relatively large ionic radii such as La, Ce, Pr, Nd, Sm, Eu, Gd, Tb, Dy etc. are expected to form in the perovskite structure with rhombohedral or orthorhombic symmetries. However, $RMnO_3$ based manganites with smaller R ions such as Ho, Er, Tm, Yb, Lu, Y, Sc etc. are found to crystallize in the hexagonal structure. Moreover CMR materials are prepared by doping various alkaline earth, alkali ion, etc., in place of R ions. So the effective ionic radius of A site ion, $\langle r_A \rangle$ depends on the R ion and the dopant. So, depending upon $\langle r_A \rangle$ various crystal structure or crystal structure transition have been observed [11]. Typical crystal structure of $(R_{1-x}A_x)MnO_3$ compounds with orthorhombic symmetry is shown in Figure 1.2 (a), where we can see the reduced crystal symmetry compared to ideal cubic due to the tilting of MnO_6 octahedra. If a_p is the unit cell dimension of cubic symmetry, the lattice parameters of orthorhombic structure can be approximately written as, $a \cong b = \sqrt{2}\, a_p$ and $c = 2a_p$. It has Pbnm space group symmetry. The general atomic positions are given as following,

Table 1.1: Atomic positions of $RMnO_3$ in Pbnm space group.

Ion	Site	(x, y, z)
R	4c	(x, y, ¼) ≅ (0.99, 0.03, ¼)
Mn	4b	(1/2, 0, 0) ≅ (1/2, 0, 0)
O_1	4c	(x, y, ¼) ≅ (0.07, 0.49, ¼)
O_2	8d	(x, y, z) ≅ (0.72, 0.28, 0.04)

The CMR materials such as $(La_{1-x}Ca_x)MnO_3$ [12] and $(La_{1-x}Ba_x)MnO_3$ [13, 14] are found to exhibit above Pbnm space group with typical lattice parameters, $a = 5.474$, $b = 5.460$ and c= 7.715 Å and Mn-O-Mn bond angle in the order of 155 to 160°. The number of formula units per unit cell, Z in the above orthorhombic structure is 4.

The typical rhombohedral crystal structure of $(R_{1-x}A_x)MnO_3$ compounds is shown in Figure 1.2 (b). Here also the Mn is octahedrally coordinated with O ions. The rotation of MnO_6 octahedra along the three fold axis of the ideal cubic structure gives rise to rhombohedral symmetry. These structural parameters are generally referred in hexagonal co-ordinate system. It follows the $R\bar{3}c$ space group. The atomic positions of rhombohedral cell in hexagonal co-ordinates are given as following:

Table 1.2: Atomic positions of $RMnO_3$ in $R\bar{3}c$ space group in hexagonal coordinate.

Ion	Site	x,	y,	z
R	6 *a*	0	0	¼
Mn	6 b	0	0	0
O	18e	0.55 (x)	0	¼

Unlike the orthorhombic case, there is no buckling of MnO_6 octahedra and hence the Mn-O bond lengths are identical in all the three directions. The Mn-O-Mn bond angle in this structure is found to be slightly larger than that of orthorhombic cell and is around 165°. The Z value is found to be 6.

Most of the mono-valent and alkali ion doped manganites with relatively large A site ionic radius $<r_A>$ exhibits such rhombohedral structure [14-20]. The typical lattice parameters of $La_{0.82}Na_{0.18}MnO_3$ compound with rhombohedral structure are reported to be $a = b = 5.490$ Å and c= 13.319 Å with typical Mn-O bond-length and Mn-O-Mn bond angle 1.951 Å and 165.2° respectively [15].

Unlike the above two perovskite structures for manganites, hexagonal structure with $P6_3mc$ space group is generally formed for relatively small $<r_A>$. The crystal structure of hexagonal cell is shown in Figure 1.2 (c). Unlike the perovskite structure, the Mn is co-ordinated with five O ions forming MnO_5 polyhedrons. In each MnO_5 polyhedron, Mn is surrounded by three oxygen ions in a plane and two apical oxygen ions as shown in Figure 1.2 (c). Each adjacent triangular O ions are separated by a layer of triangular R ion. The atomic position in $P6_3mc$ space group of hexagonal cell is given as following;

Table 1.3: Atomic positions of $RMnO_3$ in $P6_3mc$ space group.

Atom	Site	(x, y, z)	
R_1	2 *a*	(0, 0, z)	≅ (0, 0, 0.27)
R_2	4 b	(1/3, 2/3, z)	≅ (1/3, 2/3, 0.23)
Mn	6 c	(x, 0, 0)	≅ (0.32, 0, 0)
O_1	6 c	(x, 0, z)	≅ (0.32, 0, 0.16)
O_2	6 c	(x, 0, z)	≅ (0.63, 0, 0.34)
O_3	2 *a*	(0, 0, z)	≅ (0, 0, 0.48)
O_4	4 b	(1/3, 2/3, z)	≅ (1/3, 2/3, 0.02)

$YMnO_3$ based materials are found to exhibit hexagonal structure [21, 22]. The typical lattice parameters are reported to be $a = b = 6.205$ Å and c= 11.394Å. The Mn-O bond length in the plane and perpendicular to the plane are respectively 1.86 Å and 2.00 Å. Materials with such crystal structure mainly show antiferromagnetic behaviour.

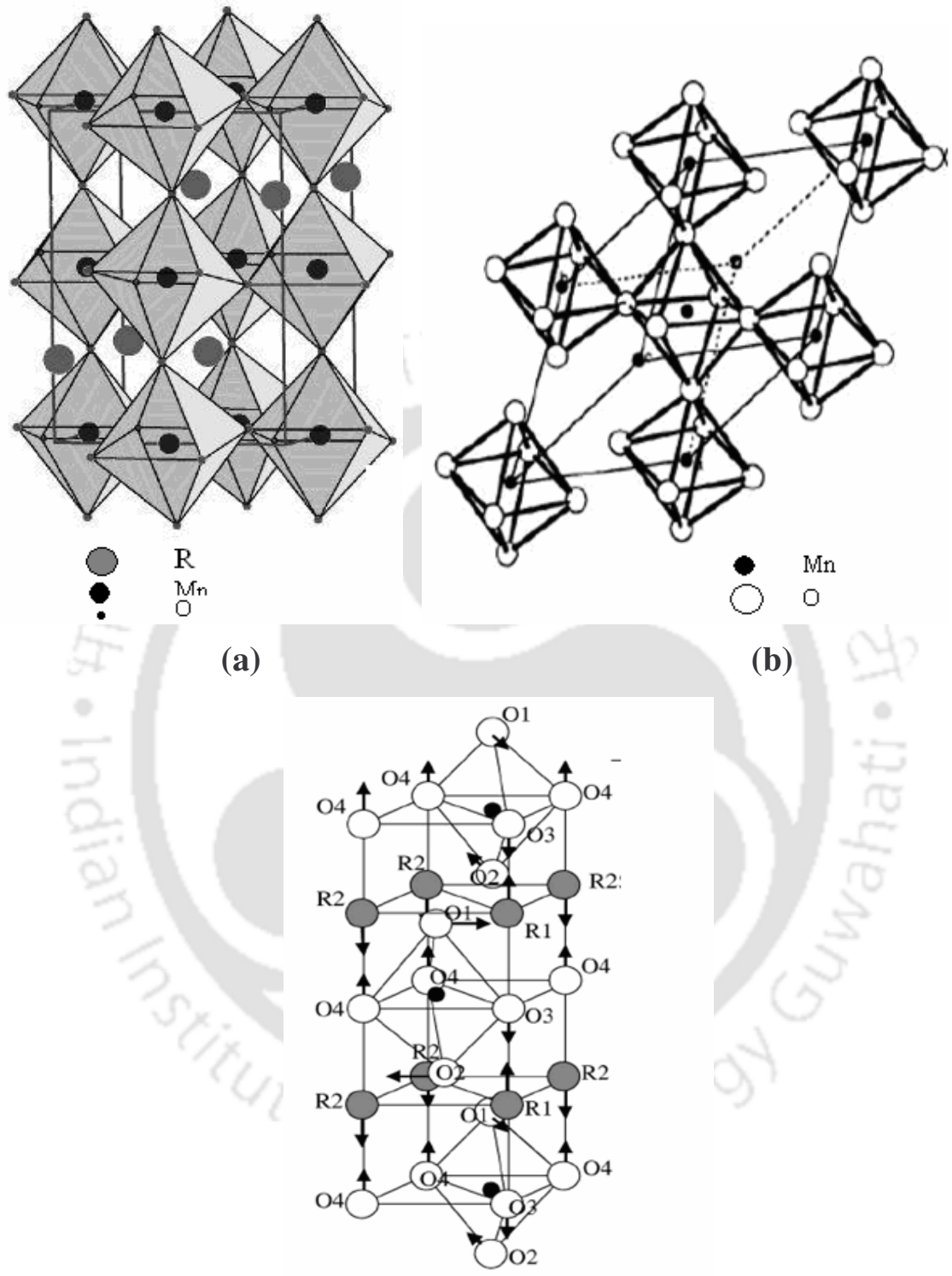

Figure 1.2: (a) Orthorhombic structure of manganites (b) Rhombohedral Structure of manganites (c) Typical hexagonal structure of manganites.

1.2. Crystal Field and Jahn-Teller Distortion

Atoms in a solid with a regular crystal structure are no longer free and they are under the influence of electric field derived from the neighbouring atoms in the crystal. Such electric fields are called crystal field [23]. Crystal fields depend on the local environments such as octahedral, tetrahedral co-ordination, etc. In perovskite manganites, each Mn ions is surrounded by O ions in octahedral co-ordination. So, in this case the crystal field originates from electrostatic repulsion from oxygen orbitals. Since the atomic environment and electron density of orbitals (except s-orbital) are not spherical in nature, so, different electronic orbitals are expected to behave in a different manner to the crystal field.

The transition metal ions such as Mn^{3+}, etc. have 3d orbital at the outermost and the electron energy levels in 3d shell are under the influence of crystal field. Since the magnetic properties of transition elements depend on the spin of the electrons in the 3d orbital, the magnetic properties of these materials are very sensitive to crystal field. The d shell has five orbitals namely d_{xy}, d_{yz}, d_{zx}, d_{z^2}, $d_{x^2-y^2}$; out of them, the first three are called t_{2g} orbitals and last two are called e_g orbitals. In the absence of crystal field, all the five levels are degenerate. The t_{2g} orbitals point along in between x, y and z axes, but the e_g orbitals point along the direction of x, y and z axes. So, in MnO_6 octahedral environment, the electrons in 3d shell of Mn ions are under the Coulomb interaction of electrons from the 2p shell of O ions. Since the p_x, p_y, p_z orbitals of O point along x, y and z directions respectively, there will be a overlapping of e_g orbitals of Mn with p electron orbitals of O and hence the energy of e_g orbitals is raised compared to t_{2g} orbitals. Figure 1.3(a) shows the typical overlapping of one of e_g orbitals ($d_{x^2-y^2}$) with p orbital of neighbouring O in a two dimensional diagram. On the other hand, we can see no such overlapping with t_{2g} orbital, as shown in Figure 1.3 (b).

In view of the above crystal field effect, the five fold degeneracy of d orbitals are lifted by raising the energy of e_g orbitals with respect to t_{2g} orbitals as shown in Figure 1.3 (c) for octahedral co-ordination [23].

The energy difference between t_{2g} and e_g orbitals due to crystal field effect on $LaMnO_3$ is approximately 1.5eV [10]. It may be noted that for tetrahedral co-ordination, the energy splitting will be in the opposite way, i.e. t_{2g} levels will be lifted compared to e_g level. So, the environment plays a very important role in crystal field. Because of the crystal field effect, the magnetic moment of transition metal ions does not follow the estimated theoretical moment based on total angular momentum, $\mu_{th} = g\mu_B\sqrt{J(J+1)}$ as stipulated by Hund's

rules. The crystal field energy is mostly stronger than spin-orbit coupling as per Hund's third rule and it leads to orbital quenching, i.e. L=0. It is rather close to magnetic moment due to spin only contribution, $\mu_{th} = g\mu_B\sqrt{S(S+1)}$.

Jahn-Teller (JT) distortion is a particular type of lattice distortion such as elongation of MnO_6 octahedra in a particular direction. The Jahn-Teller distortion is significant for partially filled orbitals, where there is a net energy gain. The JT distortion leads to increase in elastic energy and decrease in electronic energy such that there is a net reduction in energy. Mn^{3+} ions are JT active, while Mn^{4+} ions are inactive for JT distortion in octahedral environment. Mn^{3+} ions have one e_g electron out of two orbitals namely, d_{z^2} and $d_{x^2-y^2}$. The elongation of MnO_6 octahedra along z-axis gives rise to reduction in d_{z^2} level compared to $d_{x^2-y^2}$ level. Since, there is only one e_g electron which occupies d_{z^2} level, there is a reduction in electronic energy. The splitting of e_g and t_{2g} orbits due to JT distortion is shown in Figure 1.3 (c). On the other hand, Mn^{4+} ion does not have e_g electron, so reduction in electronic energy is not feasible and hence no JT distortion.

The Mn-O bonds are primarily responsible for the electrical conduction throughout the sample and long range ferromagnetic (FM) double exchange interaction. In an octahedral environment, the orbitals in the Mn t_{2g} triplet (xy, yz and zx symmetries) have poor overlap with the oxygen 2p orbitals and electrons are all strongly localized. However, the e_g orbitals (d_{z^2} and $d_{x^2-y^2}$) are more diffuse and point towards the O 2p orbitals. So, e_g electrons in manganites play a major role for FM metallic conduction and CMR behaviour. The shorter the Mn-O bond length, better the chance of Mn-O-Mn bonds being linear (180°) and better the overlap between e_g and 2p orbitals. Thus the presence of JT distortion increases the Mn-O bond length along z-direction and reduces electron overlap and which in turn gives rise to reduction in long range DE interaction. Hence JT distortion plays a crucial role in the magnetic properties of manganites.

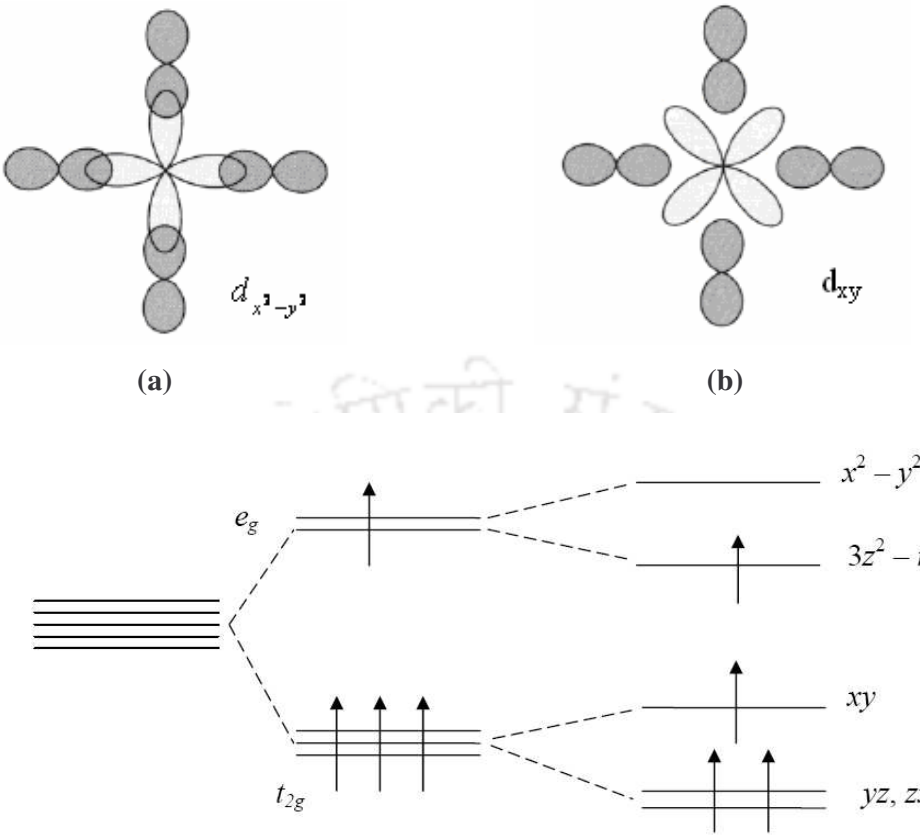

Figure 1.3 (a): Typical overlapping of one of the e_g orbitals ($d_{x^2-y^2}$) with p orbital of neighbouring O in a two dimensional diagram **(b)** One of the t_{2g} orbitals with p orbital **(c)** The crystal field splitting of d shell in octahedral environment. The Jahn-Teller distortion leads to a further splitting of both the t_{2g} and e_g states.

1.3. Charge and Orbital Ordering in Manganites

The charge ordering is an interesting phenomenon that occurs in transition metal oxides, where there is an ordering of cations of different charges on specific lattice sites. This phenomenon of charge ordering is well known in Fe_3O_4, where it is called Vervey transition [24]. The charge ordering in rare earth manganites was discovered from the pioneering experimental work of Wollan and Koehler [25] and the simultaneous qualitative theoretical work of Goodenough [9]. Wollan and Koehler studied the magnetic structure of $La_{1-x}Ca_xMnO_3$ compounds for different x values by recording neutron diffraction patterns. They have found that the patterns recorded for x=0.50 sample could be explained only by the combination of C-type and E-type magnetic structure, such that there is a coherent stacking of octants of C-type and E-type structure. Goodenough [9] explained on the basis of covalent and semi-covalent bonding hypothesis that such structure is possible for regular arrangement of Mn^{3+} and Mn^{4+}.

In alkaline earth doped manganites for x<0.5, the concentration of Mn^{3+} ions is more than that of Mn^{4+} ions. In such case, the Mn^{3+} and Mn^{4+} ions are highly in a disordered state, i.e. they are randomly distributed in the allowed Mn lattice site. The Mn^{3+}-O^{2-}-Mn^{4+} network is degenerated with Mn^{4+}-O^{2-}-Mn^{3+}. So, the e_g electrons are freely transported within the networks leading to FM double exchange interaction. However for x=0.5, where the concentration of Mn^{3+} and Mn^{4+} ions are equal, these ions undergoes charge ordering below certain temperature. Typical plot of charge ordered state is shown in Figure 1.4 (a), where $Mn^{3+}$and Mn^{4+} ions are regularly arranged at alternative site. This ordering is possible because of migration of e_g electrons from Mn^{3+} to Mn^{4+} at the charge ordering transition temperature, T_{CO}. This ordering is also facilated by lattice distortion to keep the net electro-static and elastic energy minimum and they dominate over the electronic energy.

In the charge ordered state, the degeneracy of Mn^{3+}-O^{2-}-Mn^{4+} network is lost, so the double exchange FM interaction is ceased leading to electrically insulating behaviour of the material. The charge ordering in CE-type structure leads to antiferromagnetic interaction and would be discussed under magnetic properties section.

Kanamori [26] pointed out that the carriers in mixed valence manganites may be strongly coupled to local lattice distortions. Orbital ordering can occur at certain carrier concentrations when the d electrons occupy an asymmetric orbital, as shown in Figure 1.4(b). The driving force is partly due to direct electrostatic repulsion of the charge clouds; however

the coupled Jahn-Teller distortions of adjacent octahedral stabilize such effect. Figure 1.4(c) illustrates the coupled charge and orbital ordering, which is expected for x= 1/2.

The charge ordering has been studied by several groups [27-29]. Knizek *et al.* [27] reported that $Pr_{1-x}Sr_xMnO_3$ exhibits charge ordering at 160 K for x=0.50. The charge ordering is associated with shortening of c-axis length and elongation of a and b axes length of unit cell in Pbnm space group. The charge ordering has been seen as super-lattice points in the electron diffraction patterns recorded by Ramirez *et al.* [28] and Chen *et al.* [29] on (La, Ca)-Mn-O series.

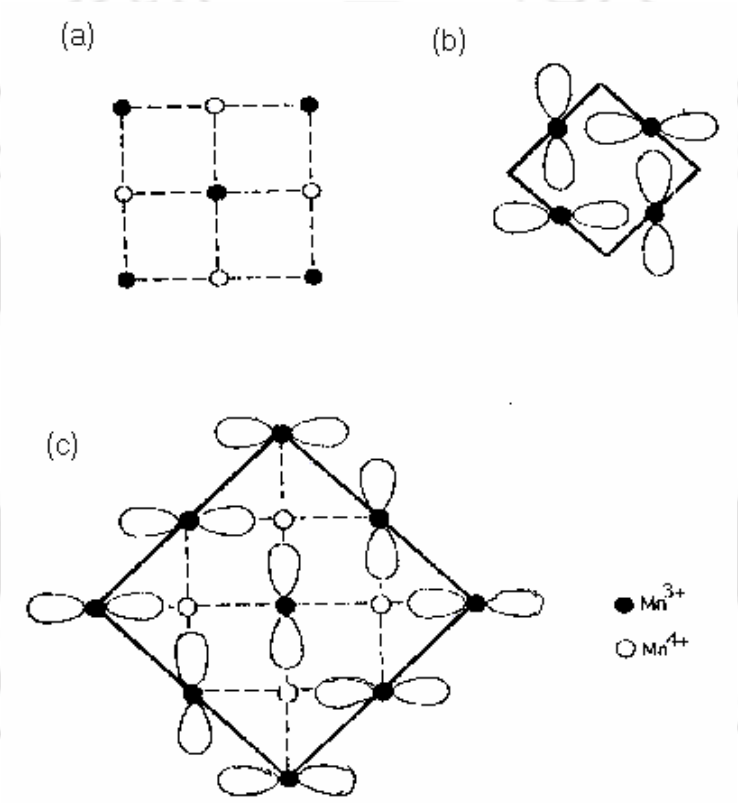

Figure 1.4: (a) Charge ordering of Mn^{3+} and Mn^{4+} ions in a crystal with x = ½. (b) Orbital ordering of the d_{z^2} orbitals of Mn^{3+} and Mn^{4+} when x = 0. (c) Combined charge and orbital ordering when x = ½ (Mn^{4+} sites shown by full dots, Mn^{3+} by lobes).

The charge-ordered state can be melted into a metallic ferromagnetic state, by the application of external magnetic field [30-32]. The transition from AFM insulating behaviour in the absence of field to FM metallic behaviour in the presence of field is nothing but a first order insulator to metal transition induced by the applied field [33, 34]. The above effect is

generally accompanied by considerable hysteresis [33]. Rao *et al.* [35] reported that the charge ordering transition temperature T_{CO} increases with decrease in average A site ionic radius $<r_A>$in rare earth manganites.

Investigations on charge ordering have shown that the lattice distortion localize the charge carriers and initiate charge-ordering. Eventually, the coulomb interaction wins over the kinetic energy of the electrons to form long range CO state. The scale of the energy involved with CO is around 0.5-1eV. This is similar to the unscreened bare nearest neighbour coulomb repulsion. This is also close to the approximate energy required to create ~1% orthorhombic distortion.

Li *et al.* [36] found the evidence for the existence of a CO transition in $Nd_{0.75}Na_{0.25}MnO_3$ by analyzing the electron diffraction patterns recorded at different temperatures. Pillai *et al.* [37] found that the replacement of Bi ions by La ions resulted in the collapse of high temperature charge ordering state of $Bi_{0.5}Sr_{0.5}MnO_3$ and it order ferromagnetically (FM) with T_C around 355 and 330 K for x=0.1 and 0.4, respectively. Murata *et al.* [38] have investigated the microstructure formed in association with charge ordering transition in perovskite manganites such as $Pr_{0.55}Ca_{0.45}MnO_3$ and $Nd_{0.5}Sr_{0.5}MnO_3$. They have investigated the magnetic field dependence of T_{CO} by magnetization measurements and found that the T_{CO} decreases parabolically with increase in magnetic field.

Thus the CO plays a very important role in shaping the structural, electrical and magnetic properties of the materials.

1.4. Magnetic Ordering

Materials having appreciable magnetic moment in macroscopic scale are generally referred as magnetic materials. The fundamental object of magnetism is magnetic moment. The origin of magnetic moment in material lies in the orbital and spin motions of electrons and how the electrons interact with one another. The magnetism in microscopic scale depends upon how atoms or group of atoms interact among themselves and to external field. The best way to introduce the different types of magnetism is to describe how materials respond to magnetic fields. The main distinction is that in some materials there is no collective interaction of atomic magnetic moments, whereas in other materials there is a very strong interaction between atomic moments [23, 39, 40]. The magnetic behaviour of materials can be classified into the following major groups:

1. Diamagnetism 2. Paramagnetism 3. Ferromagnetism 4. Antiferromagnetism

Materials in the first two groups are those that exhibit no collective magnetic interactions and are not magnetically ordered except for a special case i.e. in superconductors. Materials in the last two groups exhibit long-range magnetic order below a certain critical temperature. Ferromagnetic materials are usually what we consider as being magnetic. The remaining three are so weakly magnetic that they are usually thought of as nonmagnetic.

1.4.1. Diamagnetism

Diamagnetism is a fundamental property of all matter, although it is usually very weak. It is due to the non-cooperative behaviour of orbiting electrons when exposed to an applied magnetic field. Diamagnetic substances are composed of atoms, which have no net magnetic moments (i.e. all the orbital shells are filled and there is no unpaired electron). However, when exposed to a magnetic field, the electrons orient themselves such that they try to oppose the applied magnetic field. So, they register negative magnetization and hence negative susceptibility.

1.4.2. Paramagnetism

Some of the atoms or ions in this class of materials have a net magnetic moment due to unpaired electrons in partially filled orbital. However, the individual magnetic moments do not interact magnetically, and like diamagnetism, the magnetization is zero in the absence of external magnetic field. In the presence of a field, there is a partial alignment of the atomic magnetic moments in the direction of the field, resulting in a net positive magnetization and positive susceptibility. In addition, the efficiency of the field in aligning the moments is

opposed by the randomizing effects of temperature. So, they exhibit a temperature, T dependent susceptibility, χ known as the Curie Law, $\chi = \frac{C}{T}$, with a Curie constant C.

In classical theory, each atomic moment is considered as magnetic dipole along a particular angle θ as with respect to applied field and the average magnetic moment is written as, $< \mu^z > = \mu L(x)$. Here, μ is the magnetic moment of each dipole and L(x) is the Langevin function, $L(x) = Coth\, x - \frac{1}{x}$. L(x) is the analog of Brillouin function. This function explains well the magnetization of small particles made up of atomic clusters.

By considering the quantization of total angular momentum of each atom, the average magnetic moment per atom aligned along the magnetic field direction, (i.e. z direction) of any paramagnetic sample can be written as [23, 39, 40].

$$\langle \mu_J^z \rangle = g\mu_B\, JB_J(x) \qquad \text{---------- (1.1)}$$

Here, g is Lande' s factor and it depends on spin-orbit coupling of electrons in atom. J is total angular momentum quantum number. $\mu_B = 9.27 \times 10^{-24}$ J/T is Bohr magneton. $B_J(x)$ is Brillouin function which can be written as,

$$B_J(x) = \frac{1}{J}\left[\left(J + \frac{1}{2}\right) Coth\left(J + \frac{1}{2}\right)x - \frac{1}{2} Coth\,\frac{x}{2}\right] \qquad \text{---------- (1.2)}$$

Here the variable $x = \frac{g\mu_B}{kT}B$, where k is the Boltzmann constant and T is the temperature. If N is number of atoms per unit volume, the volume magnetization M can be written as,

$$M = N\langle \mu_J^z \rangle = Ng\mu_B\, JB_J(x) \qquad \text{---------- (1.3)}$$

For the selection of magnetic field B and temperature T such that x is small, $B_J(x) \sim \frac{(J+1)}{3}x$. Such assumption holds true for paramagnetic sample for a wide temperature region. So,

$$M = Ng\mu_B\, J\frac{(J+1)}{3}x = \frac{Ng^2\mu_B^2 B}{3kT}J(J+1) \qquad \text{---------- (1.4)}$$

or, the susceptibility, $\chi = \frac{\mu_0 Ng^2\mu_B^2}{3kT}J(J+1)$ ---------- (1.5)

It is in the form of Curie law C/ T.

Thus the magnetic susceptibility based on Brillouin function expression reduces to Curie-law.

1.4.3. Ferromagnetism

Unlike paramagnetic materials, the atomic moments in these materials exhibit very strong interactions. These interactions are produced by electronic exchange forces and result in a parallel alignment of atomic moments. The exchange force is a quantum mechanical phenomenon due to the relative orientation of the spins of two electrons. Ferromagnetic materials exhibit parallel alignment of moments resulting in large net magnetization even in the absence of a magnetic field. Two distinct characteristics of ferromagnetic materials are spontaneous magnetization and Curie temperature

The spontaneous magnetization is the net magnetization that exists inside a uniformly magnetized microscopic volume called domain even in the absence of a magnetic field. All the magnetic moments align in a single unique direction. This effect is generally due to exchange interactions. The magnitude of this magnetization, at 0 K, depends on the individual atomic magnetic moments in the magnetic domain. A related term is the saturation magnetization. The saturation magnetization is the maximum induced magnetic moment per unit volume that can be obtained in a magnetic field (H_{sat}); beyond this field no further increase in magnetization occurs. The difference between spontaneous magnetization and the saturation magnetization has to do with magnetic domains.

Even though electronic exchange forces in ferromagnets are very large, thermal energy eventually overcomes the exchange and produces a randomizing effect. When a FM material is heated, the thermal energy causes their magnetic moments to fluctuate. If the thermal energy becomes larger than the exchange energy, which keeps the moments parallel to each other, the materials tend to lose their magnetic ordering, becoming PM. The temperature at which this transformation occurs is called Curie temperature, (T_C). So, they undergo transition from disordered PM state to ordered FM state at T_c.

The phenomenon of ferromagnetism can often be well described by a mean field or molecular field model. The molecular field model simply assumes that all the interactions from the neighbouring magnetic species can be described in terms of an effective internal or molecular field B_m, which is proportional to the magnetization, i.e. $B_m = \lambda M$, where λ is the Weiss molecular field constant. The total magnetic field on an atom is then the sum of the applied field B_a and the molecular field B_m. So, the expression for magnetization can be written by following equation 1.3 with the modification that

$$x' = \frac{g\mu_B}{kT}\left(B_a + \lambda M\right) \qquad \text{---------- (1.6)}$$

$$M = Ng\mu_B \, JB_J\left(x^{/}\right) \qquad \text{---------- (1.7)}$$

At temperature close to T_c, B_J ($x^{/}$) is small and can be approximated to

$$B_J\left(x^{/}\right) \to \frac{(J+1)}{3}x^{/} \qquad \text{---------- (1.8)}$$

or, $$M = \frac{Ng^2\mu_B^2 J(J+1)}{3kT}\left(B_a + \lambda M\right) \qquad \text{---------- (1.9)}$$

or, $$\chi = \frac{C}{T-\theta} \qquad \text{---------- (1.10)}$$

where the above equation is in the form of Curie-Weiss law with the Curie temperature, $\theta_C = \frac{\lambda C}{\mu_0}$ and it is equivalent to ferromagnetic transition temperature.

1.4.4. Antiferromagnetism

In antiferromagnetic materials, the spins of electrons align in a regular pattern with neighbouring spins pointing in opposite directions, below a certain temperature called Néel temperature. Above the Néel temperature, the material is typically paramagnetic. The magnetic susceptibility of antiferromagnetic material will appear to go through a maximum as the temperature is lowered.

The antiferromagnetic ordering is possible based on different type of magnetic unit cell structures as shown in Figure 1.5 except B type, which is a FM one. The magnetic structure of rare earth manganites falls into different categories depending on the level of A site (Rare earth site) doping [25].

In A-type structure, the magnetic ions are coupled ferromagnetically in each (001) plane but with alternate planes aligned in opposite spin orientation. So, there are anti-ferromagnetic interactions between the planes. The parent compound $LaMnO_3$ exhibits A-type structure. In a three dimensional network of magnetic ions, each ion has six nearest neighbouring magnetic ions and out of them four are ferromagnetically coupled and two are antiferromagnetically coupled. B-type structure is a ferromagnetic one with all six nearest magnetic ions are coupled ferromagnetically. In C-type structure, the atoms in (109) and $(\bar{1}10)$ planes are ferromagnetically aligned. Each atom has two ferro and four antiferromagnetic nearest neighbours such that there is a net antiferromagnetic unit cell.

In G-type structure each ion is coupled antiferromagnetically to all six nearest neighbours. Hence the atoms of positive and negative spins are arranged periodically. The other types of magnetic structures, D, E and F along with relative number of FM and AFM

bonds are given in Figure 1.5. Some of the materials follow a structure which is a result of coupling of two types of magnetic structures. One such example is CE type, where there is coherent stacking of octants of C and E type structures. The charge ordered manganites [25] exhibit such CE type magnetic structure.

Level	Cubic Octant of Magnetic Unit Cell	Relative no. of Bonds		Level	Cubic Octant of Magnetic Unit Cell	Relative no. of Bonds	
		FM	AFM			FM	AFM
A	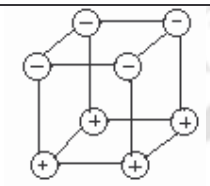	4	2	E	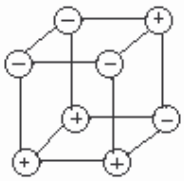	2	4
B	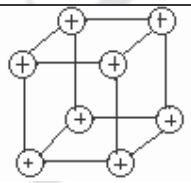	6		F	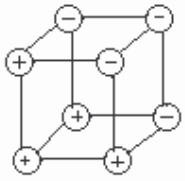	3	3
C	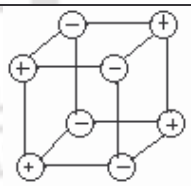	2	4	G	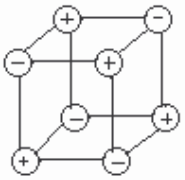		6
D	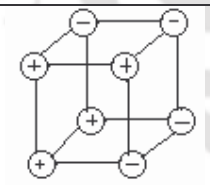	2	4				

Figure 1.5: Possible magnetic structures in manganite perovskites and their arrangements.

Ferrimagnetism is a special class of antiferromagnetism and for a long time it was mistaken for ferromagnetism. Here the magnetic moment of atom in two sublattices A and B are not equal in magnitude. As a result, in antiparallel arrangement, there is a non-zero net magnetic moment. The familiar example is magnetite, Fe_3O_4. It exhibits all the hallmarks of ferromagnetic behaviour such as spontaneous magnetization, Curie temperatures, hysteresis, and remanence. However, ferromagnet and ferrimagnet have very different magnetic ordering.

1.5. Magnetic Frustrations

Great efforts are being made to understand the magnetic ordering and phase transitions. It has been found in several occasions that the ordering could not be explained by a single type of magnetic interaction and in such case the idea of magnetic frustrations has been invoked. Here a magnetic spin or number of spins could not minimize its total energy by minimizing each energy bond with their nearest neighbour. In other words, a magnetic spin could not find an orientation to satisfy the magnetic interaction with all its neighbours. Frustrations are caused either by competing interactions or by lattice structure [41]. The triangular face centered and hexagonal close packed lattice structures with anti-ferromagnetic nearest neighbour interaction would lead to frustration. Let us illustrate a case, where the frustration is due to competing magnetic interaction. Consider a chain of spins where the nearest neighbour interaction J_F is ferromagnetic, while the next nearest neighbour interaction J_{AF} is anti-ferromagnetic. The ground state is ferromagnetic if $J_F >> J_{AF}$. If, J_{AF} exceeds a critical value, the ground state FM is no longer valid. So, nearest neighbour and next neighbour bonds are not freely satisfied.

1.5.1. Spin Glass

Spin glass is class of magnetic frustrating system which undergoes transition from disordered spins to metastable frozen disordered system, when the system is cooled [41-45]. Here each spin is under the competing magnetic interactions with the nearest or next nearest ions. The spins can not find a ground state by simultaneously minimizing their energy with each neighbouring spins, so they are frozen in a metastable random direction to minimize the total energy. Unlike the other phase transitions, where a system undergoes transition from disordered to ordered state, here the system undergoes transition from one disordered state to another disordered state. The debate was, whether it is really a thermodynamic phase transition. More or less, it is agreed that spin glass is a phase transition because the high temperature disorder is due to random thermal fluctuations without any interaction between magnetic spins. On the other hand, the low temperature frozen disordered state is due to long range magnetic interaction of opposite signs. It is explained as following.

At high temperature, there is a collection of paramagnetic spins with independent and rapidly rotating spins. When the temperature is lowered but still above spin glass freezing temperature, T_f, the rotating spins build themselves into locally correlated clusters. Some

spins, which are not part of any cluster, take part to transmit interaction among clusters. As, $T \to T_f$, there is a long range interaction between various spin components due to reduced thermal energy. The system tries to settle in ground state configuration for a particular spin distribution and exchange interaction and they lock themselves in random alignment depending on local anisotropy.

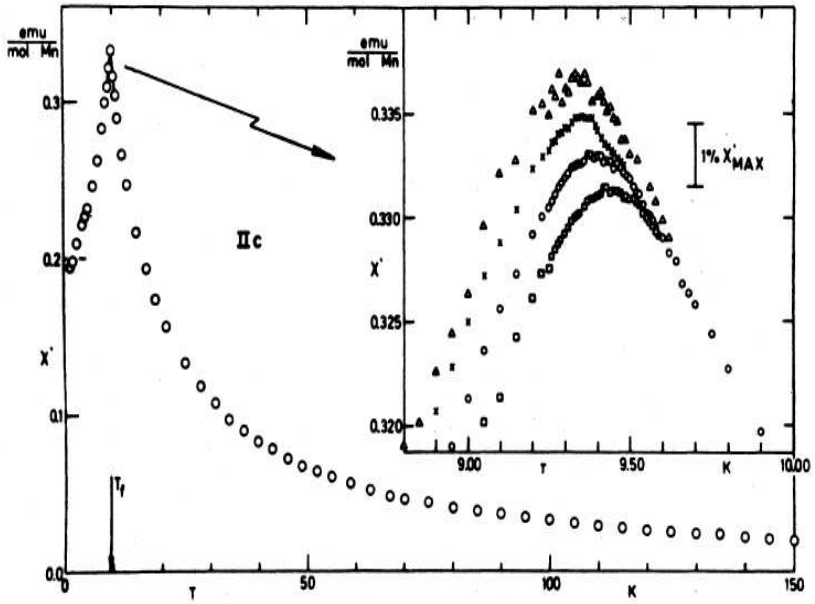

Figure 1.6: Spin glass transition observed in CuMn (with 0.84 at. % Mn) alloys from frequency variation of ac susceptibility measurement (Reproduced from C. A. Mulder *et al.* [46]).

Conventional spin glass materials are basically the transition element doped metallic alloys known as diluted magnetic alloys, namely CuMn, AgMn, AuFe, etc. [41, 42 and references therein]. Typical spin glass transition observed in CuMn alloys from ac susceptibility measurement is shown in Figure 1.6, where one can see a sharp cusp. The interesting feature of the transition is its frequency dependence due to relaxation behaviour of frozen spins. The dc susceptibility of conventional spin glass materials exhibit bifurcation of zero field cooled (ZFC) and field cooled (FC) curves at T_f as reported by Nagata *et al.* [47] way back to 1979. The frequency dependence of T_f was analysed in terms of various empirical relations [45, 47]. According to Arrhenius law, for thermal activation,

$$\tau = \tau_0 \exp\left(\frac{E_a}{kT}\right) \qquad \text{---------- (1.11)}$$

where, $\tau = \frac{1}{f}$ is the relaxation time corresponding to the driving frequency in ac susceptibility measurement. τ_0 is a characteristic time constant (the spin flipping time constant) and E_a is thermal activation energy. However the analysis using the above relation was found to yield unphysical values. Another relation used in the literature is Vogel-Fulcher law [42],

$$\tau = \tau_0 \exp\left[\frac{E_a}{k_B\left(T_f - T_0\right)}\right] \qquad \text{---------- (1.12)}$$

where, T_0 is a characteristic temperature. Vogel-Fulcher model is found to explain the frequency dependence of T_f for number of conventional spin glass system [42-44, 48-50]. However, the physical meaning of T_0 could not be understood.

The third approach originates from conventional scaling theory near phase transition, where the relaxation time τ is related to correlation length ξ as, $\tau \sim \xi^z$. The correlation length diverges with temperature as, $\xi \sim \left(\frac{T_f - T_g}{T_f}\right)^{-\upsilon}$, where T_g is the spin glass transition temperature. So we have the power law relation [51],

$$\tau = \tau_0 \left(\frac{T_f - T_g}{T_f}\right)^{-z\upsilon} \qquad \text{---------- (1.13)}$$

The experimental data on several conventional spin glass materials were analysed based on the above power law relation and the parameters τ_0, T_g, $z\upsilon$ were found to be reasonable [44].

Another important parameter in studying the spin glass transition is non-linear susceptibility χ_{nl}. The magnetization in spin glass system can be expressed in odd power of the magnetizing field, H

i.e. $$M = \chi_1 H + \chi_3 H^3 + \chi_5 H^5 + \ldots \qquad \text{---------- (1.14)}$$

Here, even powers of H are ignored because of inversion symmetry of magnetization of spin glass materials [44, 52]. If a phase transition occurs at T_g, the linear susceptibility term χ_1 is non-divergent, whereas higher order term diverges in the critical region. So the nonlinear susceptibility χ_{nl} diverges at the transition [52-54].

$$\chi_{nl} = \chi_1 - \frac{M}{H} \qquad \text{---------- (1.15)}$$

Similarly ac susceptibility technique with ac field amplitude h at a frequency ω can be used for studying the non-linear susceptibility and the magnetization expression is given as follows,

$$M(\omega) = \sum_i M_i' Cos\omega t + M_i'' Sin\omega t \qquad \text{---------- (1.16)}$$

Where, $M_1' = \chi_1' h + \frac{3}{4}\chi_3' h^3 + \frac{5}{8}\chi_5' h^5 + ...$ ---------- (1.17)

$$M_3' = \frac{3}{4}\chi_3' h^3 + \frac{5}{16}\chi_5' h^5 + ... \qquad \text{---------- (1.18)}$$

$$M_5' = \frac{1}{16}\chi_5' h^5 + ... \qquad \text{---------- (1.19)}$$

Here the experimentally measured fundamental susceptibility is

$$\chi_{1e}' = \chi_1' + \frac{3}{4}\chi_3' h^2 + \frac{5}{8}\chi_5' h^4 + ... \qquad \text{---------- (1.20)}$$

Similarly the experimental higher harmonic susceptibility can be equated. For low applied field, the amplitude of third harmonic susceptibility χ_3' diverges as,

$$\chi_3' \sim \left(\frac{T - T_g}{T_g}\right)^{-\gamma} \qquad \text{---------- (1.21)}$$

where, γ is the critical exponent. In conventional spin glass system such as AgMn and PdMn, the values of γ are reported to be 2.3 and 2.2 respectively [55, 56]. On the other hand, it is reported to be 3.2 ± 0.2 in $Ni_{77}Mn_{23}$ ferromagnetic spin glass system [57].

So far, we discussed about conventional spin glass behaviour, where a system undergoes transition from disordered paramagnetic spins to disordered metastable frozen state. On the other hand in ferromagnets with weak random frustration, the Curie temperature decreases with increasing disorder upto a certain level, where the random frustration is so strong that the system exhibits spin glass transition. So, the system exhibits paramagnetic to ferromagnetic transition followed by spin glass transition as the temperature is lowered. It is generally referred as reentrant spin glass behaviour, because the system reenters into the disordered (spin glass) state after undergoing disordered (paramagnetic)-ordered (ferromagnetic) phase transition. The insulating Heisenberg ferromagnetic system, $Sr_{1-x}Eu_xS$ [58, 59] and several perovskite rare earth manganites falls under this category [60-65].

In certain level of doping, spin-glass type of behaviour with random canting of magnetic spins are observed in $La_{(2-x)/3}Ba_{(1+x)/3}Mn_{1-x}Cu_xO_3$ [60]. Here, as a result of competing interaction between FM ordering with AFM interactions, the spins are frozen in

random direction below certain temperatures and it results in sharp fall in susceptibility or magnetization such that their values are quite low.

The Mn site doped manganites are also found to exhibit spin-glass behaviour. For instance, replacement of about 20% of the Mn in $(La_{0.67}Ca_{0.33})MnO_3$ compound with Cu, results in destruction of ferromagnetic metallic state and it exhibits reentrant spin glass behaviour [61]. The reentrant spin glass behaviour has been reported by Dho *et al.* [63] in $La_{0.46}Sr_{0.54}Mn_{1-y}Cr_yO_3$ for y = 0.02 from the study of frequency variation of ac susceptibility and bifurcation of dc magnetization in ZFC and FC conditions. Several other groups have used frequency variation of ac susceptibility, ZFC and FC dc magnetization and, nonlinear ac susceptibility to study the reentrant spin glass behaviour [63-67]. Detailed discussions are given in section 1.8.

1.5.2. Super-Paramagnetism

We know that in paramagnetic materials the atomic moments are non-interactive and random in direction in the absence of applied field. In superparamagnetic (SPM) materials, the non-interacting and randomly oriented moment entities are tiny clusters rather than atomic moments. Each cluster contains group of atoms with strong ferromagnetic interaction, so the moments are aligned parallel to each other. However, the alignment of moments in each cluster is random in direction due to local anisotropy. The sources of anisotropy could be magneto-crystalline, shape anisotropy due to demagnetizing effect, dipolar anisotropy, etc. The anisotropy and energy per unit volume can be written as $K\sin^2\theta$, where K is a positive anisotropy constant and θ is the angle between anisotropy axis and magnetization. So, each cluster is under the energy barrier E=KV, where V is the volume of the cluster. The energy barrier can be overcome either by applied magnetic field or appropriate thermal energy k_BT.

Generally, SPM materials contain tiny clusters separated for away from each other [23], so there is no interaction among clusters. Since the magnetization can find two easy directions for θ=0 and π, there are two minima and the spins relax between these two minima. This is possible because thermal energy k_BT is comparable to KV. The relaxation time (τ) of magnetization between two states is given by Arrehenius law, $\tau = \tau_0 \exp\left(\frac{E_a}{kT}\right)$.

Here, τ_0 is the microscopic limiting relaxation time and it is in the order of 10^{-9}s. As the temperature is reduced, the spins can not easily overcome the anisotropy energy, so the spin fluctuations reduce or relaxation time increases. If the relaxation time is longer than the

measuring time of any experimental techniques such as magnetization or ac susceptibility at a particular temperature T_B, it appears that the spins are localized in one of their easy directions. T_B is called blocking temperature with $T_B = KV/\left[k_B \ln\left(\tau/\tau_0\right)\right]$. So, below T_B, the clusters-spins are frozen in random direction.

The temperature dependent magnetization and ac susceptibility of SPM materials are comparable to that of spin glass materials. However, spin glass is due to long range magnetic interaction and it is basically a phase transition. On the other hand, the gradual blocking process of SPM is not a phase transition. The particles in magnetic recording medium can be compared with SPM, so it has a technological application.

1.5.3. Bound Magnetic Polarons

The tendency of formation of inhomogeneous charge and spin states and to phase separation is of fundamental importance for the physics of manganites and other systems with strongly correlated electrons. The most widely discussed type of phase separation is the formation of small bound magnetic droplets (bound magnetic polarons). Bound magnetic polarons (BMPs) are entities, where the carrier spins couple to the localized spins of the magnetic elements through the exchange interactions [68].

Bound magnetic polarons (BMP) are produced in magnetic semiconductors by the exchange interaction between carrier spins and magnetic ion spins. At low temperatures, carriers bound to impurities align nearby magnetic ions, creating a finite local magnetization. The bound hole (electron) interacts with the spins of the magnetic ions within the sphere of Bohr orbit and tends to produce ferromagnetic alignment in those spins. Thus, in a simple model, the material can be considered as an irregular assembly of ferromagnetic spheres in a matrix which may be antiferromagnetic or paramagnetic, depending upon the temperature conditions, etc.

In manganites, for small values of x in $R_{1-x}A_xMnO_3$, local distortions of the structure tend to trap the doped charge carrier. The localization of these trapped (bound) charge carriers will increase their interaction with the surrounding (magnetic) environment. Due to the interaction, the latter spins can have a significant net ferromagnetic alignment in which case the BMP resembles a ferromagnetic bubble embedded in a matrix of transition ions that surround it.

This behaviour can be investigated by various types of magnetic measurements, the most common being measurements of magnetic susceptibility as a function of temperature and measurements of magnetization, M as a function of magnetic field, H at various temperatures.

McCabe *et al.* [69] used these types of measurement to investigate the behaviour of BMPs in the antiferromagnetic p-type magnetic semiconductor alloy $Cu_2Mn_{0.9}Zn_{0.1}SnS_4$. They showed that BMPs were present upto a temperature of about 60 K.

According to BMP model, the measured magnetization can be fitted to the relation [69, 70].

$$M = M_0 L(x) + \chi_m H \qquad \text{---------- (1.22)}$$

where the first term is from BMP contribution and the second term is due to paramagnetic matrix contribution. Here $M_0 = Nm_s$, N is the number of BMPs involved and m_s is the effective spontaneous moment per BMP. $L(x) = \coth x - 1/x$ is the Langevin function with $x = m_{eff} H/(k_B T)$, where m_{eff} is the true spontaneous moment per BMP and at higher temperature it can be approximated to $m_s = m_{eff}$. χ_m is the susceptibility of the matrix.

1.6. Magnetic Interactions

The magnetic properties of the manganites are largely determined by transfer of electrons between the manganese and oxygen orbitals that point towards each other. The direct overlap between the atomic manganese orbital is small and the magnetic interaction is mediated by intervening 2p-orbitals of oxygen. The Mn ions are surrounded by oxygen in manganites as shown in Figure 1.1. The Mn ions underlying in such octahedron are subjected to a crystal field splitting of d orbitals as shown in the Figure 1.3. The crystal field splitting between the t_{2g} and e_g states is about 1eV. In Mn^{3+} based parent compounds, e_g state electrons tend to localize such that Mott insulator is formed. However, the e_g electron can be itinerant by electron vacancies or in other words by hole creation in the crystals. Thus the hole doping leads to creation of Mn^{4+} ions in the crystal. Unlike e_g electrons, the t_{2g} electrons are less hybridized with O-2p orbitals and they are stabilized just by crystal field splitting. Thus t_{2g} electrons are localized with a local spin S = 3/2, even in the metallic site. There is a strong coupling between e_g conduction electron spin (S = ½) and t_{2g} localized electron spins (S = 3/2). The exchange energy J_H (Hund's rule coupling energy) is as large as 2 to 3 eV for the manganites and exceeds the intersite hopping interaction t_{ij}^0 of the e_g electrons between the neighbouring sites, i and j. According to Anderson-Hasegawa [71], in the case of the strong coupling limit, i.e with $J_H/t_{ij} \rightarrow \infty$, the effective hopping interaction t_{ij} can be written as,

$$t_{ij} = t_{ij}^0[\cos(\theta_i/2)\cos(\theta_j/2) + \exp[i(\phi_i - \phi_j)]\sin(\theta_i/2)\sin(\theta_j/2)] \quad \text{---------- (1.23)}$$

where, the core spins are treated as purely classical object and described by unit vectors θ_i, ϕ_i and θ_j, ϕ_j at site i and j respectively. Here θ and ϕ are polar and azimuthal angles. By neglecting the Berry phase term $\exp[(i(\phi_i - \phi_j)]$, one can get,

$$t_{ij} = t_{ij}^0 \cos(\theta_{ij}/2) \quad \text{---------- (1.24)}$$

So, the absolute magnitude of the effective hopping depends upon the relative angle θ_{ij} between the neighbouring spins. The ferromagnetic interaction via the exchange of the conduction electrons whose spin shows the on-site (Hund's rule) coupling with the local spin is called "Double-exchange interaction" (discussed in next section). The ferromagnetic metallic state is stabilized by maximizing the kinetic energy of the conduction electron (θ_{ij} = 0). When temperature is raised close to T_c, the configuration of the spin is dynamically disordered and accordingly the effective hopping interaction is also subjected to disorder and, the average hopping interaction is reduced. This leads to enhancement of the resistivtiy near

and above T_c. Therefore, large magnetoresistance (MR) can be expected around T_c, since the local spins are aligned easily by an external field and hence, the randomness of the e_g hopping interaction is reduced. It was the initial explanation of CMR behaviour. However the physics of the CMR behaviour is more complex. In addition to the DE interaction, other interactions such as, the electron-lattice interaction, antiferromagnetic superexchange interaction between the t_{2g} local spins, inter-site Coulomb repulsion among e_g electrons, etc. have to be taken into account**.** Among all the interactions, the electron-lattice interaction frequently occur in manganites, which causes the Jahn-Teller type coupling of the e_g electrons with oxygen displacement. The Jahn-Teller type lattice distortion that lifts the orbital degeneracy and lowers the electronic energy is frequently observed for the orbital degenerate d-electron configuration.

In this section, I have discussed the different type of magnetic interactions:

1.6.1. Magnetic Dipole-Dipole Interaction

Magnetic dipole-dipole interaction [23], also called dipolar coupling, refers to the direct interaction between two magnetic dipoles. The energy of the interaction is as follows:

$$H = -\frac{\mu_0}{4\pi r_{ij}^3}\left[3\left(\mu_i . \hat{r}_{ij}\right)\left(\mu_j . \hat{r}_{ij}\right) - \left(\mu_i . \mu_j\right)\right] \qquad \text{---------- (1.25)}$$

where, r_{ij} is a unit vector parallel to the line joining the centers of the two dipoles; μ_i and μ_j are the moments of two dipoles separated by a distance $|r_{ij}|$. This interaction is important in the properties of those materials, which order at milli Kelvin temperature. The magnetic dipolar interaction is too weak to account for the ordering of most of the magnetic materials. There is a built in anisotropy to the dipolar interaction which can orient the spins either parallel (FM) or anti-parallel (AFM). If the spins are oriented along r_{ij}, they couple ferromagnetically and if they are oriented perpendicular to r_{ij}, they couple antiferromagnetically.

1.6.2. Direct Exchange Interaction

If the electrons on neighbouring atoms interact directly to each other without any mediating ions, this is known as direct exchange. This is because the exchange interaction proceeds directly without the need for an intermediary. The direct exchange involves the overlapping of electronic wave functions of neighbouring atoms and the Coulomb electrostatic repulsion. The Pauli's exclusion principle keeps the electrons with parallel spins away from each other to reduce Coulomb repulsion. So, mostly anti-parallel spin

configuration is favoured in direct exchange. The wave functions of the magnetic d or f electrons decrease exponentially, thereby too small overlap of wave functions and the direct exchange interaction is very weak.

1.6.3. Superexchange Interaction

Kramer [72], Anderson and his group [71, 73], Goodenough [9] and Kanamori [26] pointed out that ferromagnetic and anti-ferromagnetic interactions are possible by a mechanism called superexchange (SE) interactions. In superexchange, the two magnetic ions interact through an intermediate non-magnetic ion. This is a common interaction in the insulating magnetic oxides, where the intermediate ion is O^{2-}. The basic interaction mechanism is as follows.

For example consider two Mn^{4+} ions with an intermediate O ion. Let us discuss the case, where the unoccupied 3d orbital of Mn^{4+} ions point towards O-2p orbital as shown in Figure 1.7(a). Due to this overlapping, the two spins of O-2p with opposite spins are likely to spend some time on the unoccupied 3d-orbitals and thus there is a simultaneous bond formation of the anion (O) with the cations (Mn^{4+}) on both sides. If the spins of the cations are anti-parallel, the positive spin of O-2p orbital forms the partial bond with the cation having positive spins and the negative spin of O-2p orbital forms the bond with the other cation having negative spin. So, there is FM coupling between electron of anion and cation and, this process leads net anti-ferromagnetic interaction as shown in Figure 1.7 (a). Similar superexchange interaction is possible between two Mn^{3+} ions separated by O [9]. The above type of bond formation can not occur if the spins of the cations are parallel.

According to Goodenough [9], the superexchange interaction in Mn-O-Mn network can be also ferromagnetic, if one of the Mn-O bonds is covalent, while the other Mn-O bond is ionic. Below the Curie temperature, the covalent bond becomes semi-covalence (bonding occurs between parallel spins) and the O^{2-} ion is left out with a singe electron, since the other electron is associated with Mn ion in covalence bonding. There is a direct exchange interaction (AFM) between magnetic moment of anion (due to its isolate electron) and that of other Mn ion, which ionically bound to it. Thus two Mn ions are coupled FM as shown in Figure 1.7(b).

Thus according to Goodenough, the superexchange between Mn^{3+}-O^{2-}-Mn^{3+} and Mn^{4+}-O^{2-}-$Mn^{4+}$are anti-ferromagnetic in nature, while Mn^{3+}-O^{2-}-Mn^{4+} is ferromagnetic. The superexchange interaction mainly leads to insulating behaviour.

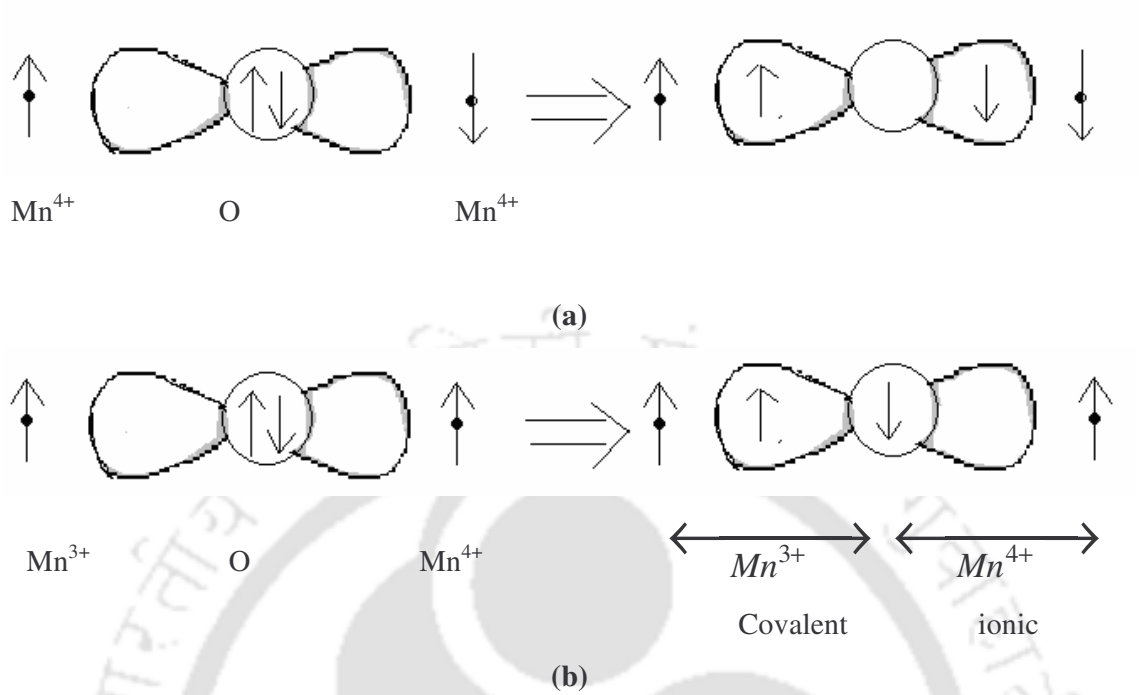

Figure 1.7: Schematic diagram showing the arrangement of spins and orbitals in superexchange (a) Anti-ferromagnetic super-exchange interaction (b) Ferromagnetic super-exchange interaction.

1.6.4. RKKY Interaction

In metals the exchange interaction between magnetic ions can be mediated by the conduction electrons. A localized magnetic moment spin-polarizes the conduction electrons and this polarization in turn couples to a neighbouring localized magnetic moment a distance r away. The exchange interaction is thus indirect because it does not involve direct coupling between magnetic moments. It is known as the RKKY interaction. The coupling takes the form of an r-dependent exchange interaction $J_{RKKY}(r)$ given by

$$J_{RKKY}(r) \propto \frac{\cos(2k_F r)}{r^3}. \qquad \text{---------- (1.26)}$$

at large r (assuming a spherical Fermi surface of radius k_F).The interactions is long range and has an oscillatory dependence on the distance between the magnetic moments. Hence depending on the separation it may be either ferromagnetic or antiferromagnetic [23].

1.6.5. Double Exchange Interaction

In 1951 Zener presented a theory of indirect magnetic exchange between 3d atoms [8, 74]. Carrier electrons can hop between two ions only if the electron spins of the two ions are parallel, and Zener showed that ferromagnetic interactions are energetically favoured when conduction electrons are present. To describe the exchange between Mn^{3+} and Mn^{4+} ions via an oxygen ion, Zener introduced the concept of double exchange, i.e. simultaneous transfer of an electron from Mn^{3+} to oxygen and from the oxygen to Mn^{4+}. Two simultaneous motions are involved in this process, and so it is called double exchange (DE) interaction. The movement of electron can be shown as, $Mn^{3+}_{1\uparrow} O_{2\uparrow,3\downarrow} Mn^{4+} \rightarrow Mn^{4+} O_{1\uparrow,3\downarrow} Mn^{3+}_{2\uparrow}$, where the electron spins are labeled as 1, 2 and 3. Anderson and Hasegawa [71] presented the DE mechanism in detail by visualizing a second order process in which the electron transfer takes as follows $Mn^{3+}_{1\uparrow} O_{2\uparrow,3\downarrow} Mn^{4+} \rightarrow Mn^{3+}_{1\uparrow} O_{3\downarrow} Mn^{3+}_{2\uparrow} \rightarrow Mn^{4+} O_{1\uparrow,3\downarrow} Mn^{3+}_{2\uparrow}$.

Double exchange is always ferromagnetic; if the spins of the d-electrons of the two manganese ions are parallel, the configurations Mn^{3+}-O^{2-}-Mn^{4+} and Mn^{4+}-O^{2-}-Mn^{3+} will be degenerated. If the manganese spins are not parallel, the electron transfer becomes more difficult due to strong onsite Hund's coupling. The electron transfer is also more difficult if the Mn-O-Mn bond is bent; when the angle is 180° the overlap of the manganese d-orbitals and the oxygen p-orbital is the largest and the interactions are the strongest, and will decrease on deviation from this angle. It has been presented that, the effective hopping integral for the electron to move from one Mn site to another Mn site is proportional to the square of the hoping integral between p-oxygen and d-manganese orbitals. If the localized spins (t_{2g}, S = 3/2) are considered as classical objects and if they are canted with an angle θ between the nearest neighbour spins, the effective hopping integral would be proportional to cos(θ/2). For θ = 0, cos(θ/2) attains maximum value 1 and the hopping is maximum and, it corresponds to a ferromagnetic interaction. If θ = 180^0, the cos(θ/2) becomes 0 and it corresponds to antiferromagnetic interaction [71].

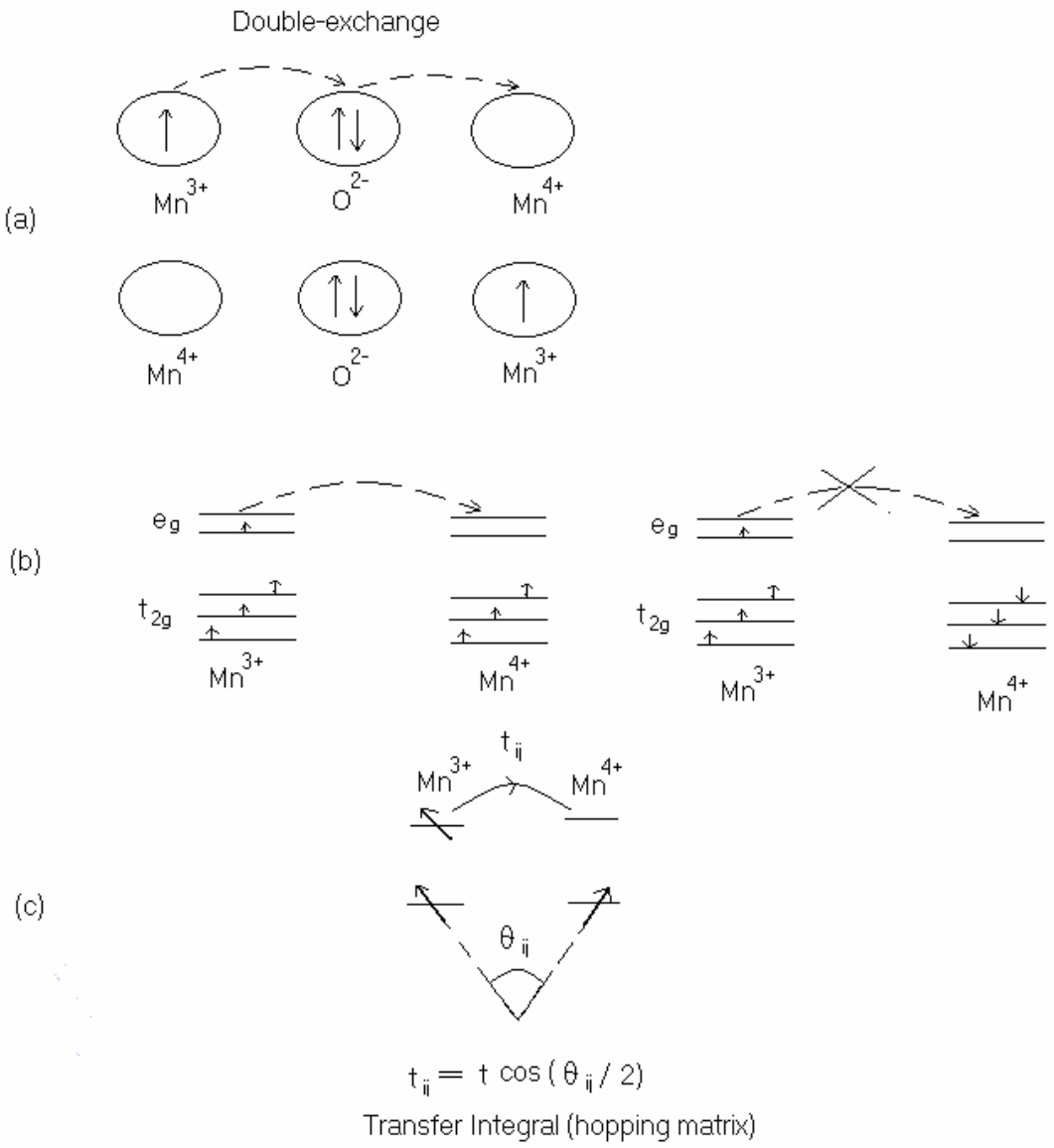

Figure 1.8: (a) Sketch of the double exchange mechanism which involves two Mn ions and one O ion. (b) The mobility of e_g electrons improves if the localized spins are polarized. The transfer integral is shown in the Figure (c).

1.7. Electrical Resistivity and Magneto-resistivity

The parent compounds $RMnO_3$ and $AMnO_3$ are electrical insulators, where the Mn is in Mn^{3+} and Mn^{4+} state respectively. The solid solution with general chemical formula $R_{1-x}A_xMnO_3$ (where R is a trivalent rare earth element and A is divalent alkaline or monovalent alkali element) exhibits metal to insulator transition for certain composition range depending upon nature of R ion. These materials consist of Mn^{3+} and Mn^{4+} mixture.

The sharpness of the transition often depends on the sample quality. For samples with grain size of the order of 5μm or more, transition is relatively sharp. The temperature dependent resistivity curve can be divided into three regions, high temperature (insulating region), low temperature (metallic region) and critical region (the intermediate region). Critical behaviours are best described by thermodynamic measurements, which couple directly to the magnetic correlation length. High temperature data have been explained by Variable Range Hopping model (VRH), Small Polaron Hopping (SPH) model and simple semiconducting behaviour [75-79]. The electrical resistivity in the ferromagnetic region has been investigated by several groups. In the region just below T_c, ρ falls rapidly. For $T < 0.5T_c$, typically the variation is less rapid, but it is different from what is generally seen in a metallic ferromagnet. Few attempts have been made to understand the critical region by assuming the existence of both insulating and metallic behaviour.

1.7.1. Magneto-Resistance (MR)

Magneto-Resistance (MR) can be defined as the change of a resistivity of a material under the influence of an external magnetic field. MR has been observed in different physical systems and there appears to be a wide range of physical mechanism responsible for the effects. Attempts to increase the magnitude of the MR have largely been driven by the needs of the technology industry to keep up with the demand for increased magnetic storage industry and other applications. In general, Magneto-resistance of a material is defined as

$$MR(T) = \frac{\rho(H,T) - \rho(0,T)}{\rho(0,T)} \qquad \text{---------- (1.27)}$$

Here, ρ(H, T) and ρ(0, T) are the electrical resistivity measured in the presence and absence of applied magnetic field.

Table 1.4: Schematic features of the various MR effects.

Type of Magneto-Resistance	Origin	Applications
(a) Ordinary Magneto-Resistance 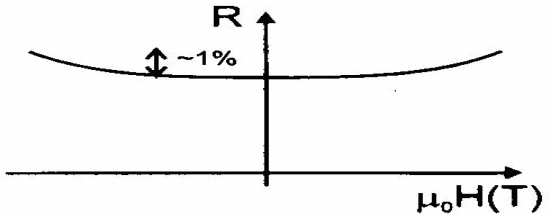	Lorentz force	Field sensors (some semiconductor)
(b) Anisotropy Magneto-Resistance 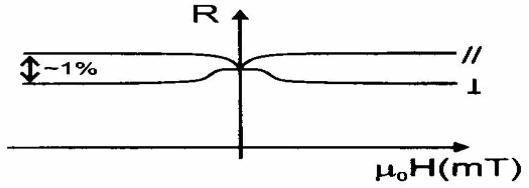	Spin-orbit coupling	Read heads
(c) Giant Magneto-Resistance (GMR) 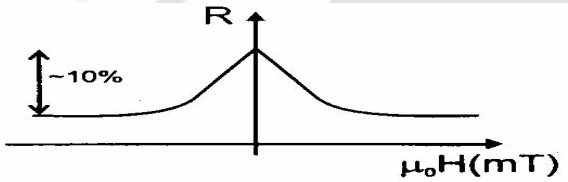	Spin dependent scattering	Read Heads
(d) Colossal Magneto-Resistance (CMR) 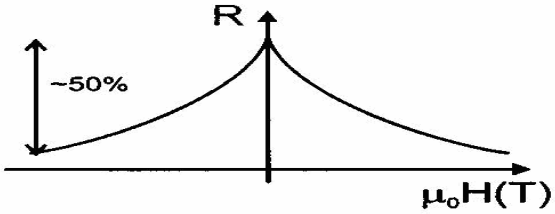	Double exchange and Jahn-Teller Effect	Study of spin polarized transport
(e) Tunneling Magneto-Resistance (TMR) 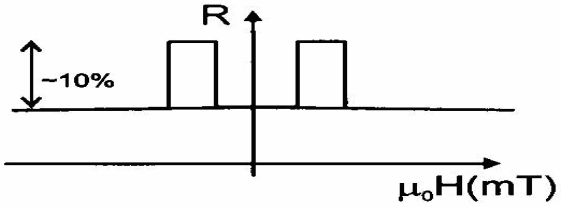	Spin dependent Tunneling	Read heads and MRAM

The electrical resistivity in magnetic materials depends on the direction of the applied magnetic field relative to the orientation of the crystal itself [80], a phenomenon known as anisotropic magneto-resistivity. On the other hand, the ordinary magneto-resistivity, which is related to the Hall effect, originates from the impact of the Lorentz-force on moving charge carriers. In absolute numbers, the magnitudes of the anisotropic and the ordinary magneto-resistivity are moderate and typically not more than a few percentage. In the end of 1980's, it was discovered that multi-layers of magnetic and nonmagnetic metallic materials could show much higher negative magneto-resistivity compared to the previously known MR [80] and it is called giant magneto-resistivity (GMR). Only about half a decade later, it was discovered that doped rare-earth manganese oxides by themselves could possess even higher magneto-resistivity (in some cases close to 100%) [1-3, 11, 81]. The magneto-resistivity values in manganites are found to be even higher than that of GMR and hence the term colossal [1, 82] was used to describe the MR of manganites. In magnetic tunnel junctions, there is another type of magneto-resistivity, known as tunneling magneto-resistivity or junction magneto-resistivity, as shown in Figure. The resistivity of a magnetic tunnel junction would be lower for a parallel configuration of magnetization of electrodes. The anisotropic, ordinary and colossal MR can be considered as intrinsic effects of the material, while giant and tunnelling MR depend on extrinsic parameters. The magneto-resistivity in manganite perovskite is associated with a crossover from metallic to insulating state, and accompanied by a magnetic phase transition. The large MR effect is essentially linked to the presence of an adequate amount of Mn^{4+} (around 33%) which can be introduced by cation substitution or cation deficiency.

1.7.2. Electrical Resistivity in Metallic Region

The electrical resistivity, ρ in the metallic region, i.e. below M-I transition temperature, where dρ/dT >0, is analysed in terms of various empirical relations corresponding to various scattering mechanism. The general empirical relation can be written as:

$$\rho(T) = \rho_0 + \rho_m T^m + \rho_n T^n \qquad \text{---------- (1.28)}$$

Where, ρ_0 is the temperature-independent residual resistivity due to scattering by impurities, defects, grain boundaries, and domain walls, etc. Here m and n are exponents and their values are generally 2, 2.5, 3, 4.5 or 5 depending upon the nature of scattering mechanism.

In manganites, several groups analysed and fitted, the resistivtiy data in metallic region to the following empirical relation,

$$\rho(T) = \rho_0 + \rho_2 T^2 \qquad \text{---------- (1.29)}$$

Where, ρ_0 is the temperature-independent residual resistivity. The second term with the coefficient ρ_2 is ascribed to the electron–electron [83-84] or single magnon [3-4, 85**,** 86] scattering. Many researchers attributed the T^2 dependence to the electron–electron scattering process [83-84]**.** But later on, many researchers [3-4, 85-86] emphasized that the T^2 contribution reflects the reappearance of minority spin states that are accessible to thermally excited magnons. They explained the T^2 dependence in terms of the single-magnon scattering. Jaime *et a.l* [85] argued that the T^2 dependence is because of single magnon scattering and they extended the calculation established by Mannari *et al.* [87] for the case in which the minority and majority spin sub-bands differ in energy by a constant amount yielding the same T^2 dependence.

The low temperature resistivity of manganites has been calculated separately by Wang and Zhang [88] and by Furukawa [89]. Their calculation yields a temperature dependent resistivity that scales as $T^{2.5}$ above T ~ 60K and contains a $T^{1.5}$ contribution below this temperature. Schiffer et al**.** [84] could successfully fit the low temperature resistivity of their $La_{1-x}Ca_xMnO_3$ sample to the expression,

$$\rho(T) = \rho_0 + \rho_{2.5} T^{2.5} \qquad \text{----------} \qquad (1.30)$$

The above model predicts a significant magneto-resistivity at low temperature; however Hwang *et al* [90] have not observed any such magneto-resistance on single crystals and thin films.

Furukawa [89] considered the existence of minority spin states created as a result of spin fluctuations leading to a T^3 temperature dependence as,

$$\rho(T) = \rho_0 + \rho_3 T^3 \qquad \text{----------} \qquad (1.31)$$

This model has been used to fit the low temperature resistivity of $La_{1-x}Sr_xMnO_3$ (x = 0.2, 0.3, 0.4) to much lower temperatures than the T^2 fit (i.e. explain the deviation from T^2 at low temperatures).

A $T^{4.5}$ dependence was observed by Snyder *et al*. [91] and this was attributed to double magnon scattering process as calculated by Kubo and Ohata [92]. However the temperatures involved are too high at which there would be substantial density of states at the Fermi level for the minority spins states and hence single-magnon scattering (the stronger process) can not be ruled out. So, they proposed the expression for resistivity as,

$$\rho(T) = \rho_0 + \rho_2 T^2 + \rho_{4.5} T^{4.5} \quad \text{----------} \quad (1.32)$$

Jaime *et al*. [85] have fitted the low temperature resistivity data to the expression,

$$\rho(T) = \rho_0 + \rho_2 T^2 + \rho_5 T^5 \quad \text{----------} \quad (1.33)$$

where, the second term with the coefficient ρ_2 is ascribed to single magnon and the third term with the T^5 contribution arises from electron-phonon process.

Recently Ravindranath *et al.* [93] have fitted the resistivity data in the metallic regime to an equation of the following form:

$$\rho(T) = \rho_0 + \rho_1 T^2 + \rho_2 T^{4.5} \quad \text{----------} \quad (1.34)$$

which, indicates a combination of electron-electron, electron phonon and electron-magnon scattering.

1.7.3. Electrical Resistivity in Semiconducting Region

According to Millis *et al.* [10], the existing models based upon double exchange interaction strongly underestimate the magnitude of resistance change during metal-insulator transition. The transition from metallic to insulating phase is described as localization of itinerant electrons as per Mott-transition. The charge transport still occurs in the insulating regime, but the carriers are more localized than in the metallic phase. Already de Gennes [94] demonstrated that for small values of x in $R_{1-x}A_xMnO_3$, local distortions of the antiferromagnetic structure tend to trap the doped charge carrier. Localization of charge carriers will increase their interaction with the surrounding (magnetic) environment and hence a virtual effective mass is added to the hopping electrons. But charge hopping is also connected to the lattice distortions as described by the Jahn-Teller effect. This transport of lattice and spin distortions is usually referred as magnetic polarons. Several studies have indicated the charge localization and the formation of small polarons in perovskite manganite materials above T_c [95-98]. If the charge carriers with their association to crystalline distortion are less than the size of the unit cell, they are called small polarons. In this case, the charge carriers are always found at the lattice site. The temperature variation of resistivity above T_c is mostly found to follow the small polaron model [99], i.e,

$$\rho = \rho_{sp} T^n \exp\left(\frac{E_{sp}}{k_B T}\right) \quad \text{----------} \quad (1.35)$$

Here, E_{sp} is the hopping energy, T is the temperature and k_B is the Boltzmann constant. n = 1 corresponds to adiabatic small polaron hopping and n = 3/2 corresponds to non-adiabatic small polaron hopping. According to adiabatic small polaron hopping, the charge carriers hop

more rapidly and each time the carrier hops, the configuration of the vibrating atoms in the adjacent site coincides with that of occupied state. In non-adiabatic case the motion of small polaron is quite slow.

In polycrystalline samples, very thin films and un-annealed samples, i.e. samples with oxygen deficiency, etc. variable-range-hopping (VRH) and non-adiabatic small polaron hopping models are found to explain the data [75-77]. According to three dimensional Mott variable range hopping (Mott-VRH) model, the expression for electrical resistivity can be written as, [78, 79],

$$\rho = \rho_{0m} \exp\left(\frac{T_{0m}}{T}\right)^{1/4} \quad \text{---------- (1.36)}$$

Here, ρ_{0m} is the Mott residual resistivity and T_{0m} is the Mott characteristic temperature. The density of states in the vicinity of Fermi level, $N(E_F)$ and, hopping distance $R_{hop}(T)$ and hopping energy, $E_{hop}(T)$ can be written as,

$$N(E_F) = \frac{18}{k_B T_{0m} a^3} \quad \text{---------- (1.37)}$$

$$R_{hop}(T) = \frac{3}{8} a \left(\frac{T_{0m}}{T}\right)^{1/4} \quad \text{---------- (1.38)}$$

$$E_{hop}(T) = \frac{1}{4} k_B T^{3/4} T_{0m}^{1/4} \quad \text{---------- (1.39)}$$

Here a is the localization length. According to VRH model, the charge carriers hop from one localized to another localized state having overlapping electron wave function. The energy required for such hopping is taken from Phonon (lattice vibration). The above Mott -VRH resistivity equation has been derived for 3-dimensional case by neglecting the coulomb interaction between carrier charges. However, Efros and Skhlovskii (ES) [100] have modified the Mott-VRH model by taking into account the coulomb interaction between the charge carriers and the corresponding resistivity expression is,

$$\rho = \rho_{0s} \exp\left(\frac{T_{0s}}{T}\right)^{1/2} \quad \text{---------- (1.40)}$$

where, ρ_{0s} is the ES residual resistivity and T_{0s}, the ES characteristic temperature is defined as,

$$T_{0s} = \frac{\beta_1 e^2}{k_B a 4\pi\varepsilon_0\varepsilon_r} \quad \text{---------- (1.41)}$$

Here a is the localization length, ε_r is the dielectric constant and β_1 is a numerical constant = 2.8.

A parallel contribution theory (both insulating and metallic behaviour) has been proposed to understand the resistivity behaviour. The expression for parallel contribution theory is given as [101],

$$\rho(T) = \left\{ \frac{f(T)}{\rho_{lt}(T)} + \frac{[1-f(T)]}{\rho_{ht}(T)} \right\}^{-1} \qquad \text{----------} \qquad (1.42)$$

where, $f(T) = \{[\exp(T-T_{MI})/\Delta]+1\}^{-1}$ is the fraction of the carriers in the metallic state, T_{MI} is the M-I transition temperature, Δ is the effective width of the transition interval around T_{MI}, $\rho_{lt}(T)$ is the metallic resistivity (below T_{MI}) expression and $\rho_{ht}(T)$ is the semiconducting (above T_{MI}) resistivity expression. Huhtinen *et al.* [102] fitted the resistivity data in the whole temperature range with the above expression for their $La_{0.7}Ca_{0.3}MnO_3$ sample. Here they have taken equation (1.32) for $\rho_{lt}(T)$ and equation (1.36) for $\rho_{ht}(T)$.

1.8. La Based Manganites

$La_{1-x}A_xMnO_3$ (A=Sr, Ca, Ba and Pb) based colossal magneto-resistivity (CMR) materials are widely studied compared to other rare earth based CMR materials. They exhibit relatively large ferromagnetic (FM) T_c compared to other rare earth based CMR materials. This is mainly due to enhanced double exchange interaction as a result of large e_g bandwidth. The e_g electron bandwidth is related to average A site ionic size in ABO_3 perovskite structure. In last couple of years, there are quite many reports on electron doped and Mn site doped materials in the above series and also hole doping using monovalent elements. So, they are reviewed under different subheadings as given below.

1.8.1. Hole Doped Materials

The hole doping in $LaMnO_3$ series is achieved either by divalent alkaline earth elements or monovalent alkali ions in place of La. The widely studied divalent doped manganites are $La_{1-x}A_xMnO_3$ (A = Sr, Ca, Ba and Pb). The divalent substituted, $La_{1-x}Ca_xMnO_3$ compounds were the first series to be investigated for ferromagnetic metallic state in 1950s [103]. Later, the phase diagram of $La_{1-x}Ca_xMnO_3$ has been constructed by Schiffer *et al.* [84] and Gong *et al.* [104, 105]. The materials for $0<x<0.50$, show paramagnetic to ferromagnetic transitions with T_c ranging from 160 to 272K. However, metal-insulator (M-I) transitions were observed for $0.20 < x < 0.50$ with a maximum T_c for $x \approx 0.33$ [106]. The

maximum magnetoresistance (MR) was found to be around 80% at $T_c \approx 240K$ for an applied field of 6T (60kOe) [107]. At $x \approx 0.50$, this compound undergoes paramagnetic to ferromagnetic transition at around 225K and then to a charge ordered antiferro-magnetic phase at $T_{CO} \approx 155K$ [84]. Such charge ordering (CO) with hysteresis in electrical resistivity has been reported by Zhao *et al.* [108].

After the pioneering work of Jonker *et al.* [103] and Wollan *et al.* [25] on polycrystalline $La_{1-x}Sr_xMnO_3$ compounds, Urushibara *et al.* [109] carried out detailed study of electrical and magnetic properties on $La_{1-x}Sr_xMnO_3$ crystals for x = 0 to 0.60. According to them, for $x \geq 0.10$, these materials exhibit PM to FM transition with T_c ranging from 145K for x = 0.10 to 370 K for x = 0.3 and 0.4. They have observed M-I transitions in the vicinity of FM T_c for $0.175 \leq x \leq 0.40$ with a maximum magneto-resistivity of 90% for 5T field. Zhou *et al.* [110] studied the x=0.12 and 0.15 samples and found that they exhibit M-I transition followed by low temperature reentrant semi-conducting behaviour at around 150 and 190 K respectively. The low temperature reentrant behaviour has been attributed to charge ordering by correlating the neutron diffraction results [111]. Such phenomenon has been observed by other groups especially for $x \leq 0.15$ [109, 112, 113]. Materials in the above series exhibit change in crystal structure with increase in doping concentration and also with temperature variation [109, 110, 114]. There are other reports on Sr doped, $La_{1-x}Sr_xMnO_3$ compounds and they are also found to exhibit M-I transition, PM-FM transition and CMR behaviour in the vicinity of room temperature [115-120].

In $La_{2/3}Ba_{1/3}MnO_3$, Von Helmolt *et al.* [1] reported M-I transition above room temperature on thin film sample with magneto-resistivity values as high as 60% at room temperature for a field of 5T. Several authors reported M-I and FM transition at around 340 to 350 K for the composition close to x= 0.30, in $La_{1-x}Ba_xMnO_3$ [60, 121-122]. Trukhanov *et al.* [123] performed a systematic study on $La_{1-x}Ba_xMnO_3$ series for x=0 to 0.5. They found that materials undergo structural transition from orthorhombic for $x<0.10$ to rhombohedral for $0.10< x < 0.25$ followed by transition into cubic cell for $x > 0.27$. Ferromagnetism (FM) with competing antiferromagnetism (AFM) has been observed without any M-I transition. Unlike other alkaline earth doped materials, Ba doped series was studied only for limited composition range, due to the difficulty in preparing them in single phase form as a result of segregation of $BaMnO_3$. Kar and Ravi studied the $La_{1-x}Ba_xMnO_3$ series for a wide composition range i.e x=0.3 to 0.8 and observed M-I transitions with T_{MI} upto 340 K for optimum hole doped material [124].

Other than alkaline earth elements, the Pb doped $La_{1-x}Pb_xMnO_3$ compounds are also found to exhibit M-I transition, PM-FM transition and CMR behaviour in the vicinity of room temperature [125-129]. Banerjee *et al.* [130] found that T_{MI} values vary from 230 to 275K in polycrystalline $La_{1-x}Pb_xMnO_3$ ($0 \leq x \leq 0.50$).

Itoh *et al.* [16] were the first one to demonstrate M-I and FM transitions on mono-valent alkali ion doped, $La_{1-x}A_xMnO_3$ (here A= Na, K, Rb, etc.) compounds. According to them, the FM T_c of Na substituted samples varies from 219 to 336K for $0.04 \leq x \leq 0.12$. The maximum T_c of K and Rb substituted compounds are found to be 330 and 234K respectively. Similar studies have been carried out by many other groups [15, 131-133]. In Li doped series FM T_c upto 240 K with typical magneto-resistivity of 25% was reported for 0.8 T field [18]. Roy *et al.* [17] studied the Na doped $La_{1-x}Na_xMnO_3$ materials. Their FM T_c value was found to vary from 220 to 330K for the doping concentration of 0.07 to 0.40. They also observed M-I transition in the vicinity of T_c. The maximum MR of 45% was obtained at room temperature for 5T field.

Das *et al.* [134-137] have extensively studied the electrical conductivity, magnetoresistance, thermoelectric power, magnetic entropy change of monovalent (K) doped polycrystalline $La_{1-x}K_xMnO_3$. They found that the conductivity as well as the Curie temperature (T_C) of the system increases with K doping. Curie temperature increases from 260 to 309 K with increase in K content.

Similar to alkali ions, the Ag doping also falls into the category of mono-valent doping, where each doped element is expected to oxidize two Mn^{3+} ions into Mn^{4+} state. The Ag doping has been studied by a few groups and reported M-I and FM transition in the vicinity of room temperature [138, 139, 20]. Since their T_c is close to room temperature, they have potential application in magnetic refrigeration [19, 140]. The mechanism of electrical resistivity in the presence and absence of magnetic field was studied by Kar *et al.* in the $(La_{1-x}Ag_x)MnO_3$ series [20].

Kar and Ravi have reported that Cu substitution also plays the role of monovalent hole doping with FM and MI transitions [141, 142]. Metal–insulator transition temperature was found to vary from 43 to 92 K for $x \leq 0.10$. Paramagnetic to ferromagnetic transitions with a signature of competing AFM interaction have been observed.

1.8.2. Electron Doped Materials:

The alkaline earth manganites $AMnO_3$ (A = Ca, Sr, Ba) are also basically anti-ferromagnetic insulators, similar to those of $RMnO_3$. However in $AMnO_3$ series, the Mn is in Mn^{4+} state [143, 144]. So, the substitution of trivalent elements in place of alkaline earth elements, $A_{1-x}R_xMnO_3$ is expected to produce mixture of Mn^{4+}/Mn^{3+} ions and such materials are called electron doped materials.

$CaMnO_3$ based materials were widely studied by electron doping, i.e. by doping trivalent rare earth elements such as La [29, 145, 146] in place of Ca. These materials mostly show CO insulating behaviour without any M-I transition.

Unlike $CaMnO_3$ series, there were only limited reports on electron doped $BaMnO_3$ series. Yuan *et al.* [147] were the first one to report M-I transition in electron doped $La_{1/3}Ba_{2/3}MnO_3$ compound without any charge ordering. Raveau *et al.* [148] have reported that the electron doped $La_{0.35}Ba_{0.65}MnO_3$ compound is generally a mixture of two main phases, namely hexagonal $BaMnO_3$ and cubic perovskite $La_{0.65}Ba_{0.35}MnO_3$. According to them, the appearance of metallic conductivity below the M-I transition is mainly due to the presence of cubic perovskite (ferromagnetic phase) above the percolation threshold. However, Kar and Ravi [124, 149] have shown that the electron doped $Ba_{1-x}La_xMnO_3$ (x =0.3 to 0.5) series could be prepared in single phase form. They have also shown that the electron doped materials exhibit FM T_C ranging from 280 to 240 K with increase in doping, along with M-I transition and colossal magneto-resistivity. A reentrant semiconducting behaviour has been observed for x=0.5 sample.

There are a few reports on electron doped materials in $(Sr_{1-x}La_x)MnO_3$ series and they have been studied mostly in the composition range close to $x \approx 0.50$ [150, 151]. In the composition range $0.5 < x \leq 0.60$, FM to AFM transition has been reported in the temperature range 200 to 250 K [151]. In the vicinity of above AFM transition upturn in electrical resistivity was observed. AFM transitions due to charge ordering have been reported by Sundaresan *et al.* [152] and Wakai *et al.* [153] in $La_{0.5}Ca_{0.5-x}Sr_xMnO_3$. Kar and Ravi [154] have prepared electron doped $Sr_{1-x}La_xMnO_3$ series for x=0 to 0.5 and found that they exhibit structural transition from hexagonal ($P6_3$) to rhombohedral ($R\bar{3}C$) with increase in doping. They exhibit FM transition with T_c ranging from 375 to 393 K followed by low temperature AFM transition. However, no metal-insulator transition has been reported.

In order to explore the possible double exchange interaction in Mn^{2+}-O^{2-}-Mn^{3+} networks, recently electron doping in $RMnO_3$ series has been carried out by several groups

by substituting tetravalent Ce, etc. in place of R [155-165]. The first such report was on $La_{0.7}Ce_{0.3}MnO_3$ compound with an observation of increase in metal-insulator transition temperature with oxygen annealing [155]. Most of the authors have shown that, the above materials behave like hole doped materials with positive thermo-electric power and hall coefficient [157, 158, 160-163]. So the observed electrical and magnetic properties are due to DE interaction between Mn^{3+}-Mn^{4+} ions rather than between Mn^{2+}-Mn^{3+} ions.

Most of the authors have emphasized that even though $La_{0.7}Ce_{0.3}MnO_3$ thin film samples could be prepared in single phase form, the bulk samples were found to contain CeO_2 impurity [159, 160]. Raychaudhury *et al.* [166] have reported that decrease in oxygen pressure during the growth of $La_{0.7}Ce_{0.3}MnO_3$ thin film gives rise to increase in M-I transition temperature. Based on the above observation, they have suggested the electron doping nature of the above compound. Similarly, Han *et al.* [167] and Mitra *et al.* [168] have confirmed the electron doping in $La_{0.7}Ce_{0.3}MnO_3$ thin film from photo electron spectroscopy measurements, where the presence of Mn in the mixture of Mn^{2+}-Mn^{3+} has been observed. The electron doping was also achieved by using other substitutional elements such as Te, Sb, etc. [169-176]

1.8.3. Mn Site Doped Materials

It is known that the Mn ions in $RMnO_3$ series play a crucial role in shaping the magnetic properties. In double exchange Ferro magnets, the magnetic properties have a direct role in controlling the electrical transport and their mechanism. In order to explore the nature of magnetic interaction and possible stronger double exchange interaction with other transition elements, it is obvious to carryout other transition element substitution in place of Mn ions. This is reflected on the voluminous publications in Mn site doping.

Most of the Mn site doping has been carried out by using other transition elements such as Cr, Fe, Co, Ni, etc. There are several works on Co doped materials and one of the reasons is that cobalates themselves exhibit double exchange FM with negative magneto-resistivity [177-180]. Rubinstein *et al.* [181] carried out Co doping in $La_{2/3}Ca_{1/3}MnO_3$ series and found that the FM T_c falls from 250 K to 150K and metal-insulator transition temperature falling to 120 K even for 10 at% of Co doping. For Co doping beyond 10 at %, no metal-insulator transition was observed.

Gayathri *et al.* [182] and Ganguly *et al.* [183] studied systematically the Co doping in the above series. They have also observed that metal-insulator transitions upto around 10 at%

of Co doping, even though FM transition has been observed for a wide doping concentrations. So, basically Co doping gives rise to weakening of DE FM interaction. Similar behaviour has been observed by other groups in doping of Co in (La, Ca)-Mn-O series [184, 185]. Song *et al.* [186] estimated the saturation magnetization (M_S) by assuming that doped Co ions are in Co^{3+} state and they take part in SE AFM interaction with Mn ions in Co-O-Mn networks. The estimated M_S value was found to match with their experimental value for 5 at% doping of transition elements (Fe, Co, Ni). Similar reduction in FM T_c, with short range FM ordering or cluster glass like behaviour with large bifurcation between ZFC and FC magnetization have been reported in other series such as (La, Sr)-Mn-O [187] (La, Ba)-Mn-O [188-190] and (La, Pb)-Mn-O [191-193]. In most of the reports, the doped Co was in the mixture of $Co^{3+}$and Co^{4+} state.

Pollert *et al.* [194] reported Co doping in $(La_{0.8}Na_{0.2})MnO_3$ series and explained that the doped Co ions are in Co^{2+} state and, the charge compensation is achieved by converting some of the Mn^{3+} into Mn^{4+} state. Eventhough there is a sharp fall in M-I transition temperature from 333 K to 95 K for 2 at% of doping, only a small fall in M_s value has been reported. They have explained that some of the DE FM interaction in Mn^{3+}-O^{2-}-Mn^{4+} networks was replaced by FM super-exchange (SE) interaction in Mn^{4+}-O^{2-}-Co^{2+} networks.

Cr is another interesting transition element where the Cr^{3+} ion is iso-electronic in configuration with Mn^{4+} ions, i.e. three t_{2g} electrons. Moreover the ionic size of Cr^{3+} is comparable to that of Mn^{3+}. So, many researchers studied the Cr substitution in place of Mn to explore the possible double exchange FM interaction in Mn^{3+}-O^{2-}-Cr^{3+} networks. Ganguly *et al.* [195], Sun *et al.* [196], Wu *et al.* [197], and Gao *et al.* [198] carried out Cr substitution in $La_{2/3}Ca_{1/3}MnO_3$ series and found that FM T_c decreases with doping concentration but rather slowly compared to Co doped materials. For example, the T_c falls from 260 K for x=0 to about 200 K for x=0.2. It is explained on the basis of FM super-exchange interaction in Mn^{3+}-O^{2-}-Cr^{3+} networks. Since Cr^{3+} ions replace Mn^{3+} ions, the relative concentration of Mn^{4+} increases with respect to Mn^{3+}, so AFM SE interactions in Mn^{4+}-O^{2-}-Mn^{4+} and Cr^{3+}-O^{2-}-Cr^{3+} also contribute considerably. This has been observed as low temperature fall in M (T) at around 50 K in some of the samples. The low temperature transition has been observed as a secondary peak in $\chi^{//}$ (T) plots and they are found to have frequency dependence. CMR have been observed upto around 10% Cr doping and beyond that the materials were following semiconducting behaviour. Hong *et al.* [199] analysed the frequency dependence of $\chi^{//}$ (T) peak in terms of power law model on Cr doped $La_{0.8}Ca_{0.2}MnO_3$ compound and found the

characteristic relaxation time $\tau_0 = 10^{-10}$ s and critical exponent $z\upsilon = 12.4$. They have explained on the basis of cluster glass relaxation.

The doping of Cr ions on parent compound or on under-doped manganites has given different results. This was carried out by Gundakaram *et al.* [200] in $LaMnO_3$ even before the reports on substitution of Cr in (La, A)-Mn-O based CMR materials. Similar work was carried out by Zhang *et al.* [201] and Morales *et al.* [202]. The doped Cr ions are found to destroy the A type AFM ordering and enhances the FM interaction by increasing the FM T_c. The magnetic moments were also found to increase considerably with doping. In some of the cases, even M-I transitions have been observed. These authors interpreted the results in terms of double exchange interaction in Mn^{3+}-O^{2-}-Cr^{3+} networks. Similar type of increase in FM T_C has been reported upon Cr doping in under doped CMR materials, i.e. $(La_{0.9}Ca_{0.1})Mn_{1-x}Cr_xO_3$ [203]. Dho *et al.* [63] reported the melting of charge ordering at 8% of Cr doping in $(La_{0.46}Sr_{0.54})Mn_{1-x}Cr_xO_3$ series.

The substitution of Fe in place of Mn has been carried out by several authors especially in (La, Ca)-Mn-O series [204-211]. Unlike other transition elements, Fe could be substituted only upto around 10%, and in most of the cases, M-I transition has been observed only upto 5 at% of doping. The doped Fe is found to be in Fe^{3+} state and it introduces strong AFM interaction in Fe-O-Mn networks. For example, Ogale *et al.* [206] reported the fall of metal-insulator transition from 250 K for x=0 to 25 K for x=0.05 in $(La_{0.75}Ca_{0.25})Mn_{1-x}Fe_xO_3$ series. Cai *et al.* [211] and Hasanian *et al.* [64] reported reentrant spin glass behaviour in Fe doped samples; on the other hand, Kundaliya *et al.* [208] showed that the large irreversibility observed in M(T) data are mainly due to magnetic anisotropy. In $(La_{0.7}Pb_{0.3})Mn_{1-x}Fe_xO_3$, Pena *et al.* [212] and Gutiérrez *et al.* [213] reported a strong suppression of FM T_c from 350 to ~ 230 k for 10% of Fe doping. Strong suppression of FM T_c has been also reported in (La, Sr) Mn-O series due to Fe doping [214].

Recently Zhao *et al.* [215] carried out systematic magnetization study on $(La_{0.7}Sr_{0.3})Mn_{0.9}M_{0.1}O_3$ series, by doping 10 at% of various elements, M=Al, Cr, Mn, Fe, Co, Ni, Cu, and Ga. They have calculated the saturation magnetization by taking a probability function for 10% of Fe doping with an assumption that all the nearest neighbours of Fe is Mn (no Fe-Fe nearest neighbour), and AFM coupling in Fe^{3+}-O^{2-}-Mn^{3+} and FM coupling in Mn^{3+}-O^{2-}-Mn^{4+} networks. Their calculated M_s values were found to be very close to the experimental data. Similar type of study has been done by Troyanchuk *et al.* [216] on $(La_{0.7}Sr_{0.3})Mn_{0.9}M_{0.1}O_3$ and $(La_{0.7}Ba_{0.3})Mn_{0.9}M_{0.1}O_3$ series.

Helmholtz *et al.* [60] and Pi *et al.* [217] studied the Cu doping in the Mn site of (La, Ba)-Mn-O and (La, Sr)-Mn-O series respectively. They have found that Cu cations induce AFM SE interaction by weakening DE interaction and as a result FM completely disappears beyond certain level of doping.

Similar suppression of FM has been observed in (La, Ca)-Mn-O [218] and (La, Pb)-Mn-O series [219]. Recently Freitas *et al.* [220] have reported phase segregation in Cu doped (La, Sr)-Mn-O series, where FM clusters are embedded in AFM matrix.

In addition to the above transition elements doping, non-magnetic element such as Al substitution has been also studied. The non-magnetic impurity such as Al is expected to contribute to a dilution of double exchange ferromagnetic interaction and introduction of random electrical potential without any complicated magnetic phase separation. Al substitution in Mn has been studied by Blasco *et al.* [221] and Deac *et al.* [222] in $(La_{2/3}Ca_{1/3})MnO_3$ series and observed strong suppression of T_c at the rate of $dT_c/dx = 12$ K/Al%. However in large e_g band width materials such as (La, Ba)-Mn-O and (La, Sr)-Mn-O system, such suppression is small [216, 223].

There are a few reports on other transitions elements such as Ni [224], V [225-226], Mo [227], Ti [228], Nb [229] etc.

1.9. Other Rare Earth Based Manganites

1.9.1. Nd-Mn-O Based Compounds

The $La_{1-x}A_xMnO_3$ series is found to have large e_g electron band width due to its large A site ionic size. On the other hand, Nd-Mn-O series falls in the category of medium size e_g band width and hence the ionic size of doped materials plays a very sensitive and crucial role in tuning the magnetic properties in this system. Troyanchuk *et. al.* [230] studied systematically the magnetic properties of $Nd_{1-x}Ca_xMnO_3$ compounds and observed ferromagnetic (FM) transition with T_c around 110 K followed by broad peak at around 72K. The maximum saturation magnetization was found to be 2.8 μ_B at 5 K for 1 T field. Large difference between zero field cooled (ZFC) and field cooled (FC) magnetization was observed with electrical resistivity following a semi-conducting behaviour. Liu *et. al.* [231] prepared the $Nd_{1-x}Ca_xMnO_3$ compounds for x=0 to 1 and found that all the materials exhibited semiconducting behaviour with the magnetic properties demonstrated by charge ordering and antiferromagnetic (AFM) transition. However, the application of magnetic field was found to induce semiconductor–metal and AFM-FM transitions in the composition range

$0.30 \leq x \leq 0.45$. The charge ordering [232] and its destruction by the application of large magnetic field were reported by Tokunaga *et. al.* [233] in $Nd_{0.5}Ca_{0.5}MnO_3$.

Rao *et. al.* [234] demonstrated the destruction of charge ordering and the introduction of FM transition by preparing the material in nano-phase form. In $Nd_{0.7}Sr_{0.3}MnO_3$ series, FM and metal-insulator (M-I) transitions have been observed with T_c in the range of 230 K to 250 K because of its relatively large A site ionic size ($< r_A > =1.212$) compared to (Nd, Ca)-Mn-O series [235-237]. However in half doped $Nd_{0.5}Sr_{0.5}MnO_3$ material, charge ordering has been reported at around 150 K from detailed neutron diffraction, magnetization and electrical resistivity studies [238-242].

In $Nd_{1-x}Ba_xMnO_3$ series, even though the $< r_A >$ value is quite large, FM was observed in a narrow composition range of x= 0.2 to 0.4 with relatively lower transition temperature of 120 K and with electrical resistivity in the order of kΩ cm [243, 244]. Thus the double exchange (DE) interaction is not purely driven by the $<r_A>$ size or e_g electron bandwidth. There are a few reports on the single crystal samples of $Nd_{0.7}Sr_{0.3}MnO_3$, where FM and M-I transitions have been observed at around 150 K [245-247].

It was also predicted that in these materials, Nd ions order anti-ferromagnetically with spin canting. According to the neutron diffraction results of Wu. *et. al.* [248] and Munoz *et. al.* [249] in $NdMnO_3$ parent compound, it was found that both ferromagnetic and anti-ferromagnetic ordering takes place with spin canting.

Recently the mono-valent alkali ion doped, $Nd_{1-x}Na_xMnO_3$ series was studied by a few groups for x= 0.1 to 0.25 and found that these materials exhibit charge ordering at around 180 K followed by weak FM transition at 110 K [250-252]. The electrical resistivity follows semiconducting behaviour without any metal-insulator transition. However, metal-insulator transition could be induced by the application of magnetic field of the order 3T [252].

Zhang *et. al.* [253] studied the electron doped $Nd_{1-x}Ce_xMnO_3$ compounds, for x=0.04 to 0.10. They have observed ferromagnetic (FM) transition at around 60 K followed by secondary peak at around 25 K. They have explained their magnetization results based on ferromagnetic interaction between two sublattices; one having Mn^{3+} ions and other having Mn^{3+} and Mn^{2+} ions. Yanagida *et. al.* [254] reported ferromagnetic (FM) transition at 65K in single phase $Nd_{0.7}Ce_{0.3}MnO_3$ thin film. The room temperature electrical resistivity values of their samples are found to be in the order of 10^3 -10^4 Ω-cm.

1.9.2. Y-Mn-O Based Compounds

Y-Mn-O series falls in the category of small size e_g electron band width due to the smaller ionic radius of Y ion compared to La or Nd. There are very few reports on Y-Mn-O based compounds. A. Muñoz *et al.* [255] have observed that $YMnO_3$ exhibits antiferromagnetic ordering below 70K from their neutron diffraction result. Tomuta *et al.* [256] reported that $YMnO_3$ exhibits antiferromagnetic transition with Neel temperature T_N=71K. Further Iliev *et al.* [257] studied the Ca doped $Y_{1-x}Ca_xMnO_3$ compounds in the doping range of $0 \leq x \leq 0.5$.They have found that Ca doping increases the conductivity, but the temperature dependence of resistivity remains semiconducting for all doping concentration. The average magnetic exchange interaction changes from antiferromagnetic for $x < 0.08$ to ferromagnetic for $x \geq 0.08$. Arulraj *et al.* [258] observed charge ordering in half doped, $Y_{0.5}Ca_{0.5}MnO_3$ compound. The electron doped $YMnO_3$ series was studied by Van Aken *et. al.* [259] and Chen *et. al*. [260] by doping Zr in place of Y and by self doping ($YMn_{1+x}O_3$) at Mn site respectively. FM transitions with a low temperature spin glass like behaviour have been observed and, the FM has been attributed to the double exchange interaction between Mn^{2+} and Mn^{3+} ions.

1.10. Motivation of the Present Thesis Work

As reviewed above, La based CMR materials, i.e. $La_{1-x}A_xMnO_3$ (A=Sr, Ca, Ba and Pb) are widely studied compared to other rare earth based CMR materials, where the La site is doped with alkaline earth elements. Since the Mn ions play a crucial role on shaping the magnetic properties, there was large number of reports on Mn site doping in the above series by using transition elements, T= Cr, Co, etc., i.e. $(La_{1-x}A_x)Mn_{1-y}T_yO_3$. There are contradicting reports on the possible ionic state of doped elements and the influence on magnetic properties. The Mn site doping mainly leads to phase segregation.

As reviewed in this chapter, one can get metal-insulator transitions with CMR behaviour even by doping mono-valent alkali ions such as Li, Na, K, etc. or Ag. These materials exhibit T_c, close to room temperature. The advantage of mono-valent doping is that one can generate desired ratio of Mn^{3+}/Mn^{4+} ions with relatively low level of doping, i.e. with reduced ionic size mismatch and distortion. $(La_{1-x}Ag_x)MnO_3$ is found to be one of the interesting CMR materials with transition temperature in the vicinity of room temperature for x=0.15. In order to understand the magnetic interaction between Mn ions and other transition elements, we have taken up Mn site doping in less distorted $(La_{0.85}Ag_{0.15})MnO_3$ series, i.e. $(La_{0.85}A_{0.15})Mn_{1-y}T_yO_3$ (T= Co, Cr and Al). In addition to Co and Cr, we have also taken up a non-magnetic element i.e. Al for a comparison and easy interpretation. I have also taken up the study of magnetic properties of already known Cu doped $LaMn_{1-y}Cu_xO_3$ series.

In order to explore CMR in Nd-Mn-O series by mono-valent doping, I have prepared $Nd_{1-x}Ag_xMnO_3$ series for x=0.05 to 0.20. The detailed analysis of magnetic properties, are reported in the thesis.

As reviewed in section 1.8.2, recently a great deal of effort is devoted to the preparation of bulk samples of electron doped materials, especially in La-Mn-O series by doping tetravalent element such as Ce etc., so that these CMR materials can be used for spintronic applications. Most of the bulk materials was found to form with impurity phase or the prepared materials was effectively found to be a hole doped materials. In an effort to prepare single phase materials we have chosen Ce doped (Y, Ce)-Mn-O series, where ionic sizes of Y and Ce are comparable. In an attempt to arrive at a perovskite structure, we also tried to prepare these materials under high pressure. We manage to prepare single phase materials but with hexagonal structure. The study of magnetic properties is given in detail. The prepared materials were found to be indeed in electron doped form.

I have prepared the following list of compounds for the present thesis work,

1. $La_{0.85}Ag_{0.15}Mn_{1-y}Co_yO_3$ (y=0-0.50)
2. $La_{0.85}Ag_{0.15}Mn_{1-y}Cr_yO_3$ (y=0-0.20)
3. $La_{0.85}Ag_{0.15}Mn_{1-y}Al_yO_3$ (y=0-0.20)
4. $LaMn_{1-y}Cu_yO_3$ (y=0-0.30)
5. $Nd_{1-x}Ag_xMnO_3$ (x=0-0.20)
6. $Y_{1-x}Ce_xMnO_3$ (x=0-0.15)

The first four series deal with Mn site doping with other transition elements and by including a non-magnetic Al. The goal is to understand magnetic interaction between Mn and other transition elements and to study their effects on electrical transport. The fifth series is to explore the CMR behaviour in Nd-Mn-O series by monovalent hole doping. The last series is the electron doped $(Y_{1-x}Ce_x)MnO_3$ series and it is mainly to explore the possible double exchange ferro-magnetic (FM) interaction between Mn^{2+}/Mn^{3+} pairs and, their influence on electrical transport. The first three series are discussed in chapter 3 and the fourth series is discussed in chapter 4. (Nd, Ag)-Mn-O and (Y, Ce)-Mn-O series are discussed in chapter 5 and 6 respectively.

Chapter 2: Experimental Techniques

As we know that experimental tools are backbone of an experimentalist. So, understanding of experimental tool is primary requirement. The samples for the current investigations were prepared by solid state route. For heat treatments during the material preparations, indigenously fabricated and commercial furnaces were used. The details about the design and fabrication of these furnaces are discussed in this chapter. The prepared materials were characterized by using X-ray diffraction to check their phase purity and lattice parameters, chemical titration to determine average Mn valency, scanning electron micrographs to study the microstructure and energy dispersive X-ray analysis for determining sample composition. The electrical transport and magnetic properties were studied by carrying out temperature variations of electrical resistivity, magneto-resistivity, ac susceptibility and dc magnetiazation measurements. The experimental set-ups used for electrical transport and magnetic measurements are also discussed in this chapter.

2.1. Sample Preparation

The most widely used method for preparing polycrystalline oxides is the solid state route reaction. Even though the desired phase is thermodynamically favored, solids do not usually react together at ambient temperature over laboratory time scales and it is necessary to heat the reactants at high temperatures to overcome the kinetic barriers. The powders are often pressed into a pellet before heating to increase the contact between particles. Reaction times are usually several days and it is best to repeat the process to ensure homogeneous samples. Starting materials are usually single cation oxides, carbonates, nitrates or hydroxides materials which decompose to form oxides when heated. Carbonates are popular for the alkali and alkaline earth elements because they are not hydroscopic and therefore can be weighed accurately in air. On the initial heating or calcination of carbonate containing mixtures, carbon dioxide is produced and escapes from the solid. This prevents good sintering of the material into a dense ceramic, requiring an additional heating.

The samples for the current investigations were prepared by solid state route. For heat treatments during the material preparations, indigenously fabricated and also commercial furnaces were used. The details about the design and fabrication of these furnaces are discussed in this chapter.

The samples were prepared from the following starting compounds and elements, such as, Lanthanum Oxide (La_2O_3, 99.9%), Neodymium oxide (Nd_2O_3, 99.9%), Yttrium Oxide (Y_2O_3, 99.9%), Silver Nitrate ($AgNO_3$, 99.9%), Manganese Acetate ($C_4H_6MnO_4.4H_2O$, 99.5%), Manganese metal (Mn, 99.9%), Copper Acetate ($(CH_3COO)_2Cu.H_2O$, 99%), Cobalt Oxide (Co_3O_4, 99%), Chromium Oxide (CrO_3, 99%), Aluminum (Al) powder.

The stoichiometric ratio of starting compounds and/or elements were weighed using an electronic balance supplied by Mettler Toledo model no. AG135 with an accuracy of ±0.01mg. The weighed compounds were grinded under the medium of acetone (99%) using an agate mortar and pestle. The homogeneous mixture of starting compounds was transferred to an alumina crucible and was presintered in the temperature range 800 to 900^0C for over 24h followed by furnace cooling to room temperature. The presintered powder was grinded again to get a homogeneous mixture. The presintering was repeated twice. The presintered powder was pressed into cylindrical shape pellets by using a 13mm die and a hydraulic press supplied by Techno Search instruments, Thane, India with a maximum load of 6 Ton/cm^2. The sintering in pellet form was carried out in a step by step process in air at different temperatures with several intermediate grindings and repelletizing. The final sintering temperatures were different for different series of the samples and these details are discussed in chapters 3, 4, 5 and 6 for respective series of materials.

2.2. High Temperature Furnaces

High temperature furnaces were used for material preparation. One home made muffle furnace with maximum operating temperature of 1200^0C and a commercial high temperature furnace with maximum operating temperature of 1400^0C were used for sintering the samples. The commercial furnace was supplied by N. R. Enterprises, Kolkata, India. It is powered by a thyristor unit of 30A rating. The temperature was controlled using; West, UK make, PID programmable temperature controller (model no. 6400) with 16 segment programming feature. The platinum versus platinum-rhodium (Platinum + 10 % Rh) thermocouple was used for sensing the temperature. The heating elements are based on Si-Carbide rods. The temperature was controlled to an accuracy of ± 1^0C. The furnace could be operated upto 1400^0C.

The home made furnace (1200^{0}C) was fabricated using a cylindrical alumina muffle with an inner diameter of 5.8cm and 50cm length. Six silicon carbide rods of 45 cm length each are used as heating element. The muffle loaded with heating elements is housed in a cylindrical container made up of galvanized aluminum sheet with dimensions 50 cm diameter and 50 cm length. High temperature ceramic bricks and ceramic wools are used as thermal insulation. The Chromel-Alumel (Cr-Al) thermocouple and a commercial on/off type temperature controller are used for temperature measurements and controlling. The input power to the furnace was regulated using a variac (dimmerstat) of 15A capacity. An external on/off relay (15A capacity) was used for controlling the power supply to the heater wire. The relay was triggered using the temperature controller. The block diagram of the furnace is shown in Figure 2.1. The furnace could be operated upto a maximum temperature of 1200^{0}C. The temperature could be controlled with an accuracy of ± 5^{0}C.

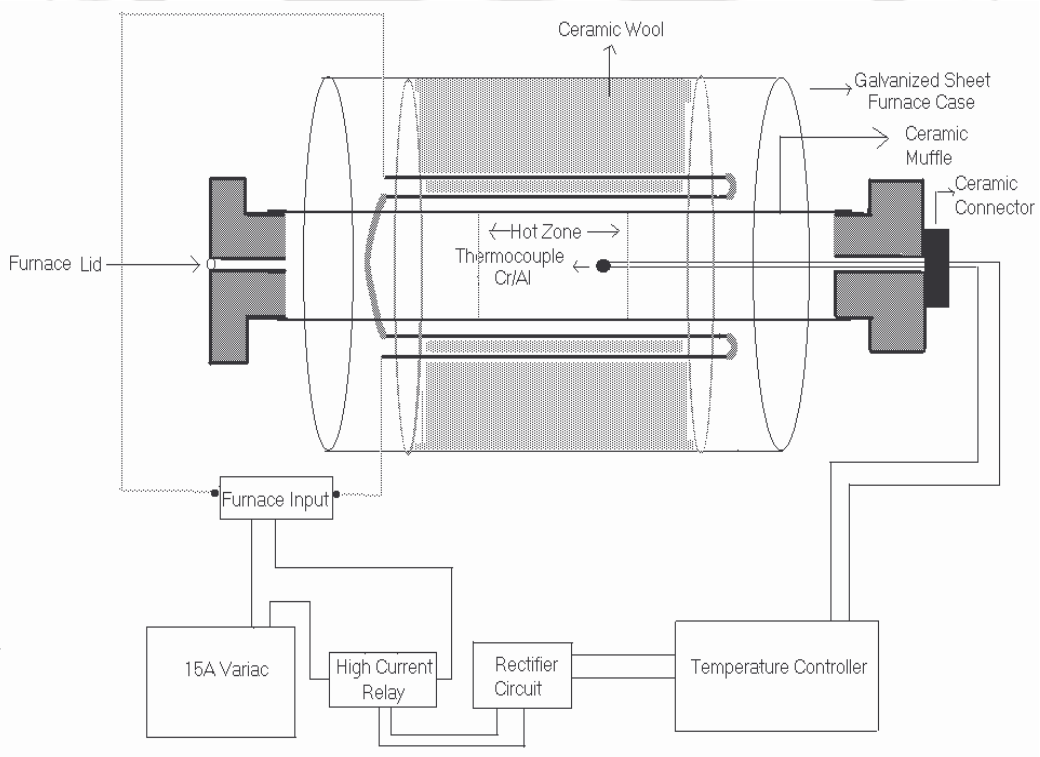

Figure 2.1: Block diagram of the furnace with maximum operating temperature of 1200^{0}C.

2.3. X-ray Diffraction

The X- ray diffraction technique has been used to study the phase purity and crystal structure of the prepared compounds. Powder X-ray diffraction (XRD) measurements were carried out at room temperature using a commercial X-ray diffractometer supplied by Seifert-model no. 3003TT/ Bruker model no. D8 by employing CuK_{α} radiation (1.5418Å). In the present investigation, all the XRD data were collected with the setting of 30mA current and 40kV voltage for X-ray generator. The instrument is based on the Bragg-Brentano geometry as shown in Figure 2.2. In this geometry, the source to sample distance and the sample to detector distance are kept equal. A perspex sheet with rectangular groove was used for sample mount where the powder sample was filled uniformly in the groove. The data were collected in an usual θ-θ scan with an angular speed 1-2^0/minute and a step size of 0.03-0.05^0.

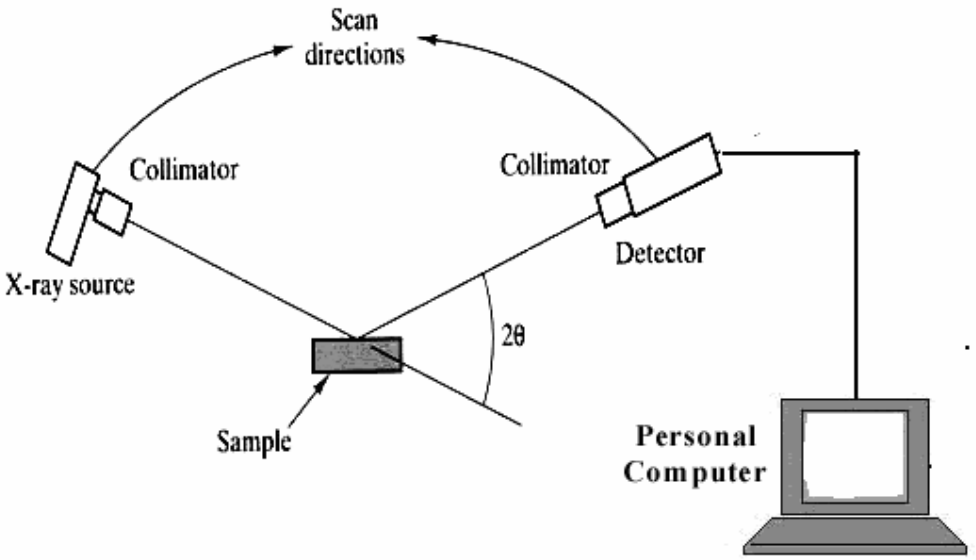

Figure 2.2: Ray diagram of X- ray diffractometer.

The XRD patterns were analysed with the help of Fullprof program by employing Rietveld refinement technique [261]. The background was refined using a polynomial function. Pseudo-Voigt function was chosen for peak shape. The global parameters, such as coefficients of background polynomial, scaling factor, half width parameters (u, v, w) and lattice parameters (a, b, c) were mainly varied during the refinement. In addition to that nuclear structure variables such as fractional atomic co-ordinates (x, y, z), isotropic displacement (temperature) parameters and occupancy values were varied. Here, occupancy is the chemical occupancy normalized to the multiplicity of the general position of the group.

The occupancy of oxygen was taken as 1 for all the refinements and it was not varied during the refinement. The quality of the refinements are known based on the values of reliability factors such as, R_p, R_{wp}, R_{exp}, R_{Bragg}, R_F and χ^2 and they are defined as follows.

$$\text{Profile factor, } R_p = 100\frac{\sum_{i=1,n}\left|y_i - y_{c,i}\right|}{\sum_{i=1,n} y_i} \quad \text{----------} \quad (2.1)$$

Here y_i is the observed point (experimental) and $y_{c,i}$ is the calculated point and n represents the number of data points.

$$\text{Weighted profile factor, } R_{wp} = 100\left[\frac{\sum_{i=1,n}\omega_i\left|y_i - y_{c,i}\right|^2}{\sum_{i=1,n}\omega_i y_i^2}\right]^{1/2} \quad \text{---------} \quad (2.2)$$

Here $\omega_i = \frac{1}{\sigma_i^2}$, σ_i^2 is the variance of observation y_i.

$$\text{Expected weight factor, } R_{exp} = 100\left[\frac{n-p}{\sum_{i=1,n}\omega_i y_i^2}\right]^{1/2} \quad \text{--------} \quad (2.3)$$

Here (n – p) is the number of degrees of freedom. n is the total number of experimental points and p is the number of refined parameters.

$$\text{Reduced chi-square, } \chi^2 = \left[\frac{R_{wp}}{R_{exp}}\right]^2 \quad \text{----------} \quad (2.4)$$

$$\text{Bragg factor, } R_B = 100\frac{\sum_h\left|I_{obs,h} - I_{calc,h}\right|}{\sum_h I_{obs,h}} \quad \text{----------} \quad (2.5)$$

Here h is the vector which levels the Bragg reflections. The $I_{obs,h}$ is the observed integrated intensities and $I_{calc,h}$ is the calculated intensities.

$$\text{Crystallographic } R_F \text{ factor, } R_F = 100\frac{\sum_h\left|F_{obs,h} - F_{calc,h}\right|}{\sum_h F_{obs,h}} \quad \text{----------} \quad (2.6)$$

Here $F_{obs,h}$ and $F_{calc,h}$ are the observed and calculated structural factors respectively.

Inter atomic distances (bond length) and bond angles were calculated using the refined fractional coordinates and lattice parameters by using Fullprof software.

The average crystallite size (S_C) has been calculated from the peak broadening by using the Scherrer's formula [262]

$$S_C = \kappa\lambda / \beta\cos\theta \qquad \text{----------} \qquad (2.7)$$

where, constant k depends upon the shape of the particle(grain) size. Here it is taken as 0.89 by assuming the circular shape of particle, β = Full Width at Half Maximum (FWHM) of intensity versus 2θ profile, λ is wavelength of the CuK_α radiation and θ is the Bragg's diffraction angle. The instruments broadening effect has been taken into account.

2.4. Scanning Electron Microscope (SEM)

Recording of microstructure image and compositional analysis have been carried out by using LEO Scanning Electron Microscope (SEM) equipped with Oxford energy dispersive spectrometer (EDS). Elemental analysis of the samples has been done by recording energy dispersive spectrum. Basic principles of SEM and EDS analysis are given briefly as following.

The scanning electron microscope (SEM) is a type of electron microscope that images the sample surface by scanning it with a high-energy beam of electrons in a raster scan pattern. The electrons interact with the atoms that make up the sample producing signals that contain information about the sample's surface topography, composition and other properties such as electrical conductivity. The types of signals produced by the SEM include secondary electrons, back scattered electrons (BSE), characteristic x-rays, light (cathode-luminescence), specimen current and transmitted electrons. These types of signal require specialized detectors and all such detectors are not present in a single machine. The signals result from interactions of the electron beam with atoms at or near the surface of the sample. In the most common or standard detection mode, secondary electron imaging (SEI) can produce very high-resolution images of a sample surface, revealing details about 1 to 5 nm in size. Due to the way these images are created, SEM micrographs have a very large depth of field yielding a characteristic three-dimensional appearance useful for understanding the surface structure of the sample. A wide range of magnifications is possible, ranging from about 25X (about equivalent to that of a powerful hand-lens) to about 250,000X, about 250 times the magnification limit of the best optical microscopes.

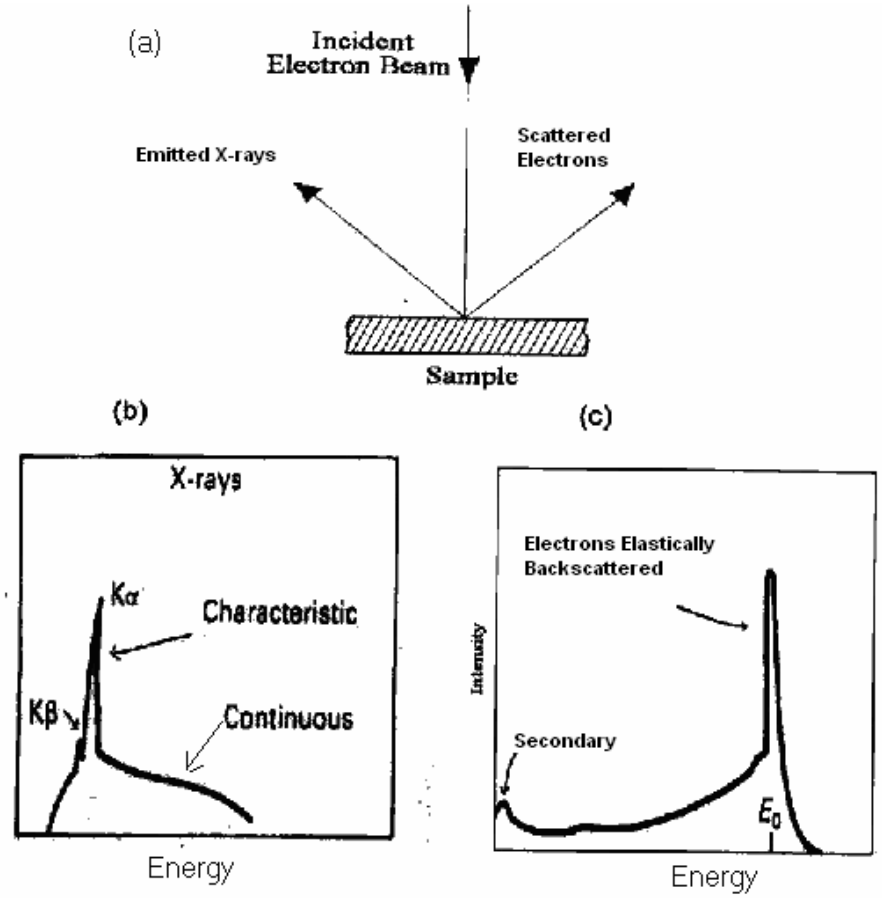

Figure 2.3: (a) The scattering process of an electron beam in a SEM. The energy distribution of (b) X-rays and (c) electrons, after emission from the sample surface.

Energy dispersive X-ray spectroscopy (EDS, EDX or EDXRF) is an analytical technique used for the elemental analysis or chemical characterization of a sample. Its characterization capabilities originate from the fact that each element has a unique atomic structure, which emits its unique characterestic X-ray. To stimulate the emission of characteristic x-rays from a specimen, a high energy beam of charged particles such as electrons or protons, or a beam of x-rays, is focused into the sample being studied. At rest, an atom within the sample contains ground state (or unexcited) electrons in discrete energy levels or electron shells bound to the nucleus. The incident beam may excite an electron in an inner shell, ejecting it from the shell while creating an electron hole where the electron was. An electron from an outer, higher-energy shell then fills the hole, and the difference in energy between the higher-energy shell and the lower energy shell is released in the form of an x-ray. The x-ray released in the above process is then detected and analysed by the energy

dispersive spectrometer. These x-rays are characteristic of the difference in energy between the two shells, and of the atomic structure of the element from which they were emitted.

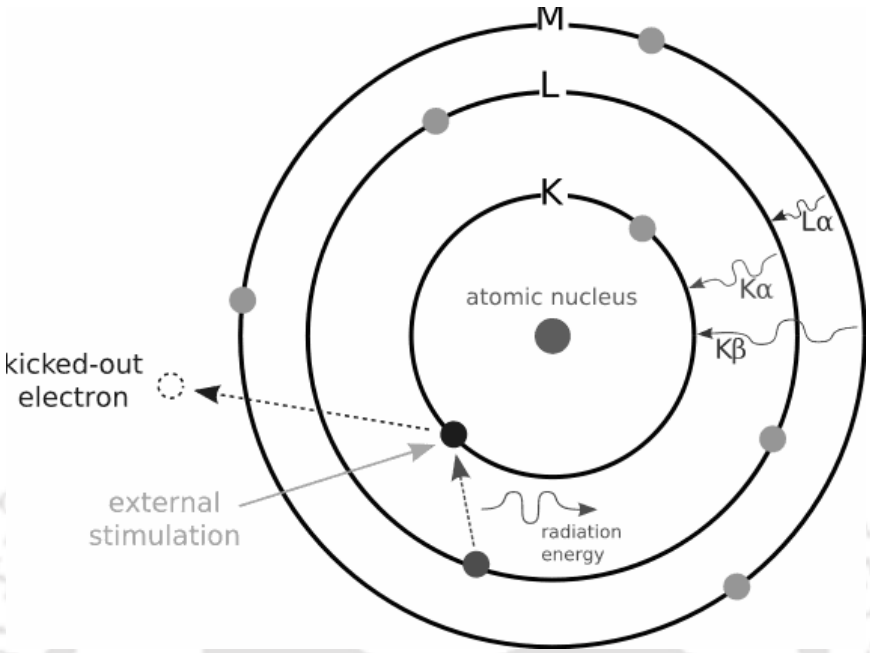

Figure 2.4: Principle of EDX.

2.5. Chemical Titration

The oxidation state of Mn was determined by a chemical titration method, in which the samples were dissolved in dilute sulphuric and phosphoric acids with an addition of excess amount of Mohr salt, $Fe(NH_4)_2(SO_4)_2.6H_2O$ and were titrated against self-indicating potassium permanganate, $KMnO_4$ solution [263, 264]. Here, the valency of Fe and Mn are +2 and +7 respectively. During titration Fe^{2+} is oxidized to Fe^{3+} and Mn^{7+} is reduced to Mn^{2+}. The reaction is as follows,

$$MnO_4^- + 8H^+ + 5Fe^{2+} \rightarrow Mn^{2+} + 5Fe^{3+} + 4H_2O \quad \text{----------} \quad (2.8)$$

$$Mn^{7+} + 5e \rightarrow Mn^{2+}$$

$$5Fe^{2+} - 5e \rightarrow 5Fe^{3+}$$

$$Mn^{7+} + 5Fe^{2+} \rightarrow Mn^{2+} + 5Fe^{3+} \quad \text{----------} \quad (2.9)$$

The normality of Mohr salt and $KMnO_4$ was kept constant during the titration. The normality (N) for any solution is defined as,

$$N = M \times \text{number of reduced valency or oxidized valency} \quad \text{----------} \quad (2.10)$$

Here M is the molarity of the solution. The molarity of a solution is 1 when the solution is prepared by adding an amount of molecular weight of the sample in 1000 ml of water. To prepare 250 ml solution of y molar concentration, one has to add z_1 gm (z_1 = molecular wt. × 250 × y/1000) of material into 250 ml of water.

Generally, fresh solutions were prepared to perform the titrations. Molecular weight of Mohr salt and $KMnO_4$ are 392.13 gm and 158.04 gm respectively. In a 250 ml volumetric flask, z_1 = 49.016 gm (1/8 of the molecular weight) of Mohr salt was taken and deionized water was added upto the mark on the volumetric flask. It was shaken thoroughly at the time of adding water and it leads to a molarity of 0.5M (0.5N). Similarly, in another 250ml volumetric flask, z_1 = 3.95 gm (1/40 of the molecular weight) of $KMnO_4$ was taken alongwith added deionized water upto the mark of the volumetric flask. It leads to a molarity of 0.1 M (0.5N). So, the normality of the above two solutions was equal. 20 ml of Mohr salt solution was taken in a conical flask with the help of a 20 ml pipette. 2 ml of dilute phosphoric (H_3PO_4) and 2 ml of dilute sulphuric (H_2SO_4) acids were added to it. $KMnO_4$ solution was taken in a burette and was titrated against Mohr salt solution and, was shaken at the time of adding. At the end point, faint pink colour of Mohr salt solution was turned into a straw colour i.e. all iron was oxidized. The quantity of $KMnO_4$ solution added was determined from the initial and final burette readings. Titration was repeated two times, and the average value has been taken for finding the equivalence of $KMnO_4$ solution (say u_1 ml) for 20ml of Mohr salt solution. Let u_2 ml of $KMnO_4$ solution is equivalent to 1 ml of Mohr salt.

To standardize the titration procedure, commercially supplied MnO_2 (Mn^{4+}) was used. For determining the valency of Mn in MnO_2, a small amount of known weight of MnO_2 was added into the 20ml of Mohr salt solution before titration. As a result of the addition of MnO_2, some of the Fe^{2+} ions are oxidized to Fe^{3+} ions. The Mohr salt solution containing MnO_2 was titrated against $KMnO_4$ solution. The consumption of $KMnO_4$ solution (say u_3 ml) was found to be less than the value obtained from the earlier titration, i.e. titration against pure Mohr salt solution. The difference between the equivalent Mohr salt solution (u_1) and the consumption of $KMnO_4$ solution (u_3) can be found and, this quantity of Mohr salt solution is called consumed Mohr salt solution (say u_4 ml). The reduced valency (R_v) of Mn in MnO_2 was calculated using the formula,

$$R_v = \frac{x_1 y_2}{x_2 y_1} \quad \text{----------} \quad (2.11)$$

where, x_1 and x_2 are the atomic weight of Mn and Fe respectively. y_1 is the mass of Mn present in the MnO_2 compound added to the Mohr salt solution in gram. y_2 is the mass of Fe present in the consumed Mohr salt solution, i.e. in u_4 ml of Mohr salt solution. So, the actual valency can be calculated as,

$$\text{Mn Valency} = 2 + R_v \text{ ----------} \quad (2.12)$$

2.6. ac Susceptibility Set-up

ac susceptibility technique can be used for studying the magnetic properties of the materials [265-269] and it has advantage over other techniques in terms of cost and one can get additional information such as loss components, etc. The details of ac susceptometer are given as follows. It is basically designed by employing mutual inductance bridge method. It consists of a primary coil and coaxially wound two identical secondary coils as shown in Figure 2.5. One secondary coil is used for mounting the sample and is called sample secondary and the other one is reference coil. The primary coil is energized using a sinusoidal signal of desired frequency and voltage, $E = E_0 e^{i\omega t}$. Magnetic field, $H = H_0 e^{i\omega t}$ is generated along the axis of the solenoid (primary coil) corresponding to applied voltage in the primary. In the absence of the sample, the induced voltage in each secondary coil would be almost equal and its differential output would be close to zero. When sample is inserted into sample secondary coil, the induced emf, e is a measure of susceptibility of the material, as given in the following expression [270],

$$e = (\alpha n_s V_s \omega \mu_0 H_0)\chi \quad \text{----------} \quad (2.13)$$

where, n_s is the number of turns per unit length in the secondary coil; ω is the angular frequency of input signal to primary coil and V_s is the volume of the sample. The filling factor coefficient, α depends on the geometry and dimension of the sample and secondary coils. χ is the susceptibility of the material.

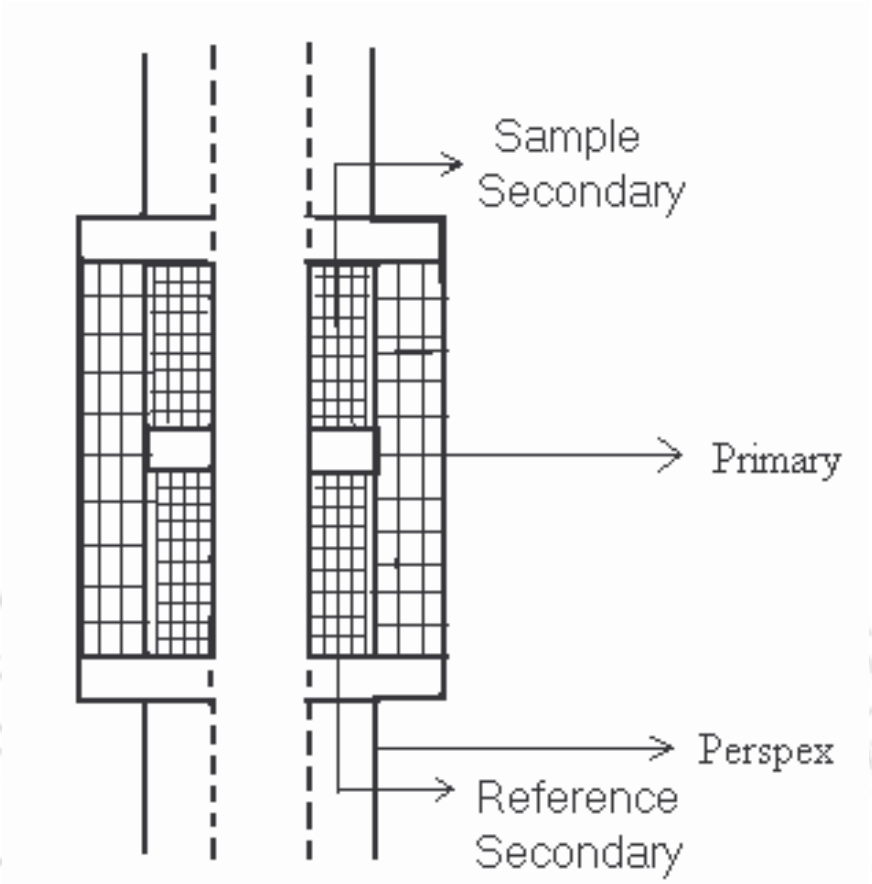

Figure 2.5: Block diagram of Mutual Inductance Coil assembly.

The outline of the mutual inductance coil assembly is shown in Figure 2.5. Two identical secondary coils of length 15 mm each were wound with 39SWG (diameter 0.1312 mm) insulated copper wire on a perspex tube of outer diameter 12 mm and inner diameter 6 mm.They are separated by a distance of 3 mm along the length of the coil. The primary coil with same SWG was wound over the secondary coils with inner diameter 18 mm and outer diameter 23 mm. The number of turns in each secondary coil was 1370 and that of primary coil was 2689.

The temperature variation down to 20 K was achieved using a closed cycle Helium refrigerator cryostat along with the temperature controller. However, a separate sample insert assembly was fabricated for ac susceptibility measurements. The schematic diagram of the CCR cryostat is shown in Figure 2.6. The sample chamber of $1''$ diameter is covered by non-magnetic radiation shield and vacuum shroud as shown in Figure 2.6. The sample chamber is cooled with the help of helium exchange gas.

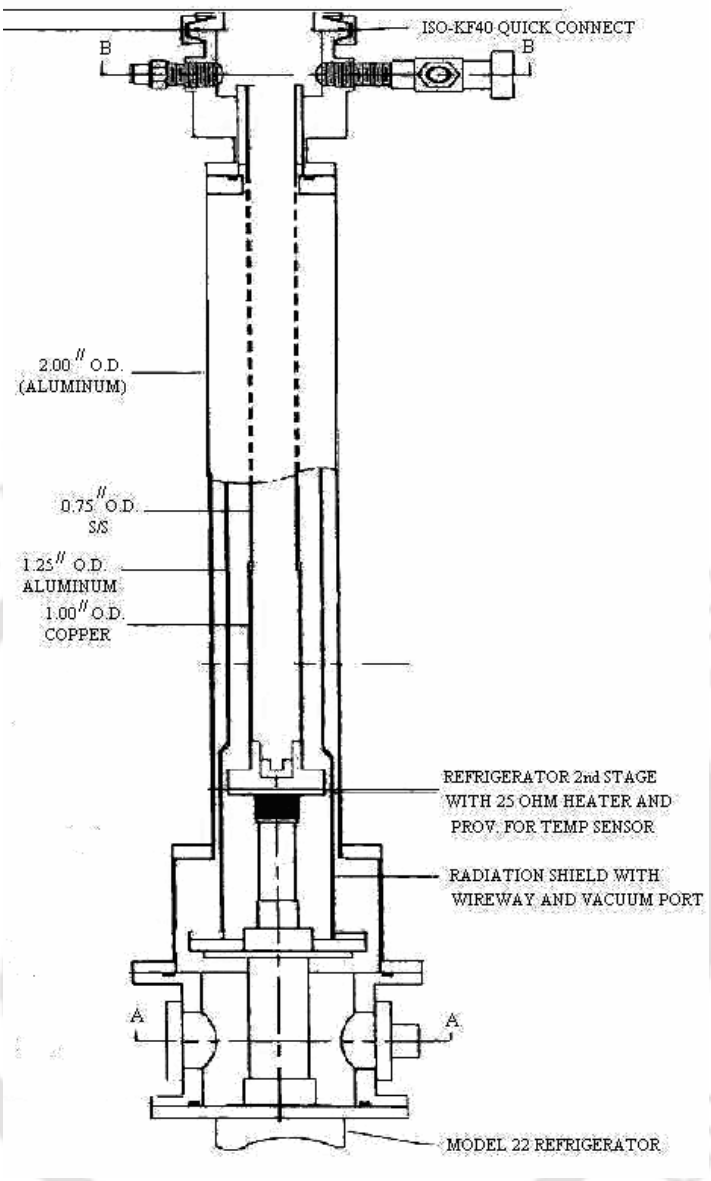

Figure 2.6: Block diagram of CCR cryostat.

A sample insert assembly attached with a sample holder has been designed and fabricated for quick loading and unloading of samples. The schematic diagram of the sample insert assembly along with Coil housing assembly for mutual inductance bridge is shown in Figure 2.7. The non magnetic thin walled stainless steel (SS) tube with outer diameter 10 mm and length 550 mm is coupled to the sample holder made up of Perspex rod of length 100 mm. The bottom part of Perspex rod was made into a flat surface to load the sample and temperature sensor. The other end of the SS tube passing through the Wilson nut is fitted with an electrical feed through and it is used for connecting the sensor leads mounted nearby sample area. Electrical feed through adapter attached to aluminum flange was used for

connecting the primary and secondary Coil leads. The position of sample holder can be adjusted with the help of Wilson nut arrangement. A Lakeshore supplied Si diode sensor, which follows a standard curve was mounted in the vicinity of sample position as shown in the Figure 2.7.

The block diagram of the ac susceptibility set-up is shown in Fig. 2.8. The primary coil is connected to the oscillator output of a dual phase lock-in amplifier supplied by Perkin–Elmer, model no. 7265. The maximum oscillator output of lock-in amplifier is 5V (rms). The magnetic field was calculated using the standard relation of the solenoid,

$$H = \frac{NI}{L} \text{ (A/m)} \quad \text{----------} \quad (2.14)$$

or,

$$H = \frac{NI}{L} 4\pi \times 10^{-3} \text{ (Oe)} \quad \text{----------} \quad (2.15)$$

Here, N is the total number of turns in the primary coil, I is the amplitude of current flowing through the primary in Ampere and L is the length of primary in meter. The maximum amplitude of magnetic field in the present set-up was found to be around 12Oe. The output of both the secondary coils is connected to the differential input (A-B) of the lock-in amplifier, which can measure the in-phase and out of phase components of ac susceptibility signal simultaneously. For controlling the temperature, Lakeshore supplied silicon diode sensor (model no. DT-470) has been used. This sensor was mounted at the cold tip of the CCR, where a heater wire of 50Ω resistance was also installed. Four leads of the controlling sensor are connected to the A-channel input of the Lakeshore supplied temperature controller model no. 331. The sample temperature is measured using another silicon diode sensor (model no. DT-670) which is connected to the B-channel input of the temperature controller. Both the temperature controller and the lock-in amplifier were connected to a personal computer equipped with a GPIB board for data acquisition. The necessary software in the language of Quick Basic was developed for running the temperature variation of ac susceptibility. The accuracy of temperature measurement was ±50mK.

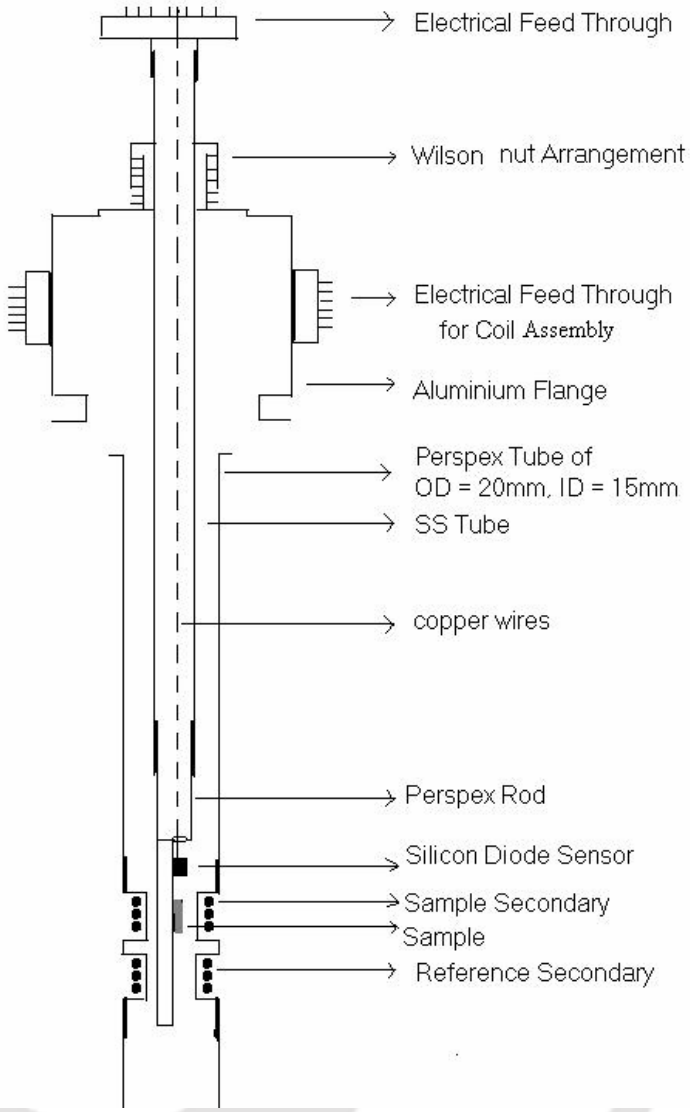

Figure 2.7: Sample insert and Coil housing assembly.

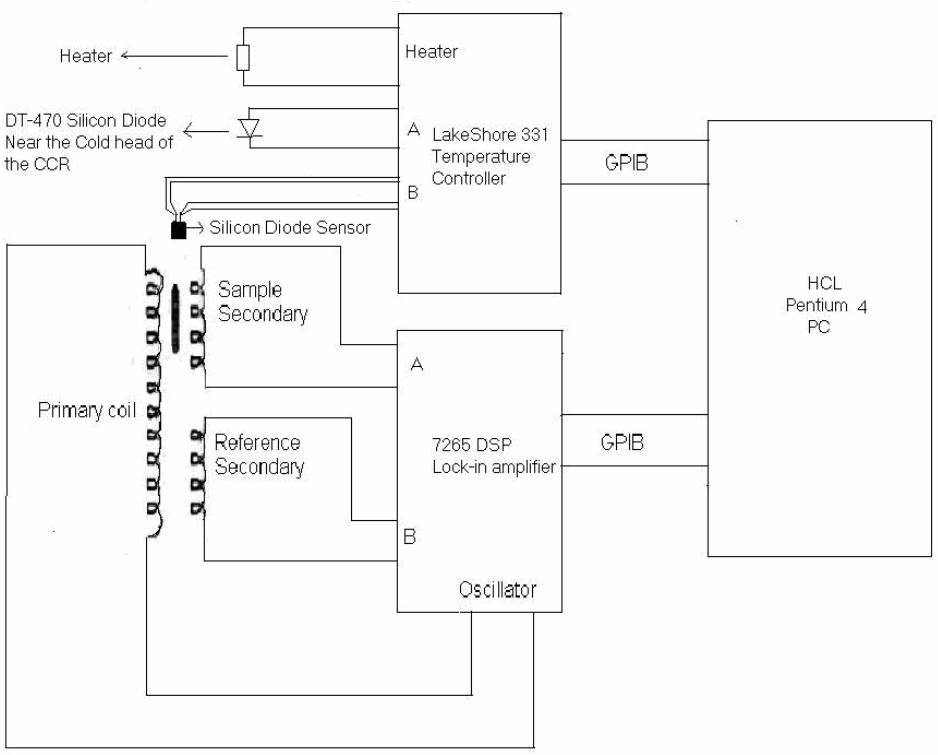

Figure 2.8: Block diagram of ac susceptibility set-up.

To completely separate the real and imaginary components of ac susceptibility, appropriate reference phase angle needs to be set, in the lock-in amplifier. The phase angle ϕ was obtained by adjusting the reference phase in the lock-in amplifier such that the signal of the out of phase (loss/imaginary component) component is zero about the FM transition temperature. One can also numerically separate the real and imaginary components, by measuring the susceptibility in zero phase and using the following expressions [271],

$$\chi' = \chi_0' \cos\phi + \chi_0'' \sin\phi \text{ ----------} \quad (2.16)$$

$$\chi'' = \chi_0'' \cos\phi - \chi_0' \sin\phi \text{ ----------} \quad (2.17)$$

Where χ_0' and χ_0'' are the measured susceptibilities before phase adjustment (at zero phase).

AC susceptibility measurement is a compatible technique to probe the associated magnetic phase and its sensitivity towards several influencing factors of a system. Investigation of the nonlinear χ_{ac} is one of the most important tools to understand any magnetic phase transition. In general, the nonlinearity of magnetization (M) can be expanded with the help of power series with respect to an oscillating applied magnetic field (H) as,

$$M = \chi_1 H + \chi_2 H^2 + \chi_3 H^3 + \ldots\ldots\ldots\ldots \quad (2.18)$$

Here χ_1, χ_2 and χ_3 etc. are, respectively, linear, second and third harmonic susceptibilities. In fact, several subtle features not discernible using linear χ_{ac} can be picked up using nonlinear χ_{ac}. Direct measurement of the non-linear susceptibility, gives the choice to us to clearly distinguish the spin glass freezing from to other non-equilibrium systems like super-paramagnetism. According to the critical behaviour of spin glass material, $\chi'_3 \alpha \varepsilon^{-\gamma}$, where $\varepsilon = (T-T_g)/T_g$ and γ is the critical exponent. The non-linear susceptibility was measured by setting a appropriate harmonic selection in the lock-in-amplifier.

Calibration of the ac susceptometer was carried out by using the standard paramagnetic salts Gd_2O_3 [272]. Its temperature dependent gram susceptibility is given as, [273]

$$\chi = \frac{45684}{T+18} \times 10^{-6} \text{ c.g.s} \qquad \text{----------} \qquad (2.19)$$

2.7. DC Magnetization Measurement

DC magnetization as a function of temperature and field was measured by using the vibrating sample magnetometer at CIF, IIT Guwahati. The magnetization measurement in one of the series was measured by using SQUID magnetometer at BARC, Mumbai.

2.7.1 Vibrating Sample Magnetometer (VSM)

The vibrating sample magnetometer (VSM) has become a widely used instrument for measuring the magnetic properties of a large variety of magnetic materials. The vibrating sample magnetometer (VSM) developed originally by Foner [274] has however, been the most successful for low temperature and high magnetic field studies of correlated electron systems. It has a flexible design and combines high sensitivity with ease of sample mounting and exchange. Samples can be changed rapidly even at any operating temperature. Using a vibrating sample magnetometer one can measure the DC magnetic moment as a function of temperature, magnetic field and time. So, it allows to perform susceptibility and magnetization studies. Magnetic moments as small as 5×10^{-5} emu are measurable with a VSM [274].

The temperature variations of zero field cooled (ZFC) and field cooled (FC) magnetization (M) were measured by using Lakeshore, model no. 7410 vibrating sample magnetometer from 80 K to 400 K. The magnetic field was produced by using 10 // electromagnet. The magnetization loop was measured by varying B upto 2T. Calibration of

the vibrating sample magnetometer was done by measuring the magnetic moment of a standard pure Ni sample. Block diagram of the vibrating sample magnetometer is shown in Figure 2.9.

The VSM is based upon Faraday's law, according to which an emf is induced in a conductor by a time-varying magnetic flux. If a sample of any magnetic material is placed in a uniform magnetic field, a dipole moment will be induced. If the sample vibrates with sinusoidal motion, there is some magnetic flux change. This induces a voltage in the pick-up coils, which is proportional to the magnetic moment of the sample. Voltage, V(t) can be detected to a high resolution and accuracy by means of suitable VSM signal detector (e.g. Lock in Amplifier).

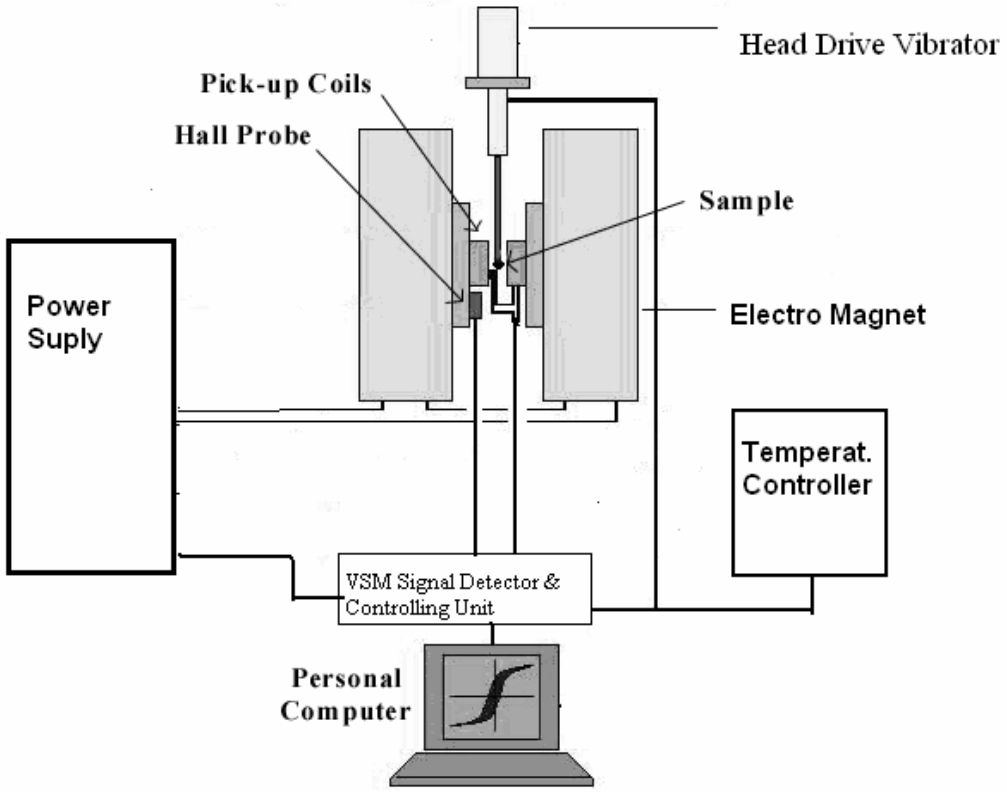

Figure 2.9: Block diagram of the vibrating sample magnetometer.

2.7.2. SQUID Magnetometer

The magnetization measurement for one of the series was measured by using Quantum Design (model no. MPMS5), SQUID (Superconducting Quantum Interference Device) magnetometer.

The main components of a SQUID magnetometer are: (A) Superconducting magnet (B) Pick up coil (C) SQUID connected to the pick up coil. (D) Superconducting magnetic shield. The block diagram for SQUID magnetometer is shown in Figure 2.10. A brief details about these components and the principle of operation of SQUID magnetometer are given below.

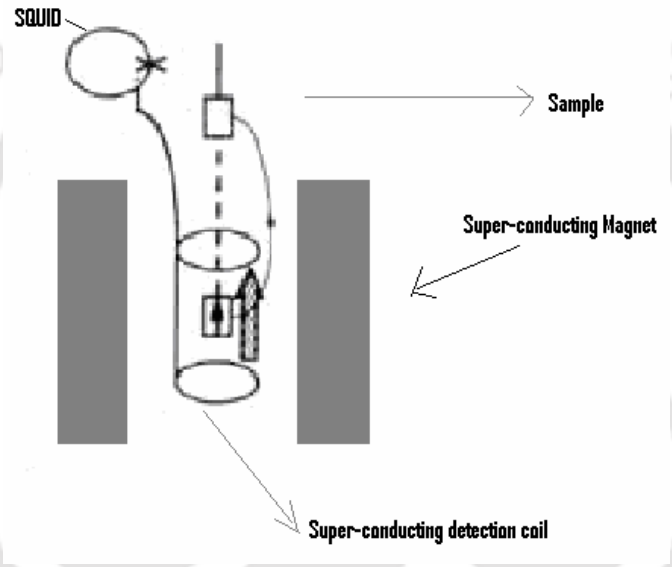

Figure 2.10: Block diagram of the SQUID magnetometer.

(A) Superconducting magnet: A superconducting magnet is a solenoid made up of superconducting wire. This solenoid must be kept at liquid helium temperature in a liquid-helium Dewar. The uniform magnetic field is produced along the axial cylindrical bore of the coil. A superconducting magnet requires an appropriate programmable bipolar power supply to operate it.

(B) Pick up coil: This is a single piece of superconducting wire configured as a second-order gradiometer (shown in Figure 2.11). In this geometry, this pick-up coil system is placed in the uniform magnetic field region of the solenoidal superconducting magnet. The SQUID coils detect the longitudinal component of the magnetization as the sample is pulled through them as shown in Figure 2.10. When the sample is pulled up and down, it produces an alternating magnetic flux in the pick up coil which leads to induced emf. Pick-up coil system is

connected to the SQUID, which experiences the alternating voltage, depending on the moment of the sample.

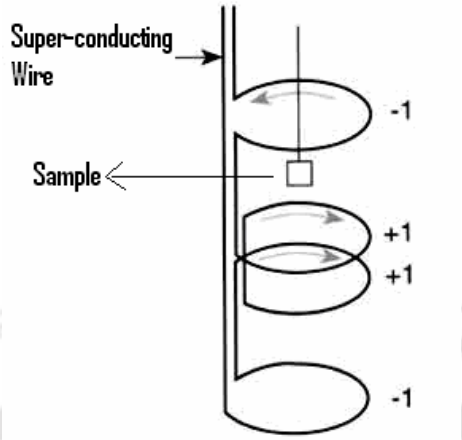

Figure 2.11: Second-order gradiometer superconducting pick-up coils.

(C) SQUID (detection unit): The SQUID utilizes the Josephson (the weak link) effect in superconducting ring, where the flux passing through the weak link is quantized. The SQUID consists of a superconducting loop with one (rf SQUID) or two (dc SQUID) weak link Josephson junctions. The electrical current density through the Josephson junctions depends on the phase difference in wave functions $\Delta\Phi$ between two parts of the superconductors. Moreover, the time derivative of $\Delta\Phi$ is correlated with voltage across the Josephson junctions. A change in the magnetic flux in the pick up coils changes the persistent current in the detection circuit. So, the change in the current in the detection coils produces variation in the SQUID output voltage proportional to the magnetic moment of the sample. The above operation is schematically shown in Figure 2.12.

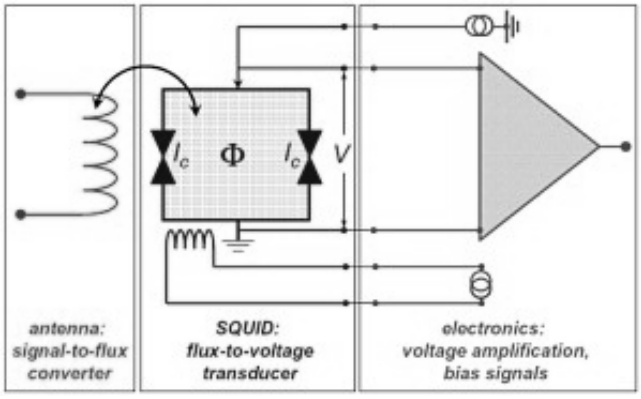

Figure 2.12: SQUID magnetometer-flux-to-voltage converter

(D) Superconducting magnetic shield: It is used to shield the SQUID sensor from the fluctuations of the ambient magnetic field of the place where the magnetometer is located and from the large magnetic field produced by the superconducting magnet.

2.8. Electrical Resistivity and Magneto-Resistivity Measurements

Temperature variation of dc electrical resistivity and transverse magneto-resistivity measurements down to 20 K were carried out to study the electrical transport. For carrying out the above measurements, a top loading helium exchange gas cooled type closed cycle helium refrigerator cryostat fabricated by; Cryo Industries of America, USA using a CTI make compressor and cold head motor has been used. The temperature was controlled using a Lakeshore temperature controller, Model no.331 and a Lakeshore calibrated Si-diode sensor mounted on the cold head. The sample can be positioned at the centre of pole face using the Wilson nut arrangement. The pole pieces of $10''$ diameter are tapered to $3''$ diameter. The magneto-resistivity measurements have been carried out by applying a magnetic field strength of 10 kOe (1 T).

Standard linear four probe technique was used to eliminate the contribution from contact resistance and lead resistance coming into picture. Current through the sample was passed using a programmable Keithley constant current source, model no. 224. The voltage drop across the sample was measured using Keithley nanovoltmeter, model no. 2182. To eliminate the thermo-emf generated across the voltage leads, measurements were carried out for both positive and negative currents. The experimental data were collected using a personal computer equipped with GPIB board. The Fabricated sample holder attached to the CCR cryostat for resistivity and Magneto-resistivity measurements is shown in Figure 2.13. The necessary software in quick Basic language was developed for temperature controlling and data acquisition using a personal computer.

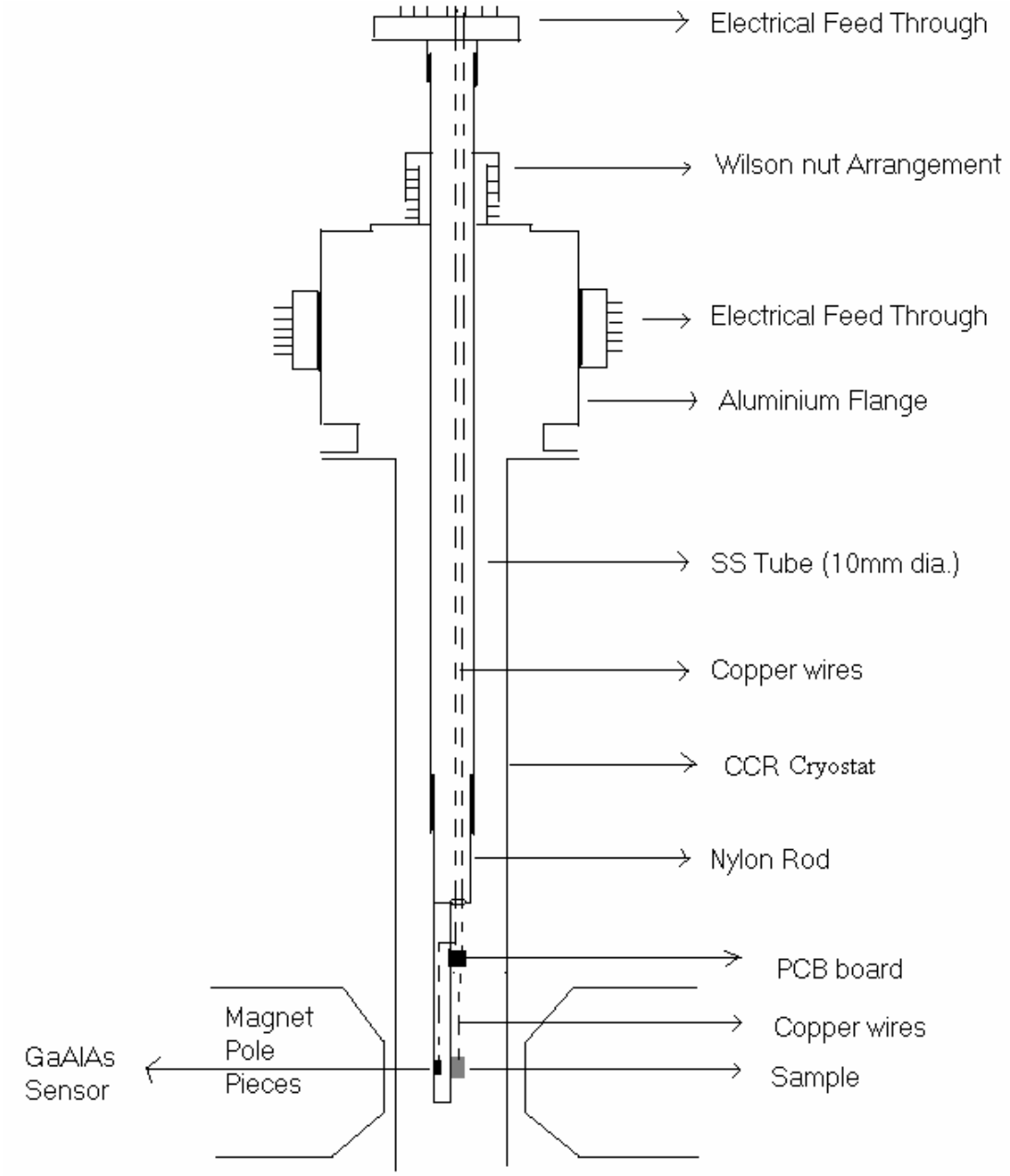

Figure 2.13: Fabricated sample holder attached to the CCR cryostat for resistivity and Magneto-resistivity measurements.

Chapter 3: Mn Site Doped (La, Ag)-Mn-O Series

The doping at Mn site in mixed valent manganites by other transition elements (T = Ti, Cr, Fe, Co, Ni, Cu, Ru, etc.) or non-magnetic impurities like Al, Ga gives rise to changes in Mn^{3+}/Mn^{4+} ratio, which leads to complicated and interesting magnetic and electrical transport properties as discussed in the introduction. The doping of these foreign elements at Mn site results in several interesting properties like multiple magnetic transitions, charge ordering, spin glass behaviour, Kondo effect, metal-insulator transition, etc.

Among all transition elements doping at Mn site in perovskite-structure manganites, the Co doping is very interesting. One of the reasons is that cobalates themselves exhibit double exchange FM with negative magneto-resistivity. Since Co ion has three kinds of spin states, i.e. low spin (LS), intermediate spin (IS) and high spin (HS), resulting from the fact that the crystal field splitting of the Co 3d states and Hund's rule coupling energy are comparable for the cobaltites. In general, the superexchange interaction between Co^{3+} (both high spin and low spin) and Co^{4+} are known to be ferromagnetic and the exchange interaction between the ions with same valency is anti-ferromagnetic [275-278].

Another interesting transition element is Cr ion. Cr^{3+} is iso-electronic with Mn^{4+} and it is a non-Jahn Teller ion [195]. The doping of Cr ion at Mn site of mixed valent manganites is expected to give mixed competing interactions and can result in several interesting magnetic properties. Unlike the magnetic impurities, the substitution of non-magnetic element Al at Mn site of mixed valent manganites is expected to play a simple role of dilution of double exchange ferromagnetic interaction and introduction of random electrical potential without any complicated magnetic phase separation [221]. Such substitution facilitates the comparison of the results with magnetic element substitution for the ease of interpretation.

There are several reports on substitution of transition elements and non-magnetic element at Mn site in divalent doped manganites (as discussed in introduction, section 1.8.3). But there are very limited reports on doping of foreign elements at Mn site in CMR materials, based on mono-valent doping in rare earth site. The monovalent doping has the advantage of creation of the required concentration of Mn^{3+}/Mn^{4+} ions with relatively small doping concentration. In this chapter, I have studied the effect of the doping of transition metal ions (Co and Cr) and nonmagnetic Al ion at Mn site of monovalent doped $(La_{0.85}Ag_{0.15})MnO_3$ compound, to understand the effect of doping on crystal structure, magnetic properties and electrical transport properties.

3.1. $La_{0.85}Ag_{0.15}Mn_{1-y}Co_yO_3$ Compounds (y=0-0.50)

This section deals with the effect of Co doping at Mn site of $La_{0.85}Ag_{0.15}MnO_3$ compound. The preparation and characterization and, the results obtained from various physical measurements such as ac susceptibility, dc magnetization, electrical resistivity and magneto-resistivity along with the analysis are presented.

3.1.1: Sample Preparation and Characterization

Polycrystalline samples of $La_{0.85}Ag_{0.15}Mn_{1-y}Co_yO_3$ (y = 0, 0.05, 0.10, 0.15, 0.20, 0.30, 0.40 and 0.50) were prepared by conventional solid state reaction method. Stoichiometric ratio of La_2O_3, $AgNO_3$, $C_4H_6MnO_4.4H_2O$ and Co_3O_4 with 99.9% purity were weighed and mixed thoroughly under acetone. The mixture was presintered at 300 ^{0}C, 400 ^{0}C, 500 ^{0}C, 600 ^{0}C and 700 ^{0}C for 5 h at each temperature and at 800 ^{0}C for 36 h with intermediate grindings. The powdered samples were pressed into cylindrical pellets of 13 mm dia and 2 to 3 mm thickness and were sintered at 1000 ^{0}C for 40 h. The final sintering in pellet form was carried at 1100 ^{0}C for 40 h.

The crystal structure and phase purity of all the samples have been studied by recording X-Ray diffraction (XRD) patterns. The XRD patterns recorded for $La_{0.85}Ag_{0.15}Mn_{1-y}Co_yO_3$ compounds for y=0 to 0.50 are shown in Figure 3.1. They are found to be in single phase form. The XRD patterns of samples for y ≤ 0.20 could be indexed to $R\bar{3}c$ space group with rhombohedral structure and the patterns for y ≥ 0.30 could be indexed to *Pbnm* space group with orthorhombic structure. Thus, the doping of Co at Mn site of $La_{0.85}Ag_{0.15}MnO_3$ gives rise to structural transition from rhombohedral to orthorhombic symmetry with increase in Co concentration.

The XRD patterns were analysed with the help of Fullprof program by employing Rietveld refinement technique [261]. Typical XRD patterns along with Rietveld refinement for y =0.05 and 0.15 samples are shown in Figure 3.2 and for y=0.30 sample it is shown in Figure 3.3. Here the experimental data are shown as open circles and the calculated intensities are shown as solid lines. The bottom line represents the difference between measured and calculated intensities.

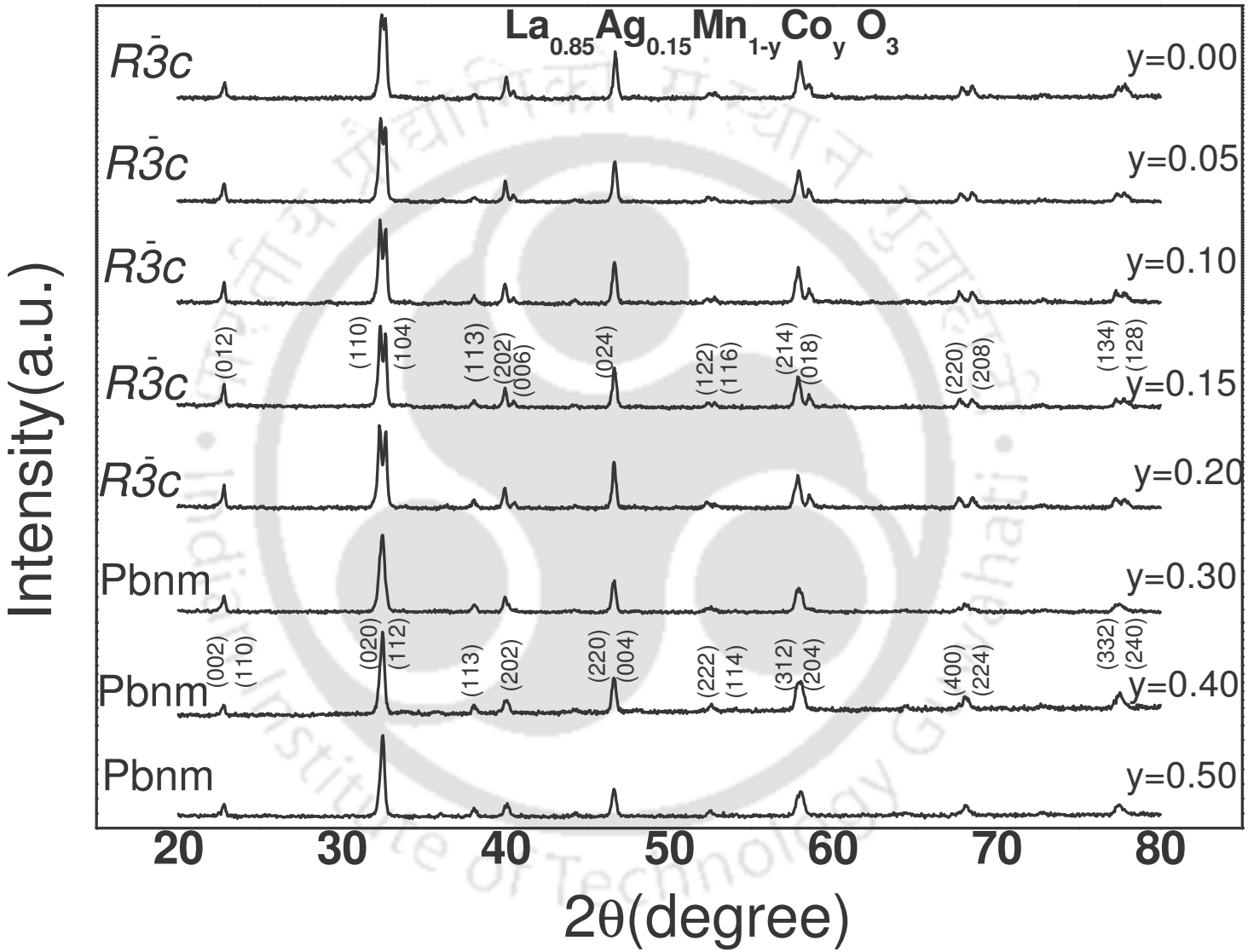

Figure 3.1: XRD patterns of the samples $La_{0.85}Ag_{0.15}Mn_{1-y}Co_yO_3$ for y = 0 to 0.50.

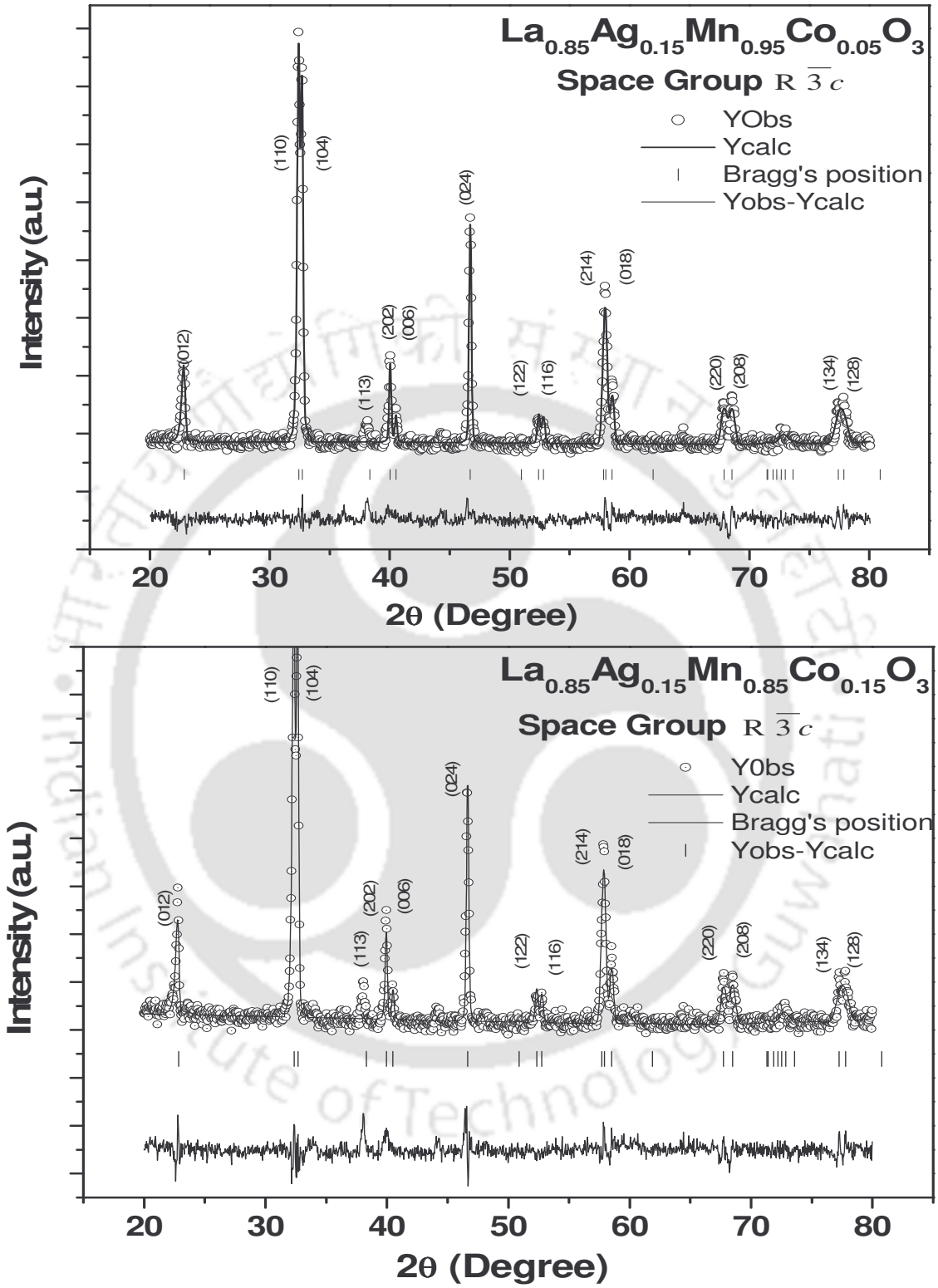

Figure 3.2: XRD patterns along with Rietveld refinement for y=0.05 and 0.15 samples. The circles represent experimental points and solid line represents Rietveld refined data. The dotted lines show the difference between experimental and refined data.

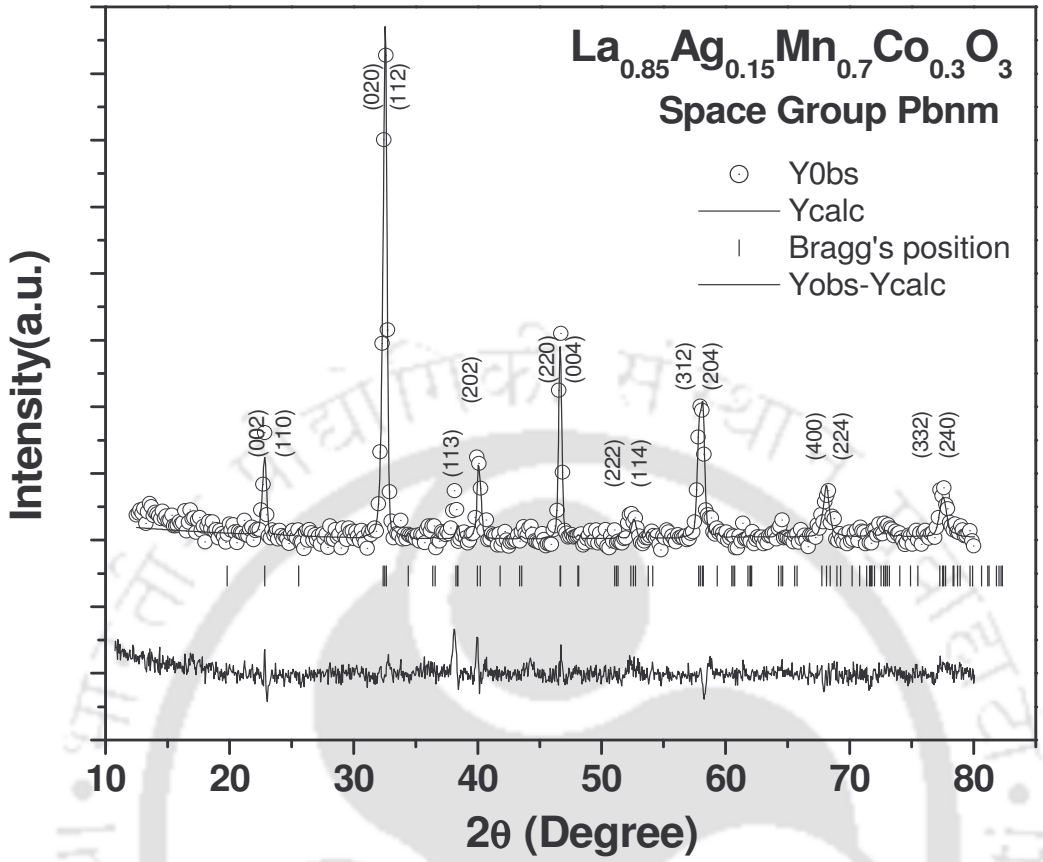

Figure 3.3: XRD pattern along with Rietveld refinement for y=0.30 sample. The circles represent experimental points and solid line represents Rietveld refined data. The dotted lines show the difference between experimental and refined data.

The room temperature lattice parameters, reliability factors (R_p, $R_{\omega p}$, R_{exp}, R_{Bragg}, R_F and χ^2) and unit cell volume values are given in Table 3.1. It can be seen that there is a systematic increase in lattice parameters *a*, *b*, *c* and unit cell volume with increase in dopant concentration in rhombohedral structured samples ($y \leq 0.20$). On the other hand, there is a reduction in lattice parameters in orthorhombic structured samples. The bond length and bond angle have been calculated from Powder Cell software. The bond length is found to increase and bond angle is found to decrease with increase in Co doping upto y=0.20. However, for $y > 0.20$, opposite effect has been observed i.e. decrease in Mn-O bond length and increase in Mn-O-Mn bond angle with some anomaly.

Table 3.1: Parameters obtained from the Rietveld analysis of XRD patterns for the samples $La_{0.85}Ag_{0.15}Mn_{1-y}Co_yO_3$ (y = 0.0, 0.05, 0.10, 0.15, 0.20, 0.30, 0.40 and 0.50). R_p, $R_{\omega p}$, R_{exp}, R_{Bragg}, R_F and χ^2 are the reliability factors. S_C is the crystallite size.

Sample/Parameters	**y = 0.00**	**y = 0.05**	**y = 0.10**	**y = 0.15**	**y = 0.20**	**y = 0.30**	**y= 0.40**	**y= 0.50**
Space group	R $\bar{3}c$	R $\bar{3}c$	R $\bar{3}c$	R $\bar{3}c$	R $\bar{3}c$	*Pbnm*	*Pbnm*	*Pbnm*
a (Å)	5.5204 (0.0012)	5.5253 (0.0009)	5.5349 (0.0017)	5.5355 (0.0016)	5.5370 (0.0010)	5.4803 (0.0014)	5.4819 (0.0012)	5.4798 (0.0016)
b (Å)	5.5204 (0.0012)	5.5253 (0.0009)	5.5349 (0.0017)	5.5355 (0.0016)	5.5369 (0.0010)	5.5275 (0.0017)	5.5254 0.0013	5.5177 0.0019
c (Å)	13.3705 (0.0034)	13.3575 (0.0024)	13.3621 (0.0045)	13.3689 (0.0043)	13.3542 (0.0027)	7.7785 (0.0028)	7.7742 (0.0020)	7.7710 (0.0031)
Volume (Å^3)	352.9 (0.2)	353.2 (0.1)	354.5 (0.2)	354.8 (0.2)	354.6 (0.2)	235.6 (0.2)	235.5 (0.1)	235.0 (0.1)
χ^2 (%)	1.15	1.87	1.76	1.48	1.68	1.68	1.05	1.45
R_p (%)	7.77	6.13	7.20	7.49	6.65	6.24	6.25	5.98
R_{wp} (%)	10.1	8.27	9.30	9.64	8.74	8.32	8.07	7.81
R_{exp} (%)	4.94	4.20	4.26	4.56	4.04	6.42	4.62	6.48
R_f (%)	14.4	12.7	13.4	10.3	9.42	18.	19.1	19.2
R_{Brag}(%)	14.5	11.3	11.8	10.9	10.7	13.2	16.3	14.2
<Mn-O_1/O_2> (Å)	1.959	1.956	1.968	1.974	1.975	2.044/ 1.984	1.997/ 1.969	2.052/ 1.981
∠ Mn-O_1/O_2-Mn (°)	165.8	165.9	163.6	161.5	160.9	144.2/ 157.1	153.8/ 161.3	142.4/ 157.1
S_C (nm)	77.3	75.6	70.6	74.7	86.3	69.6	71.8	53.2
Valency	3.29	3.31	3.41	3.44	3.48	3.50	3.52	3.68

The average crystallite size (S_C) has been calculated using the Scherrer's formula [262]

$$S_C = \kappa\lambda / \beta\cos\theta \quad \text{---------- (3.1)}$$

where, constant k depends upon the shape of the grain size (= 0.89, assuming the circular grain), β is full width at half maximum (FWHM) in radians of intensity vs. 2θ profile, λ is the wavelength of the X-Ray used in the experiment i.e. CuK_α radiation and θ is the Bragg's diffraction angle. To avoid any instrumental profile broadening effect coming into the picture, the following correction has been taken into account:

$$\beta^2 = \beta_m^2 - \beta_{ins}^2 \quad \text{---------- (3.2)}$$

Here β_m is the measured FWHM of the XRD peak and β_{ins} is the instrumental broadening.

The calculated crystallite size for all the samples is listed in Table 3.1. No systematic variation in the crystallite size is observed.

The average Mn valency for all compounds was determined from chemical titration to know the valency of Mn ions in the prepared compounds. The average Mn valency determined from chemical titration is given in Table 3.1. It is observed that the mixture of Mn^{3+} and Mn^{4+} ions are present and the Mn^{4+} concentration increases with doping. By assuming that there are three oxygen ions per formula unit, the possible valency of Co is estimated and they are found to be 2.16, 2.31, 2.51 and 2.60 for y = 0.05, 0.10, 0.15 and 0.20 respectively. The above observation suggests that there is a presence of mixture of Co^{2+}/Co^{3+} ions in rhomohedral structured compounds ($y \leq 0.20$). The Co ions are unlikely to take part in chemical titration due to the following reason. It may be noted that the energy required to oxidize Co^{2+} to Co^{3+} is 1.83 eV, whereas, the energy released by reduction of Mn^{7+} to Mn^{2+} is only 1.51 eV. So, we believe that it is not possible to oxidize the Co ions in chemical titration reaction.

The morphology of all the samples has been studied by scanning electron microscope. The typical SEM micrographs for y = 0.0 and y= 0.15 samples are shown in Figures 3.4 and 3.5 respectively. All the samples show nearly spherical shape particles and the morphology of the samples is found to be quite uniform suggesting the mono-phasic nature of the sample. The average particle size is found to be in the order of 1-3 μm.

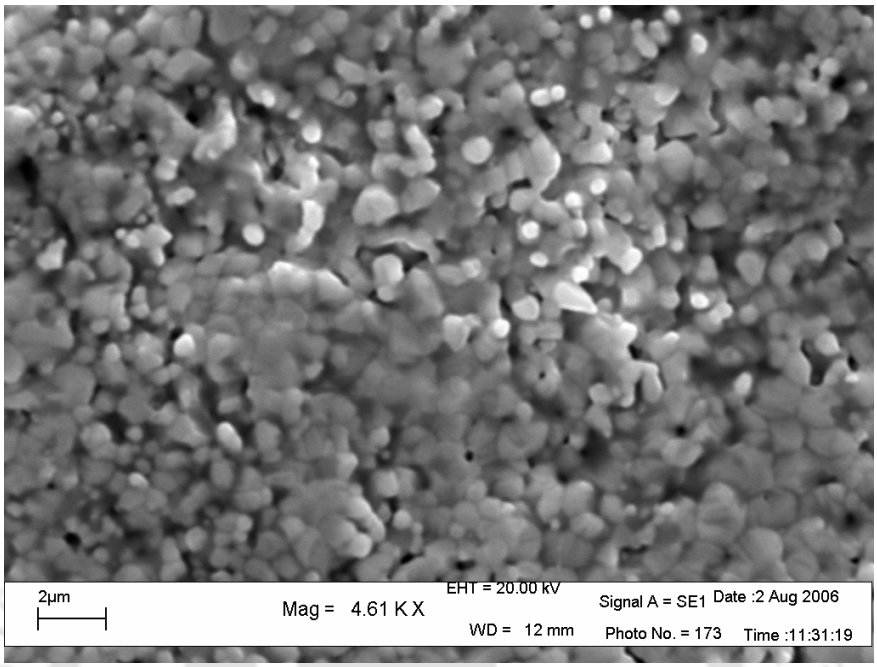

Figure 3.4: SEM photograph (magnification 46100) of the y=0 sample.

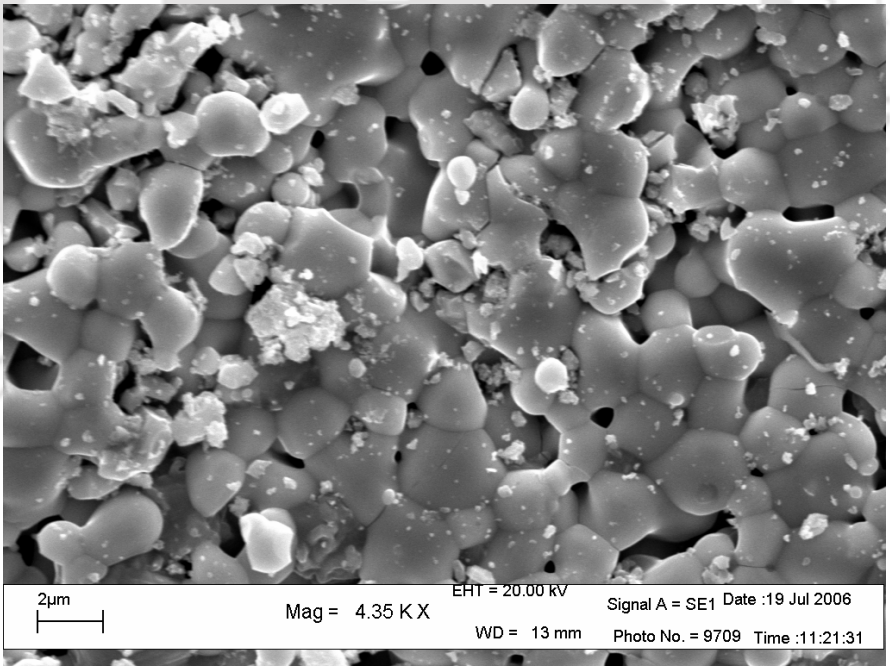

Figure 3.5: SEM photograph (magnification 43500) of the y=0.15 sample.

The elemental analysis of the prepared compounds has been carried out by recording EDS spectra. Typical EDS spectrum for y = 0.10 sample is shown in Figure 3.6. We can clearly see that all the elements are present. The chemical compositions determined from EDS analysis confirms that the composition of the prepared materials is comparable with their respective starting compositions. The cationic ratios for all the compounds are given below.

Table 3.2: Estimated cationic ratio from EDS results of $La_{0.85}Ag_{0.15}Mn_{1-y}Co_yO_3$ series.

Sample	Calculated Cationic Ratio			
	La	Ag	Mn	Co
y= 0.0	0.86	0.13	1.01	0
y= 0.05	0.89	0.11	0.93	0.07
y= 0.10	0.88	0.12	0.88	0.12
y= 0.15	0.89	0.11	0.86	0.14
y= 0.20	0.87	0.13	0.81	0.19
y= 0.30	0.88	0.12	0.72	0.28
y= 0.40	0.84	0.16	0.63	0.37
y= 0.50	0.87	0.13	0.52	0.48

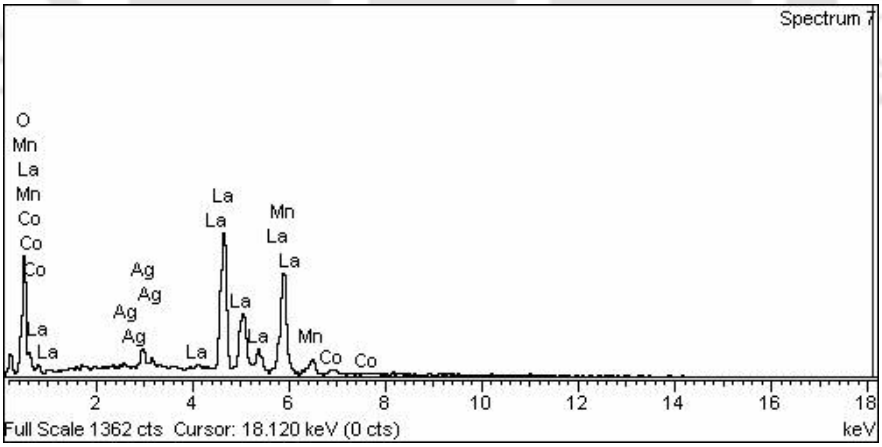

Figure 3.6: Typical SEM-EDS spectrum for y=0.10 sample.

Thus from the structural characterization we conclude that, the doping of Co at Mn site in $La_{0.85}Ag_{0.15}MnO_3$ compound, results in structural change from rhombohedral cell for y=0 to 0.2 to orthorhombic cell for y>0.2. Similar structural change from rhombohedral to

orthorhombic has been observed in electron doped $La_{0.9}Te_{0.1}Mn_{1-x}Co_xO_3$ compounds [278]. Such structural transition can be understood in the following argument. In perovskite structure, each Mn ion is bonded in the form of MnO_6 octahedra and two Mn ions are coupled by sharing one of the vertex of MnO_6 octahedra. If the doped Co ions are distributed uniformly, the required concentration of Co doping to have Co-O-Co bonding is greater than $1/6 \cong 0.17$. So, in the present case for $y \geq 0.20$, there is a probability of Co-O-Co type of bonding, which gives rise to distinct lattice distortion, which drives the system into less symmetric orthorhombic structure. The lattice parameters found for y = 0, i.e. a = b = 5.520Å and c = 13.357Å, are comparable with the reported values for $La_{0.85}Ag_{0.15}MnO_3$ compound [20, 139] and the lattice parameters of y=0.30 sample i.e. a = 5.480Å, b = 5.527Å and c = 7.778Å are comparable to those reported for orthorhombic; $La_{0.67}Ca_{0.33}Mn_{1-x}Co_xO_3$ compounds [183].

The lattice parameters and Mn-O bond length are found to increase with doping upto y=0.2 and it is in contrast to decrease in lattice parameters observed in (La, Ca)-(Mn, Co)-O system [183]. The ionic size of various Co and Mn ions are given in Table 3.3. The variations in lattice parameters can be understood on the basis of Co^{2+} ions replacing Mn^{3+} ions. However the possibility of some of the Co^{3+}/Co^{4+} ions replacing Mn^{3+}/Mn^{4+} can not be ruled out. On the other hand for y> 0.2, the decrease in lattice parameters with doping suggests the presence of Co^{3+}/Co^{4+} ions or Co^{2+}/Co^{3+} ions undergoing transition from high spin to low spin state.

Table 3.3: Ionic size of the Co and Mn ions at different valence and spin states (HS denotes high spin and LS denotes low spin) [279].

Ions	Possible Spin States	Ionic size
Co^{2+}	LS ($t_{2g}^6 e_g^1$, S=1/2)	0.65
	HS ($t_{2g}^5 e_g^2$, S=3/2)	0.745
Co^{3+}	LS ($t_{2g}^6 e_g^0$, S=0)	0.585
	HS ($t_{2g}^4 e_g^2$, S =2)	0.610
Co^{4+}	HS ($t_{2g}^3 e_g^2$, S=5/2)	0.530
Mn^{3+}	HS ($t_{2g}^3 e_g^1$, S = 2)	0.645
Mn^{4+}	HS ($t_{2g}^3 e_g^0$, S = 3/2)	0.530

3.1.2: Study of dc Magnetization

The temperature dependence of zero field cooled (ZFC) and field cooled (FC) magnetization under an applied field of 2 mT, are shown in Figure 3.7 for y=0 sample. The ZFC magnetization data shows that the undoped compound, i.e. $La_{0.85}Ag_{0.15}MnO_3$, exhibits long range paramagnetic (PM) to ferromagnetic (FM) transition. The field cooled (FC) magnetization is larger than that of ZFC, with a bifurcation below the ferromagnetic (FM) transition temperature.

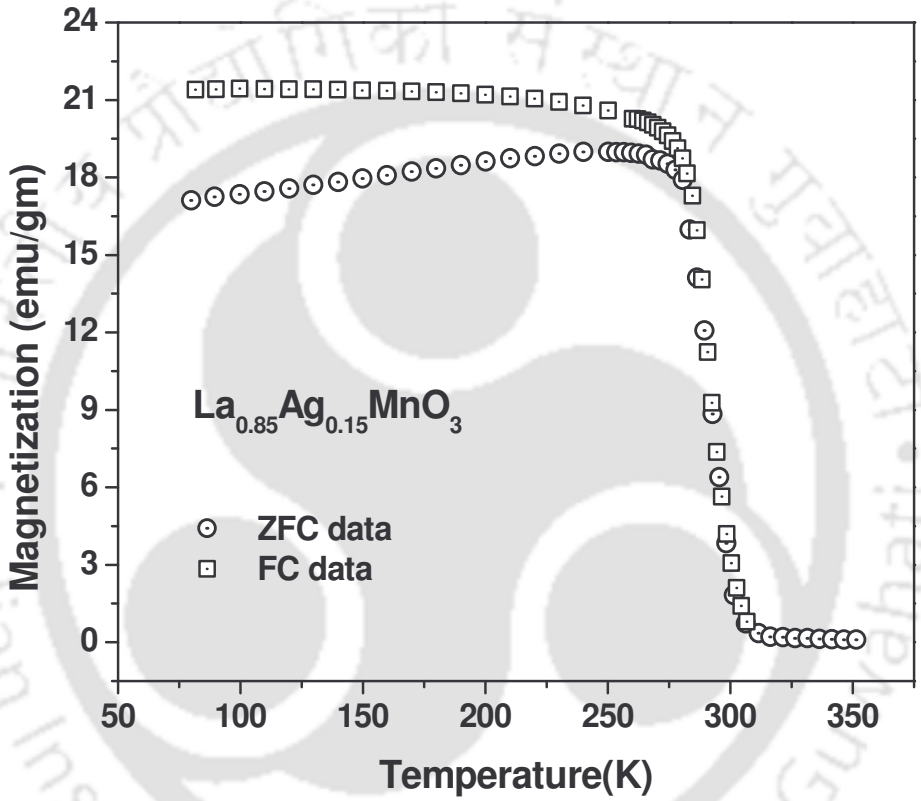

Figure 3.7: The temperature variation of (ZFC) zero field cooled (Circles) and (FC) field cooled (square) magnetization curves for y=0.0 sample (parent sample).

In addition to y=0 compound, all Co doped compounds also exhibit paramagnetic (PM) to ferromagnetic (FM) transition as can be seen from Figure 3.8 and Figure 3.9. The ZFC magnetization decreases slowly with decrease in temperature below the FM transition for y=0.05-0.20 samples and for y=0.30 to 0.50, it is almost constant.

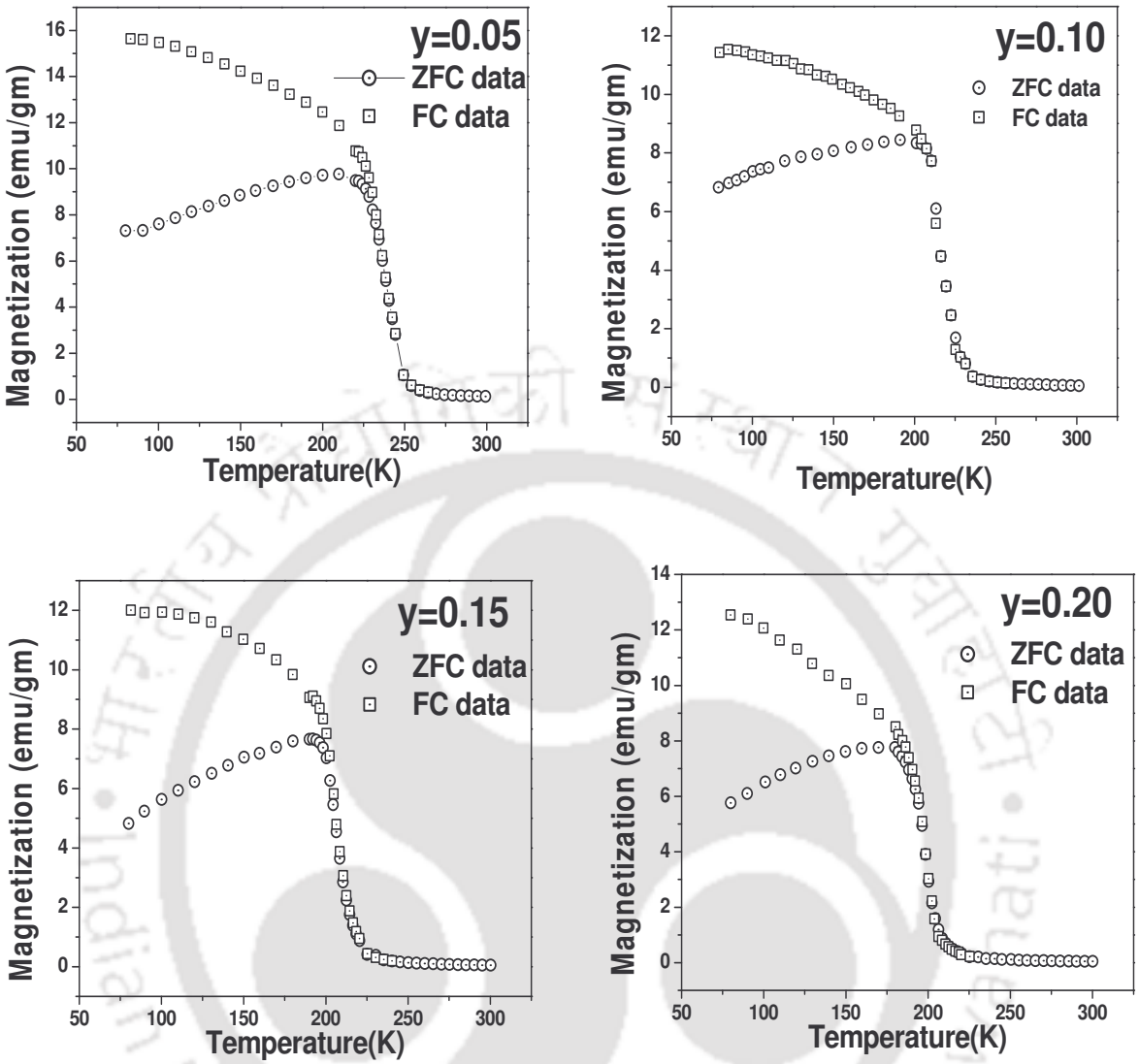

Figure 3.8: The temperature variation of (ZFC) zero field cooled (circles) and (FC) field cooled (square) magnetization curves for y=0.05, 0.10, 0.15, 0.20 samples.

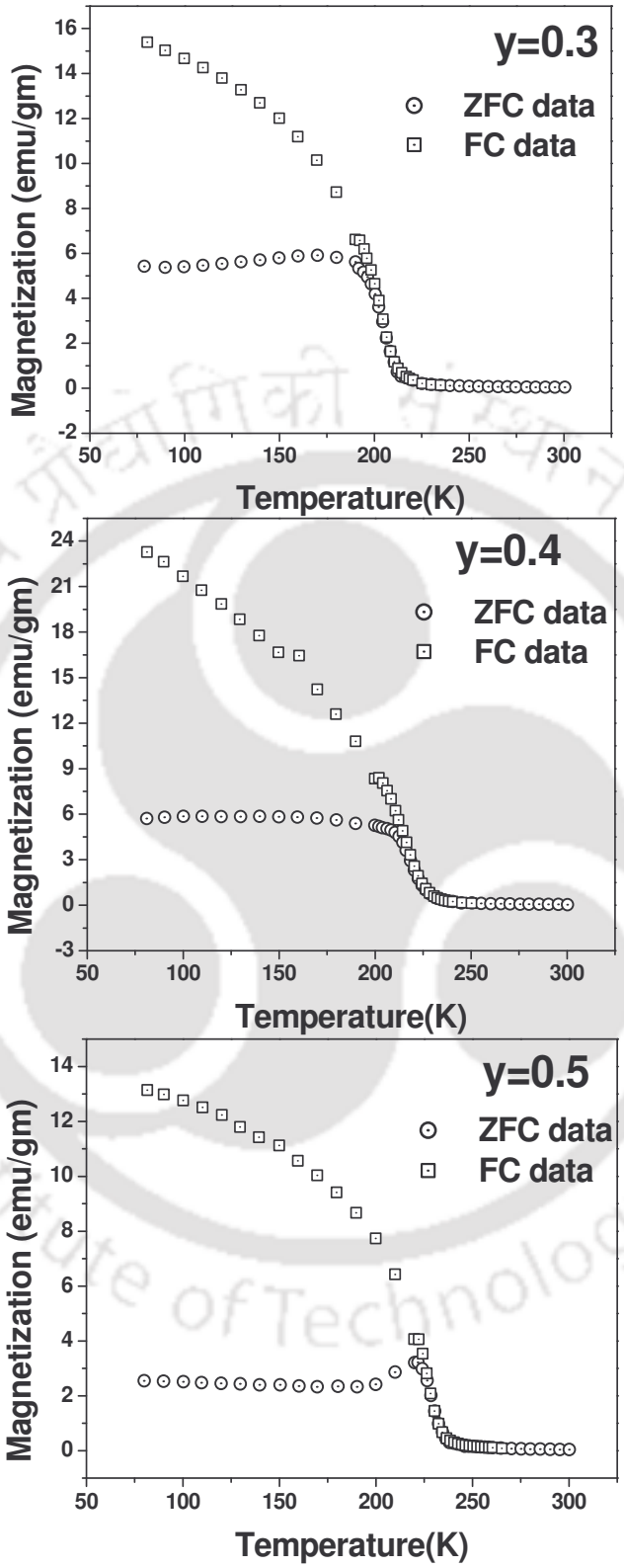

Figure 3.9: The temperature variation of (ZFC) zero field cooled (circles) and (FC) field cooled (square) magnetization curves for y=0.30, 0.40 and 0.50 samples.

The irreversibility between ZFC and FC magnetization are found to increase systematically with doping. The relative irreversibility at 78 K, $\frac{\Delta M}{M} = \frac{(M_{Fc} - M_{ZFc})}{M_{ZFc}}$ as a function of doping concentration is shown in Figure 3.10. We can see that two distinct slopes, one for the concentration range 0 to 0.20 and the other in the composition range 0.30 to 0.50.

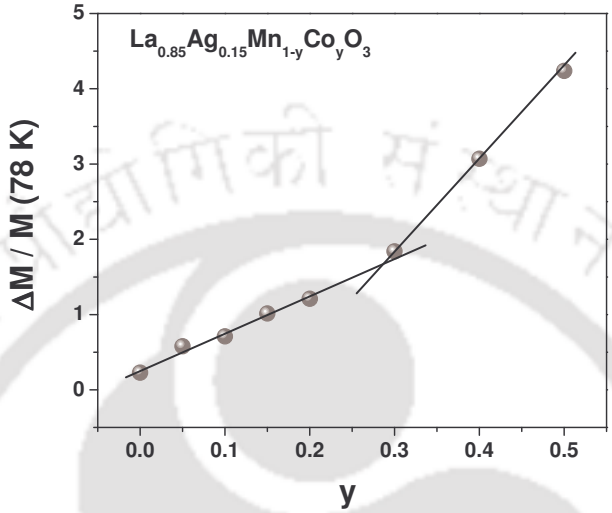

Figure 3.10: The relative magnetization irreversibility at 78 K as a function of Co concentration. Solid lines are only for the guidance.

The ferromagnetic (FM) transition temperature (T_c) has been determined from the peak observed in |dM/dT| versus temperature plot. The variation of FM Tc with doping concentration is found to be very interesting. The T_c falls sharply from ~ 292 K for y=0 to 213 K for y=0.10 and the decrease in T_c continues upto y=0.2. Interestingly, the T_c increases for y≥0.30 and it is discussed at the end of this section.

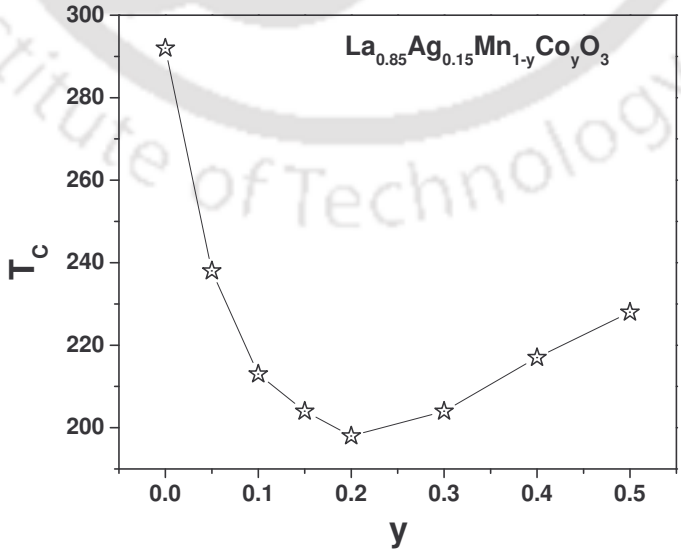

Figure 3.11: Variation of Ferromagnetic transition temperature (T_c) with Co doping.

The dc susceptibility χ_{dc} in the paramagnetic region was analysed by using Curie-Weiss law (equation 1.10). The Curie-temperature (θ_C) for all the samples is found to be positive and indicates the FM interaction. Typical plots of $1/\chi_{dc}$ versus temperature for y=0.15 and 0.40 samples are shown in Figure 3.12 along with Curie-Weiss law fitting. The FM transition temperature obtained from M versus T curve and θ_C are given in Table 3.4. The difference between T_C and θ_C are mainly due to the observed broad magnetic transition.

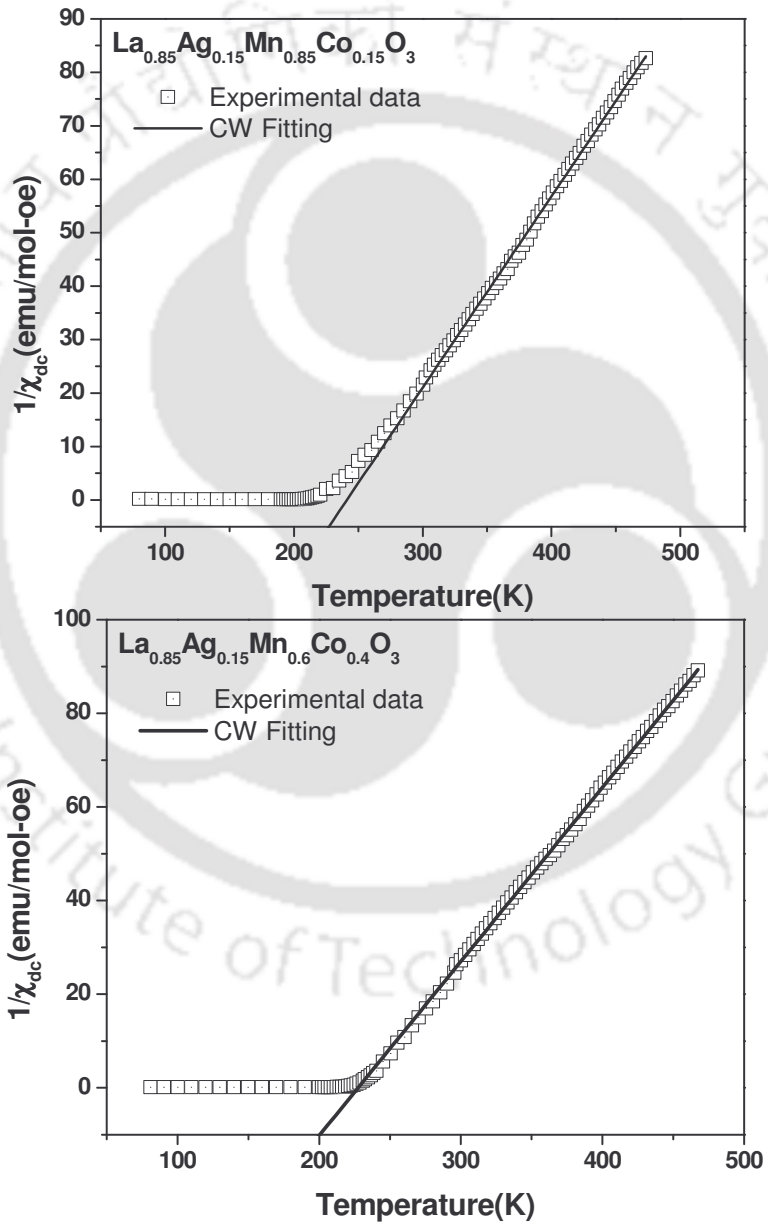

Figure 3.12: $1/\chi_{dc}$ versus temperature for the samples (a) y=0.15 and (b) y=0.40. Solid lines represent fit to the Curie-Weiss law.

The effective magnetic moment, μ_{eff} was determined from the fitted curie constant C by using the relation $\mu_{eff} = \sqrt{\frac{3k_B C}{N\mu_0\mu_B^2}}$ and are given in Table 3.4. The effective paramagnetic moment (μ_{eff}) is found to increase with increase of Co doping upto y=0.20 compounds and then it decreases for higher doped y≥0.30 samples.

Table 3.4: Parameters obtained from the magnetization measurement of $La_{0.85}Ag_{0.15}Mn_{1-y}Co_yO_3$. T_C is the ferromagnetic transition temperature. θ_C (Curie temperature), C (Curie constant) and μ_{eff} have been found from inverse dc susceptibility fitting.

Sample/ Parameters	**y= 0**	**y= 0.05**	**y= 0.10**	**y= 0.15**	**y= 0.20**	**y= 0.30**	**y= 0.40**	**y= 0.50**
T_C (K)	292.0	238.0	213.0	204.0	198.0	204.0	217.0	228.0
θ_c (K)	340.5	295.7	243.5	241.1	223.3	224.1	227.4	239.1
C (K emu /mol-Oe)	2.75	2.84	3.11	3.16	3.26	3.16	2.68	2.53
μ_{eff} (μ_B)	4.67	4.77	4.98	5.02	5.10	5.03	4.62	4.49

The effect of Co doping on magnetic properties is also revealed by their field dependence of magnetization M(H) upto 1 T at 78 K. The plots of magnetization as a function of magnetic field (M-H loop) measured at 78 K are shown in Figure 3.13 for all samples.

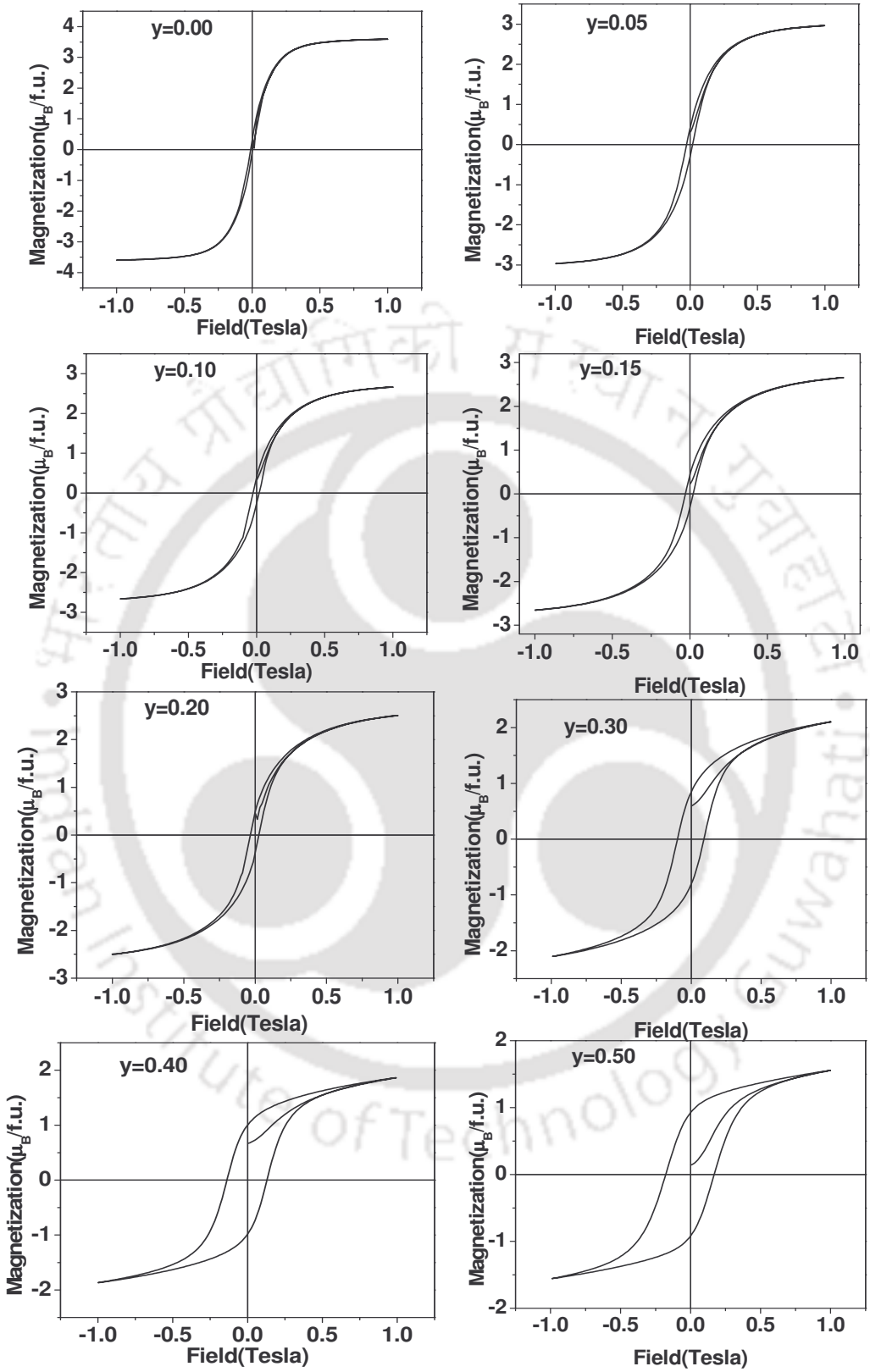

Figure 3.13: Magnetization versus magnetic field plots of the samples $La_{0.85}Ag_{0.15}Mn_{1-y}Co_yO_3$ for y = 0-0.50.

Following features characterize the hysteresis loop.

- There is decrease in saturation magnetization (M_S) as the Co doping increases.
- It can be seen that, there is an increase in the area under the hysteresis loop with increase of Co doping. For y≥0.30 compounds, hysteresis area increases sharply.
- As the doping concentration increases, considerable linear contribution is observed.
- The coercive field (H_C) and remnant magnetization (M_r) were found to increase with Co doping as can be seen from Figure 3.14. Both parameters increase sharply for doping concentration beyond 20%.

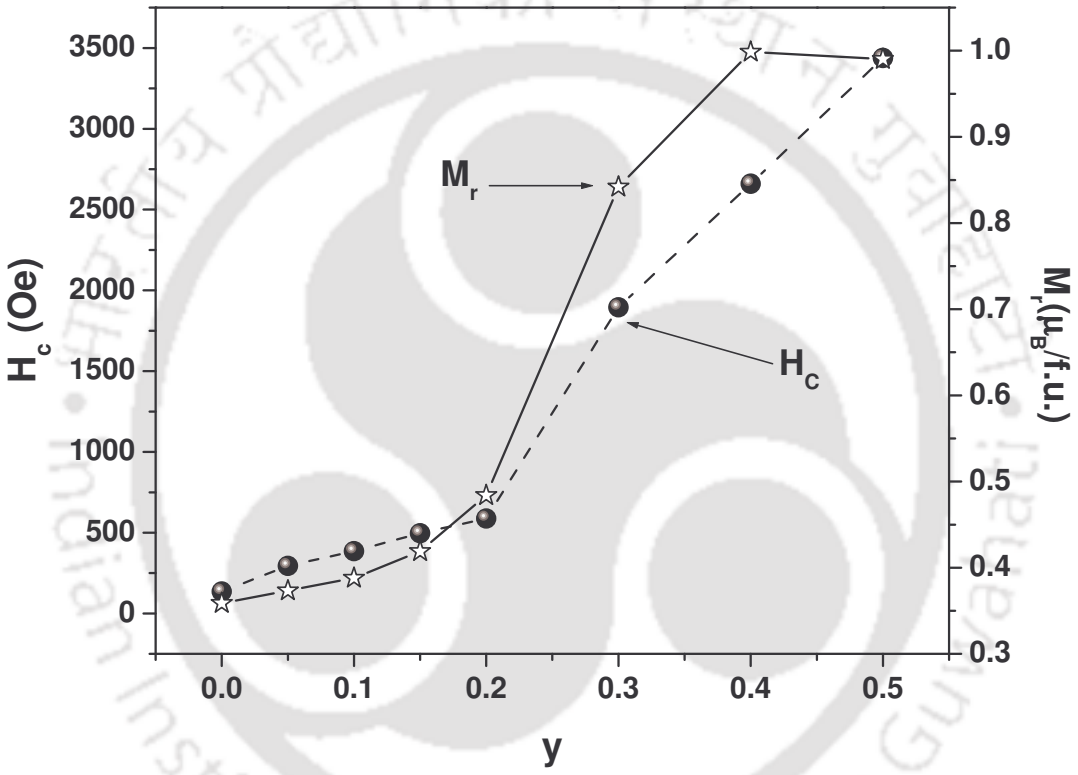

Figure 3.14: Variation of remnant magnetization (M_r) and coercive field (H_C) with Co doping.

To understand the nature of magnetic interaction, we have fitted the M versus H data to the Brillouin function model by taking into account the ferromagnetic interaction to determine the effective spin contribution towards FM interaction. The field variation of magnetization after subtracting the linear contribution was fitted to the relation,

$$M = M_0 B_S(x) \quad \text{---------- (3.3)}$$

where $$B_S(x) = \frac{1}{|S|}\left[\left(S_{eff} + \frac{1}{2}\right) Coth\ x\left(S_{eff} + \frac{1}{2}\right) - \frac{1}{2} Coth \frac{x}{2}\right] \quad \text{--------- (3.4)}$$

Here, $M_0=Ng\mu_B|S_{eff}|$, $x = \frac{g\mu_B}{kT}B$, and $B=B_a+\lambda M$. λ is the Weiss molecular field constant for ferromagnetic interaction. M_0 is taken as experimental M_S during the fit. We have carried out the fit by assuming the λ values determined from the FM T_c and Curie constant C ($T_c= \lambda C / \mu_0$) for different samples. The magnetization fit for all Co doped samples are shown in Figure 3.15.

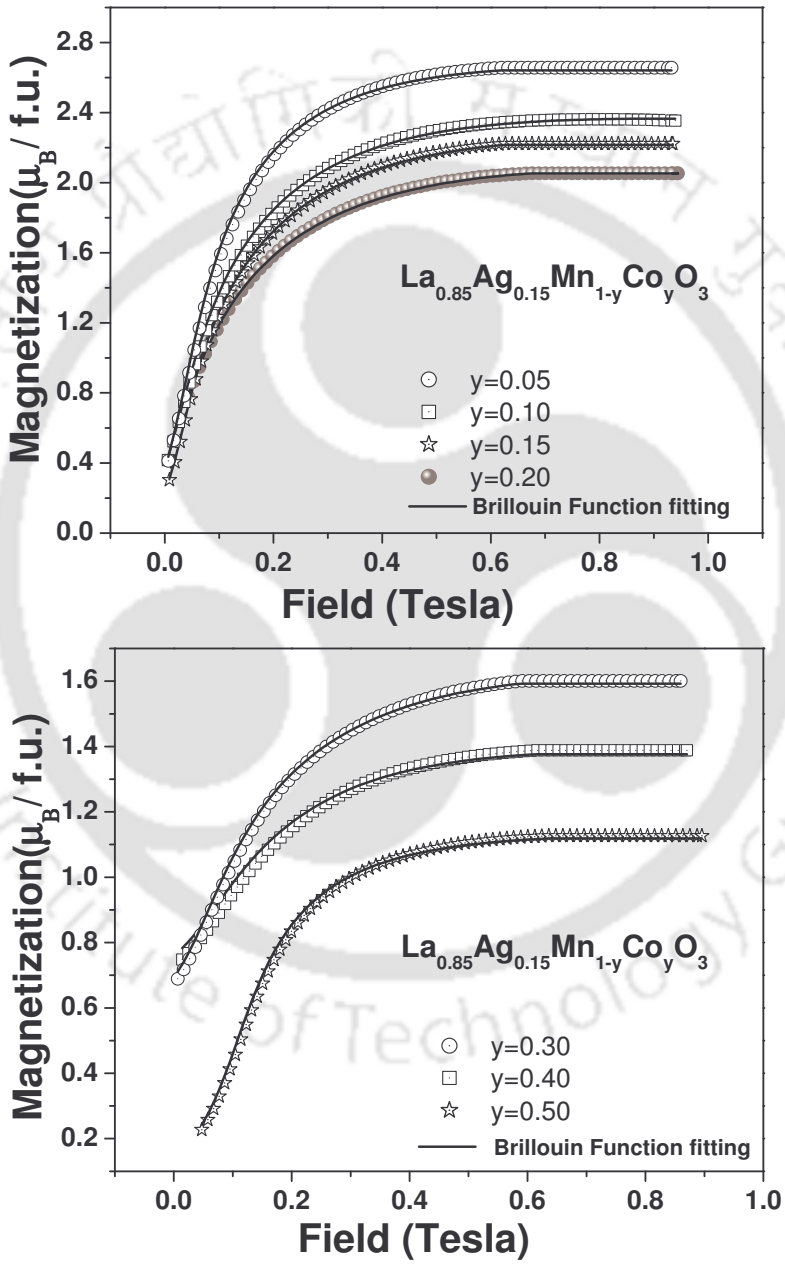

Figure 3.15: Brillouin function fit to magnetization data for y= 0.10, 0.15, 0.20, 0.30, 0.40 and 0.50 samples. The experimental data were obtained by subtracting the minor linear contribution from the measured magnetization

We can see that the fitted data closely follow the experimental data. The fitted values of S_{eff} and the experimental M_S values (after subtracting the linear contribution) are given in Table 3.5. For the undoped sample y=0, the spin contribution, S_{eff} towards FM interaction was found to be maximum. It is found to decrease upto 20% of Co doping, then it is found to increase for higher Co doping.

Table 3.5: Parameters obtained from Brillouin function fitting to magnetization data. S_{eff} is the effective spin contribution towards FM interaction. M_S is the experimental saturation magnetization.

Sample/ Parameters	**y= 0**	**y= 0.05**	**y= 0.10**	**y= 0.15**	**y= 0.20**	**y= 0.30**	**y= 0.40**	**y= 0.50**
S_{eff}	1.21	1.11	0.93	0.99	0.94	0.42	0.52	0.64
r m s (%)	0.57	0.99	0.62	0.51	0.52	1.28	1.29	1.29
M_S (μ_B/f.u.)	3.42	2.76	2.33	2.26	2.01	1.47	1.29	1.06

The magnetization results are discussed as follows.

We have seen from the ZFC data that all the compounds exhibit paramagnetic–ferromagnetic transition. Other than PM-FM transition, the magnitude of magnetization was found to decrease with decrease in temperature below the FM T_C for y=0.05 to 0.20. This can be due to the presence of antiferromagnetism at low temperature or considerable magnetic anisotropy. However the magnetization for y ≥0.30 are found to be almost constant.

The dependence of irreversibility with doping concentration with two distinct slopes can be understood in terms of increase in magnetic anisotropy due to the presence of competing antiferromagnetic (AFM) interaction in Mn-O-Co network. For y≥ 0.30, there is a probability of Co^{2+}-O^{2-}-Co^{3+} or Co^{3+}-O^{2-}-Co^{4+} bonds, which are likely to have FM interaction whose easy direction may be different from conventional Mn^{3+}-O^{2-}-Mn^{4+} double exchange (DE) FM and this gives rise to additional anisotropy and hard magnetic behaviour. So, it gives rise to strong increase in ΔM/M beyond y≥0.30. The sharp increase in H_C and M_r for y>0.2 can also be explained in the similar line, i.e. increased hard magnetic behaviour due to FM with two different easy directions. The increase in FM T_c for y> 0.2 also explains the development of additional FM behaviour in Co-O-Co networks.

To elaborate further, as discussed in sample characterization section, Co^{2+}/Co^{3+} ions are introduced by Co doping for y=0.05-0.20 compounds. Moreover, mixture of Mn^{3+}/Mn^{4+} ion is also present as confirmed from titration. Therefore, there exist FM exchange interactions between Mn^{3+}–O–Mn^{4+}, Co^{2+}–O–Mn^{4+}, Co^{3+}–O–Mn^{4+} networks and AFM exchange interactions of Mn^{4+}–O–Mn^{4+} and Co^{2+}–O–Mn^{3+} networks in y=0.05-0.20 compounds. The above two kinds of magnetic interactions compete with each other, and this competition leads to the appearance of the magnetic in-homogeneity for the samples with y=0.10-0.20. Here, it should be noted that in a canonical spin glass, the FC magnetization is expected to depart from the zero-field-cooled ZFC curve and remain temperature independent below it. The study of linear and nonlinear ac susceptibility study on this system confirms that y=0.10-0.20 samples show spin glass like behaviour as discussed in the next section. Similar type of behaviour has been observed for Co doping at Mn site in other divalent doped materials [182, 188, 193, 280].

As the doping concentration increases beyond the critical value of 1/6, there is a probability of Co-O-Co networks, which can be either FM or AFM depending on their valency and electronic configuration, which play a role in enhanced $\Delta M/M$, T_c, H_c and M_r as discussed above. Thus, in the present series, there is a possible FM interaction in Co^{2+}-O-Co^{3+} or Co^{3+}-O-Co^{4+} which give rise to reentrant FM behaviour with increase in T_c for y>0.2.

From the variation of effective paramagnetic moment, it was found that the effective paramagnetic moment (μ_{eff}) increases with increase in Co doping upto y=0.20 compounds and then it decreases for higher doping y≥0.30 samples. By considering the effective paramagnetic moment (μ_{eff}) of the Mn and Co ions in different spin and valence states (as given in Table 3.6), the initial increase of μ_{eff} proves that most of the Co ions must have been in the high spin state. When increasing y from 0 to 0.20, the ferromagnetism is suppressed, but μ_{eff} increases because of the generation of $Co^{2+}/Co^{3+}/Co^{4+}$ ions. However, the decrease in magnetic moment for higher Co doping leads to the suggestion that some of the Co ions may be undergoing transition from high spin to low spin state. This can be confirmed from the value of (S_{eff}) observed in y=0.3 to 0.5 samples compared to samples with y≤ 0.2. Presence of such Co^{2+}/Co^{3+} mixture has been reported by some authors in Co doped manganites [188, 281].

Table 3.6: Effective paramagnetic moment of the Co and Mn ions, for different valence state.

Ions	Spin Value (S)	μ_{eff} (μ_B)
Co^{2+}(HS)	3/2	3.87
Co^{3+}(HS)	2	4.90
Co^{4+}(HS)	5/2	5.91
Mn^{3+}(HS)	2	4.90
Mn^{4+}(HS)	3/2	3.87

3.1.3. ac Susceptibility Study

ac susceptibility as a function of temperature was measured for the all samples at an ac field amplitude of 6 Oe with a frequency of 333Hz. The temperature variations of the in-phase linear ac susceptibility (χ'_1), for y=0 sample is shown in Figure 3.16. We can see that the material exhibits sharp PM to FM transition with long range of ferromagnetic ordering with ferromagnetic transition in vicinity of room temperature. Below the FM transition the χ_1' value decreases slowly with decrease in temperature. This is the general behaviour of FM sample measured at low field, which is mainly due to the formation of FM domains and increase in magnetic anisotropy. Similar behaviour has been observed in ZFC dc magnetization as discussed in section 3.1.2.

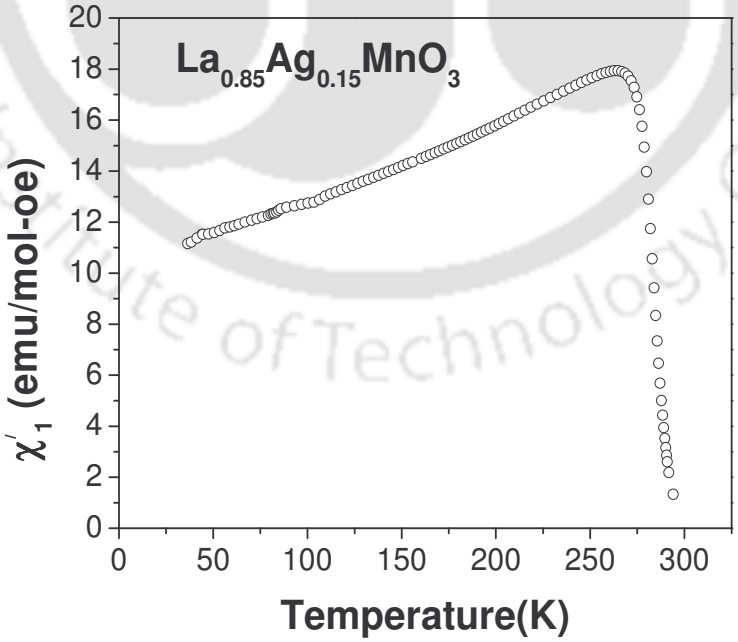

Figure 3.16: Temperature variation of linear in-phase ac susceptibility (χ'_1) of $La_{0.85}Ag_{0.15}MnO_3$ sample.

χ_1' versus T plots for all Co doped samples are shown in Figure 3.17. We can see that these materials also exhibit PM to FM transition. Unlike y = 0.0 sample, χ_1' versus T plot of y=0.10-0.20 samples exhibit sharp fall in susceptibility below the FM transition. They are generally explained on the basis of presence of competing AFM interaction. The sharpness of the fall increases with increase in Co doping. In addition to the sharp fall, low temperature hump can be seen for y=0.10-0.20 sample. However, there is no such low temperature hump below the FM transition temperature for higher doped samples. The plots of χ''_1 versus temperature for all the samples are shown in Figure 3.18. We can see that other than the major peak in the vicinity of FM T_c, there is a minor peak at around 65-70 K for y =0.10, 0.15 and 0.20 samples and they coincide with low temperature hump observed in χ_1' versus T plot.

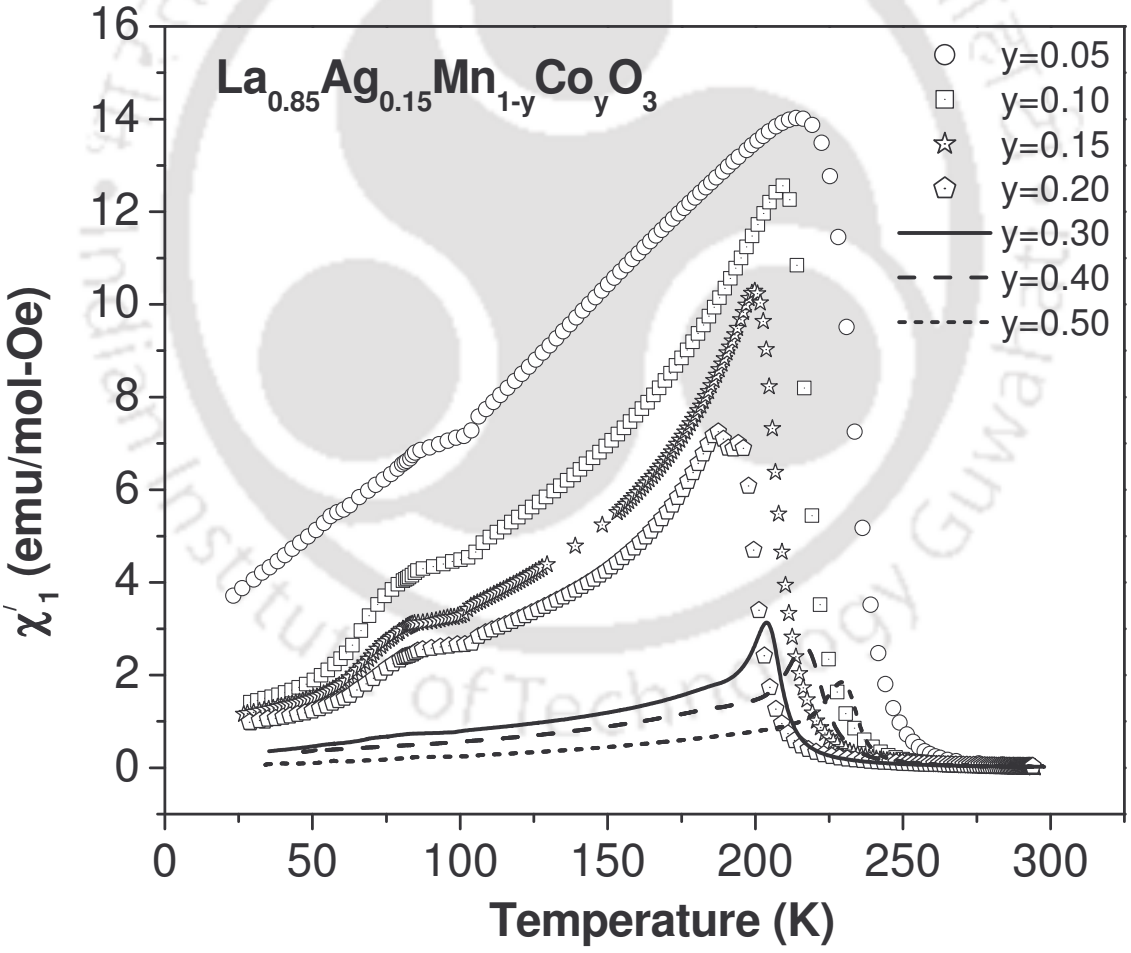

Figure 3.17: Temperature variation of linear in-phase ac susceptibility (χ'_1) of samples $La_{0.85}Ag_{0.15}Mn_{1-y}Co_yO_3$ for y = 0.05- 0.50.

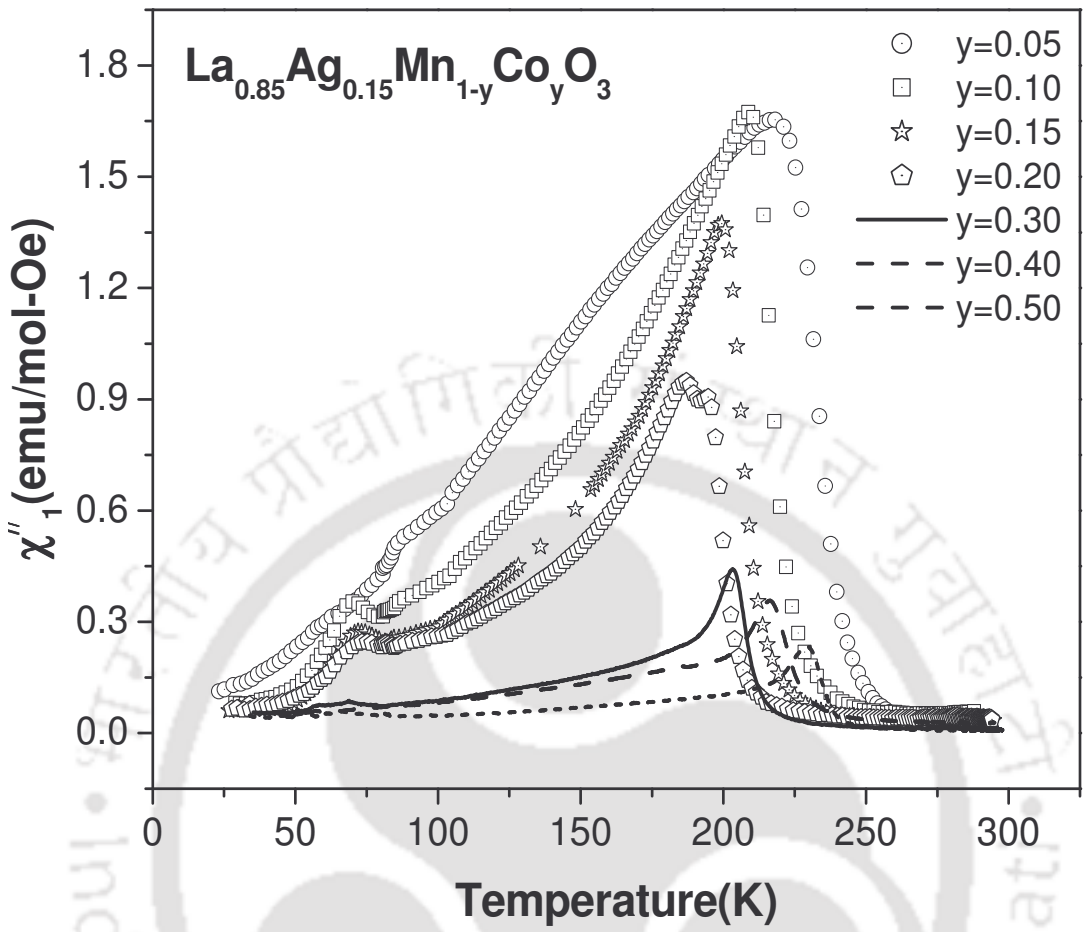

Figure 3.18: Temperature variations of linear out-phase ac susceptibility (χ''_1) of samples $La_{0.85}Ag_{0.15}Mn_{1-y}Co_yO_3$ for y = 0.05- 0.50.

To further explore the magnetic behaviour, I have carried out the frequency variation of ac susceptibility at different frequencies such as, 333 Hz, 1133 Hz, 3333 Hz, 6333 Hz and 9333 Hz. Plots of χ_1'' versus temperature at different frequencies are shown in Figure 3.19 for y = 0.10 and 0.15 samples. The low temperature peak is found to shift towards higher temperature with increase in frequency as a result of spin glass (SG) like behaviour. The low temperature peak is taken as the spin glass freezing temperature T_f. These features are commonly observed in conventional spin glass system. Similar frequency dependent susceptibility behaviour has been observed for y=0.2 sample also.

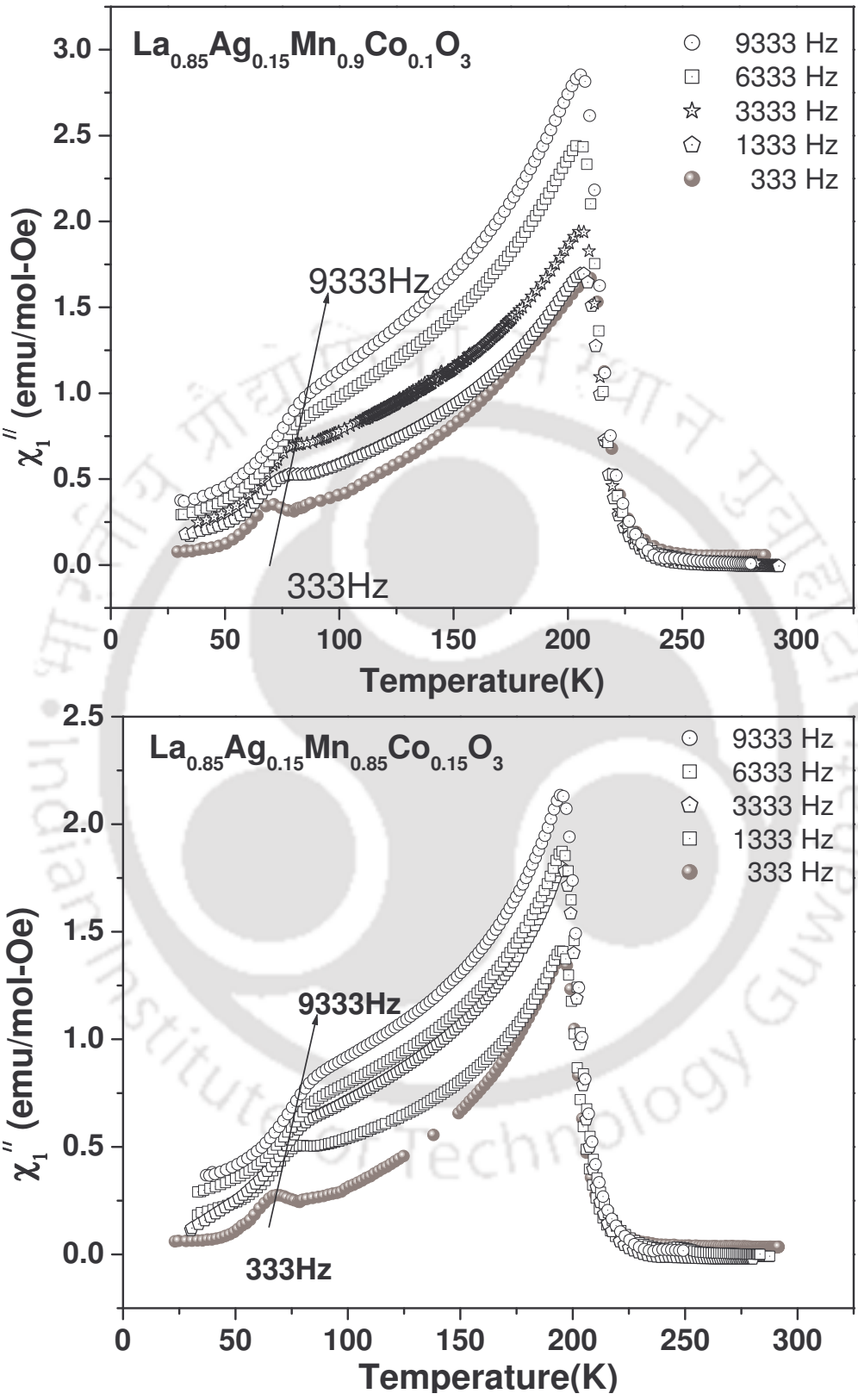

Figure 3.19: χ''_1 versus temperature (T) measured at frequencies f = 333 Hz, 1333 Hz, 3333 Hz, 6333 Hz and 9333 Hz for the sample y=0.10 and 0.15 samples.

The dynamic property of spin glass like behaviour was analysed based on conventional power law slowing down model [51]

$$\frac{\tau}{\tau_0} = \left[\frac{T_f - T_g}{T_g}\right]^{-Z\nu} \qquad \text{----------} \qquad (3.5)$$

Here, τ is the relaxation time corresponding to the measured frequency ($\tau = 1/f$), τ_0 is the spin flipping time and $z\nu$ is the critical exponent. T_g is the spin glass transition temperature, which is equivalent to the freezing temperature in the limit of $\tau \rightarrow \infty$ i.e. $f \rightarrow 0$. The plots of T_f versus frequency is shown in Figure 3.20, for the sample y = 0.15 and 0.20 samples. We can see that, they exhibit linear behaviour. These data were fitted to the linear equation to determine T_g and the fitted data are shown as solid lines. The T_g values for y=0.10-0.20 samples were determined by extrapolating the plots of T_f versus frequency to f=0.

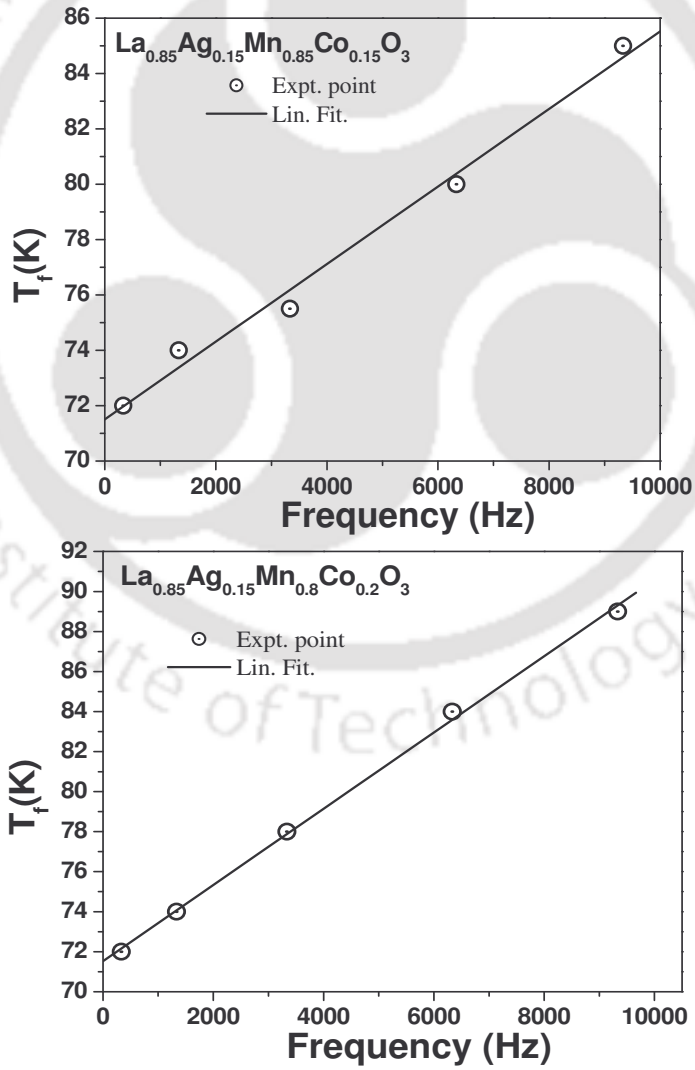

Figure 3.20: Plots of T_f versus frequency for the samples y= 0.15 and 0.20

The plot of ln(τ) versus ln[(T_f- T_g)/T_g] is shown in Figure 3.21, for y = 0.15 and 0.20 samples. These data were fitted to equation 3.5 by varying the parameters τ_0 and zν and, the fitted data are shown as solid line. The values of τ_0 and zν values are listed in Table 3.7 The τ_0 is much higher than the value observed in conventional spin glass system (10^{-13} s) [42]. It suggests that these materials exhibit reentrant spin glass behaviour, where the freezing of the spins are not in atomic scale.

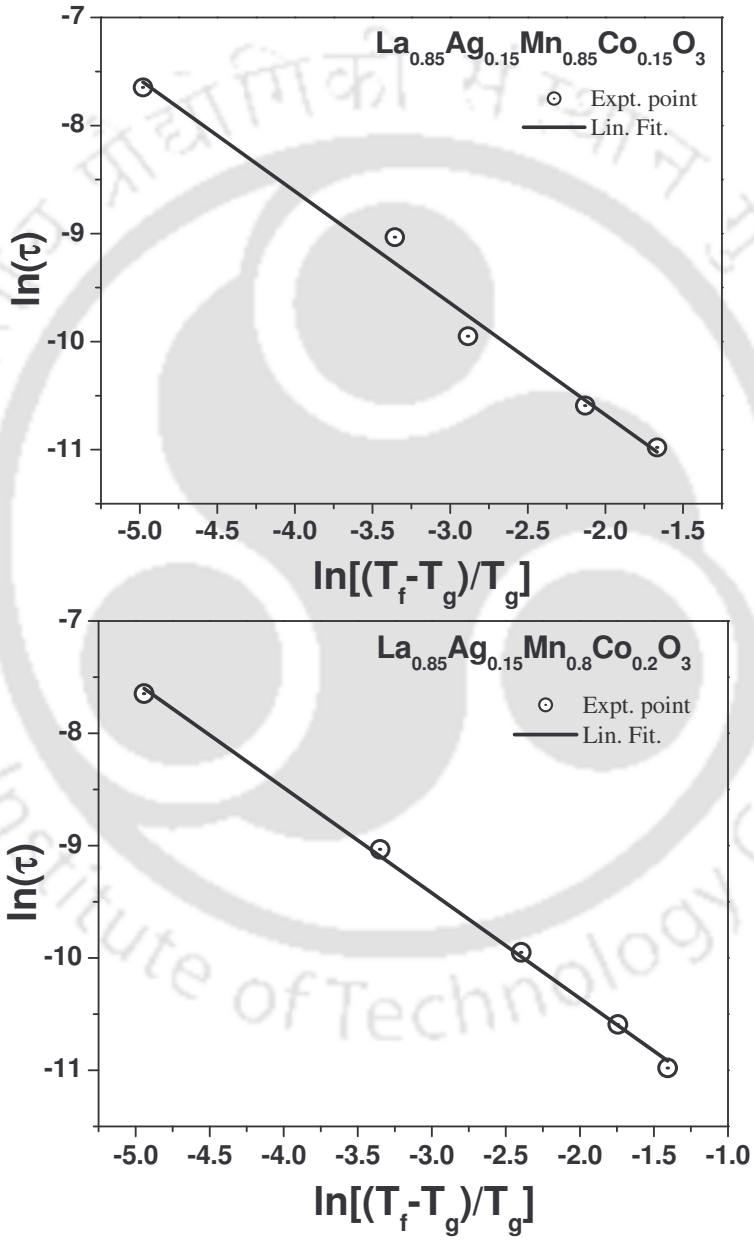

Figure 3.21: Plots of ln(τ) versus ln[(T_f-T_g)/T_g] for the samples y= 0.15 and 0.20 .

Table 3.7: Parameters obtained from the frequency variation of linear ac susceptibility of $La_{0.85}Ag_{0.15}Mn_{1-y}Co_yO_3$. T_f, T_g are spin glass freezing temperature and spin glass transition temperature respectively.

Sample/Parameters		y = 0.10	y = 0.15	y = 0.20
T_f (K)	**333Hz**	71.0	72.0	72.0
	1333Hz	73.0	74.0	74.0
	3333Hz	77.0	76.0	78.0
	6333Hz	80.0	80.0	84.0
	9333Hz	86.0	85.0	89.0
T_g (K)		70.8	71.5	71.4
$\tau_{0\ (10^{-6}S)}$		6.17	2.91	4.85
$z\nu$		0.77	1.03	0.94

The observed frequency variation of fundamental harmonic susceptibility is not the unique property of spin glass behaviour. Another interesting magnetic property i.e. super-paramagnetism also exhibits similar frequency variation of fundamental susceptibility. In order to ascertain unequivocally that the present low temperature transition is due to the spin glass like behaviour, one has to carryout the measurement and analysis of harmonic susceptibility.

The typical plot of temperature variation of third harmonic ac susceptibility, χ'_3 is shown in Figure 3.22 for y=0.10 and 0.15 samples. It exhibits a sharp negative peak at 215 K fallowed by broad positive peak at 200 K. The negative peak coincides with ferromagnetic transition temperature and the positive peak can be attributed to AFM interaction. In addition to these, there is a low temperature peak at 75 K**.** The position of low temperature peak is closely comparable to that observed from χ_1'' vs. T plot (Figure 3.19) for y=0.10 sample and it is attributed to spin glass transition temperature. Thus the harmonic susceptibility clearly depicts the presence of FM and low temperature SG state. It is comparable to the harmonic susceptibility of ferromagnetic spin glass material $Fe_{1.5}Mn_{1.5}Si$ reported by Chakravarti *et al.* [282]**.** The critical behaviour of χ'_3 could not be studied because of presence of multiple peak in close proximity.

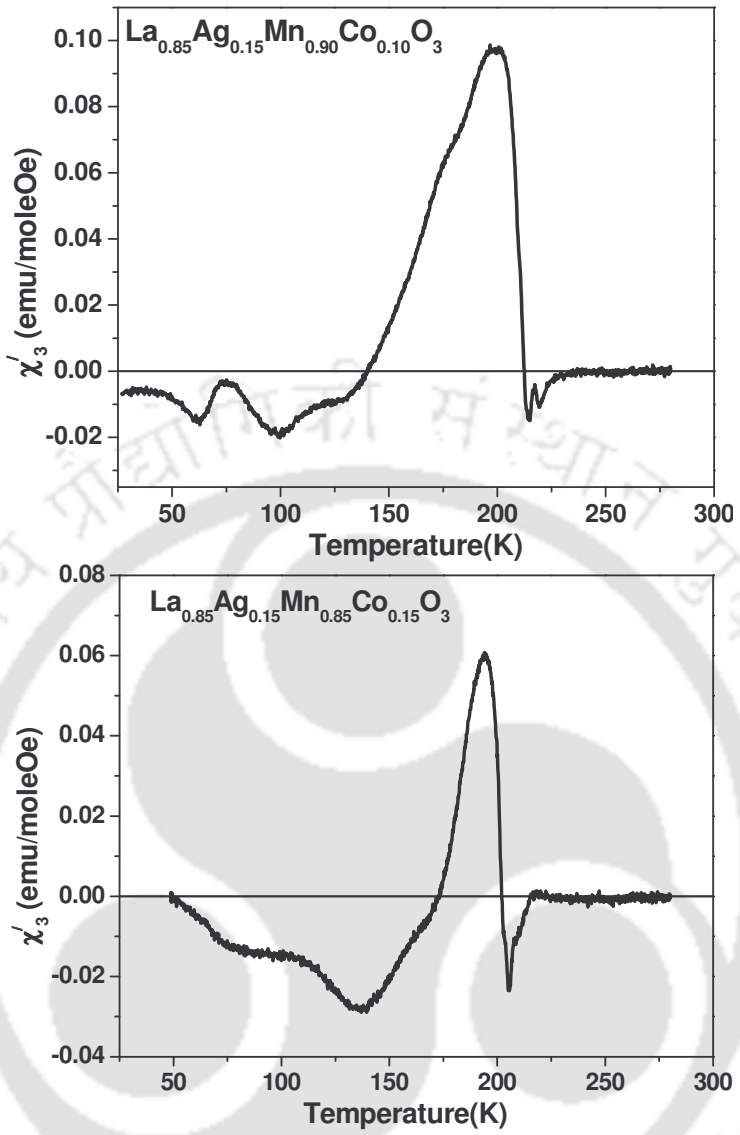

Figure 3.22: $\chi_3^{/}$ versus T for the sample $La_{0.85}Ag_{0.15}Mn_{0.90}Co_{0.10}O_3$ and $La_{0.85}Ag_{0.15}Mn_{0.85}Co_{0.15}O_3$.

Thus from the analysis of dc magnetization measurements and linear and non-linear harmonic ac susceptibility, it is found that all Co doped compounds exhibits PM-FM transition along with low temperature competing interaction. The presence of competing FM exchange interactions between Mn^{3+}–O–Mn^{4+}, Co^{2+}–O–Mn^{4+}, Co^{3+}–O–$Mn^{4+}$and AFM exchange interactions of Mn^{4+}–O–Mn^{4+} and Co^{2+}–O–Mn^{3+} gives rise to spin glass behaviour in y=0.10, 0.15 and 0.20 samples. However for higher Co doped compounds, it is believed that in addition to FM interaction due to Mn^{3+}-O^{2-}- Mn^{4+} networks, there is a possibility of FM interaction due to Co^{3+}-O^{2-}-Co^{4+} networks.

3.1.4. Electrical Resistivity and Magneto-Resistivity

Temperature variation of electrical resistivity (ρ) was measured in the absence and presence of 1 T magnetic field, and are shown in Figure 3.23 for y = 0, 0.05, 0.10 and 0.15 samples. Samples for y = 0, 0.05 and 0.10 exhibit metal insulator transition. In addition to the main peak, there exists another M–I transition at around 150 K for y=0.10 sample. Yang *et al.* also reported the double-peak phenomenon in the sample $La_{0.9}Te_{0.1}Mn_{1-y}Cu_yO_3$ [283]. It is believed to be ascribed to the coexistence of FM insulating and FM metallic phases below T_C.

However, the higher doped samples (y ≥ 0.15) exhibit semiconducting behaviour down to low temperature. For the ease of comparison, the resistivity data are shown in logarithmic scale for y=0.20-0.50 compounds in Figure 3.24. The resistivity increases with increasing Co-doping level. The resistivity at low temperatures is so high that the data could be collected in a limited temperature range. Even though the materials for y≥ 0.15 show ferromagnetic transition but no M-I transition is observed. The absence of M-I transition in y≥ 0.15 samples can be understood as, a result of lack of percolation threshold of DE-FM interaction and because of presence of AFM as discussed in the previous section 3.1.2 and 3.1.3. This combined effects result in the carrier localization although the sample keeps up FM property. Generally speaking, both FM and metallic conduction must coexist within the framework of the DE model. However, in our current samples, the FM order is of the character of short range. FM metal phases are disconnected because of the existence of insulating phases among them, which leads to the semiconducting- like conduction behaviour observed in these Co-doped samples.

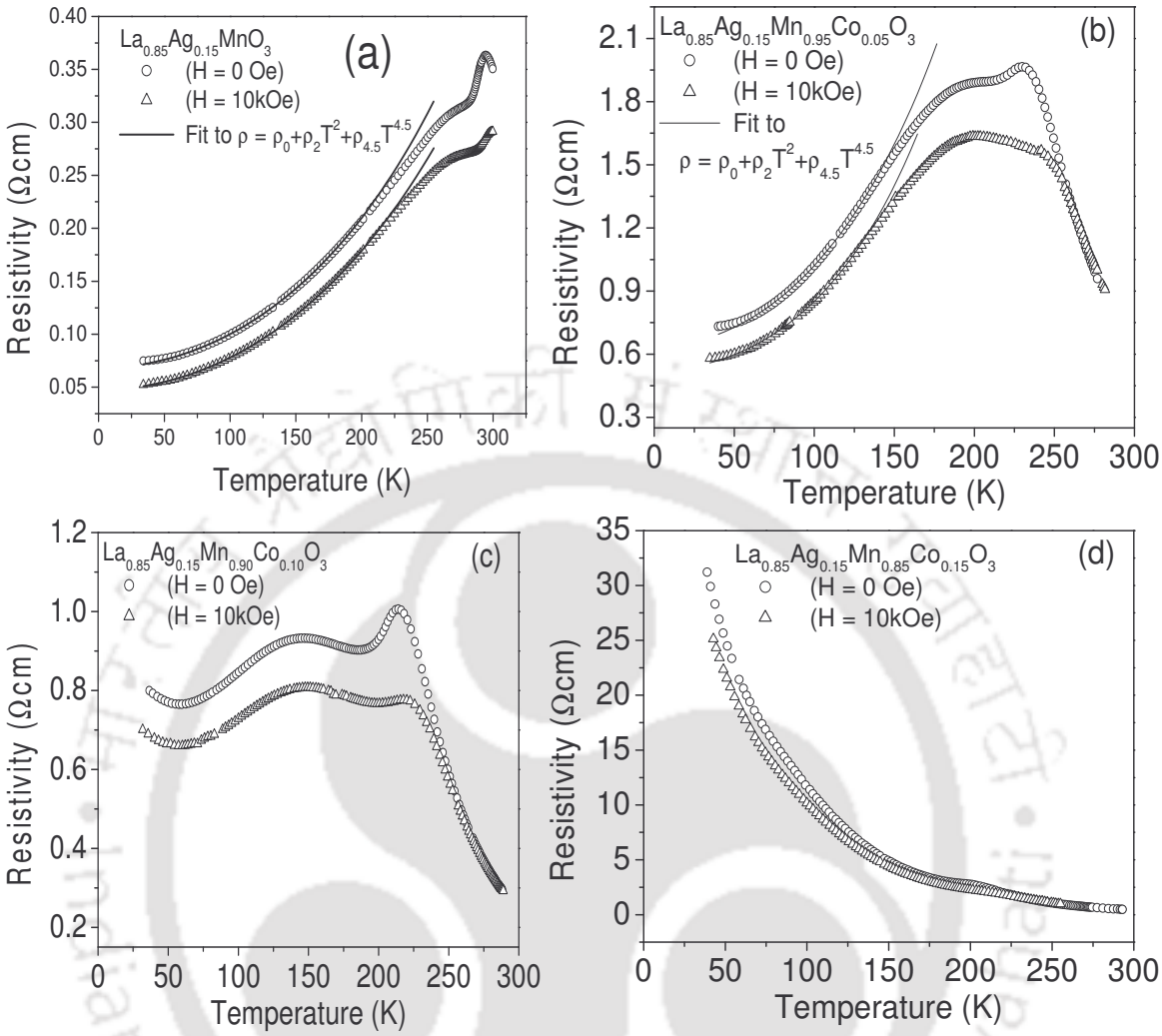

Figure 3.23: Temperature variations of electrical resistivity of $La_{0.85}Ag_{0.15}Mn_{1-y}Co_yO_3$. (a) y = 0.0, (b) y = 0.05, (c) y = 0.10 and (d) y = 0.15.

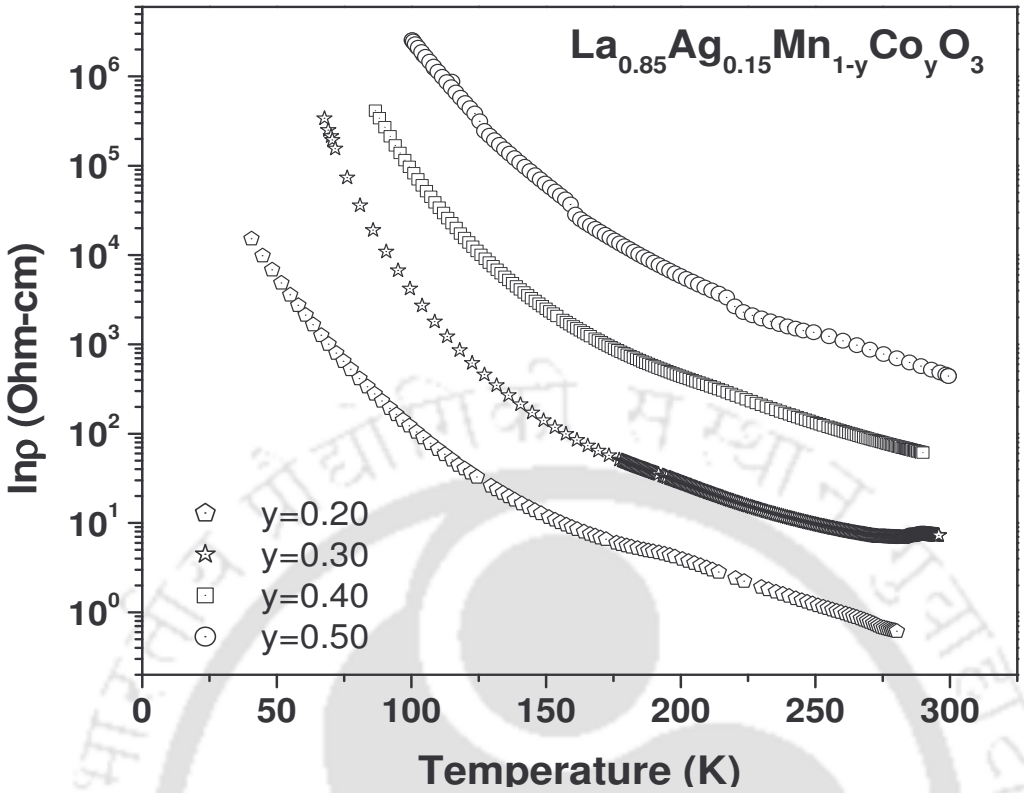

Figure 3.24: Temperature variations of electrical resistivity of $La_{0.85}Ag_{0.15}Mn_{1-y}Co_yO_3$.

The temperature variation of magneto-resistivity was calculated using the relation, $(\Delta\rho/\rho_o)=(\rho_H-\rho_o)/\rho_o$. Here ρ_H is the resistivity in the presence of magnetic field and ρ_0 is the resistivity in the absence of magnetic field at a given temperature. The temperature variation of negative magneto-resistivity $(-\Delta\rho/\rho_0)$ is shown in Figure 3.25 for y=0.05, 0.10 and 0.15 samples. Magneto-resistivity peaks have been observed in the vicnity of ferromagnetic transition temperature (FM T_c) observed from dc magnetization measurements. The increase in magneto-resistivity with decrease in temperature can be explained on the basis of presence of considerable magnetic anisotropy and it is suppressed due to applied magnetic field. The contribution of intergranular tunneling can be also one of the reasons for the observed MR.

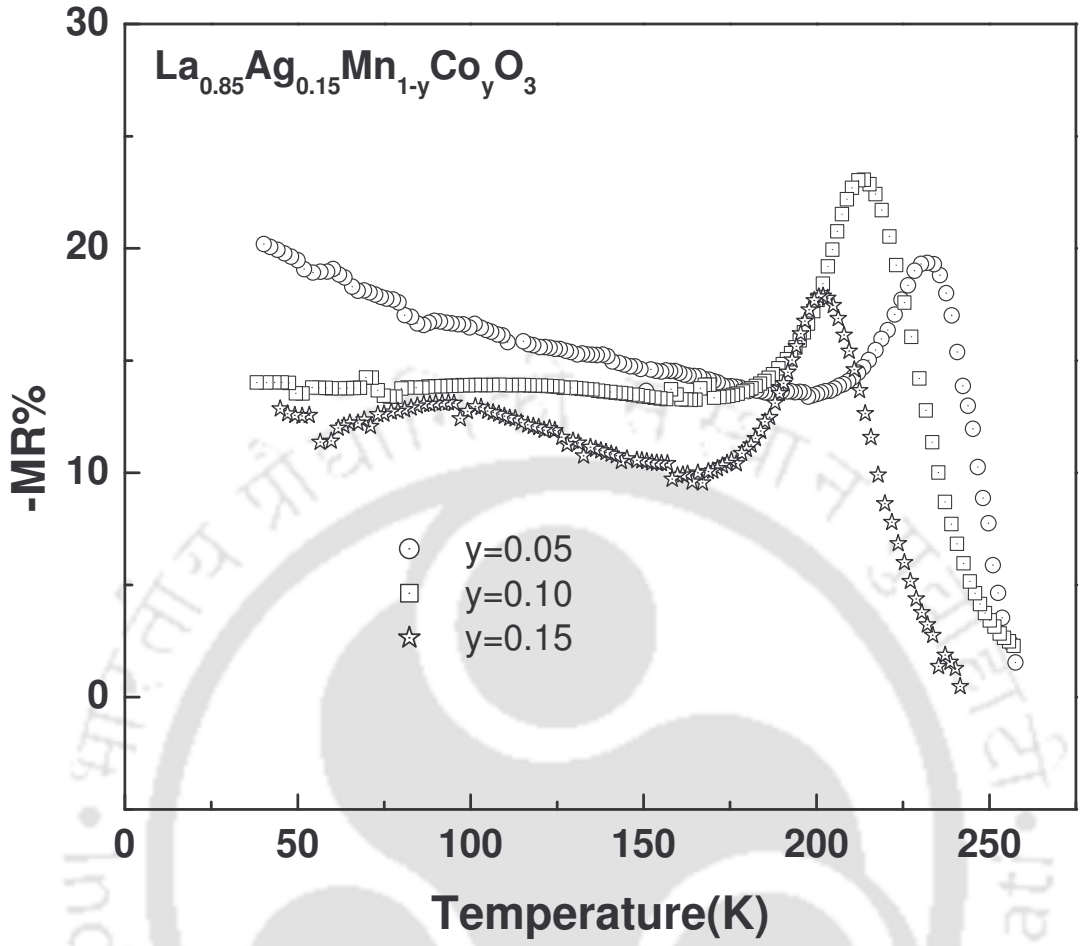

Figure 3.25: Temperature variation of magneto resistivity ($(-\Delta\rho/\rho_0)$ for the y= 0.05, 0.10 and 0.15 samples.

The electrical resistivity in the metallic region for the samples y = 0.0 and 0.05 were analysed by using equation,

$$\rho(T) = \rho_0 + \rho_m T^m + \rho_n T^n \qquad (3.6)$$

where, ρ_0 is the temperature-independent residual resistivity due to scattering by impurities, defects, grain boundaries, and domain walls, etc. Here m and n are exponents and their values are generally 2, 2.5, 3 or 4.5 depending upon the nature of scattering mechanism [85, 87-89, 91]. The resistivity data was analysed by taking different values of m and n. Better fit was obtained for m = 2 and n = 4.5 and the fitted data are shown as solid lines in Figure 3.23. The fitted parameters for H=0 and 1T are listed in Table 3.8. Thus the electrical resistivity in metallic region can be explained by the magnon scattering mechanism for the samples y = 0.0 and 0.05 samples.

Table 3.8: The data obtained from the resistivity analysis in metallic region.

Sample	Magnetic Field (T)	ρ_0(Ωcm)	ρ_m (10^{-6}Ωcm/K^m)	ρ_n (10^{-6} Ωcm/K^m)
y = 0.0	0.0	0.068	3.13	6.86
	1.0	0.048	3.00	4.93
y = 0.05	0.0	0.637	36.02	243.56
	1.0	0.523	29.30	353.14

The resistivity data for y ≥ 0.20 have been analysed using Mott variable range hopping (Mott-VRH), Efros-Shklovskii VRH (ES-VRH), and small polaron hopping (SPH) models as discussed in section 1.7.2. The resistivity data of y=0.20 sample in the semiconducting region could be fitted to Mott-VRH model with relatively low root mean square deviation value (0.5%) and for easy reference they equation (equation 1.36) is reproduced below, i.e.

$$\rho = \rho_{0m} \exp\left(\frac{T_{0m}}{T}\right)^{1/4} \quad \text{----------} \qquad (3.7)$$

Here ρ_{0m} is the Mott residual resistivity and T_{0m} is the Mott characteristic temperature. The ln(ρ) versus $(1/T)^{1/4}$ plot in Figure 3.26 shows linear behaviour and the fitted data are shown as solid line. The density of states in the vicinity of the Fermi level ($N(E_F)$), hopping distance, $R_{hop}(T)$ and hoping energy $E_{hop}(T)$ have been estimated from the fitted parameters and using the relations given in section 1.7.3 and for easy reference they (equations 1.37-1.39) are reproduced here,

$$N(E_F) = \frac{18}{k_B T_{0m} a^3} \quad \text{----------} \qquad (3.8)$$

$$R_{hop}(T) = \frac{3}{8} a \left(\frac{T_{0m}}{T}\right)^{1/4} \quad \text{----------} \qquad (3.9)$$

$$E_{hop}(T) = \frac{1}{4} k_B T^{3/4} T_{0m}^{1/4} \quad \text{----------} \qquad (3.10)$$

Here a is the localization length and k_B is the Boltzmann constant. By following Viret *et al.* [284], the value a = 4.5Å is taken in the above calculations. The value of Mott residual resistivity, ρ_{0m} and Mott characteristic temperature, T_{0m} are found to be 0.61×10^9 Ω cm and

0.28×10^8 K for y=0.20 sample. However, hopping length $R_{hop}(K)$, hopping energy, $E_{hop}(K)$ at 280 K are found to be 29.71 Å and 113.72 meV respectively.

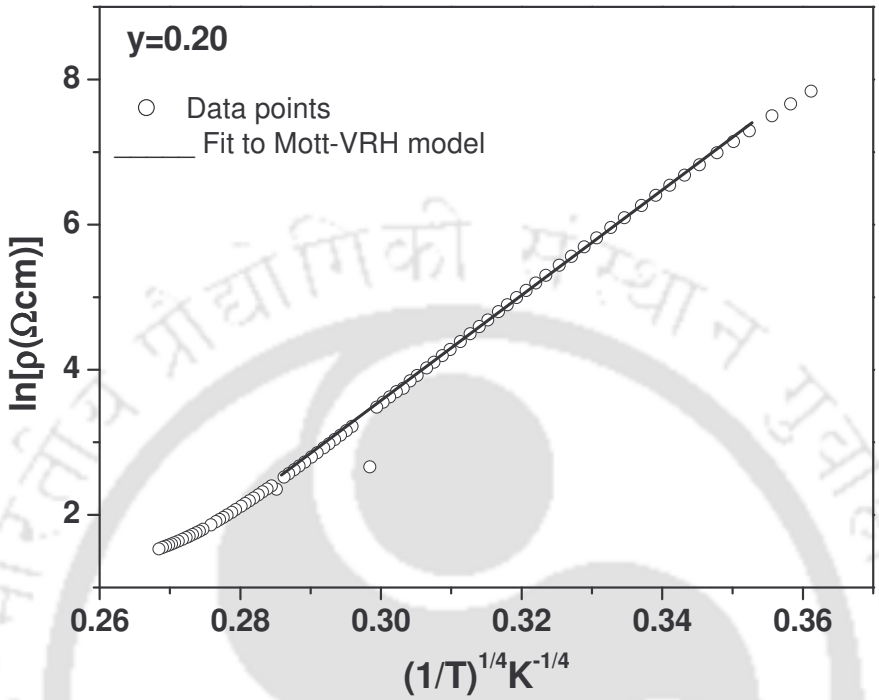

Fig. 3.26: Resistivity versus $T^{-1/4}$ for the sample y = 0.20. The solid line shows the fit to Mott-VRH model.

However, the resistivity data for y≥0.30 samples could be fitted to adiabatic small polaron hoping model. The expression for small polaron hopping model is given in the section 1.7.3 and for easy reference it is reproduced here,

$$\rho = \rho_{sp} T^n \exp(\frac{E_{sp}}{\kappa_B T}) \qquad \text{----------} \qquad (3.11)$$

The typical plot of ln(ρ/T) versus (1/T) for the sample y = 0.30 and 0.50 is shown in Figure 3.27. We can see that the adiabatic small polaron model fits well throughout the semiconducting regions. The fitted data are shown as solid line. The fitted and estimated parameters from the resistivity analysis are tabulated in Table 3.9.

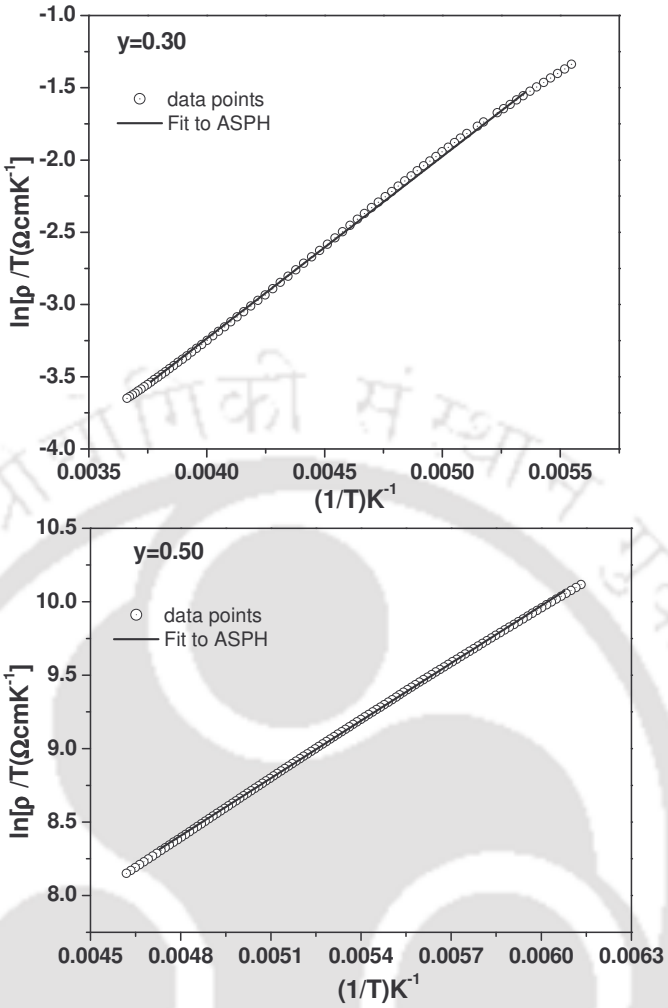

Figure 3.27: Plots of ln[ρ/T(ΩcmK^{-1})] versus (1/T) for y= 0.30 and 0.50 samples. Fit to ASPH model is shown as solid line.

Table 3.9: Parameters obtained from the resistivity fitting. ρ_{sph} is the residual resistivity and E_{sph} is the polaron hopping energy.

Sample Parameters	**y=0.30**	**y = 0.40**	**y=0.50**
ρ_{sp} (10^{-4} Ωcm)	2.53	0.55	8.54
E_{sp} (10^{-1} meV)	1.09	0.90	1.12

3.2. $La_{0.85}Ag_{0.15}Mn_{1-y}Cr_yO_3$ Compounds (y=0-0.20)

This section deals with the effect of Cr doping on Mn site of $La_{0.85}Ag_{0.15}MnO_3$ compounds. The preparation and characterization and, results and analysis of ac susceptibility, dc magnetization and electrical resistivity and magneto-resistivity measurements are presented in this section.

3.2.1. Sample Preparation and Characterization

Polycrystalline samples of $La_{0.85}Ag_{0.15}Mn_{1-y}Cr_yO_3$ series for y=0, 0.05, 0.10, 0.15, 0.20 were prepared by conventional solid state reaction method. Stoichiometric ratio of La_2O_3, $AgNO_3$, Mn metal powder and CrO_3 with 99.9% purity were weighed and mixed thoroughly under acetone. The mixture was presintered at 300 ^{0}C, 400 ^{0}C, 500 ^{0}C, 600 ^{0}C and 700 ^{0}C for 5 h at each temperature and at 800 ^{0}C for 36 h with intermediate grindings. The sintering in pellet form was carried for 36 h at 1000 ^{0}C and 1100 ^{0}C respectively with a few intermediate grindings. All the above sintering was carried out in atmospheric pressure.

The XRD patterns recorded for the above samples are shown in Figure 3.28. We can see that the samples are in single phase form. The patterns for all the samples could be refined using $R\bar{3}c$ space group. It is consistent with those reported for $La_{0.85}Ag_{0.15}MnO_3$ [20, 139]. Typical XRD patterns along with Rietveld refinement are shown in Figure 3.29 for y = 0.10 and y=0.20 compounds. Here, the experimental data are shown as circles and calculated intensities are shown as solid lines. The bottom lines represent the difference between measured and calculated intensities. The allowed Braggs positions for $R\bar{3}c$ space group are marked as small vertical lines. One can see that all the observed peaks coincide with allowed Bragg 2θ positions.

The refined lattice parameters and unit cell volume are listed in Table 3.10. The lattice parameters and unit cell volume are found to decrease with Cr doping. The average Mn-O bond length and ∠Mn-O-Mn bond angle are calculated from the refined atomic positions and lattice parameters and, these values are tabulated in Table 3.10.

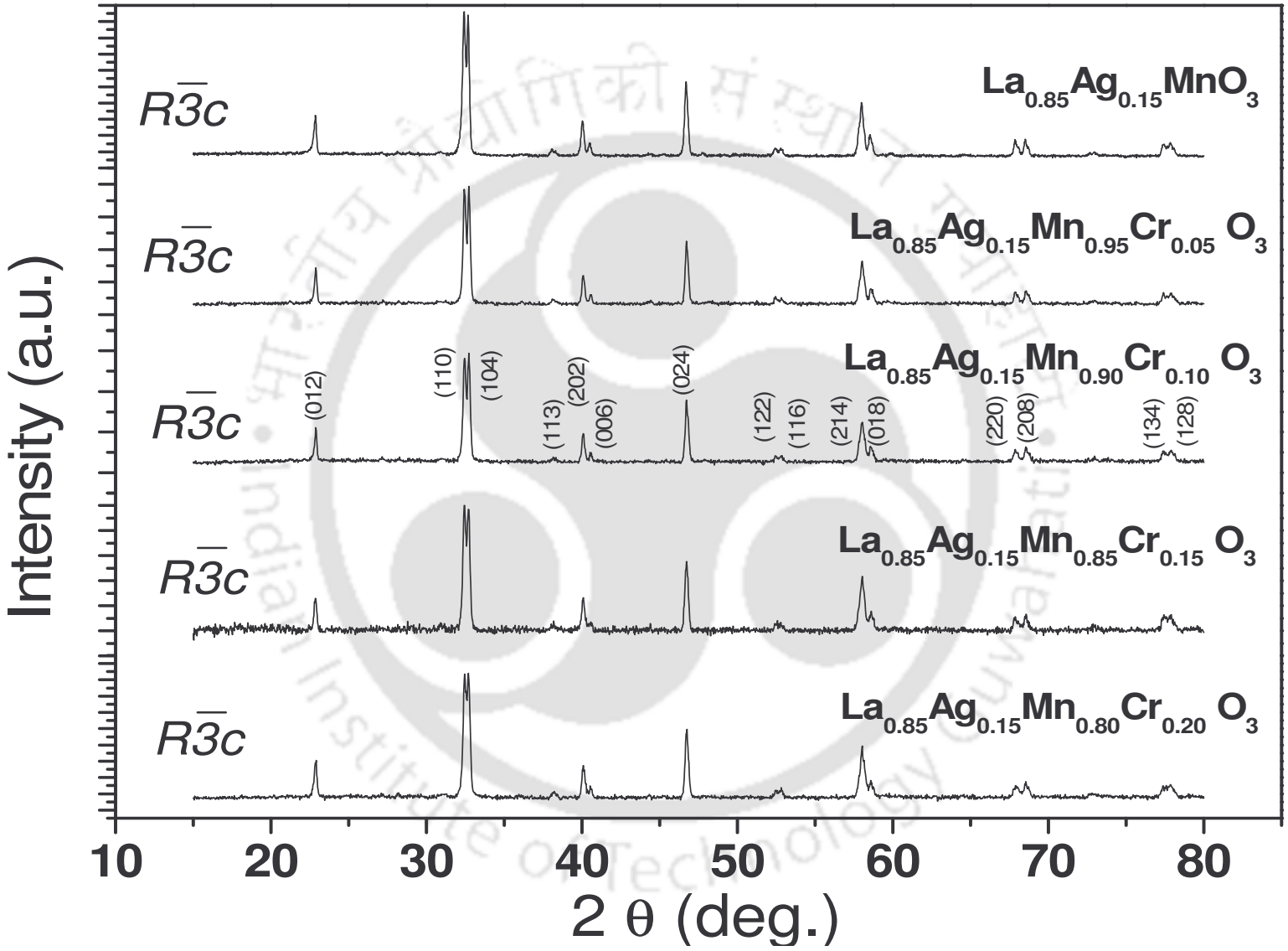

Figure 3.28: XRD patterns of the samples $La_{0.85}Ag_{0.15}Mn_{1-y}Cr_yO_3$ (y = 0, 0.05, 0.10, 0.15 and 0.20).

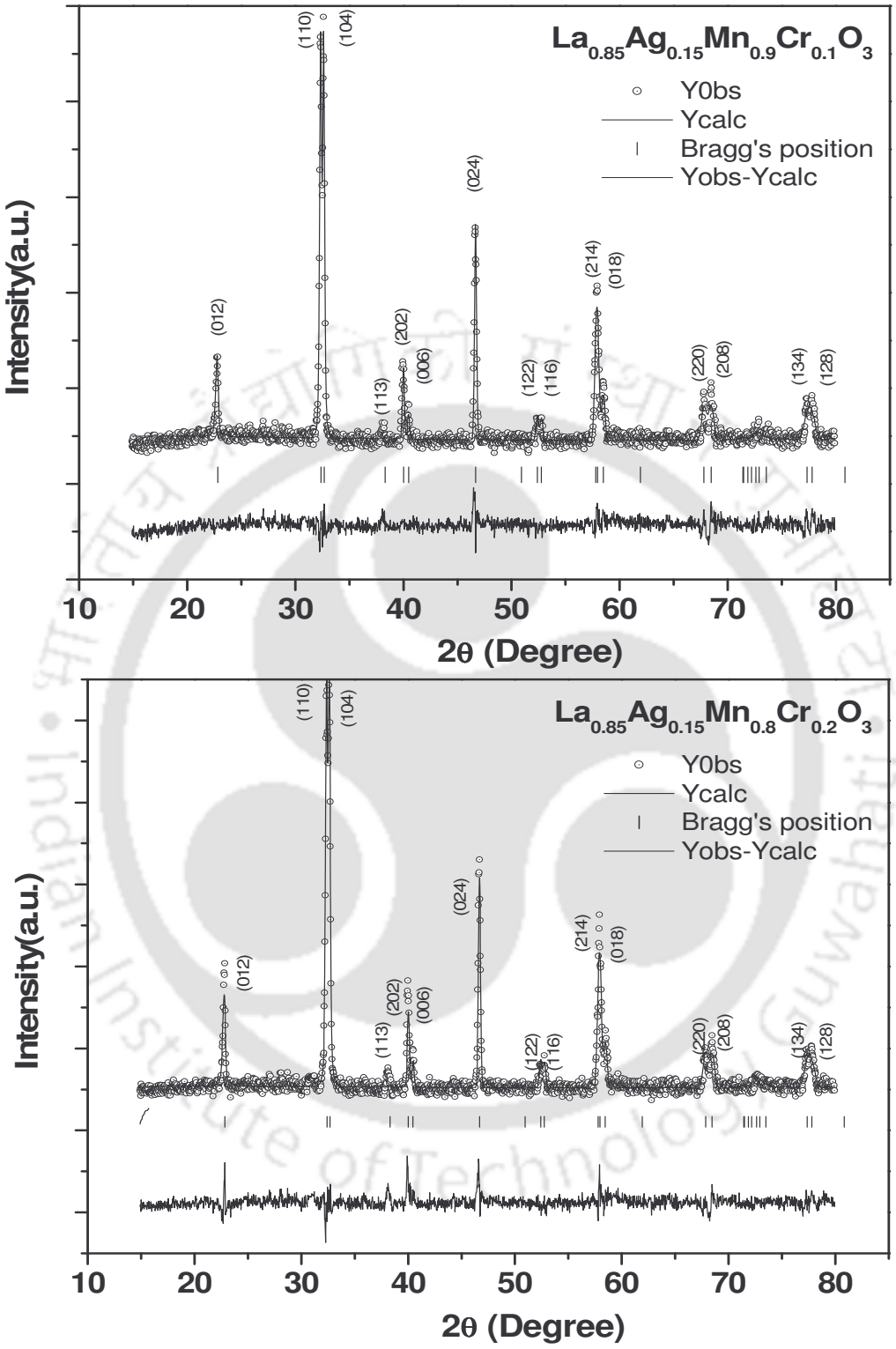

Figure 3.29: XRD patterns for the samples y = 0.10 and 0.20. The circles represent experimental points and solid line represents Rietveld refined data. The bottom line shows the difference between experimental and refined data. The marked 2θ positions are the allowed Bragg peaks.

Table 3.10: Parameters obtained from the Rietveld analysis of XRD patterns for the samples $La_{0.85}Ag_{0.15}Mn_{1-y}Cr_yO_3$ (y = 0.05, 0.10, 0.15 and 0.20). Errors of lattice parameters and unit cell volume are shown in bracket.

Samples/ Parameters	**y = 0.05**	**y = 0.10**	**y = 0.15**	**y = 0.20**
Space Group	R $\bar{3}c$	R $\bar{3}c$	R $\bar{3}c$	R $\bar{3}c$
a=b (Å)	5.5318 (0.0013)	5.5306 (0.0014)	5.5265 (0.0019)	5.52780 (0.0014)
c (Å)	13.3772 (0.0034)	13.3763 (0.0037)	13.3715 (0.0050)	13.3826 (0.0036)
Volume(Å^3)	354.5 (0.1)	354.3 (0.2)	353.7 (0.2)	354.2 (0.2)
χ^2 (%)	2.48	2.28	2.05	2.25
R_p (%)	7.83	8.34	7.74	7.75
R_{wp} (%)	10.3	10.9	9.84	10.1
R_{exp} (%)	6.52	7.21	6.88	6.74
R_f (%)	9.86	11.9	12.4	10.5
R_{Brag} (%)	8.63	10.5	15.1	9.94
<Mn-O> (Å)	1.970	1.967	1.965	1.964
∠Mn-O-Mn(°)	162.5	163.8	163.9	165.1
S_C (nm)	48.2	46.0	43.0	42.8

Typical SEM micrograph for $La_{0.85}Ag_{0.15}Mn_{0.85}Cr_{0.15}O_3$ is shown in Figure 3.30. The morphology of the sample is found to be uniform. Typical EDS spectrum for y = 0.15 sample is shown in Figure 3.31. We can clearly see that all the elements are present. Further, the chemical compositions determined from EDS analysis confirms that the composition of the prepared materials is comparable to that of nominal starting composition except some shortage of Ag concentration. The cationic ratios for all the compounds are given in Table 3.11.

Table 3.11: Estimated cationic ratio from EDS results of $La_{0.85}Ag_{0.15}Mn_{0.85}Cr_{0.15}O_3$ series.

Sample	Calculated Cationic Ratio			
	La	Ag	Mn	Cr
y= 0.0	0.86	0.13	1.01	0
y= 0.05	0.87	0.13	0.96	0.04
y= 010	0.88	0.12	0.89	0.11
y= 0.15	0.88	0.12	0.84	0.16
y= 0.20	0.90	0.10	0.82	0.18

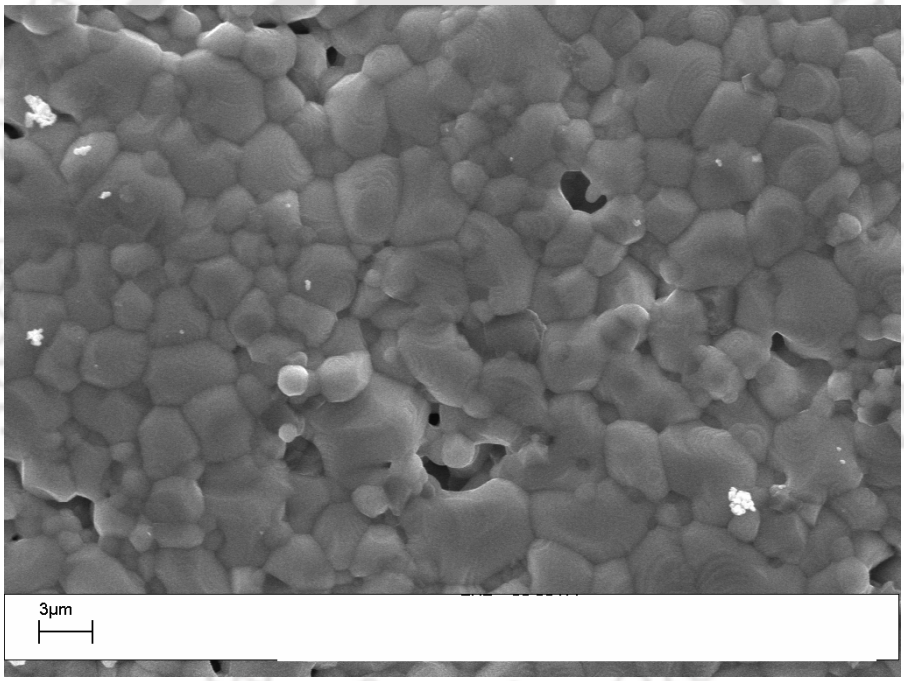

Figure 3.30: SEM image (magnification 8000) of $La_{0.85}Ag_{0.15}Mn_{0.85}Cr_{0.15}O_3$ sample.

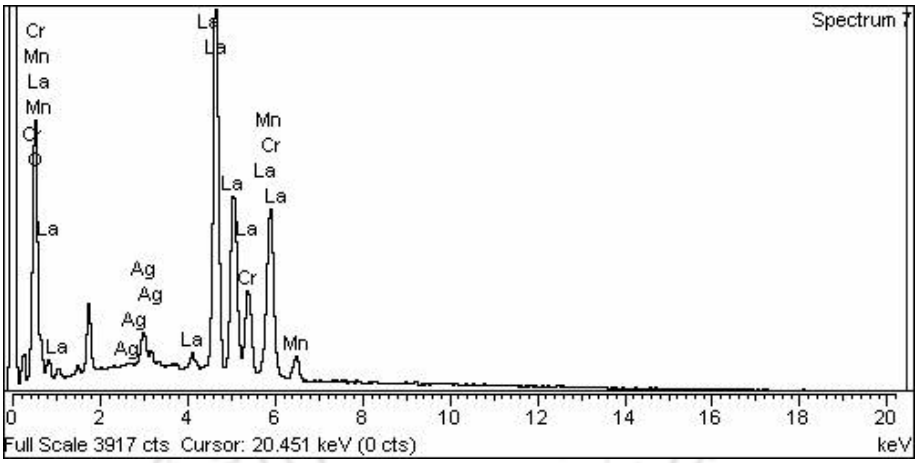

Figure 3.31: Typical SEM-EDS spectrum for y=0.15 sample.

Thus from the structural analysis we have observed that, all the Cr doped compounds are found to crystallize in rhombohedral structure. The decrease in lattice parameters with doping can be explained on the basis of Cr^{3+} of ionic size 0.615 Å replacing Mn^{3+} of ionic size 0.645 Å. Such decrease in lattice parameters are reported by other group in Cr doping on (La, Ca)-Mn-O and La-Mn-O series [195, 202, 203]. The decrease in Mn-O bond length and increase in ∠ Mn-O-Mn bond angle are in expected line in the present doping. The crystallite size is found to decrease marginally with doping.

3.2.2: dc Magnetization

The temperature variations of zero field cooled (ZFC) and field cooled (FC) magnetization under an applied field of 2 mT, are shown in Figure 3.32 for $La_{0.85}Ag_{0.15}Mn_{1-y}Cr_yO_3$ (y=0.05-0.20) compounds. All the ZFC data show paramagnetic (PM) to ferromagnetic (FM) transition. Bifurcation between ZFC and FC magnetization curves is observed for all samples below a certain temperature. The thermo-magnetic irreversibility between ZFC and FC data can arise from the magnetic anisotropy or it can originate from non-equilibrium systems such as spin-glasses, super paramagnets. The study of linear and nonlinear ac susceptibility in this system shows that all the Cr doped samples exhibit spin glass behaviour as discussed in the next section.

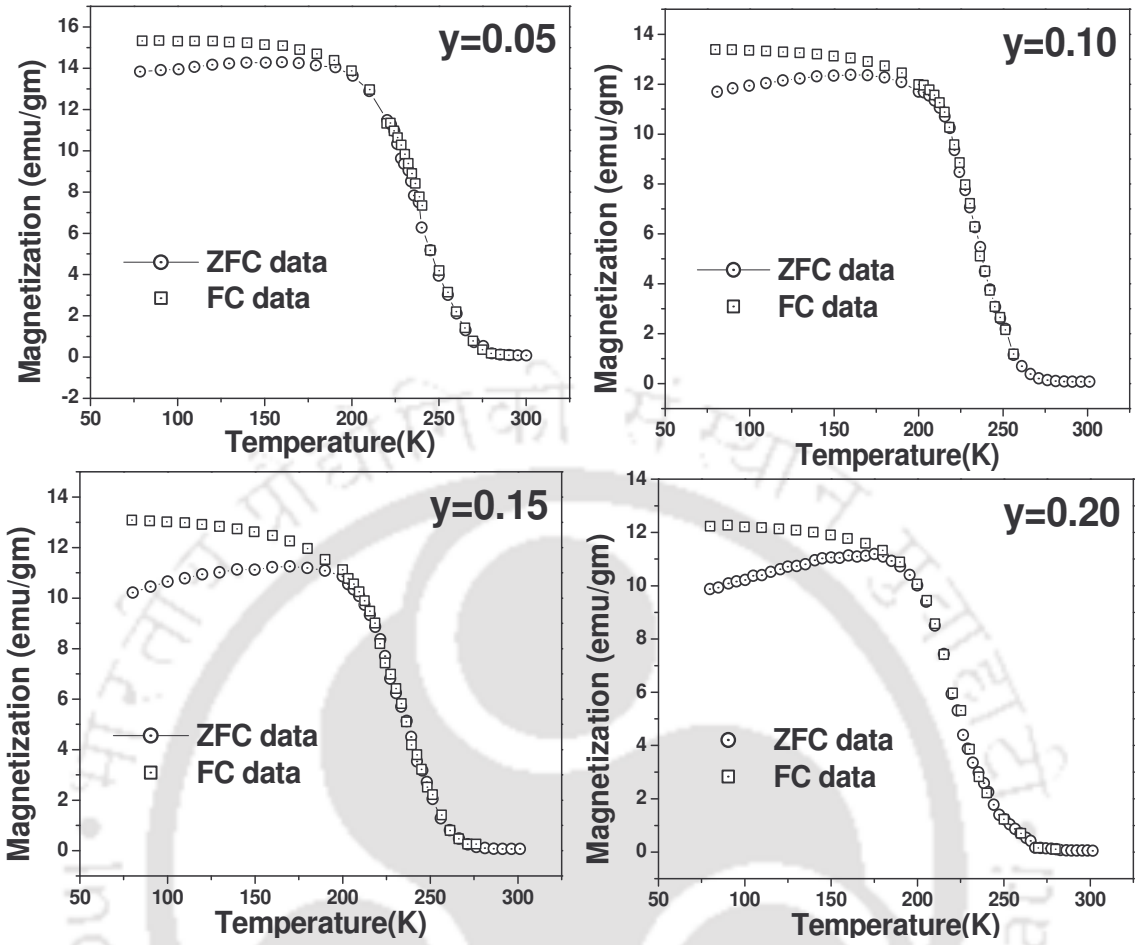

Figure 3.32: The temperature dependence of (ZFC) zero field cooled (Circles) and (FC) field cooled (square) magnetization for y=0.05, 0.10, 0.15, 0.20 samples.

The ferromagnetic (FM) transition temperature (T_c) has been determined from the peak observed in |dM/dT| versus temperature plot. The values of FM T_c are given in Table 3.12 and they decrease with increase in doping. However, the fall in T_c $(\frac{\Delta T_c}{T_c}\times 100)$ is about 23%, 25% 27% and 28 % for y = 0.05, 0.10 0.15 and 0.20, with respect to y = 0 sample, which is quite small compared to Co doped samples. The plot of T_c versus doping concentration y is shown in Figure 3.33 and the T_c is found to decrease linearly, for y≥0.05.

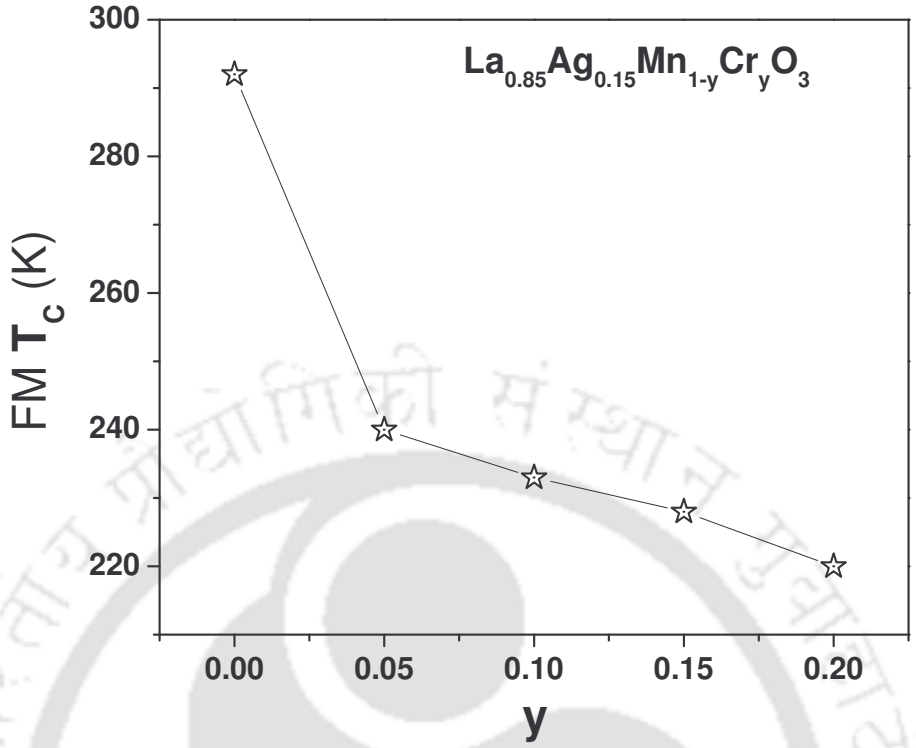

Figure 3.33: Plot of ferromagnetic (FM) transition temperature, T_c as a function of doped Cr concentration, y.

The plot of inverse dc susceptibility ($1/\chi_{dc}$) versus temperature (T) exhibits a linear behaviour in the paramagnetic region as shown in Figure 3.34 for y= 0.10 and 0.15 samples. We have fitted the data by using the Curie-Weiss law, $\chi=C/(T-\theta_C)$ (equation 1.10) and the values of C, θ_C and μ_{eff} are given in Table-3.12. One can see that θ_C is positive as expected for paramagnetic to ferromagnetic transition behaviour. θ_C is found to decrease with increase in Cr concentration, which reflects the decrease in double exchange FM interaction and it is in correlation with variation of FM T_c with doping. Even though θ_C and T_c follow the same trend with doping, θ_C value is found to be higher than that of T_c for each sample. This could be mainly due to smearing of FM transition as a result of different type of FM interaction or dilution of DE FM interaction. The value of effective paramagnetic moment was found to decrease with Cr doping and such variation could be understood in terms of Cr^{3+} ions of paramagnetic moment 3.87 μ_B replacing the Mn^{3+} ions of paramagnetic moment 4.90 μ_B.

The theoretical moment, μ_{th} can be estimated using the relation,

$$\mu_{th}^2 = (1-2x-y)\mu_{Mn^{3+}}^2 + 2x\mu_{Mn^{4+}}^2 + y\mu_{Cr^{3+}}^2 \qquad \text{---------- (3.12)}$$

where, x and y are concentration of Ag and Cr respectively. The estimated μ_{th} and μ_{eff} are comparable; the deviation is about 5% and it could be mainly due to oxygen off stichiometry or all the doped ions might not have contributed for the oxidation of Mn^{3+} ions into Mn^{4+} state.

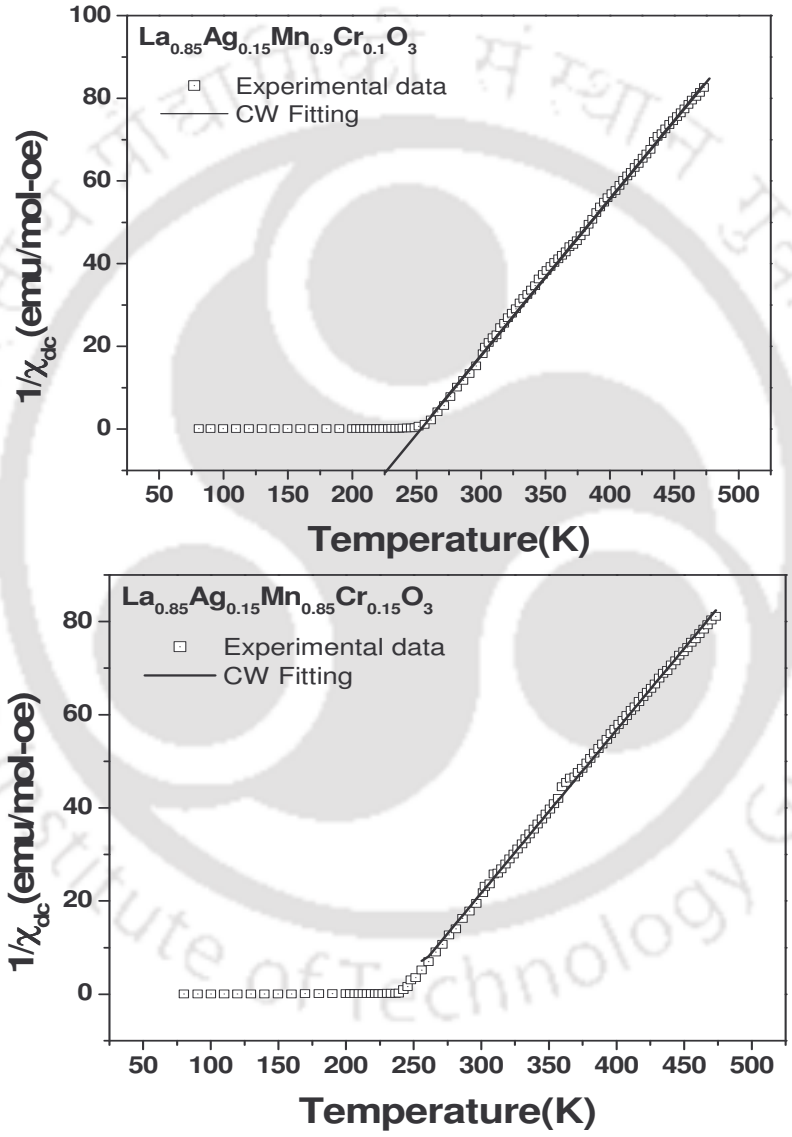

Figure 3.34: $1/\chi_{dc}$ versus temperature for the samples (a) y=0.10 and (b) y=0.15. Solid lines represent fit to the Curie-Weiss law.

Table 3.12: Parameters obtained from magnetization measurements of $La_{0.85}Ag_{0.15}Mn_{1-y}Cr_yO_3$. θ_C (Curie temperature), C (Curie constant), μ_{eff} (μ_B) have been found from inverse dc susceptibility fitting. μ_{th} is the theoretical paramagnetic moment.

Sample/ Parameters	**y=0.05**	**y=0.10**	**y=0.15**	**y=0.20**
T_c (K)	240.0	233.0	228.0	220.0
θ_C (K)	246.7	240.6	236.9	235.2
C (emu K/mol-Oe)	2.91	2.88	2.86	2.83
μ_{eff} (μ_B)	4.82	4.79	4.78	4.75
μ_{th} (μ_B)	4.62	4.57	4.52	4.51

The plots of magnetization as a function of magnetic field (M-H loop) measured at 78 K are shown in Figure 3.35 for all samples. There is decrease in saturation magnetization (M_S) as the Cr doping increases. The magnetization was found to almost saturate and it shows the presence of ferromagnetic behaviour. The values of M_S are given in Table 3.13. To understand the nature of magnetic interaction, the M versus H data is fitted to the Brillouin function model (equations 3.3 and 3.4) by taking into account the ferromagnetic interaction to determine the effective spin angular momentum contribution towards FM interaction. The fitted data are shown as solid line along with experimental data in Figure 3.36. We can see that the fitted data closely follow the experimental data. The fitted values of S_{eff} and M_S are given in Table 3.13. S_{eff} is found to decrease with Cr doping. This is in consistence with ferromagnetic transition temperature variation.

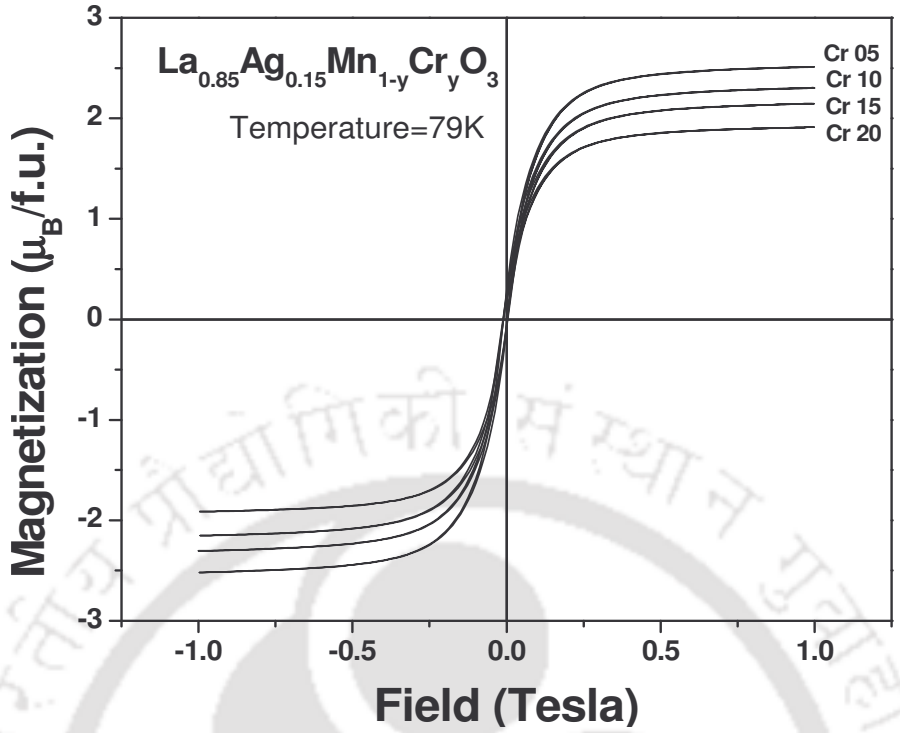

Figure 3.35: Magnetization versus magnetic field plots of the samples $La_{0.85}Ag_{0.15}Mn_{1-y}Cr_yO_3$ for y = 0.05-0.20.

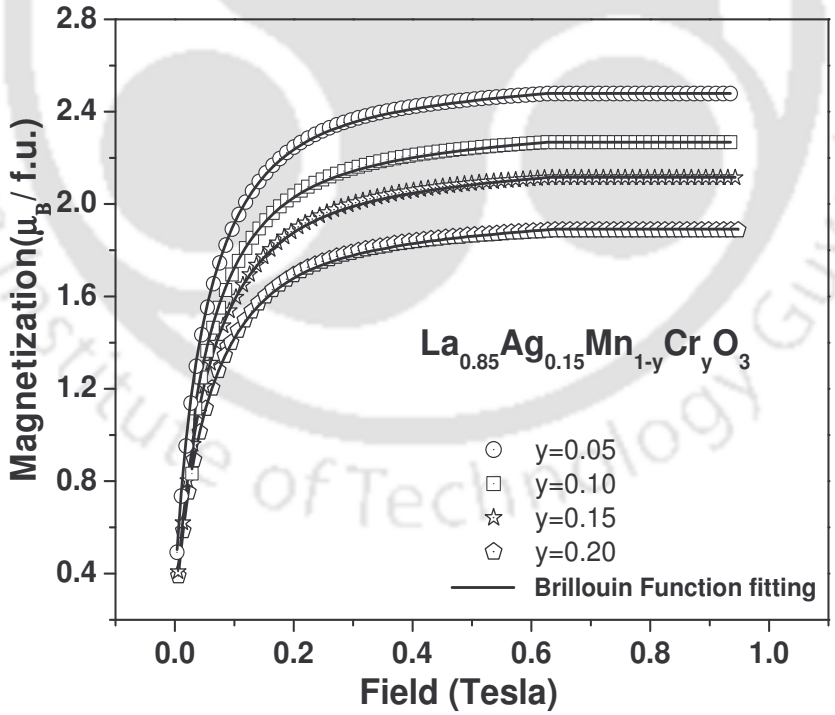

Figure 3.36: Brillouin function fit to magnetization data for y = 0.05-0.20 samples. The experimental data were obtained by subtracting the minor linear contribution from the measured magnetization

Table 3.13: Parameters obtained from Brillouin function fitting to magnetization data. S_{eff} is the effective spin contribution towards FM interaction. M_S is the experimental saturation magnetization.

Sample/ Parameters	y=0.05	y=0.10	y=0.15	y=0.20
S_{eff}	1.19	1.02	0.94	0.92
r m s (%)	0.52	0.58	0.56	0.71
M_S (μ_B/f.u.)	2.39	2.2	2.05	1.85
$M_{S,\,th}$ (μ_B/f.u.)	3.29	2.56	2.29	1.82

Thus from the study of magnetization, we have observed that all Cr doped materials exhibit PM-FM transition. The FM transition could be understood due to the double exchange interaction between Mn^{3+}-O^{2-}-Mn^{4+} networks. The ferromagnetic transition temperature was found to decrease with Cr doping. It could be due to dilution of the strong double exchange ferromagnetic interaction in Mn^{3+}-O^{2-}-Mn^{4+} networks. The fall in T_c was found to be quite small compared to Co doped samples. So, the exchange interaction between Mn^{3+}-O-Mn^{4+} is not strongly suppressed by Cr^{3+} ions. The experimental M_S value is found to vary from 2.39 μ_B for y=0.05 to 1.85 μ_B for y=0.20. They are quite small compared to the expected ferromagnetic M_S value. This suggests that there is a presence of competing AFM in the present series of samples. The various possible networks are Mn^{3+}-O^{2-}-Mn^{4+}, Mn^{3+}-O^{2-}-Cr^{3+}, Mn^{4+}-O^{2-}-Cr^{3+}, Cr^{3+}-O^{2-}-Cr^{3+}. For most of the doping concentration, the probability of Cr^{3+}-O^{2-}-Cr^{3+} networks will be very small because each Mn/Cr ion has six co-ordination with O, and the minimum required doping concentration for such pair is 1/6 ≈ 0.17. By assuming that the moment of doped Cr^{3+} ions are aligned antiparallel with the existing DE FM interaction in Mn^{3+}-O^{2-}-Mn^{4+} network, the M_S value can be estimated as follows.

$$M_S = (0.7 - y)\mu_{Mn^{3+}} + 0.3\mu_{Mn^{4+}} - y\mu_{Cr^{3+}} \quad \text{---------- (3.13)}$$

Here, it is assumed that the ratio of Mn^{3+}/Mn^{4+} concentration is 0.7/0.3 in the parent CMR material, $La_{0.85}Ag_{0.15}MnO_3$. By taking the spin only contribution of z-component of magnetic moments $\mu_{Mn^{3+}}$, $\mu_{Mn^{4+}}$ and $\mu_{Cr^{3+}}$ as 4 μ_B, 3 μ_B, and 3 μ_B respectively, the M_S values were estimated. The estimated $M_{S,\,th}$ are found to be 3.35, 3.0, 2.65 and 2.3 μ_B for y=0.05, 0.10, 0.15 and 0.20 respectively. If we compare $M_{S,\,th}$ with that of M_S values, $M_{s,\,th}$ is found to be

quite large compared to M_s. So, some other competing mechanism also plays a role in bringing down the overall M_S.

The substitution of Cr^{3+} ions in place of Mn^{3+} ion would lead to the increase in Mn^{4+} concentration with respect to Mn^{3+} concentration. In other words, Mn^{3+}/Mn^{4+} ratio would be affected from their optimum value of 0.7/0.3. The relative increase in Mn^{4+} ion with respect to Mn^{3+} ions is likely to pave the way for AFM interaction in Mn^{4+}-O^{2-}-Mn^{4+} networks. Assuming that Mn^{4+} ions are randomly distributed, the probability for Mn^{4+} ion to have n (n=0, 1..) Mn^{4+} ion(s) as their nearest neighbour can be written as [215]

$$P(n, y) = \left[\frac{6!}{n!(6-n!)}\right] y^n (1-y)^{6-n} \quad \text{---------- (3.14)}$$

The probability of each Mn^{4+} ion to have one Mn^{4+} nearest neighbour for the doping concentration y=0.05, 0.10, 0.15 and 0.20 can be obtained as, P (1, 0.05) =0.232, P (1, 0.10) =0.354, P (1, 0.15) =0.40, P (1, 0.20) =0.393. Using the above P (n, y) values, the AFM contribution of Mn^{4+} ions can be incorporated in the above equation 3.14 and the $M_{S, th}$ values are given in the Table 3.13 and they are comparable to the experimental M_S values especially for higher doped samples. Thus the measured magnetization can be explained on the basis of double exchange FM interactions in Mn^{3+}-O^{2-}-Mn^{4+} networks and competing AFM in Cr^{3+}-O-Mn^{4+}, Mn^{4+}-O-Mn^{4+}, Cr^{3+}-O-Mn^{3+} networks. We have also come across the recent work of Zhao *et al.* [215] in (La, Sr)-(Mn, Cr)-O, where the AFM alignment of Cr^{3+} ions are considered.

3.2.3: ac Susceptibility Study

The temperature variations of in-phase (χ_1') and out-phase ac susceptibility (χ'') is shown in Figure 3.37 for the samples $La_{0.85}Ag_{0.15}Mn_{1-y}Cr_yO_3$ (y = 0.05, 0.10, 0.15 and 0.20). All the materials exhibit paramagnetic to ferromagnetic (FM) transition under cooling. Other than PM-FM transition, all the Cr doped samples exhibit a low temperature fall in susceptibility at around 90 K along with corresponding peak in χ_1'' vs. T plot as shown in Figure 3.37.

To understand the origin of low temperature peak observed in χ_1'' versus temperature plot (Figure 3.37), we have carried out the temperature variations of ac susceptibility at different frequencies such as, 333 Hz, 1133 Hz, 3333 Hz, 6333 Hz and 9333 Hz. The plots of χ_1'' versus temperature for different frequencies are shown in Figure 3.38 and Figure 3.39 for

y = 0.10 and 0.15 and 0.20 samples respectively. We have not found any change in the position of ferromagnetic transition temperature T_c with frequency. However, low temperature peak shifts towards higher temperature with increase in frequency. These features are commonly observed in conventional spin glass system. The temperature corresponding to the above peak is taken as spin glass freezing temperature T_f.

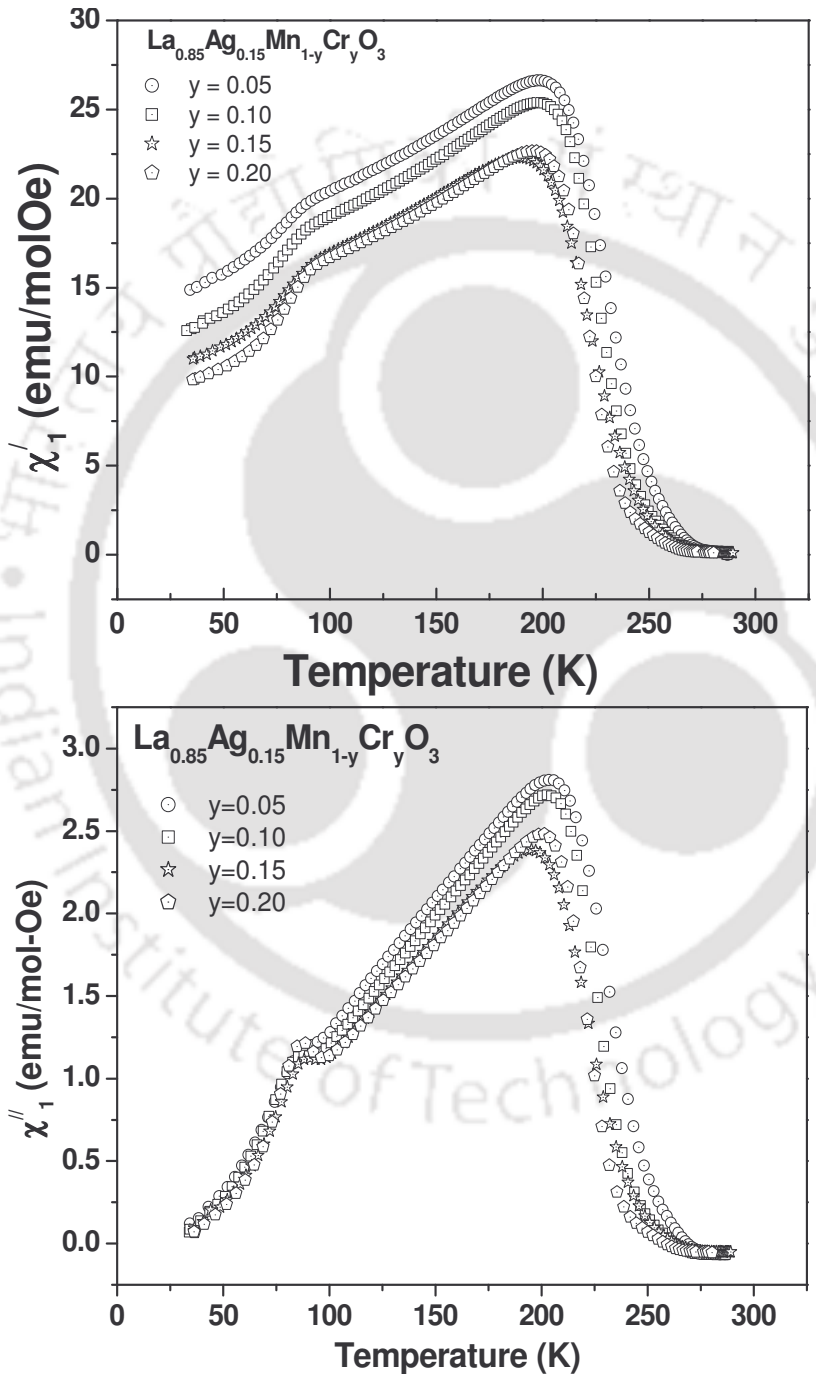

Figure 3.37: Temperature variation of in-phase (χ_1') and out-phase ac susceptibility (χ_1'') of samples $La_{0.85}Ag_{0.15}Mn_{1-y}Cr_yO_3$ (y = 0.05, 0.10, 0.15 and 0.20).

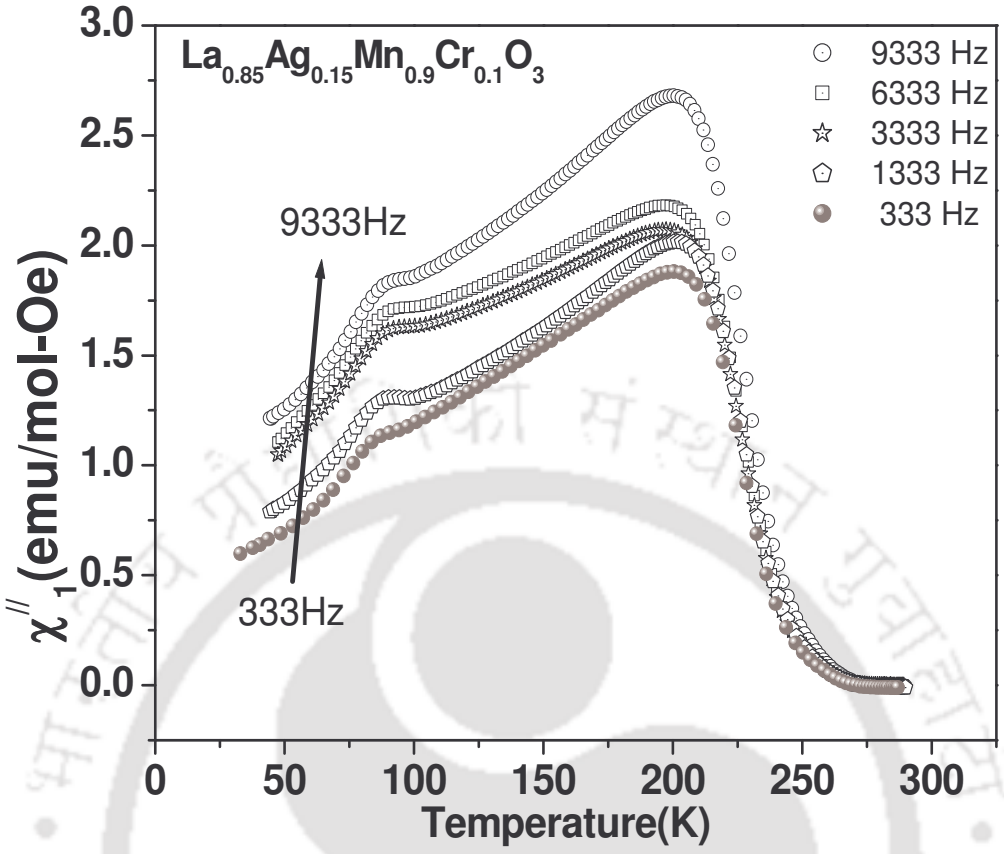

Figure 3.38: $\chi_1^{//}$ versus temperature (T) measured at frequencies f = 333 Hz, 1333 Hz, 3333 Hz, 6333 Hz and 9333 Hz for the samples y=0.10.

We have analysed the spin glass like transition at low temperature from frequency dependent data based on the power law relation (equation 3.5). The plot of T_f versus frequency is shown in Figure 3.40 (a) and (b), for the samples y = 0.15 and 0.20 respectively. These data were fitted to the linear equation to determine T_g and the fitted data are shown as solid lines. The plot of $\ln(\tau)$ versus $\ln[(T_f - T_g)/T_g]$ is shown in Figure 3.40 (c) and (d), for the samples y = 0.15 and 0.20. These data were fitted to equation 3.5 by varying the parameters τ_0 and $z\nu$ and, the fitted data are shown as solid line. The fitted value of τ_0 and $z\nu$ values are listed in Table 3.14 for all samples. Similar type of spin glass like behaviour has been observed by other groups [63, 197, 198]. The τ_0 value is found to be two orders of magnitude larger than that reported on (La, Ca)-(Mn, Cr)-O system [203]. The rather large τ_0 values suggest that the observed spin glass behaviour is not in atomic scale.

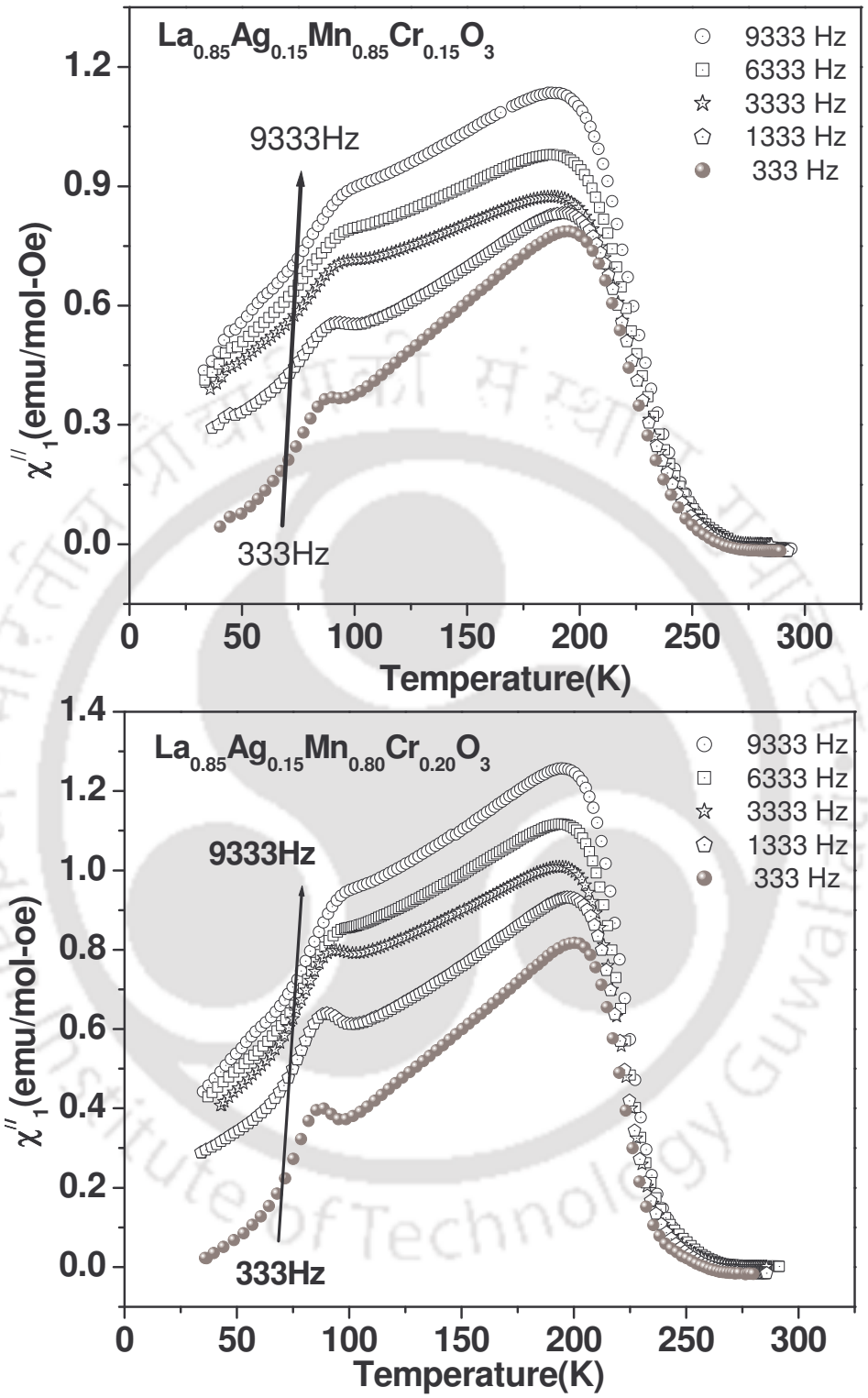

Figure 3.39: $\chi_1^{//}$ versus temperature (T) measured at frequencies f = 333 Hz, 1333 Hz, 3333 Hz, 6333 Hz and 9333 Hz for the samples (a) y=0.15 and (b) 0.20.

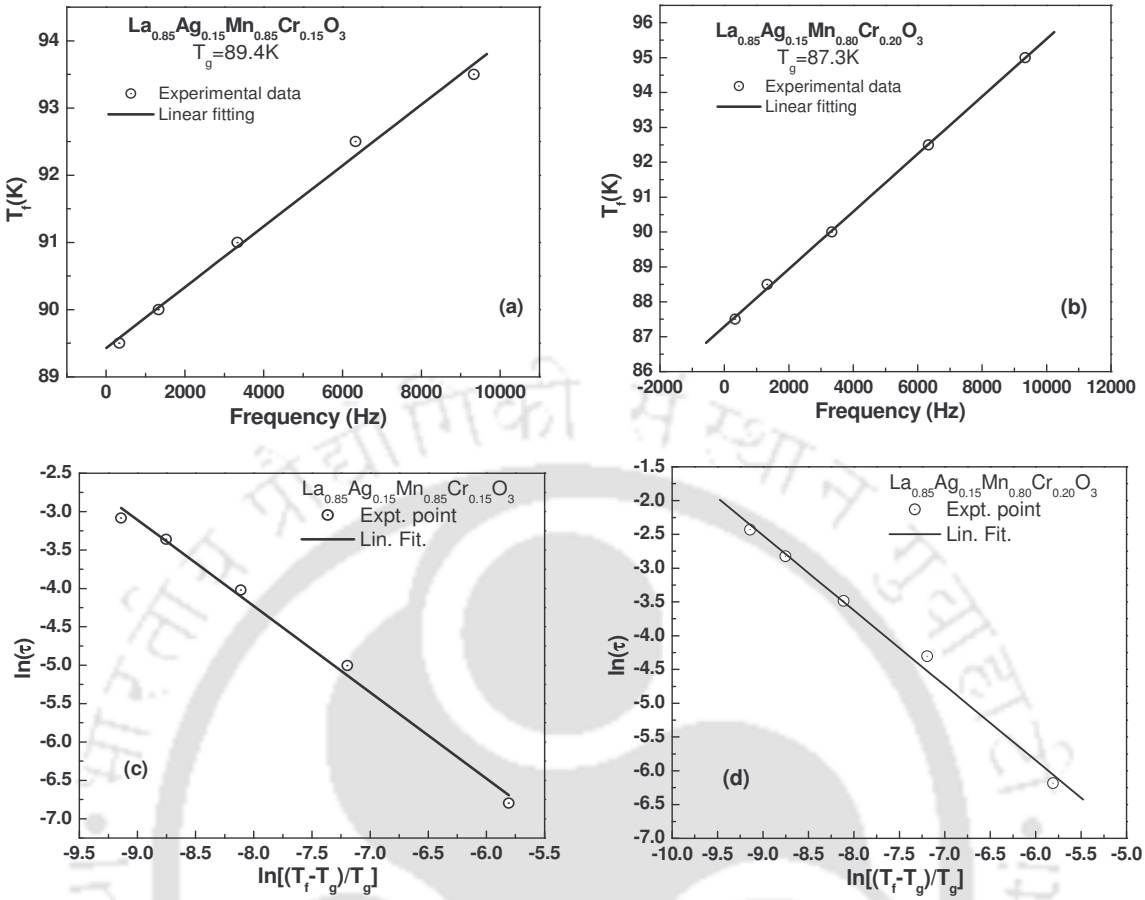

Figure 3.40: Plots of T_f versus frequency for the samples (a) $La_{0.85}Ag_{0.15}Mn_{0.85}Cr_{0.15}O_3$ and (b) $La_{0.85}Ag_{0.15}Mn_{0.8}Cr_{0.2}O_3$ and, the plots of $\ln(\tau)$ versus $\ln[(T_f\text{-}T_g)/T_g]$ for (c) $La_{0.85}Ag_{0.15}Mn_{0.85}Cr_{0.15}O_3$ and (d) $La_{0.85}Ag_{0.15}Mn_{0.8}Cr_{0.2}O_3$.

Table 3.14: Parameters obtained from frequency variation of ac susceptibility measurement. T_f, T_g are spin glass freezing temperature and spin glass temperature respectively. τ_0 is the characteristic time constant.

Sample/Parameters		y =0.05	y = 0.10	y = 0.15	y = 0.20
T_f (K)	333Hz	84.5	86.5	89.5	87.5
	1333Hz	85.5	87.0	90.0	88.5
	3333Hz	87.0	88.5	91.0	90.0
	6333Hz	89.0	90.5	92.5	92.5
	9333Hz	91.0	92.0	93.5	95.0
T_g (K)		84.4	86.3	89.4	87.3
τ_0 (10^{-6}s)		1.7	5.5	1.8	3.7
zν		1.19	1.03	1.12	1.10

We have also carried out the measurement of harmonic susceptibility. The typical plots of temperature variation of third harmonic ac susceptibility, χ'_3 are shown in Figure 3.41 for y=0.10 and 0.15 samples. They exhibit sharp negative peak at around 230 K followed by three distinct positive peaks and out of them one is very broad in nature. The negative peak coincides with ferromagnetic transition temperature and the positive peaks can be attributed to AFM interaction and spin glass behaviour. The position of low temperature peak at around 85 K is closely comparable to the low temperature peak observed from χ_1'' vs. T plot (Figure 3.39) for y=0.15 and 0.20 samples and they are attributed to spin glass transition temperature. Thus the harmonic susceptibility clearly depicts the presence of FM and low temperature SG state. It is comparable to the harmonic susceptibility of ferromagnetic spin glass material such as $Fe_{1.5}Mn_{1.5}Si$ reported by Chakravarti *et al.* [282]. The critical behaviour of χ'_3 could not be studied because of presence of multiple peaks in close proximity.

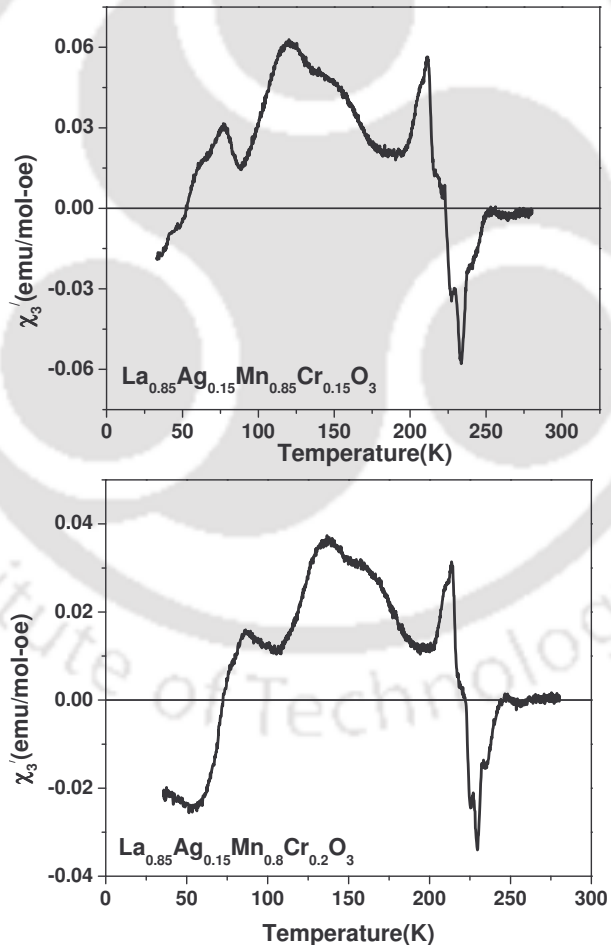

Figure 3.41: χ_3' versus T for the sample $La_{0.85}Ag_{0.15}Mn_{0.85}Cr_{0.15}O_3$ and $La_{0.85}Ag_{0.15}Mn_{0.8}Cr_{0.2}O_3$.

Thus from the ac susceptibility result, we have observed that the doping of Cr introduces the anti-ferromagnetic interaction to the existing double exchange ferromagnetic interactions in Mn^{3+}-O^{2-}-Mn^{4+} networks. These competing interactions give rise to reentrant spin glass like transition at low temperature for all Cr doped compounds.

3.2.4. Electrical Resistivity and Magneto-Resistivity

Temperature variations of electrical resistivity (ρ) in the absence and presence of 1T magnetic field are shown in the Figure 3.42 for samples $La_{0.85}Ag_{0.15}Mn_{1-y}Cr_yO_3$ (y = 0.05, 0.10, 0.15 and 0.20). A broad hump has been observed at around 120 K and 100 K for y = 0.05 and 0.10 samples respectively. The broad hump indicates that metallic behaviour competes with insulating behaviour and the system re-enters into an insulating state. Semiconducting behaviour has been observed for y ≥ 0.15 samples. Even though the Cr doped samples exhibit FM transition, we have not observed clear metal-insulator transition due to lack of percolation threshold of FM.

The temperature variation of magneto-resistivity was calculated using the relation, $(\Delta\rho/\rho_o)=(\rho_H-\rho_o)/\rho_o$. The temperature variation of negative magneto-resistivity ($-\Delta\rho/\rho_0$) is shown in Figure 3.43 for y=0.05 and 0.10 samples. Broad magneto-resistivity peaks have been observed in the vicinity of FM T_c. Thus the electrical resistivity and magneto-resistivity data show that in Cr doped samples there is a contribution from both metallic conduction due to double exchange ferromagnetic interaction and semiconducting behaviour due to antiferromagnetic super exchange interaction. Unlike the conventional CMR materials where large magneto-resistivity (MR) is observed only in the vicinity of FM T_c, here we can observe considerable MR in a wide temperature range. The increase in magneto-resistivity with decrease in temperature can be explained on the basis of presence of considerable magnetic anisotropy and it is suppressed due to applied magnetic field. The contribution of intergranular tunneling can be also one of the reasons for the observed MR.

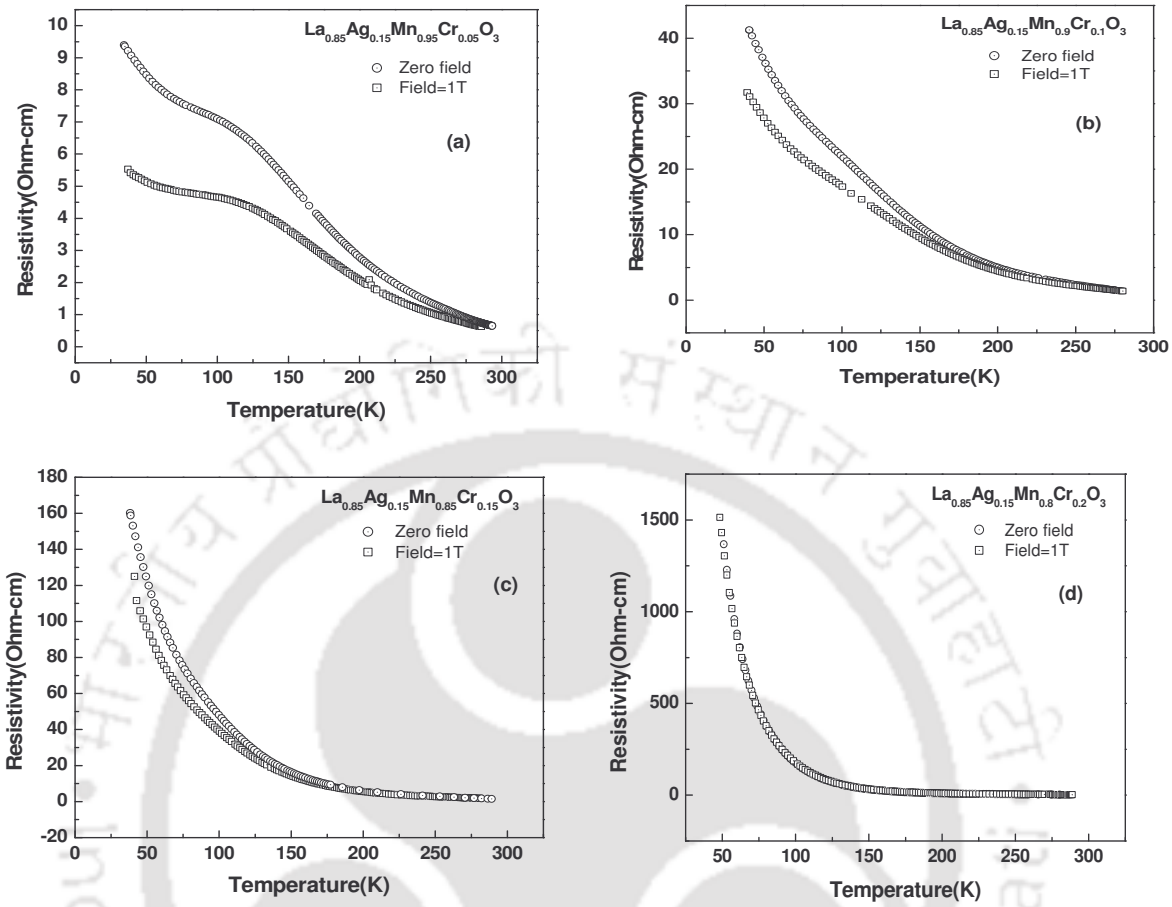

Figure 3.42: Temperature variation of electrical resistivity and magneto-resistivity of y = 0.05, 0.10, 0.15 and 0.20 samples.

The resistivity data for all the samples in the semiconducting region could be fitted to Mott-VRH model with relatively low root mean square deviation value. One typical fitting for y=0.15 sample is shown in Figure 3.44. The range of value of R_{hop}(300K), E_{hop}(300K) and N (E_F) are found to be 66-24 Å, 253-95 meV and 1-16 $\times 10^{25}$ $eV^{-1}m^{-3}$ respectively.

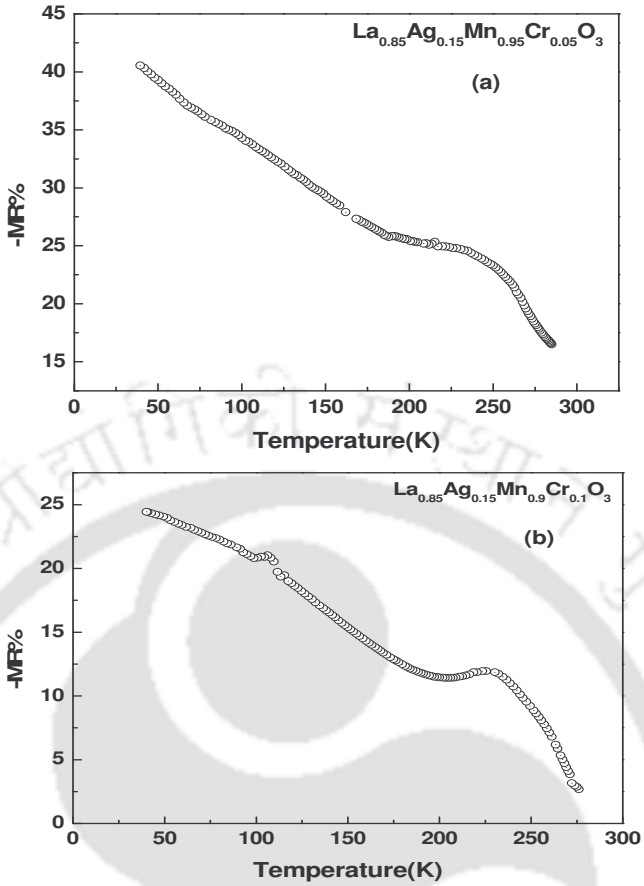

Figure 3.43: Temperature variation of magneto resistivity ($-\Delta\rho/\rho_0$) for 0.05 and 0.10 samples.

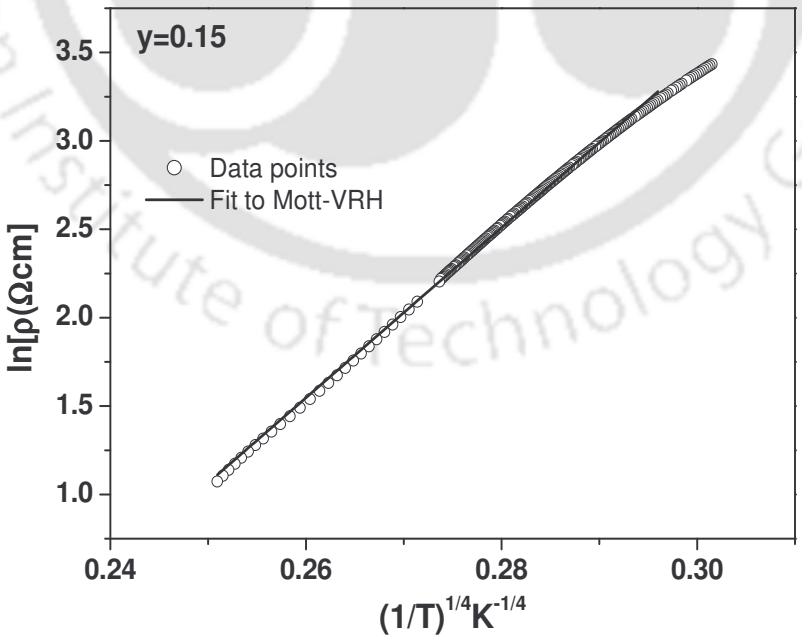

Figure 3.44: Resistivity versus $T^{-1/4}$ for the sample y = 0.15. The solid line shows the fit to Mott-VRH model.

3.3. $La_{0.85}Ag_{0.15}Mn_{1-y}Al_yO_3$ Compounds (y= 0-0.20)

Unlike the magnetic impurities, the non-magnetic impurity such as Al is expected to play a role of dilution of double exchange ferromagnetic interaction and introduction of random electrical potential without any complicated magnetic phase separation. In the present section, we report the non-magnetic Al doping in the Mn site of $La_{0.85}Ag_{0.15}MnO_3$ compound.

3.3.1. Sample Preparation and Characterization

The $La_{0.85}Ag_{0.15}Mn_{1-y}Al_yO_3$ compounds were prepared for y = 0, 0.05, 0.10, 0.15 and 0.20 by solid state route. Stoichiometric ratio of La_2O_3, $AgNO_3$, Al and $C_4H_6MnO_4.4H_2O$ with 99.9% purity were weighed and mixed thoroughly under acetone. The mixture was presintered at 800^0C for 36h with intermediate grindings. The sintering in pellet form was carried out at 1000^0C over 20h with intermediate grindings. The final sintering was carried out at 1050^0C for over 40h with intermediate grindings. All the above sintering processes were carried out in air.

The XRD patterns recorded for $La_{0.85}Ag_{0.15}Mn_{1-y}Al_yO_3$ compounds with for y=0 to 0.2 are shown in Figure 3.45. We can see that the samples are essentially in single phase form. The patterns for all the samples could be refined using $R\bar{3}c$ space group. Typical XRD patterns along with Rietveld refinement are shown in Figure 3.46 for y = 0.05 and 0.15. The refined lattice parameters and unit cell volume are listed in Table 3.15. The lattice parameters and unit cell volume decrease with increase in Al concentration. The ionic size of Al^{3+} is less than the ionic size of Mn^{3+} ions and hence there is a reduction in lattice parameters with doping. Such a reduction is observed in other Al substituted mixed valent manganites [222]**.** The average Mn-O bond length and ∠Mn-O-Mn bond angle were calculated from the refined atomic positions and lattice parameters and, these values are tabulated in Table 3.15. The average Mn-O bond length was found to increase with the increase of Al^{3+} concentration, while the average ∠Mn -O-Mn bond angle was found to decreases with doping. The average crystallite size has been calculated using the Scherrer's formula [262] to study its variation with doping. No appreciable variation in crystallite size has been observed.

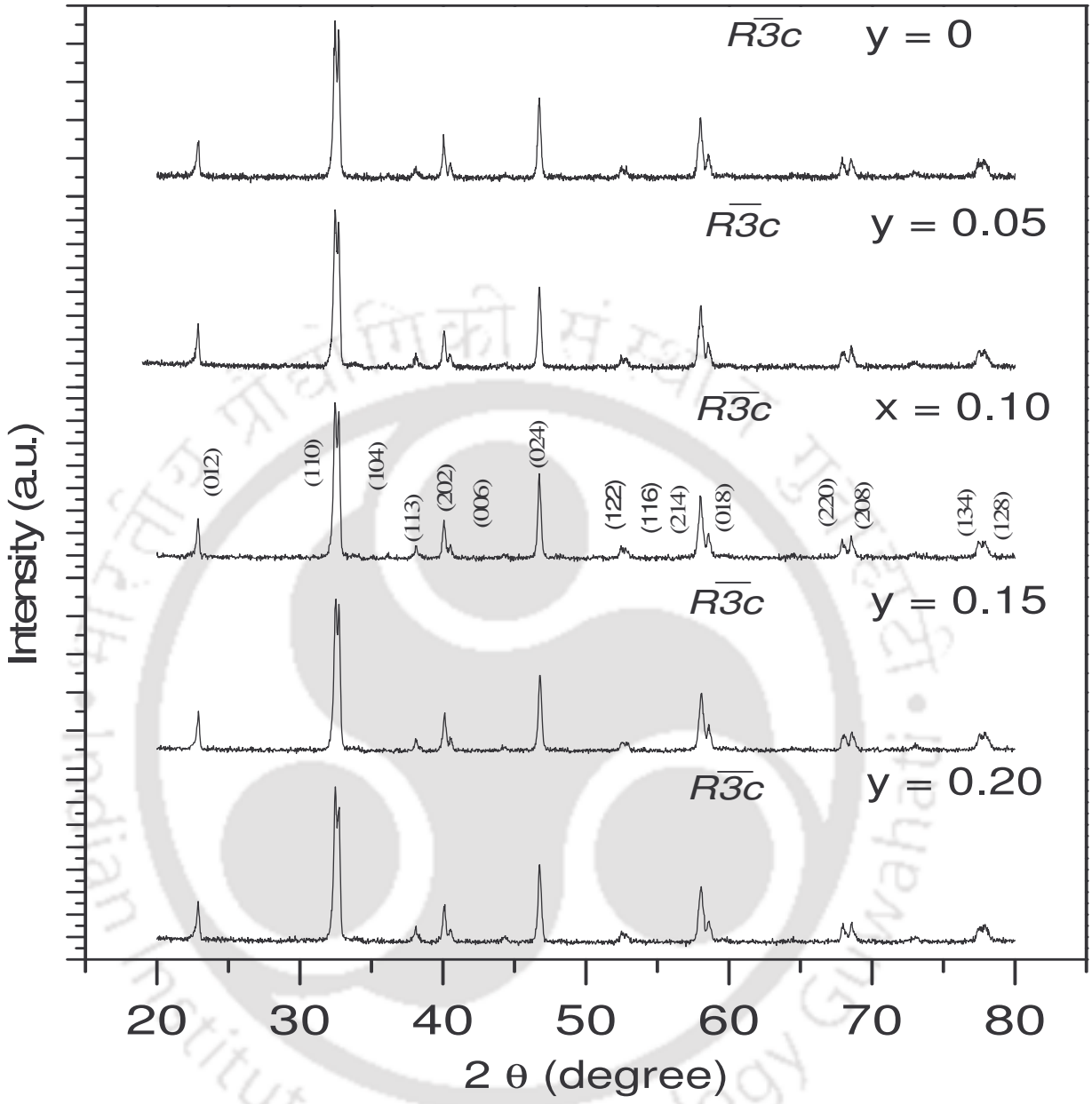

Figure 3.45: XRD patterns of the samples $La_{0.85}Ag_{0.15}Mn_{1-y}Al_y$ for y = 0, 0.05, 0.10, 0.15 and 0.20.

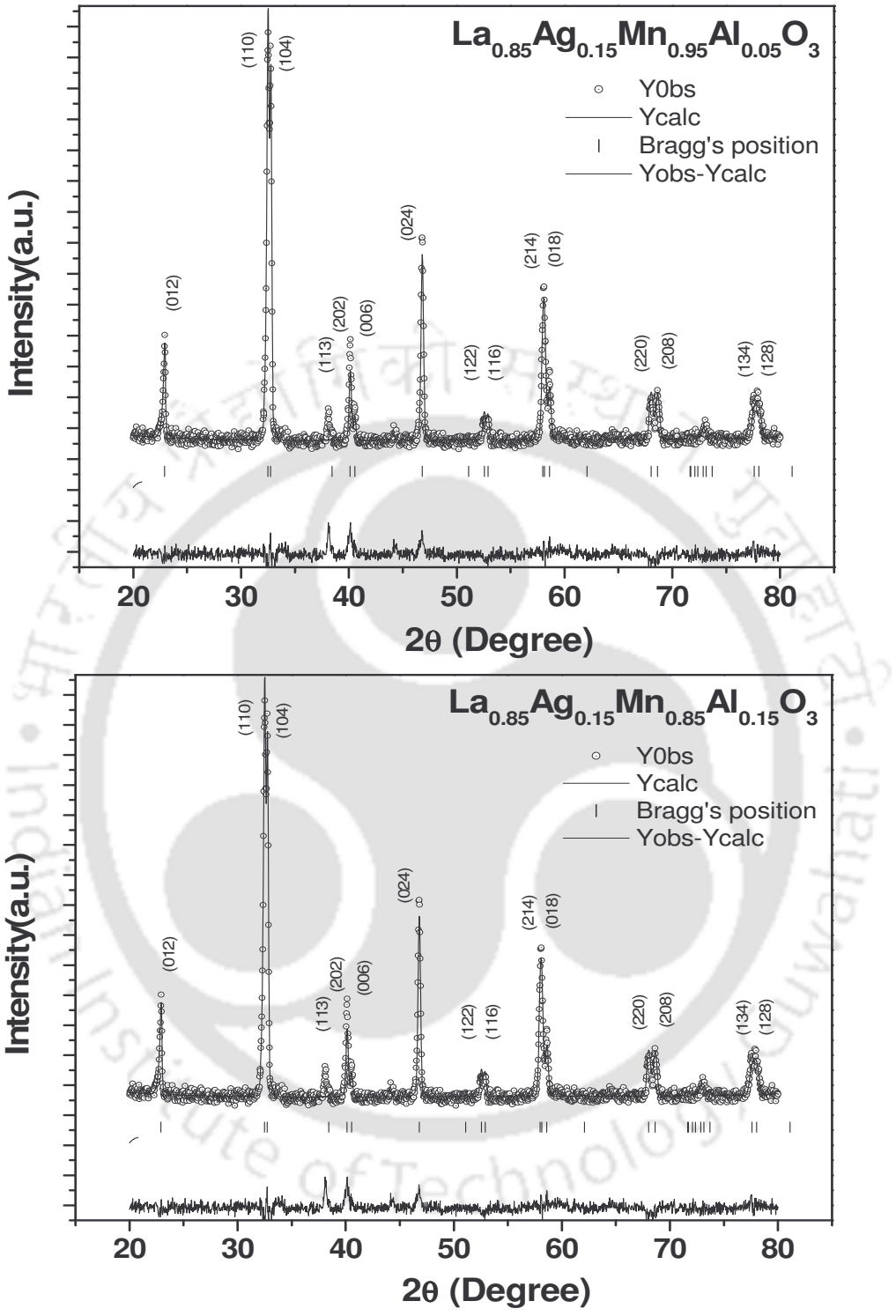

Figure 3.46:XRD patterns for the samples y = 0.05 and 0.15. The circles represent experimental points and solid line represents Rietveld refined data. The bottom line shows the difference between experimental and refined data. The marked 2θ positions are the allowed Bragg peaks.

Table 3.15: Parameters obtained from the Rietveld analysis of XRD patterns for the samples $La_{0.85}Ag_{0.15}Mn_{1-y}Al_yO_3$ (y = 0.05, 0.10, 0.15 and 0.20). R_p, $R_{\omega p}$, R_{exp}, R_{Bragg}, R_F and χ^2 are the reliability factors. S_C is the crystallite size.

Sample/Parameters	**y= 0.05**	**y= 0.10**	**y= 0.15**	**y= 0.20**
Spacegroup	R $\bar{3}c$	R $\bar{3}c$	R $\bar{3}c$	R $\bar{3}c$
a=b (Å)	5.5192 (0.0003)	5.5180 (0.0009)	5.5152 (0.0006)	5.5133 (0.0007)
c (Å)	13.3590 (0.0014)	13.3594 (0.0025)	13.3539 (0.0018)	13.3518 (0.0021)
Volume(Å)	352.41 (0.11)	352.28 (0.11)	351.47 (0.08)	351.77 (0.86)
χ^2 (%)	4.35	3.84	4.38	4.18
R_p (%)	6.58	6.34	6.68	5.94
R_{wp} (%)	8.45	8.14	8.87	7.87
R_{exp} (%)	4.05	4.16	4.24	3.85
R_f (%)	15.8	11.4	13.0	11.7
R_{Brag} (%)	13.7	9.24	14.2	13.2
<Mn-O> (Å)	1.9562	1.9581	1.9593	1.9596
∠Mn-O-Mn (°)	167.0	166.0	165.0	164.6
S_C (nm)	39.2	39.0	37.0	35.8
Mn valency	3.20	3.28	3.44	3.40

Typical SEM micrograph for $La_{0.85}Ag_{0.15}Mn_{0.15}Al_{0.15}O_3$ is shown in Figure 3.47. The SEM images show that the morphology of the materials is uniform and no trace of impurity has been observed. The composition determined from EDS analysis is found to be comparable to the nominal starting composition and they are given in Table3.16. One typical energy dispersive spectrum for y=0.20 sample is shown in the Figure 3.48. The average Mn valency determined from chemical titration is given in Table 3.15 and it is found to increase with the Al concentration. It is due to the decrease in Mn^{3+} concentration with respect to Mn^{4+} concentration.

Table 3.16: Cationic ratio determined from EDS analysis of $La_{0.85}Ag_{0.15}Mn_{1-y}Al_yO_3$ series.

Sample	Calculated Cationic Ratio			
	La	Ag	Mn	Al
y= 0.0	0.86	0.13	1.01	0
y= 0.05	0.86	0.14	0.95	0.05
y= 0.10	0.89	0.11	0.89	0.11
y= 0.15	0.87	0.13	0.84	0.16
y= 0.20	0.88	0.12	0.81	0.19

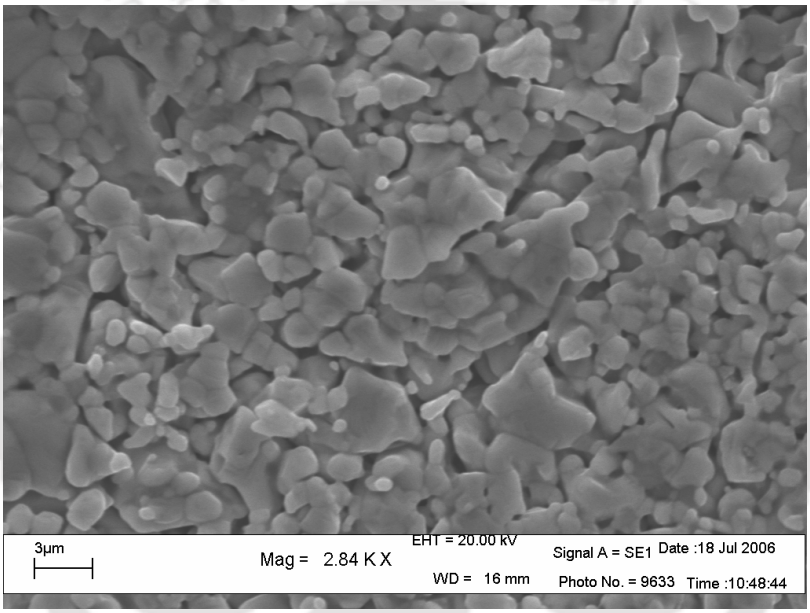

Figure 3.47 SEM image (magnification 2840) of $La_{0.85}Ag_{0.15}Mn_{0.8}Al_{0.2}O_3$ sample.

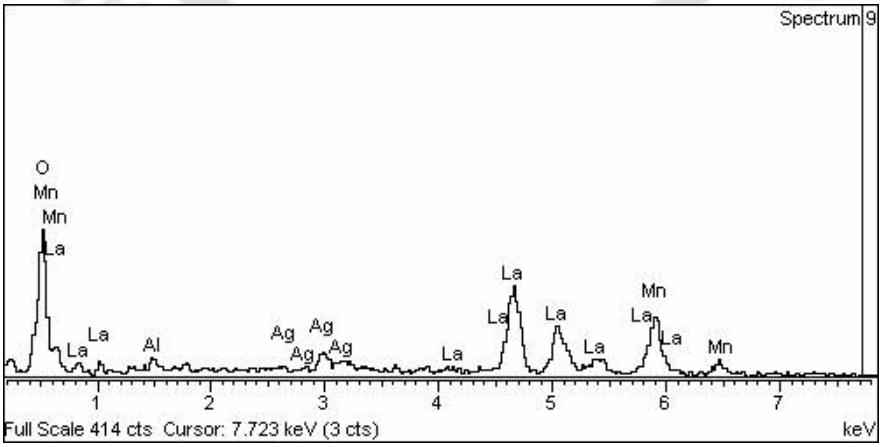

Figure 3.48: Typical Energy Dispersive spectrum for y=0.20 sample.

3.3.2: dc Magnetization

The temperature variations of zero field cooled magnetization curves under an applied field of 2 mT, are shown in Figure 3.49 for all Al doped compounds. All the compounds show paramagnetic (PM) to ferromagnetic (FM) transition due to double exchange interaction in Mn^{3+}-O^{2-}-Mn^{4+} networks. The magnitude of magnetization was found to decrease with Al doping because of dilution of double exchange ferromagnetism. The temperature variation of ZFC (Circles) and FC (squares) curves are shown in the Figure 3.50 for y=0.05 sample. ZFC and FC data show the presence of long range FM transition without any low temperature anomaly. Unlike Co and Cr doped samples, no appreciable difference between ZFC and FC data have been observed.

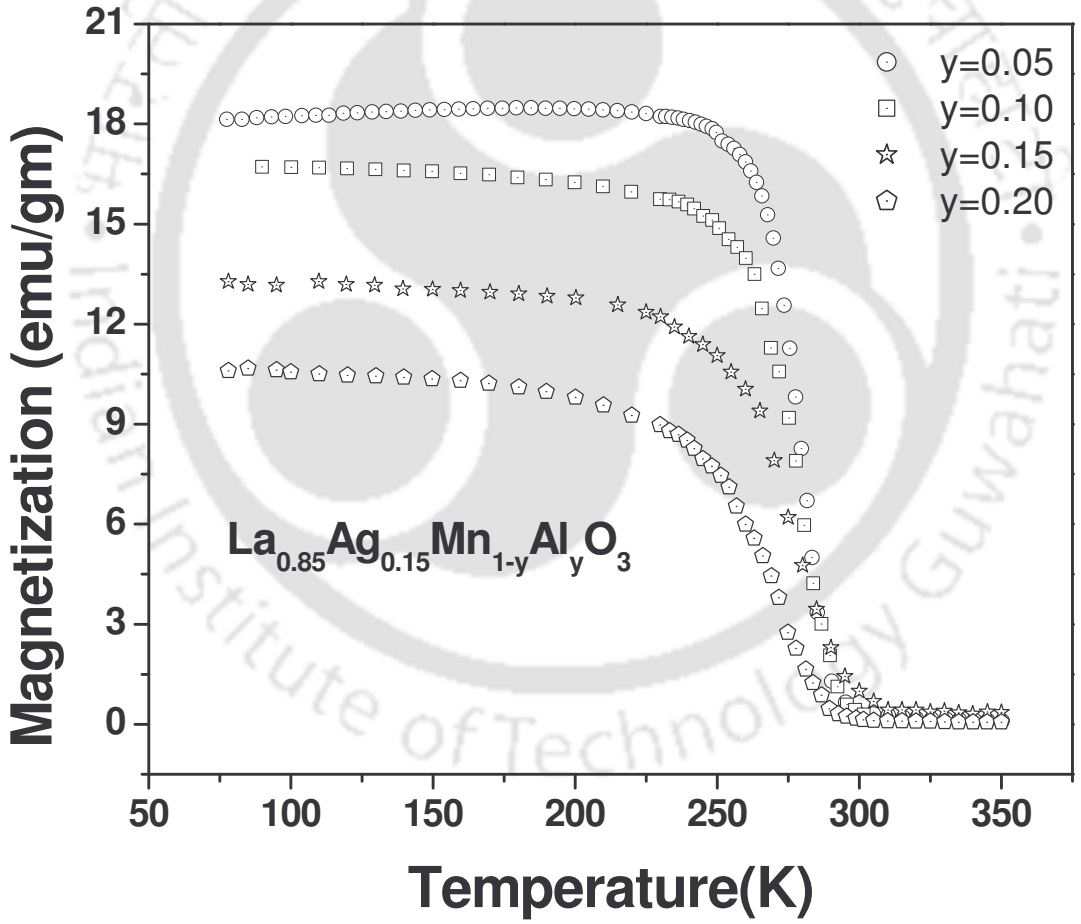

Figure 3.49: The temperature variation of zero field cooled (ZFC) magnetization curves for y=0.05, 0.10, 0.15, 0.20 samples.

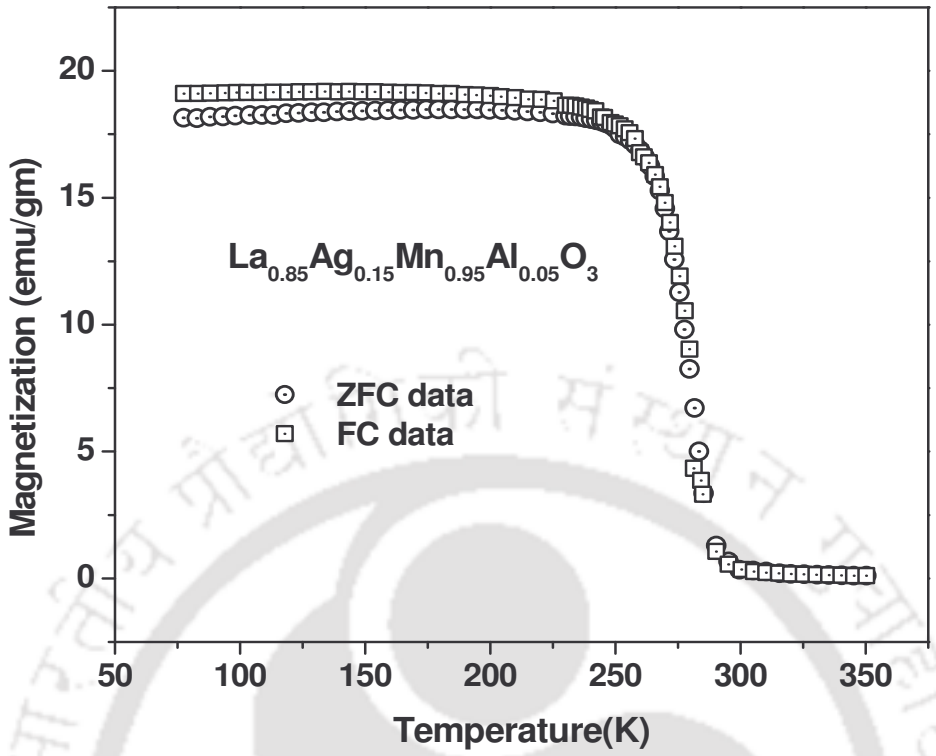

Figure 3.50: The temperature variation of (ZFC) zero field cooled (Circles) and (FC) field cooled (square) magnetization curves for y=0.05 samples.

The ferromagnetic (FM) transition temperature (T_c) has been determined from the peak observed in |dM/dT| versus T plot. The values of FM T_c are given in Table 3.17 and they decrease with increase in doping. The variation of FM T_c with Al doping is shown in Figure 3.51 and it could be understood on the basis of dilution of double exchange ferromagnetic interaction in Mn^{3+}-O^{2-}-Mn^{4+} networks. The plots of inverse dc susceptibility ($1/\chi_{dc}$) versus temperature (T) exhibit a linear behaviour in the paramagnetic region as shown in Figure 3.52 for y=0.05 and 0.15 samples. The data have been fitted by using Curie-Weiss law, $\chi=C/(T-\theta_c)$ and the values of C, θ_c and μ_{eff} are given in Table-3.17. The value of μ_{eff} is found to increase with doping and it can be because of ferromagnetic clustering even above FM T_c. One can see that θ_c is positive as expected for paramagnetic to ferromagnetic transition behaviour. θ_c is found to decrease with increase in Al.

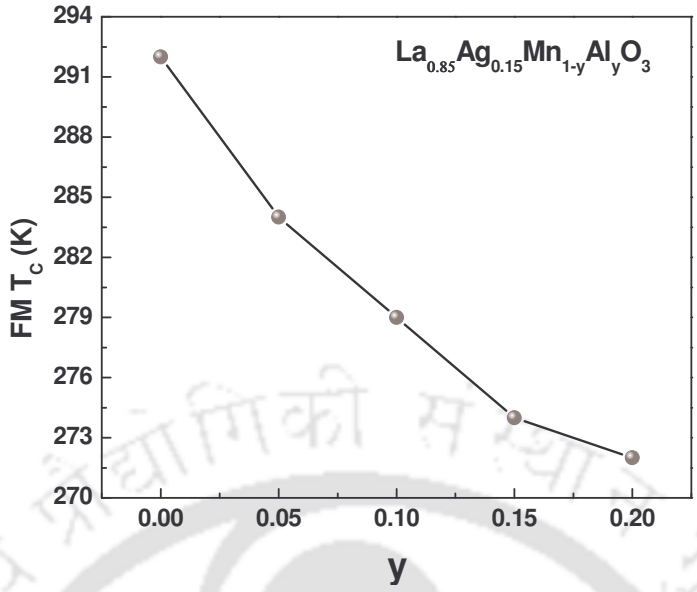

Figure 3.51: Plot of ferromagnetic transition temperature as a function of doped Al concentration.

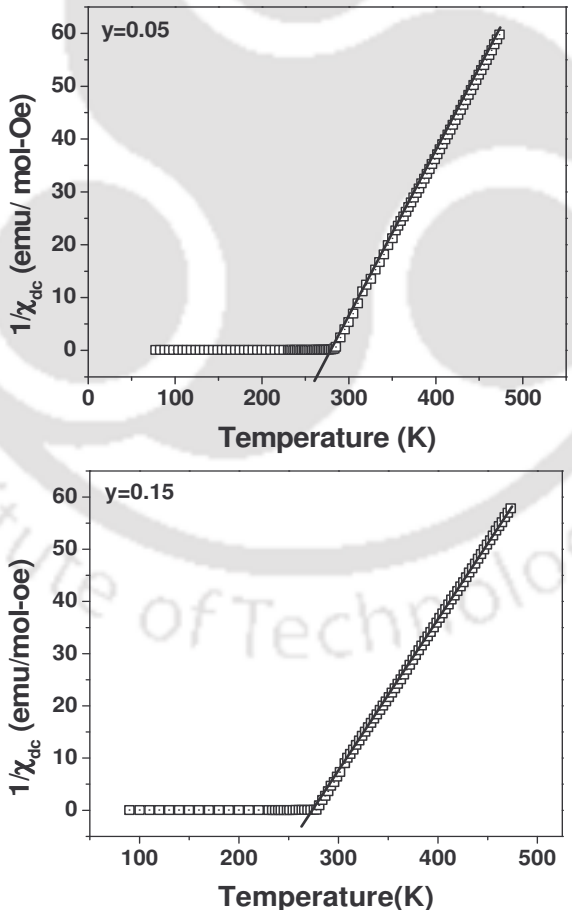

Figure 3.52: $1/\chi_{dc}$ versus temperature for the samples (a) y=0.05 and (b) y=0.15. Solid lines represent fit to the Curie-Weiss law.

Table 3.17: Parameters obtained from magnetization measurements of $La_{0.85}Ag_{0.15}Mn_{1-y}Al_yO_3$. θ_C (Curie temperature), C (Curie constant) have been found from Curie-Weiss law fit of susceptibility.

Sample/Parameters	**y=0.05**	**y=0.10**	**y=0.15**	**y=0.20**
T_c (K)	284.0	279.0	274.0	272.0
θ_C (K)	277.5	275.5	273.0	271.0
C (emu K/mol-Oe)	3.31	3.42	4.00	4.84
μ_{eff} (μ_B)	5.14	5.23	5.65	6.22

The plots of magnetization as a function of magnetic field (M-H loop) measured at 79 K are shown in Figure 3.53 for all samples. There is a decrease in saturation magnetization (M_S) as the Al doping increases. The magnetization was found to saturate and it shows the ferromagnetic behaviour. The experimental saturation magnetization, M_S are given in Table 3.18. By assuming that in the absence of doping, the fraction of Mn^{3+} and Mn^{4+} concentration are 0.7 and 0.3 and the doped Al ions do not take part in any magnetic interaction, the saturation magnetization, $M_{S,th}$ can be estimated as;

$$M_{Sth} = (0.7-y)\, 4\mu_B + (0.3)\, 3\, \mu_B \quad \text{---------- (3.15)}$$

Here, it is assumed that doped Al ion replaces Mn^{3+} ions. The magnetic moment of Mn^{3+} and Mn^{4+} ions due to their spin only contribution are taken as 4 μ_B and 3 μ_B respectively. The $M_{S,\,th}$ values are given in Table 3.18 and they are comparable to experimental values except for y=0.05.

To understand the nature of magnetic interaction, the M versus H data have been fitted to the Brillouin function model (equation 3.3) by taking into account the ferromagnetic interaction to determine the effective spin contribution electrons towards FM interaction. The fitted data are shown as solid lines in Figure 3.54 and they closely follow the experimental data. The fitted values of S_{eff} and M_S are given in Table 3.18. The effective spin contribution towards FM interaction was found to decreases with doping.

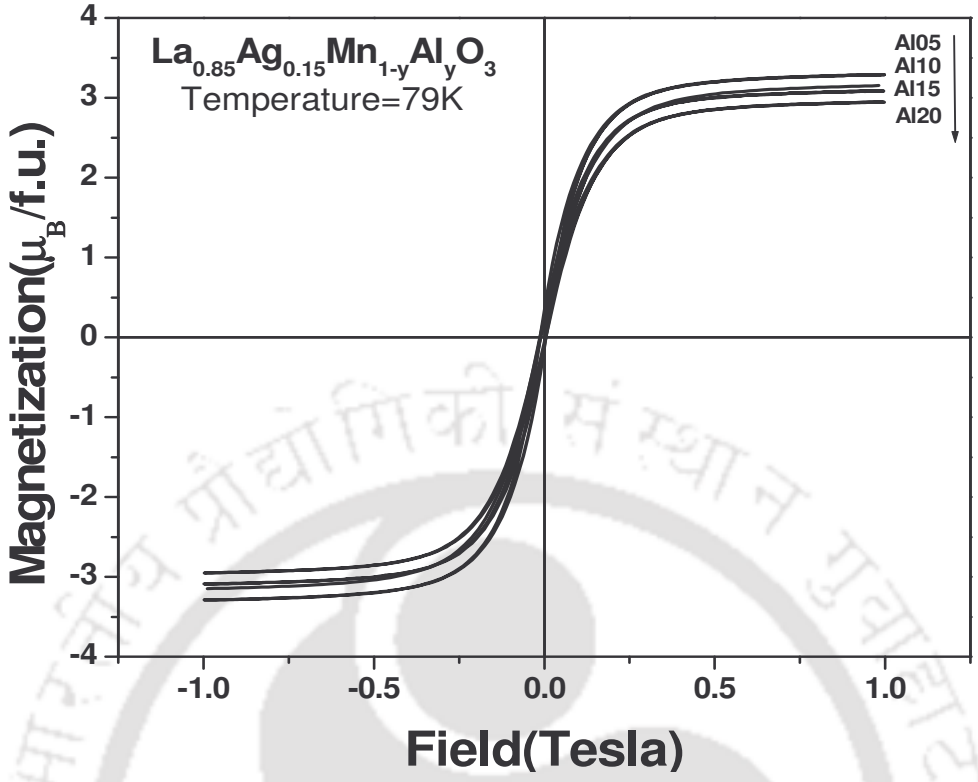

Figure 3.53: Magnetization versus magnetic field of $La_{0.85}Ag_{0.15}Mn_{1-y}Al_yO_3$ samples for y = 0.05-0.20.

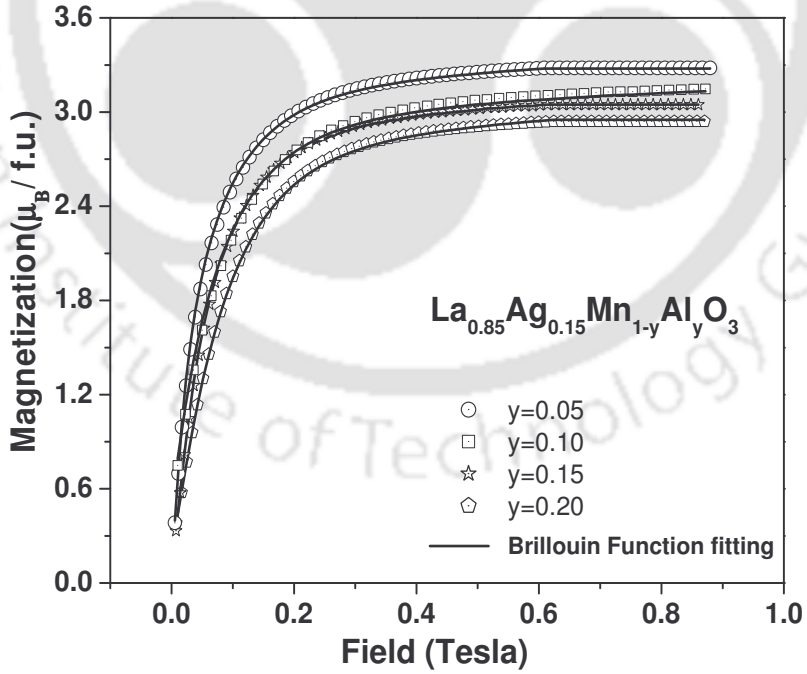

Figure 3.54: Brillouin function fit to magnetization data for y= 0.05, 0.10, 0.15 and 0.20 samples. The experimental data were obtained by subtracting the minor linear contribution from the measured magnetization.

Table 3.18: Parameters obtained from Brillouin function fitting to magnetization data. S_{eff} is the effective spin contribution towards FM interaction. M_S is the experimental saturation magnetization.

Sample/ Parameters	**y=0.05**	**y=0.10**	**y=0.15**	**y=0.20**
S_{eff}	1.27	0.98	1.15	1.0
r m s (%)	0.78	0.64	0.49	0.46
M_S (μ_B/f.u.)	3.22	3.13	3.08	2.94
$M_{S,\,th}$ (μ_B/f.u.)	3.50	3.30	3.10	2.90

3.3.3: ac Susceptibility Study

Figure 3.55 shows the inphase ac susceptibility, $\chi_1^{/}$ versus temperature (T) for the samples y = 0.05, 0.10, 0.15 and 0.20. One can see that all the Al doped samples show paramagnetic to ferromagnetic transitions when they are cooled. The ferromagnetic onset temperature is above the room temperature (300K) for y ≤ 0.10. Below FM transition, the ac susceptibility values do not fall rapidly in the present series, unlike the case of Co and Cr doped compounds. The out of phase ac susceptibility, $\chi_1^{//}$ versus temperature (T) (shown in Figure 3.56) for the samples y = 0.0, 0.05, 0.10, 0.15 and 0.20 show no trace of secondary transitions except the one corresponding to paramagnetic to ferromagnetic transition. The FM transition temperature $T_c^{/}$ was determined from the peak observed in $\left|\frac{d\chi^{/}}{dT}\right|$ versus T plot and the variation of $Tc^{/}$ with y is shown in the inset of Figure 3.56. The difference between T_c and $T_c^{/}$ is mainly due to smearing of FM transition in dc magnetization measurement due to considerable applied field.

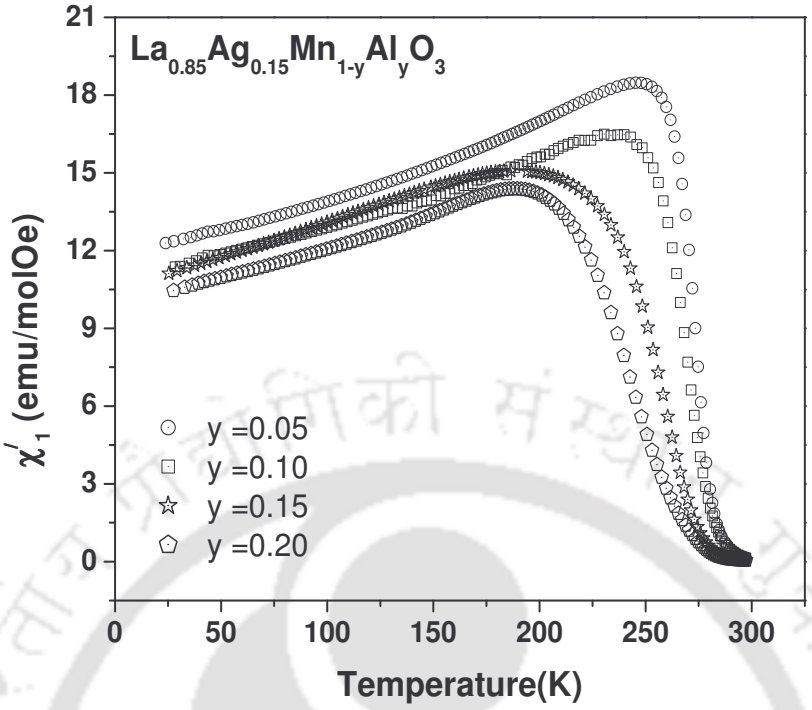

Figure 3.55: Temperature dependence of inphase ac susceptibility (χ_1') for y =0.05, 0.10, 0.15 and 0.20 samples.

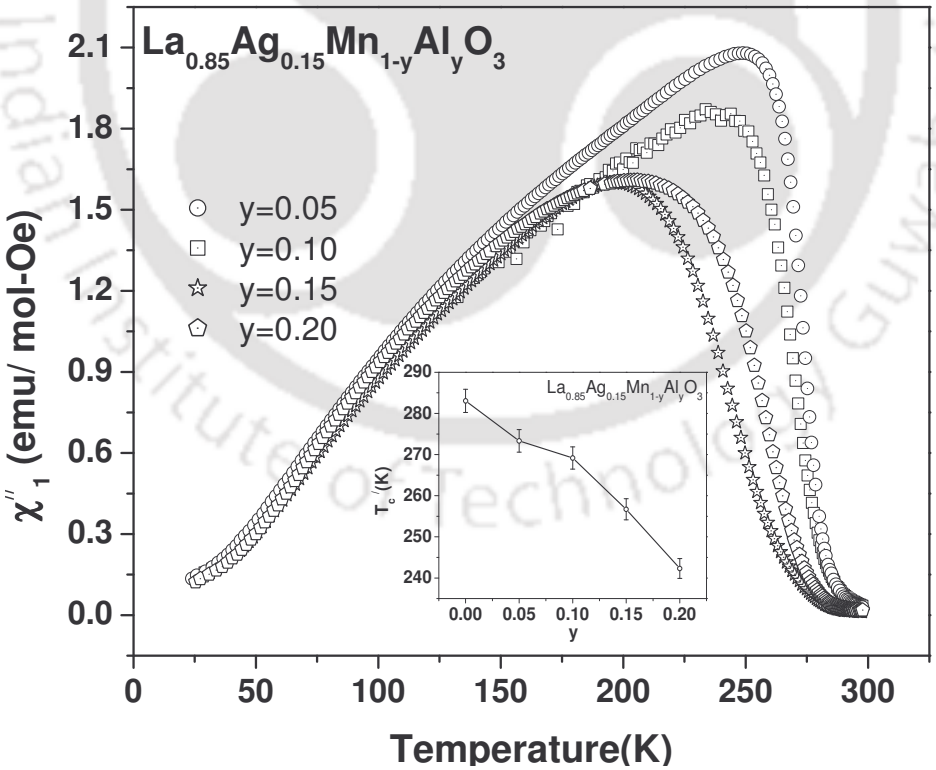

Figure 3.56: Temperature variation of out-phase ac susceptibility (χ_1'') of samples y =0.05, 0.10, 0.15 and 0.20. Inset shows variation of FM T_c with Al concentration.

3.3.4. Electrical Resistivity and Magneto-Resistivity

Plots of temperature versus electrical resistivity (ρ) of $La_{0.85}Ag_{0.15}Mn_{1-y}Al_yO_3$ are shown in Figure 3.57 for y = 0.05, 0.10, 0.15 and 0.20. All the Al doped samples exhibit metal-insulator transition. The metal insulator transition temperature (T_{MI}) varies from 285 to 213K and these values are tabulated in Table 3.19. One can find that the T_{MI} value decreases with Al concentration. It could be due to the dilution of ferromagnetic interaction by random distribution of Al^{3+} in Mn-O-Mn network.

Temperature variation of electrical resistivity measured at 1T is shown in Figure 3.57 as squares. The reduction of resistivity with the applied field has been observed and, hence a negative magneto-resistivity. The T_{MI} value shifts towards higher temperature in the presence of magnetic field, which is a common feature in mixed valent manganites.

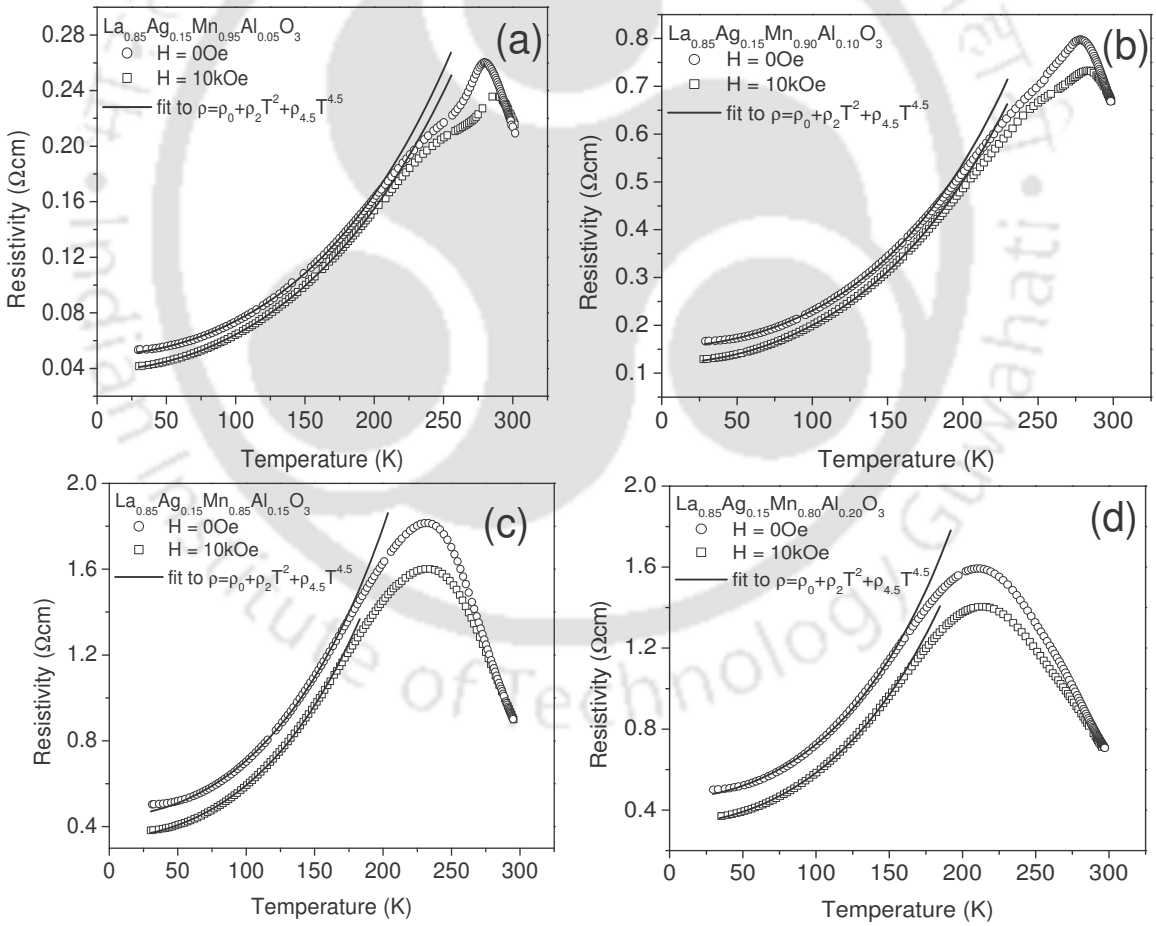

Figure 3.57: Temperature variation of electrical resistivity of y = 0.05, 0.10, 0.15 and 0.20 samples. The circles represent the zero field data and squares represent the 10kOe field data. Solid lines are fit to $\rho = \rho_o + \rho_2 T^2 + \rho_{4.5} T^{4.5}$.

The temperature variation of negative magneto-resistivity (-MR% = -$\Delta\rho/\rho_0$) is shown in Figure 3.58 for y = 0.05, 0.10, 0.15 and 0.20. A peak in the vicinity of T_c has been observed. The –MR% peak value is tabulated in Table-3.19. One can find from Figure 3.58, the magneto-resistivity increases with the decrease of temperature. Such behaviour has been observed in Ag doped $La_{1-x}Ag_xMnO_3$ samples [20]. The magneto-resistivity at low temperature is found to increase with the Al concentration.

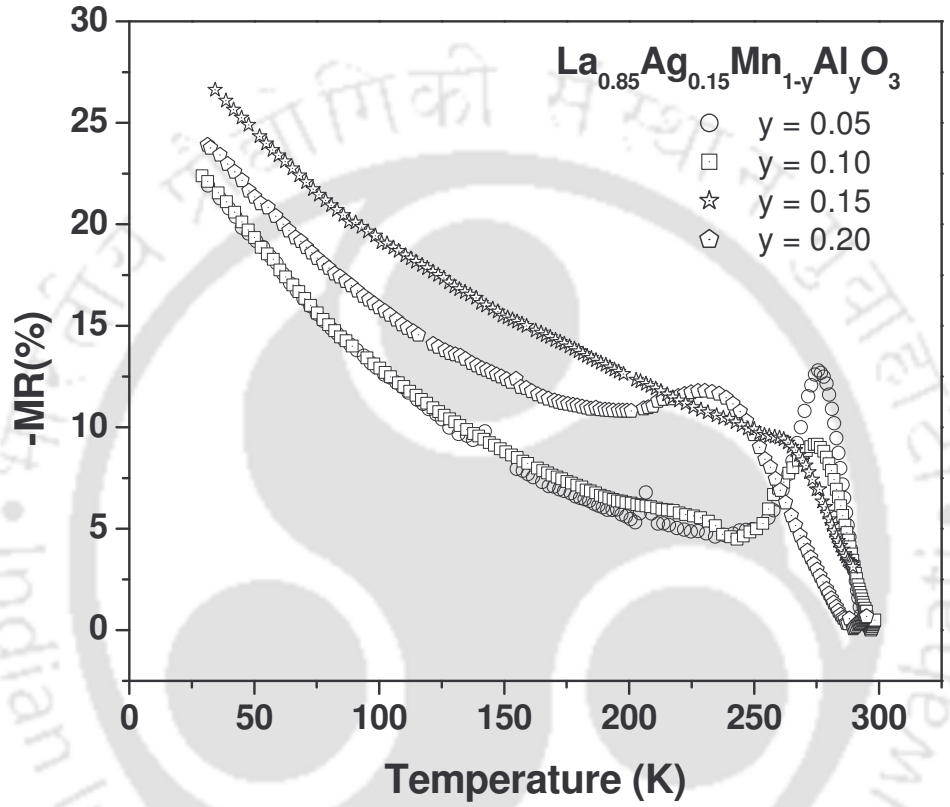

Figure 3.58: Temperature variation of negative magneto-resistivity for the sample y = 0.05, 0.10, 0.15 and 0.20.

We have fitted the resistivity data, in the metallic region using the empirical relation, [91]

$$\rho = \rho_o + \rho_2 T^2 + \rho_{4.5} T^{4.5} \quad \text{---------- (3.16)}$$

where, ρ_0 is the temperature-independent residual resistivity due to scattering by impurities, defects, grain boundaries, and domain walls. The second term with the coefficient ρ_2 is ascribed to the electron-electron [285] or single magnon [85] scattering and the third term with the coefficient $\rho_{4.5}$ corresponds to the electron magnon scattering [92]. The fitted data are shown as solid line in Figure 3.57 for the samples y = 0.05, 0.10, 0.15 and 0.20. The fitted

parameters ρ_0, ρ_2, and $\rho_{4.5}$ are tabulated in Table 3.19. The values are comparable to those reported for mixed valent manganites [20]. We have found that the conduction mechanism remains same with the Al doping and in the presence of applied field. The values of ρ_0 are found to be small compared to the case of zero field resistivity (Table 3.19) and this is mainly due to growth of domain size in the presence of magnetic field. The ρ_2 value increases with the magnetic field and it could be due to increase of the electron-electron scattering. The $\rho_{4.5}$ values decrease with the magnetic field and it could be due to reduction in numbers of magnons.

Table-3.19: Parameters obtained from electrical resistivity measurements and analysis. ρ_0 is the temperature-independent residual resistivity. ρ_2 and $\rho_{4.5}$ are respectively the coefficients of electron-electron and electron magnon scatterings.

Sample	y = 0.05		y = 0.10		y = 0.15		y = 0.20	
	H=0 Oe	H=10kOe	H=0Oe	H=10kOe	H=0Oe	H=10kOe	H=0Oe	H=10kOe
T_{MI} (K)	280	287	278	284	232	237	213	215
$\rho_0(\Omega cm)$	0.049 (02)	0.038 (002)	0.155 (02)	0.121 (006)	0.459 (07)	0.333 (004)	0.449 (08)	0.350 (04)
$\rho_2(10^{-6}\ \Omega cmK^{-2})$	2.359	2.509	7.113	7.605	24.445	23.524	24.236	22.591
$\rho_{4.5}(10^{-12}\ \Omega cmK^{-4.5})$	0.940	0.708	4.354	3.359	4.354	3.359	1.662	1.724
$-MR(\%)_{TMI}$	13		9		12		9	
$-MR(\%)_{30K}$	22		22		24		27	

3.4. Summary and Conclusions

In this chapter, effect of Mn site doping in $(La_{0.85}Ag_{0.15})MnO_3$ by using transition elements (Co, Cr) and nonmagnetic element (Al) has been discussed.

$(La_{0.85}Ag_{0.15})Mn_{1-y}Co_yO_3$ compounds were prepared in single phase form upto y=0.50. Structural transition from rhombohedral to orthorhombic has been observed with increasing doping. Both Cr and Al doped samples $(La_{0.85}Ag_{0.15})\ Mn_{1-y}M_yO_3$ (M= Cr, Al) could be prepared in single phase form upto 20% of doping. They are found to crystallize in rhombohedral structure.

In Co doping lattice parameters are found to increase with doping upto y=0.20, then it decreases. It is explained on the basis of some of Mn^{3+} ions being replaced by Co^{2+} ions having larger ionic size. On the other hand, the decrease in lattice parameters for y> 0.20 could be due to the transition of Co ions from high spin state to low spin state.

In Cr and Al doped samples, the lattice parameters are found to decrease with doping as a result of Cr^{3+} and Al^{3+} ions replacing some of Mn^{3+} ions. The ionic radii of Cr^{3+} and Al^{3+} are smaller than that of Mn^{3+} ions.

In Co doped samples, the FM T_C is found to decrease from 292 K for y=0 to 198 K for y=0.20 and the T_C was found to increase for further increase in doping. The variation of T_C, maximum magnetization irreversibility, remnant magnetization and coercive field as a function of doping concentration show two distinct behaviours; one for y≤ 0.2 and other for y>0.2. They are explained on the basis of possible Co-O-Co networks for y>0.20. The measured magnetization is explained on the basis of FM interactions in Mn^{3+}-O-Mn^{4+}, Co^{2+}-O-Mn^{4+}, Co^{3+}-O-Mn^{4+} networks and simultaneous AFM interactions in Mn^{4+}-O-Mn^{4+}, Co^{2+}-O-Mn^{3+} networks for the composition y=0.05 to 0.20. For y≥0.30, in addition to the above magnetic interactions, there is a probability of FM interaction in Co^{2+}-O-Co^{3+} and Co^{3+}-O-Co^{4+} networks, which is expected to play a role for increase in FM T_C for y≥0.30.

In Cr doped samples, the FM T_C is found to decrease to 220 K for y=0.20 and the rate of decrease in T_C is quite small compared to Co-doped samples. The experimental effective paramagnetic moment, μ_{eff} is comparable to the theoretical moment, μ_{th} which was determined by assuming that Cr^{3+} ions replace the Mn^{3+} ions. The measured saturation magnetization was explained by assuming that the doped Cr^{3+} ions exhibit antiferromagnetic interactions in Mn^{3+} and Mn^{4+} ions and there is also antiferromagnetic interaction in Mn^{4+}-O-Mn^{4+} networks. The above process compete with double exchange FM interaction in Mn^{3+}-O-Mn^{4+} networks.

In Al doped samples, the decrease in T_C with doping is found to be quite small compared to the doping of magnetic elements. The T_C was found to decrease from 292 K for y=0 to 273 K for y=0.20. The measured magnetization could be explained by simply assuming that the doped Al ions play a role of magnetic dilution, without contributing any other competing magnetic interaction.

The field variations of magnetization of all the above three series could be analysed by fitting to Brillouin function. From the above analysis, the effective spin contribution to FM interaction has been estimated.

Temperature variations of ac susceptibility have been measured in all the above three series. They basically reflect the similar type of magnetic transitions observed from their dc counter part. For Co and Cr doped samples, detailed frequency variation of fundamental susceptibility and variation of third harmonic susceptibility have been measured. From the analysis, it was found that the Co doped samples in the composition range y=0.10 to 0.20 and Cr doped samples in the composition range y=0.05 to 0.20 exhibit reentrant spin glass (RSG) like behaviour with typical spin flipping time τ_0 in the order of 10^{-6} s and the critical exponent $z\upsilon$= 0.8 to 1.20. The above values are comparable to RSG observed in other manganites, however τ_0 is quite large compared to conventional spin glass system. They highlight the absence of atomic scale spin glass behaviour in the present manganite systems.

Metal-Insulator transitions and colossal magneto-resistivity have been observed upto 10% of Co doping. All other samples show semiconducting behaviour. All Cr doped samples show semiconducting behaviour along with colossal magneto-resistivity. However, metal-insulator transition is found to hold on for all the Al doped samples. The electrical conductivity in the metallic region for Al doped samples could be explained by electron-magnon scattering. The magneto-resistivity at low temperature is found to increase with the Al concentration. The order of magnetoresistivity in the vicinity of FM T_C was found to be 20%, 25% and 15% for the Co, Cr and Al doped series respectively.

Chapter 4: Cu Doped La-Mn-O Series

As it has been discussed in Chapter1 that the doping at Mn site in mixed valent manganites by other transitions elements (T = Ti, Cr, Fe, Co, Ni, Cu, Ru etc.) or non-magnetic impurities like Al give rise to changes in Mn^{3+}/Mn^{4+} ratio and as a result change in their magnetic and transport properties. In the present chapter, Cu doped La-Mn-O series i.e. $LaMn_{1-y}Cu_yO_3$ compounds have been studied. The doping of Cu in place of Mn creates Mn^{3+}/Mn^{4+} pairs, which take part in ferromagnetic double exchange interaction. It would be also interesting to study the magnetic interaction between Mn and Cu ions. I have carried out dc magnetization and linear & non linear ac susceptibility measurements and analysis of $LaMn_{1-y}Cu_yO_3$ compounds for y = 0.05 to 0.30.

4.1: Sample Preparation and Characterization

The preparation and basic characterization of $LaMn_{1-y}Cu_yO_3$ materials are reported by Kar and Ravi [142]. The same materials have been taken up for detailed study of their magnetic properties. The preparation details are briefly reproduced as below.

The $LaMn_{1-y}Cu_yO_3$ compounds were prepared for y = 0.05, 0.10, 0.15, 0.20 and 0.30 by solid state route. Stoichiometric ratio of La_2O_3, $(CH_3COO)_2Cu.H_2O$ and $C_4H_6MnO_4.4H_2O$ were weighed and mixed thoroughly under acetone. The mixture was presintered at 800^0C for 24 h with intermediate grindings at an interval of 12 h. The sintering in pellet form was carried out at 900^0C, 1000^0C, 1050^0C, 1100^0C, 1150^0C and 1200^0C for 12 h duration in each temperature. The pellets were crushed into fine homogeneous powder and repelletized after each annealing. The final sintering has been carried out at 1200^0C for over 50 h. All the above heat treatments were carried out in air and finally the samples were furnace cooled.

XRD patterns of $LaMn_{1-y}Cu_yO_3$ compounds with y = 0.05, 0.10, 0.15, 0.20 and 0.30 are shown in Figure 4.1. The samples are reported to be in single phase form with $R\bar{3}c$ space group for y=0.05 sample and *Pbnm* space group for $0.10 \leq y \leq 0.30$ samples [142]. The lattice parameters are reproduced in Table 4.1. No appreciable variations in lattice parameters and unit cell volume have been observed. It is not surprising because the ionic size of Cu is comparable to that of Mn. The crystallite size has been calculated using the Scherrer's formula using equation 3.1 and these values are listed in Table 4.1. No appreciable change in crystallite size is observed

even for higher level of doping and this suggests that the crystal is quite stable for wide doping range due to comparable ionic size of Cu & Mn.

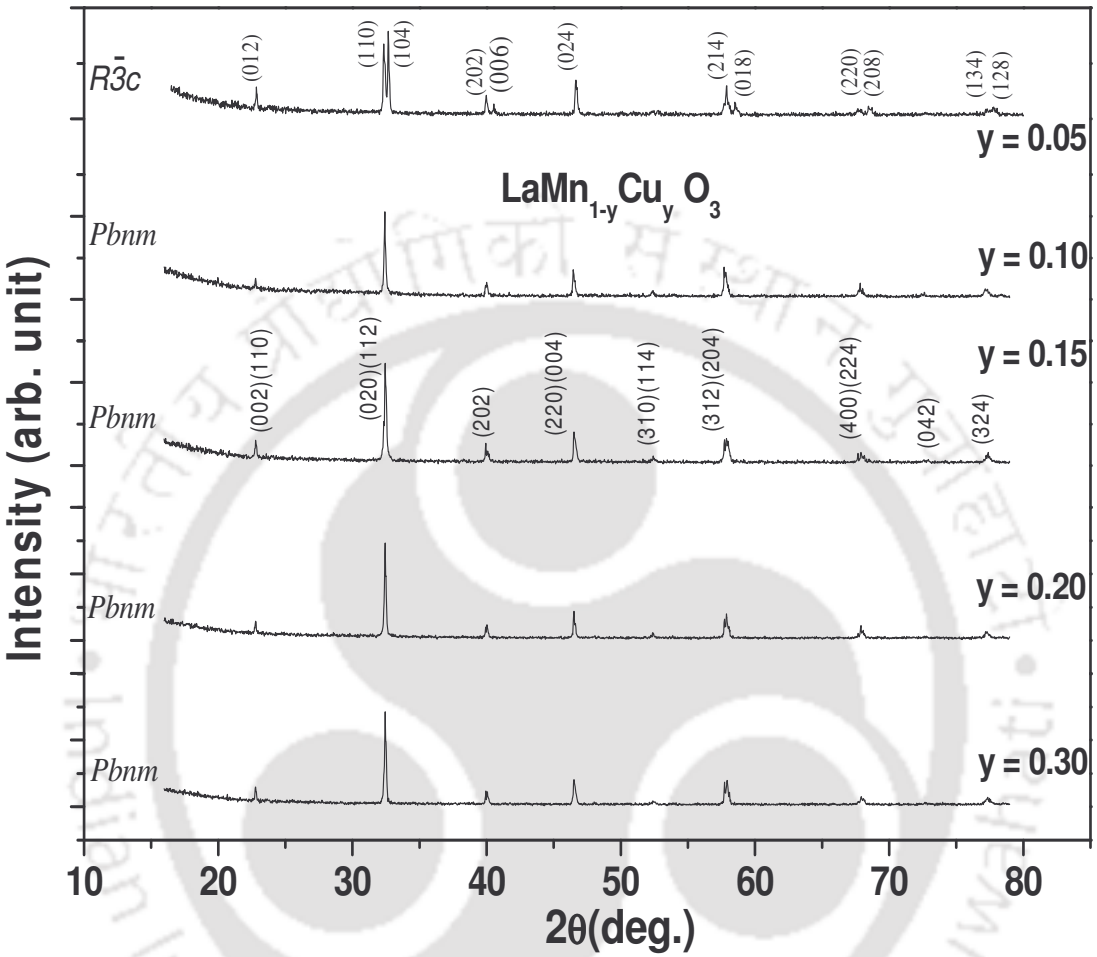

Figure 4.1: XRD patterns of $LaMn_{1-y}Cu_yO_3$ for y = 0.05, 0.10, 0.15, 0.20 and 0.30 samples.

The average valency of Mn ions determined from chemical titration is tabulated in Table 4.1. We can see that Mn valency increases with doping, thereby confirming the generation of Mn^{3+}/Mn^{4+} pairs.

Table 4.1: Parameters obtained from the XRD analysis of the samples $LaMn_{1-y}Cu_yO_3$ (y = 0.05, 0.10, 0.15, 0.20 and 0.30). S_C is the average crystallite size obtained from the line broadening of the XRD pattern.

Samples → / Parameters ↓	y = 0.05	y = 0.10	y = 0.15	y = 0.20	y = 0.30
Space Group	$R\bar{3}c$	*Pbnm*	*Pbnm*	*Pbnm*	*Pbnm*
a (Å)	5.537	5.543	5.543	5.542	5.545
b (Å)	5.537	5.519	5.512	5.518	5.517
c (Å)	13.370	7.835	7.815	7.812	7.810
Volume ($Å^3$)	355.0	239.7	238.7	238.9	238.9
S_C (nm)	44.0	38.0	37.0	37.0	41.0
Mn Valency	3.12	3.14	3.18	3.29	3.34

The morphology of all the samples has been studied by scanning electron microscope. The typical SEM micrograph for y= 0.10 sample is shown in Figures 4.2. All the samples show nearly spherical shape particles and the morphology of the samples is found to be uniform. Not much variation in the shape and size of the grains are observed. It suggests the mono-phasic nature of the sample. Another important point to be noted is the grain size. The grain size is found to be very small. The average particle size is found to be in the order of 1-2 μm.

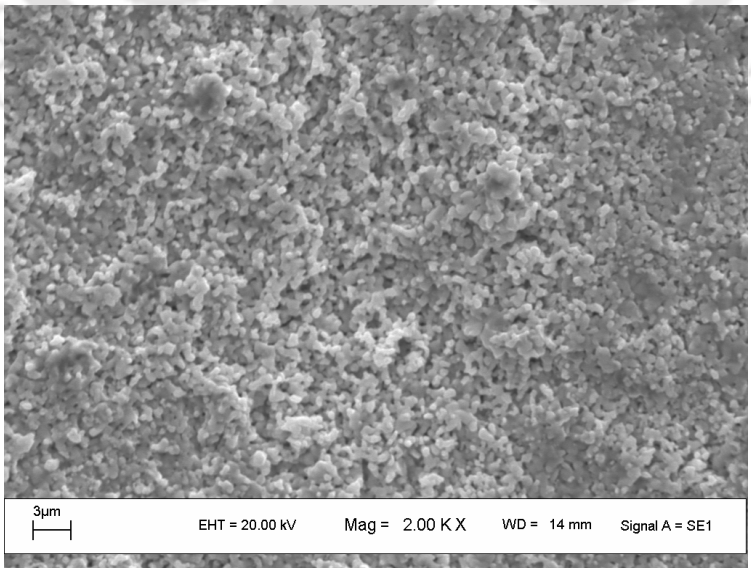

Figure 4.2: SEM photograph (magnification 2000) of the y=0.10 sample.

The elemental analysis has been carried out by recording energy dispersive spectrum (EDS) for all the compounds to have the idea about elements present in prepared compounds. Typical EDS spectrum for y = 0.10 sample is shown in Figure 4.3. We can clearly see that all the elements are present. Further, the chemical compositions determined from EDS analysis is found to be comparable to the nominal starting compositions. The cationic ratio determined from EDS analysis is given in Table 4.2.

Table 4.2: The cationic ratio determined from EDS analysis for $LaMn_{1-y}Cu_yO_3$ compounds.

Sample	Calculated Cationic Ratio		
	La	Mn	Cu
y= 0.05	1.01	0.94	0.05
y= 0.10	1.01	0.89	0.10
y= 0.15	1.02	0.84	0.14
y= 0.20	1.01	0.80	0.19
y= 0.30	0.99	0.71	0.30

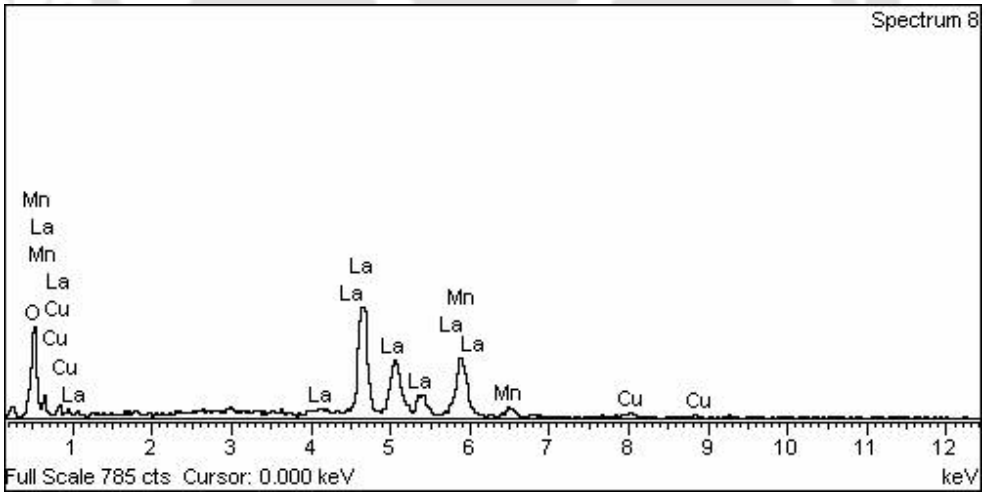

Figure 4.3: Typical SEM-EDS spectrum for y=0.10 sample.

4.2: Study of dc magnetization

The temperature variations of zero field cooled (ZFC) magnetization curves under an applied field of 2 mT, are shown in Figure 4.4 for all the samples. All the samples show paramagnetic (PM) to ferromagnetic (FM) transition. The complete transition could not be seen for y= 0.30 sample because of low temperature limitation in the present experimental set up. The magnetic moments for y=0.05 sample from temperature variation of ZFC magnetization was found to be almost constant below the transition temperature and it indicates the long range ferromagnetic ordering nature of sample. The magnitude of magnetization is found to increase upto 15% of Cu doping and, it was found to decrease for higher level of doping. The ferromagnetic transition temperature T_C was determined from dM/dT versus temperature plot. The FM T_c was found to decrease with doping and it is given in Table 4.3. Thus the parent compound with Cu doping, $LaMn_{1-y}Cu_yO_3$ for y = 0.05 to 0.30 exhibit PM-FM transitions. It reveals from the chemical titration that, Cu doping oxidizes some of Mn^{3+} ions into Mn^{4+} states, thereby generating the Mn^{3+}/Mn^{4+} mixture. The FM transition could be understood due to the double exchange interaction in Mn^{3+}-O^{2-}-Mn^{4+} networks.

The temperature variations of magnetization for y=0.05, 0.10 & 0.15 samples in zero field cooled (ZFC) and field cooled (FC) conditions are shown in Figure 4.5. There is no appreciable change in ZFC & FC data for y=0.05 sample. However, there is a bifurcation between ZFC and FC curves for y=0.10 & 0.15 samples in a narrow temperature region i.e. 80 to 100K.

The dc susceptibility χ_{dc} in the paramagnetic region was analysed by using Curie-Weiss law (equation 1.10). The Curie-temperature (θ_C) for all the five samples is found to be positive and indicate the FM interaction. Thus the Cu doping gives rise to generation of Mn^{3+}/Mn^{4+} mixture and the Zener double exchange FM interaction. Typical plots of $1/\chi_{dc}$ versus temperature for y=0.05, 0.10 and 0.15 samples are shown in Figure 4.6 along with Curie-Weiss law fitting. The FM transition temperature obtained from M versus T curve and θ_C are given in Table 4.3. The difference between T_C and θ_C is mainly due to the observed broad magnetic transition. The value of effective paramagnetic moment was found to decrease with Cu doping and it is as per theoretical expectation. The effective paramagnetic moment, μ_{eff} determined from the Curie-constant is shown in Table 4.3 and they are found to decrease with increase in Cu doping. The

magnitude of μ_{eff} is found to be larger than the expected theoretical value and one of the reasons could be presence of FM clusters even above T_c.

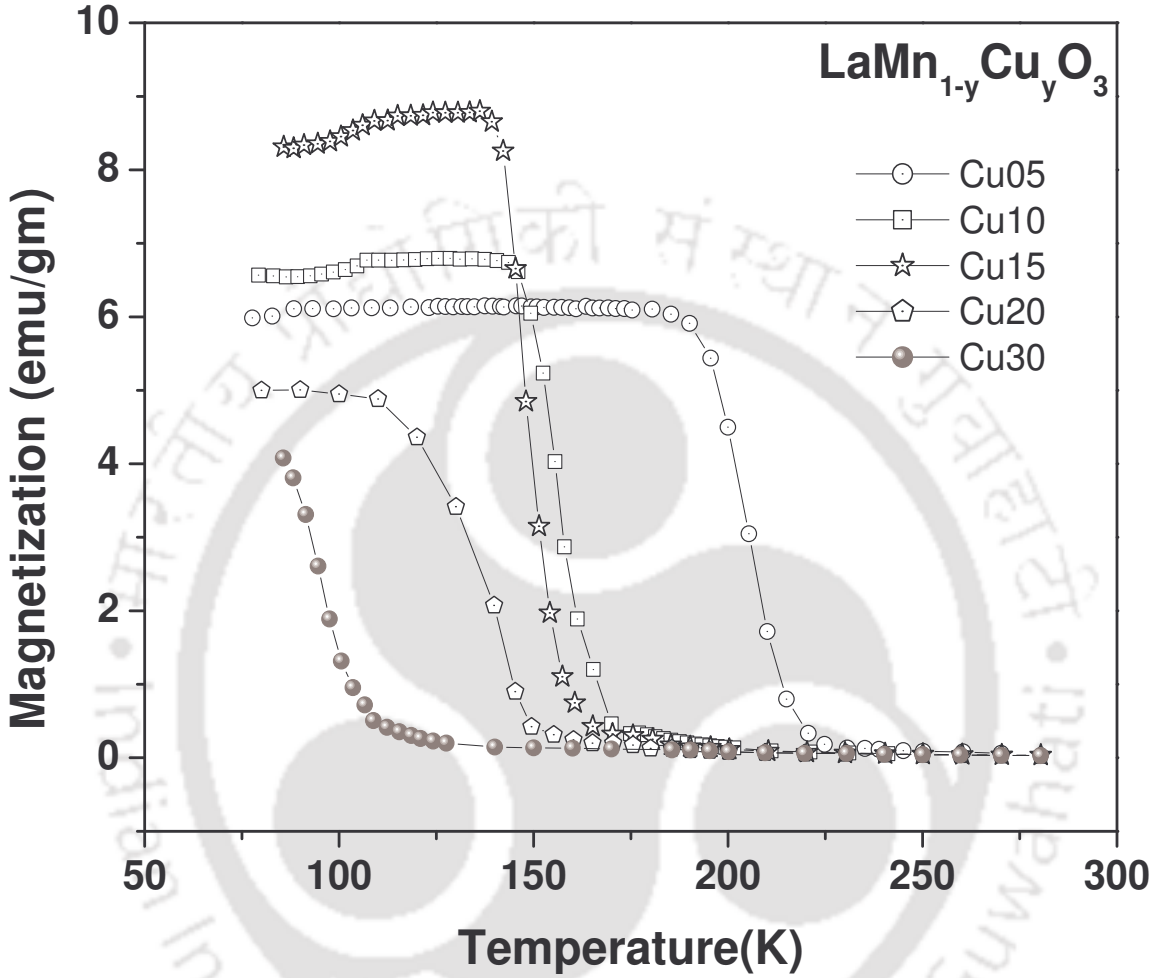

Figure 4.4: The temperature variation of zero field cooled (ZFC) magnetization curves for y=0.05, 0.10, 0.15, 0.20 & 0.30 samples.

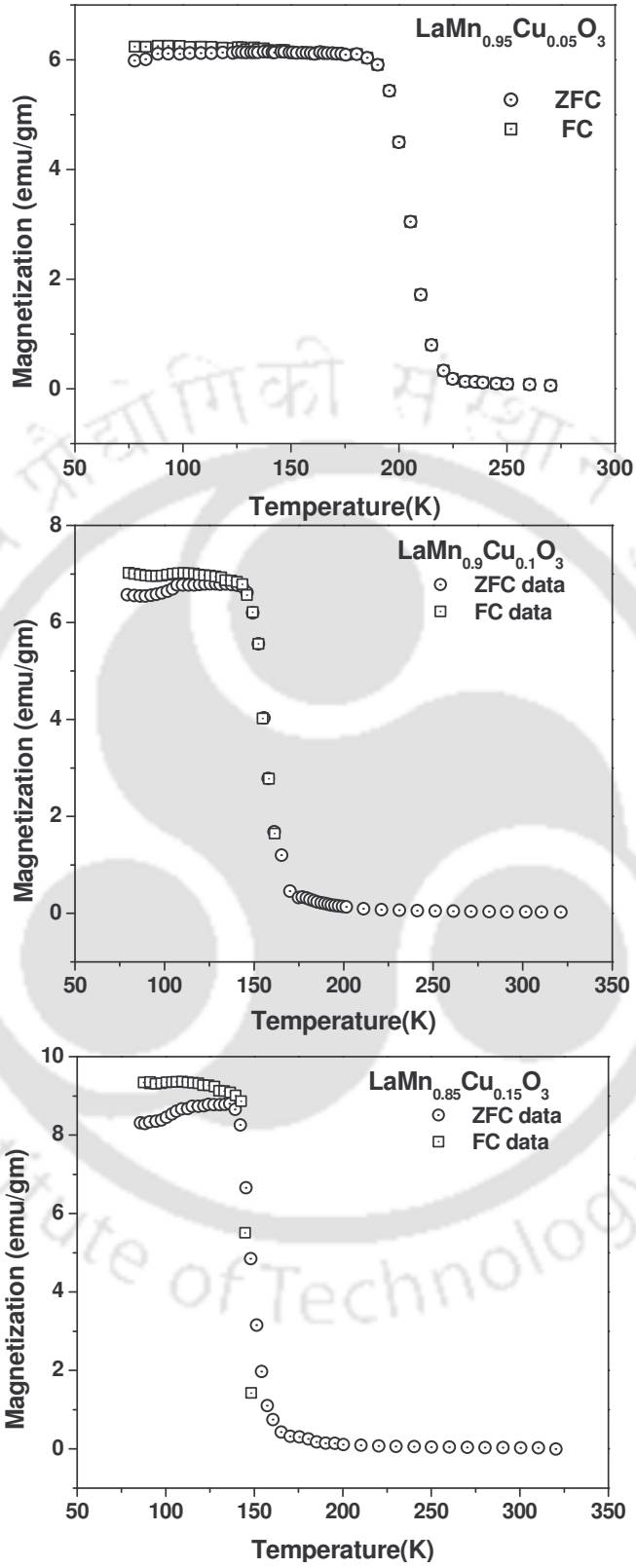

Figure 4.5: The temperature variation of (ZFC) zero field cooled (Circles) and (FC) field cooled (square) magnetization curves for y=0.05, 0.10 & 0.15 samples.

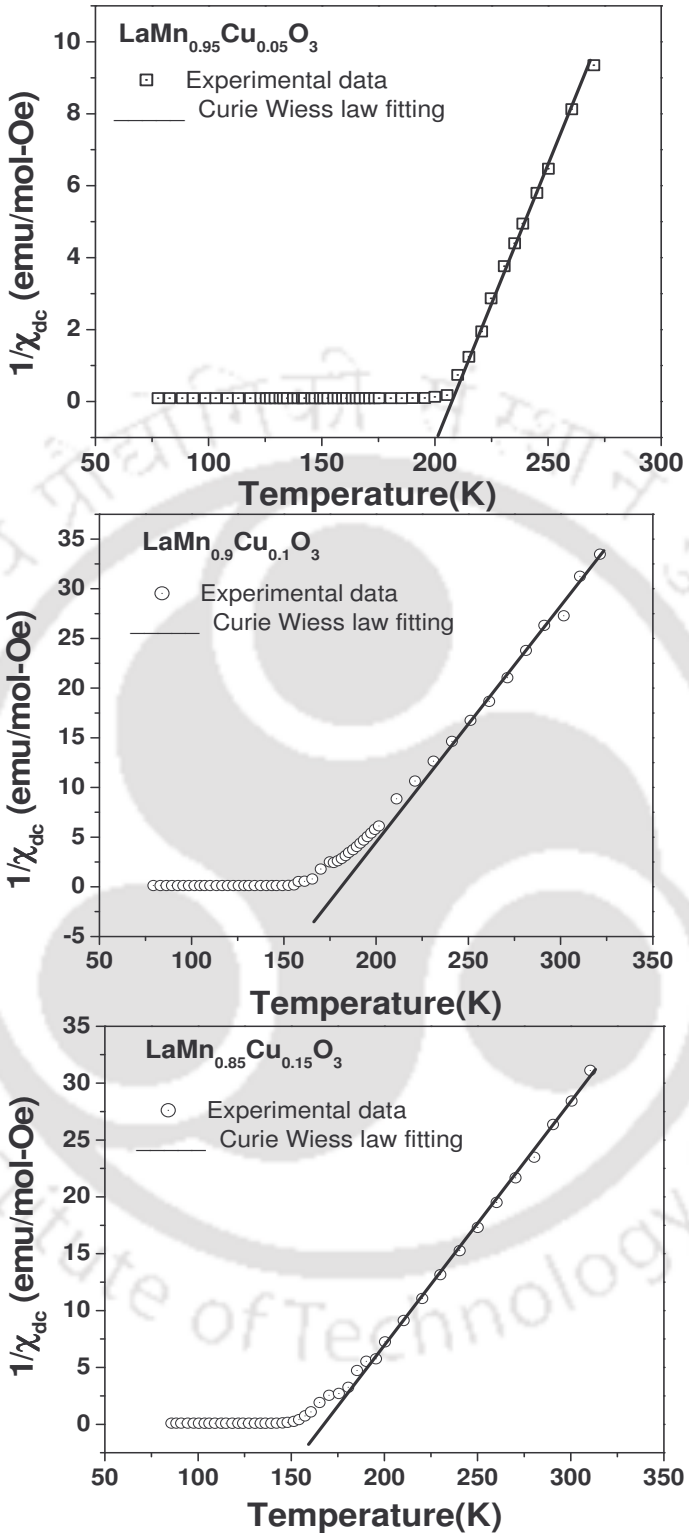

Figure 4.6: $1/\chi_{dc}$ versus temperature for the samples (a) y=0.05, (b) y=0.10 and (c) y=0.15. Solid lines represent fit to the Curie-Weiss law.

Table 4.3: Parameters obtained from magnetization measurement of $LaMn_{1-y}Cu_yO_3$. T_C is ferromagnetic transition temperature. θ_C (Curie temperature), C (Curie constant), μ_{eff} (μ_B) have been found from inverse dc susceptibility fitting.

Sample/Parameters	**y= 0.05**	**y= 0.10**	**y= 0.15**	**y= 0.20**	**y= 0.30**
T_c(K)	205.0	156.0	146.0	140	94.0
θ_C (K)	205.0	174.7	168.6	154.0	98.0
C (emu-K/mol-Oe)	7.04	4.46	4.64	3.49	3.00
μ_{eff} (μ_B)	7.50	5.97	6.09	5.28	4.89

The magnetization loops measured at 78 K for B= ± 2 T are shown in Figure 4.7. The saturation magnetization (M_S) was found to decrease with increase in Cu doping. For y=0.20 & 0.30 samples, even though there is a ferromagnetic contribution, the magnetization is found to increase linearly with increase in magnetic field and it indicates the presence of considerable AFM/paramagnetic contribution. To understand the nature of magnetic interaction, the M versus H data have been fitted to the Brillouin function model (equations 3.3 & 3.4) by taking into account the ferromagnetic interaction to determine the effective spin contribution towards FM interaction. The fitting for y=0.20 & 0.30 samples have been carried out by subtracting the linear contribution. The magnetization fit for all samples are shown in Figure 4.8. We can see that the fitted data closely follow the experimental data. The fitted values of S_{eff} and M_S are given in Table 4.4. The effective spin contribution towards FM interaction was found to be maximum for the sample y= 0.05. It is found to decrease with Cu doping. This is in consistence with ferromagnetic transition temperature variation.

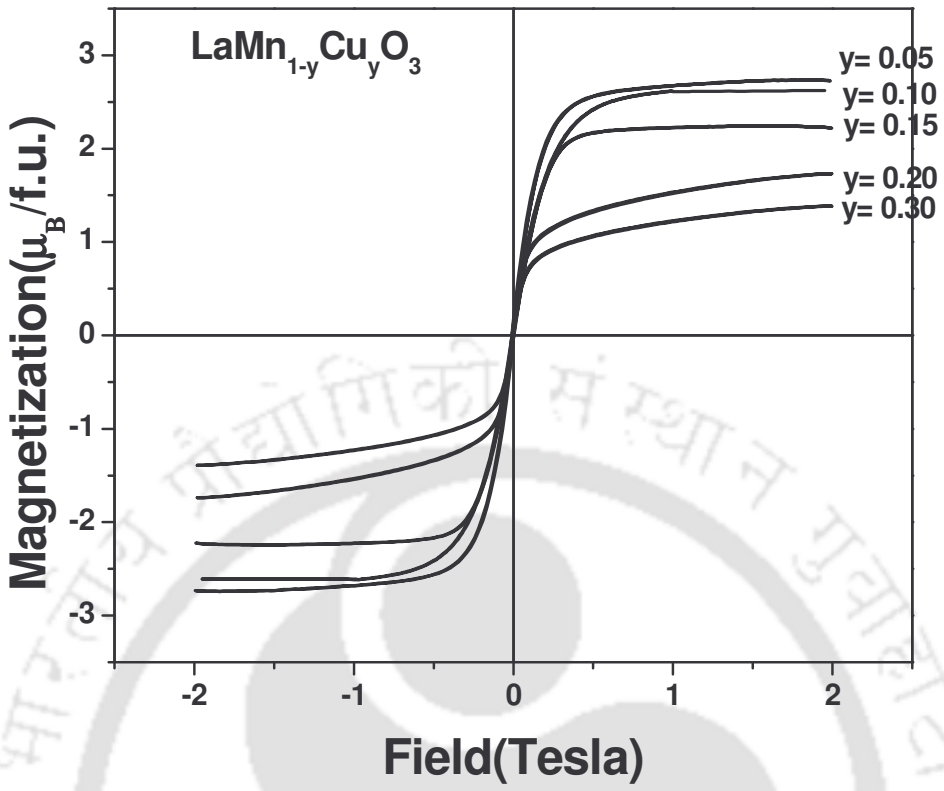

Figure 4.7: Magnetization versus magnetic field plots of the samples $LaMn_{1-y}Cu_yO_3$ for y=0.05 to 0.30.

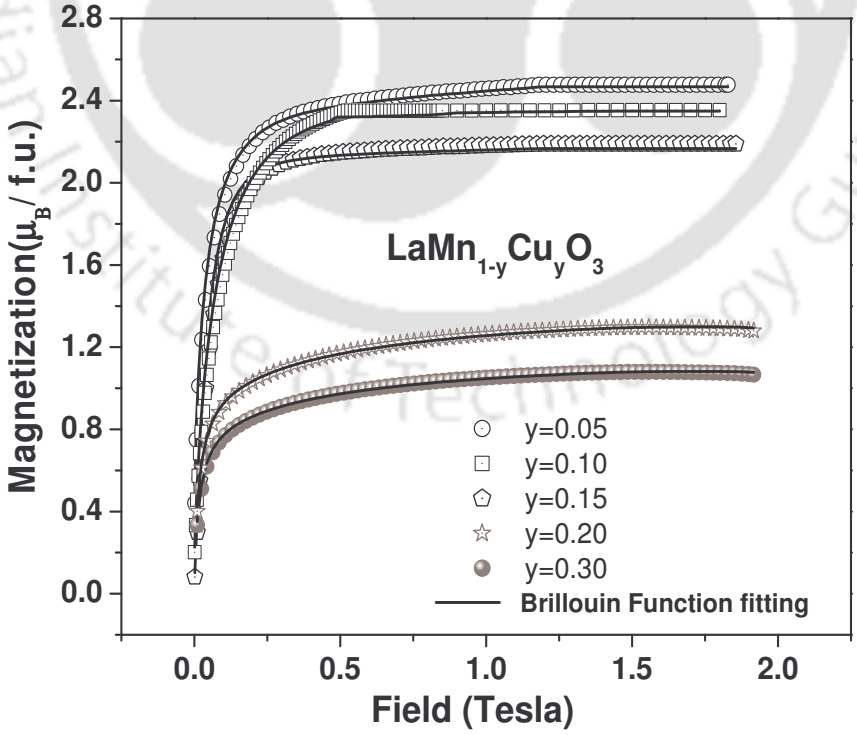

Figure 4.8: Brillouin function fit to magnetization data for y=0.05 to 0.30 samples.

Table 4.4: Parameters obtained from Brillouin function fitting to magnetization data. S_{eff} is the effective spin contribution towards FM interaction. M_S is the experimental saturation magnetization.

Sample/ Parameters	**y= 0.05**	**y= 0.10**	**y= 0.15**	**y= 0.20**	**y= 0.30**
S_{eff}	1.15	1.05	1.01	0.85	0.82
r m s (%)	2.78	2.51	1.12	1.23	0.65
M_S (μ_B/f.u.)	2.70	2.63	2.22	1.40	1.22

Thus the study of dc magnetization depicts that all the material exhibit PM-FM transition. The bifurcation of ZFC and FC curves for y>0.05 samples, manifest the presence of competing magnetic interaction such as AFM, in higher doped materials. The M-H data shows that there is decrease in magnitude of magnetization with increase in doping and it indicates the presence of considerable AFM/paramagnetic contribution. Further the fitting of M-H data with Brillouin function models gives the evidence for decrease of effective ferromagnetic spin contribution because of the introduction of mixed competing interaction.

4.3. ac Susceptibility Study

To further explore the magnetic properties of these samples, temperature variation of ac susceptibility was measured for all the samples at an ac field amplitude of 6 Oe with a frequency of 333 Hz. Figure 4.9 shows the temperature variation of χ'_1 for the sample y = 0.05. It exhibits paramagnetic to ferromagnetic transition with onset temperature at around 210K. Baring the minor anomaly at around 98 K, no appreciable low temperature secondary transition is observed. χ''_1 vs. T exhibits maximum loss in the vicinity of ferromagnetic transition.

Similarly, χ_1' and χ_1'' versus T plots for y = 0.10, 0.15 and 0.20 samples are shown in Figure 4.10. We can see that these materials also exhibit PM to FM transition like y=0.05 sample. However the FM transition temperature decreases with increase in Cu doping. Unlike y = 0.05 sample, χ_1' versus T of these samples exhibit sharp fall in susceptibility below the FM

transition. Such sharp falls cannot be explained using conventional magnetic anisotropy or the loss of long range FM ordering. They are mainly due to the presence of competing AFM interaction at low temperature, i.e. below the T_c.

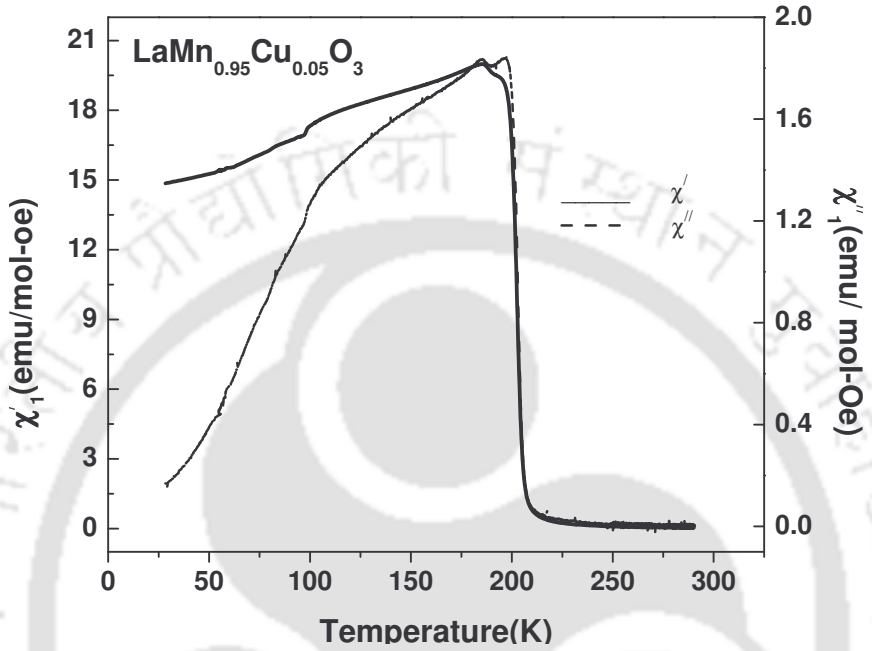

Figure 4.9: Temperature variation of in phase ($\chi_1^{/}$) and out of phase ($\chi_1^{//}$) ac susceptibility of sample $LaMn_{0.95}Cu_{0.05}O_3$.

The $\chi_1^{//}$ versus T plots show very interesting features. Each sample shows double peaks just below FM saturation (completion of FM transition). They are in the vicinity of sharp falls observed in $\chi_1^{/}$ versus T plots. For y = 0.20 sample, even though it appears that it is a single peak, careful observation reveals that it is a overlap of two peaks. The $\chi_1^{/}$ versus T plots of y = 0.30 sample (not shown) exhibits FM transition followed by strong competing AFM interaction.

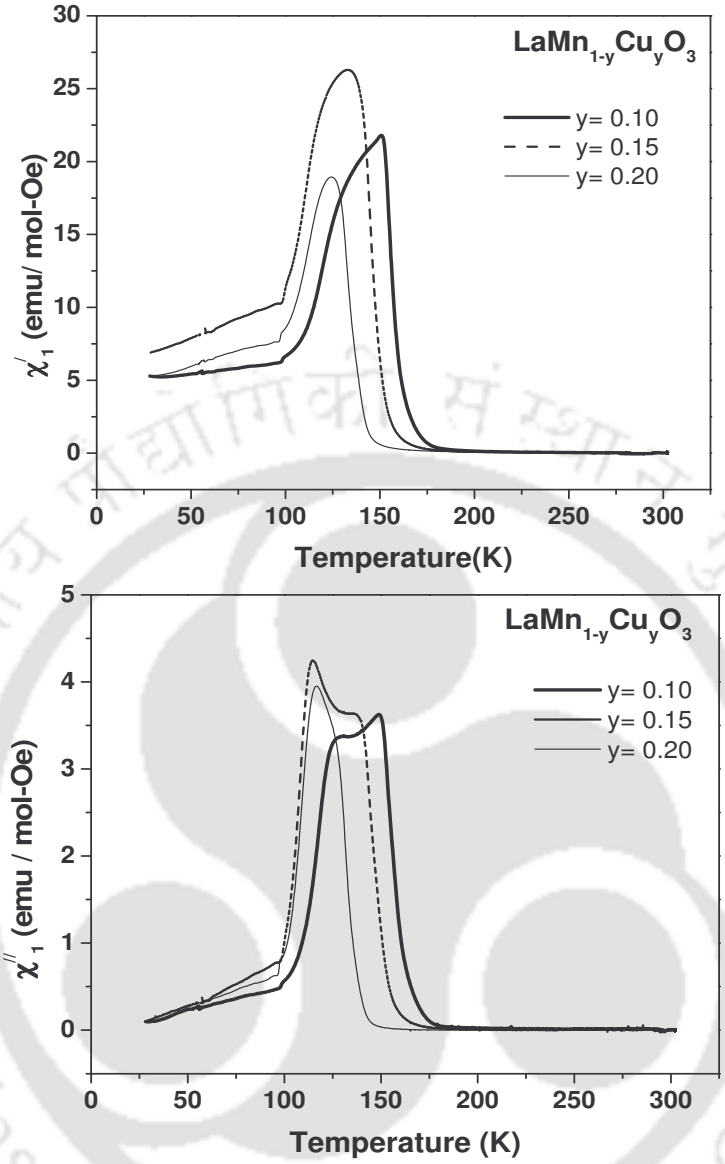

Figure 4.10: Temperature variation of χ_1' & χ_1'' ac susceptibility of samples $LaMn_{1-y}Cu_yO_3$ for y=0.10, 0.15 & 0.20.

To clearly understand the origin of low temperature peak observed in χ_1'' versus temperature plot**,** we have carried out the temperature variations of ac susceptibility at different frequencies such as, 233, 1133 and 3333Hz. Plots of χ''_1 versus T at different frequencies are shown in Figure 4.11 & Figure 4.12 for the samples y = 0.10 & 0.15 and y = 0.20 & 0.30 respectively. One can see that the low temperature peak increases and shifts towards high temperature side with the frequency as expected for a conventional spin glass system [41]. The low temperature peaks can be attributed to spin glass freezing temperature, T_f of reentrant spin

glass (RSG) state. The T_f values obtained for different samples at three different frequencies are given in Table 4.5. The competition between FM interaction between Mn^{3+}-O^{2-}-Mn^{4+} and competing random AFM interaction between Mn/Cu ions, results in freezing of spins in random direction and it is called as RSG state. The Cu doping in the present series plays the dual role of introducing double exchange ferromagnetic interaction by creating the mixture of Mn^{3+} and Mn^{4+} ions and introduction of AFM interaction between Cu & Mn ions, which is competing with FM interactions.

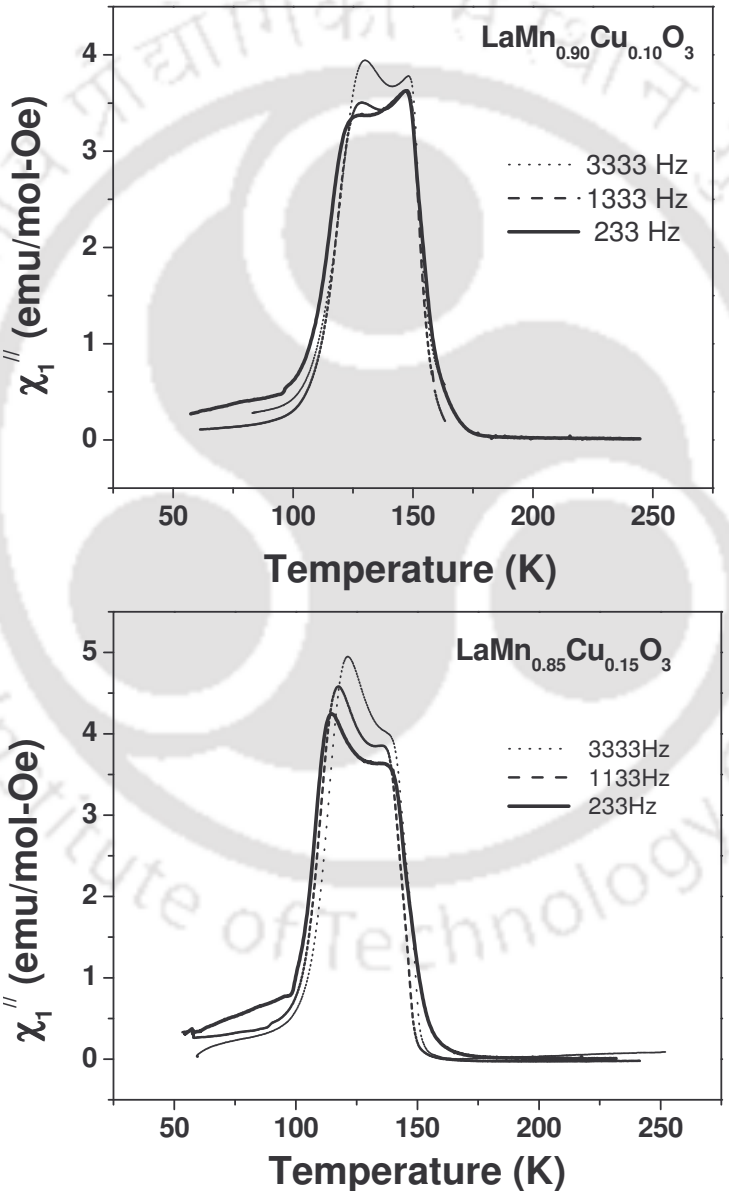

Figure 4.11: $\chi_1^{//}$ versus temperature (T) measured at frequencies f = 333 Hz, 1333 Hz & 3333 Hz for the samples (a) y=0.10 and (b) 0.15.

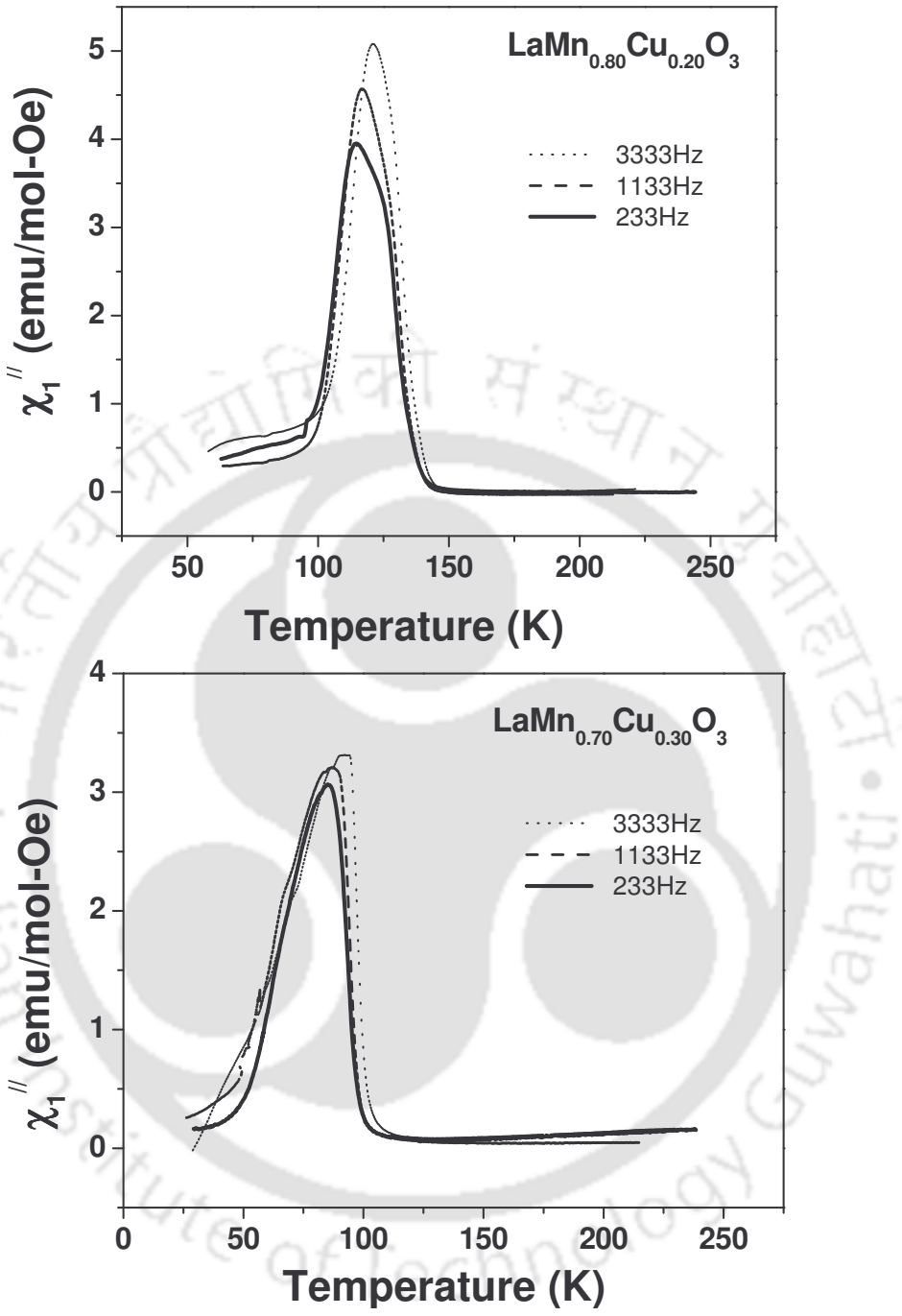

Figure 4.12: $\chi_1^{//}$ versus temperature (T) measured at frequencies f = 333 Hz, 1333 Hz & 3333 Hz for the samples (a) y=0.20 and (b) 0.30.

The frequency dependence of T_f can be analysed based on the power law relation (equation 3.5). The plots of T_f versus frequency are shown in Figure 4.13 for all the samples. We can see that, they exhibit linear behaviour. These data are fitted to the linear equation and the fitted data are shown as solid lines. The T_g values were obtained from fitted data and are tabulated in Table 4.5. Typical plots of $\ln(\tau)$ versus $\ln[(T_f-T_g)/T_g]$ are shown in Figure 4.14 for y = 0.15 & 0.30 samples. These data are fitted to power law by varying the parameters τ_0 & $z\nu$ and the fitted data are shown as solid lines. The τ_0 values are found to be in the order of 10^{-5}s as given in Table 4.5, which is much higher than the value observed in conventional spin glass system (10^{-13}s) [286].

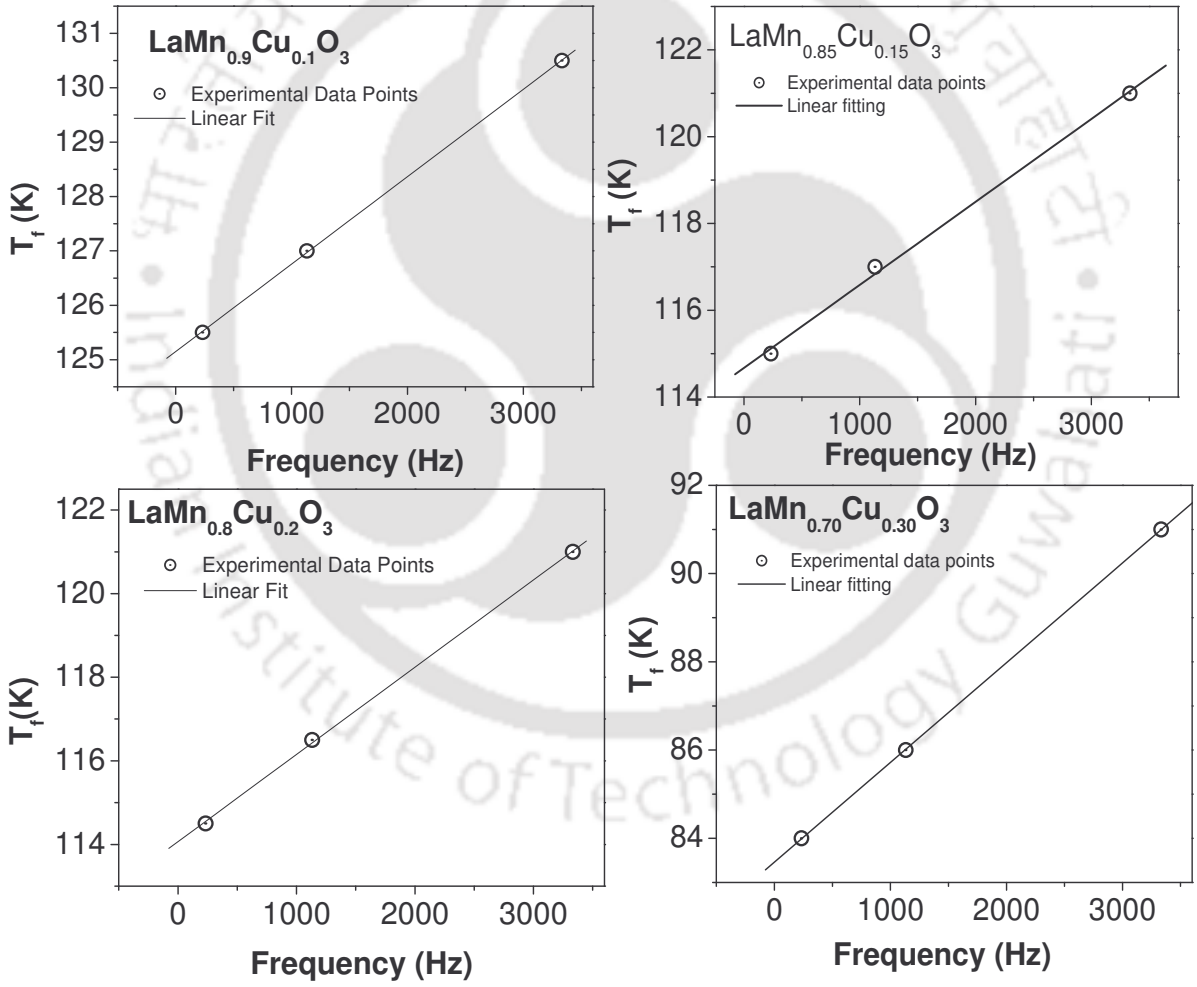

Figure 4.13: Plots of T_f versus frequency for the y=0.10, 0.15, 0.20 & 0.30 samples.

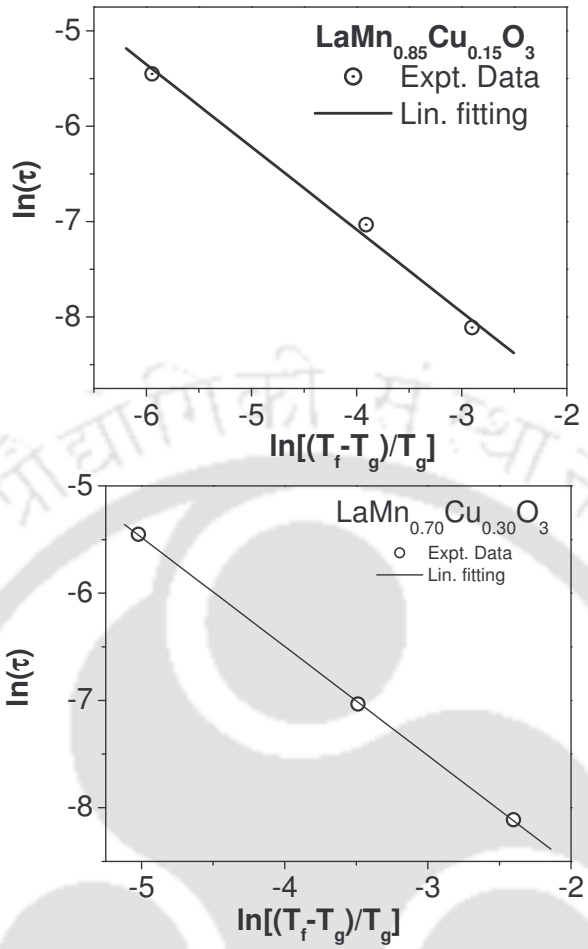

Figure 4.14: Plots ln(τ) versus ln[(T_f-T_g)/T_g] for the samples y= 0.15 & 0.30.

Table 4.5: Parameters obtained from the measurement and analysis of frequency variation of linear susceptibility. T_f and T_g are freezing and spin glass transition temperature respectively. τ_0 is the characteristic time constant and zν is the critical exponent.

Sample/ Parameter		y = 0.10	y = 0.15	y = 0.20	y = 0.30
T_f (K)	233Hz	125.5	115.0	114.5	84.0
T_f (K)	1133Hz	127.0	117.0	116.5	86.0
T_f (K)	3333Hz	130.5	121.0	121.0	91.0
T_g (K)		125.2	114.7	114.1	83.5
$\tau_{0(\times 10^{-5}s)}$		1.4	2.7	1.4	3.1
zν		0.97	0.86	1.0	0.98

The temperature variations of real part of 3rd harmonic ac susceptibility, $|\chi'_3|$ for the samples y = 0.10, 15, 0.20 and 0.30 at two different applied fields (5.3Oe and 2.7 Oe) are shown in Figure 4.15. One can see that they exhibit double peaks corresponding to ferromagnetic and spin glass like transitions. Such behaviour is observed in $Ni_{77}Mn_{23}$ sample [287]. The low temperature peak is attributed to spin glass freezing temperature and represented as T_f in Table 4.6. The peak shifts towards low temperature with the increase in field amplitude. The magnitude of $|\chi_3'|$ peak increases with applied field. Such behaviours have been observed in FM to RSG transition system [57].

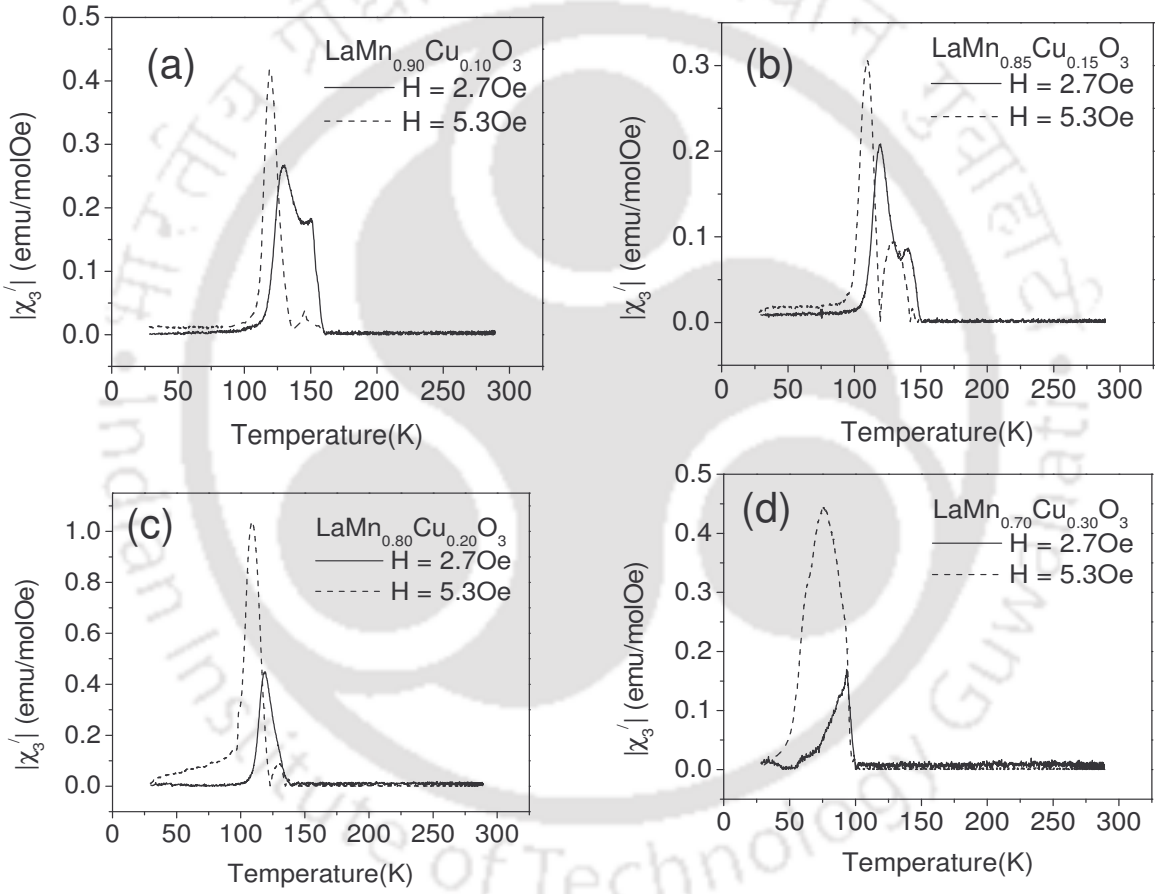

Figure 4.15: $|\chi_3'|$ versus T plots for the samples (a) y = 0.10, (b) 0.15, (c) 0.20 and (d) 0.30 for two different fields.

The third harmonic susceptibility measurement is crucial to distinguish between spin glass and superparamagnetic behaviour. In the former case, χ'_3 exhibit critical behaviour in the temperature region above T_f, while in the latter case, χ'_3 varies as $1/T^3$ above the blocking

temperature. According to the critical behaviour of spin glass material, $\chi'_3 \alpha \varepsilon^{-\gamma}$, where $\varepsilon = (T-T_g)/T_g$ and γ is the critical exponent. In order to analyze the critical behaviour of χ'_3, we have plotted $\ln|\chi'_3|$ versus $\ln(\varepsilon)$ as shown in Figure 4.16 for the samples y = 0.10. The exponent γ has been determined from the linear fit and the fitted data are shown as solid line in Figure 4.16. These values are found to be 3.2±0.02, 3.19±0.2 and 3.22±0.1 for the samples with y = 0.10, 0.15 and 0.20 respectively. The present γ values are comparable to that of Ni-Mn and Cu-Mn alloys [57, 288] and, manganites [289].

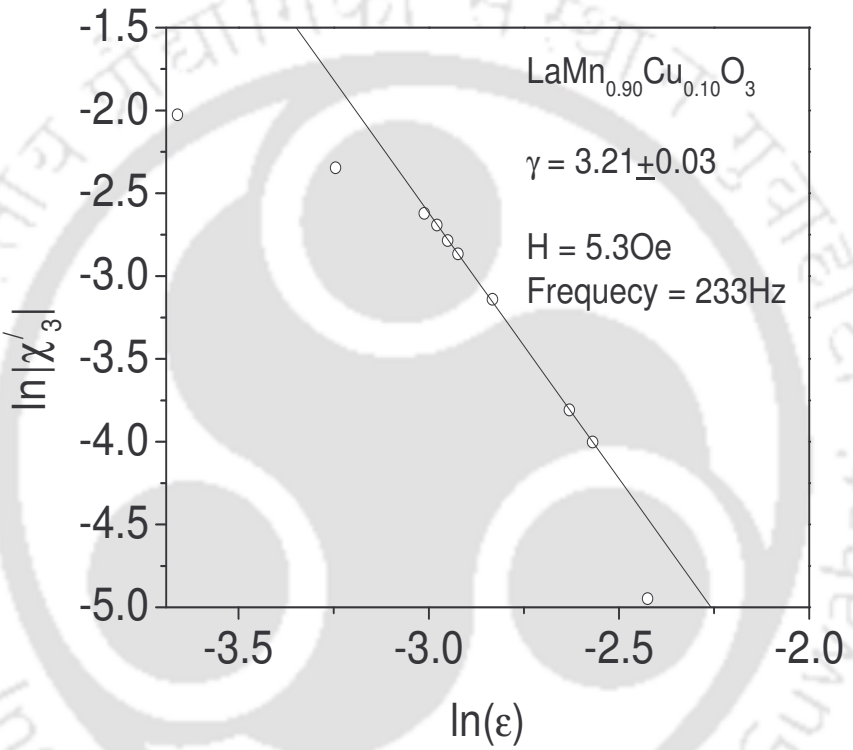

Figure 4.16: $\ln|\chi'_3|$ versus ln (ε) for the samples y=0.10 at 233Hz. Here $\varepsilon = (T-T_g)/T_g$.

Table 4.6: The spin glass freezing temperature peaks, T_f at two different field amplitudes.

Parameter/ Sample	T_f (K) Field =5.3 Oe	T_f (K) Field=2.7 Oe
y = 0.10	119.0	129.0
y = 0.15	110.0	119.0
y = 0.20	108.0	118.0
y = 0.30	75.0	94.0

Thus the study of dc magnetization, linear and non-linear ac susceptibility on Cu doped parent compound $LaMnO_3$ i.e. $LaMn_{1-y}CuyO_3$, depicts the presence of mixed competing interactions i.e. double exchange ferromagnetic interaction between Mn^{3+}-O-Mn^{4+} networks and anti-ferromagnetic interaction between Mn/ Cu ions. The ferromagnetic transition temperature is found to decrease and the mixed competing interaction results in spin glass like behaviour at low temperature. However, the doping of Cr ions on parent compound has given different results. Gundakaran *et al.* [200], Zhang *et al.* [201], and Morales *et al.* [202] studied the Cr doped $LaMnO_3$ compound. The doped Cr ions are found to destroy the A type AFM ordering and enhances the FM interaction by increasing the FM T_c. The magnetic moment also increases considerably with doping. These authors interpreted the results in terms of double exchange interaction in Mn^{3+}-O^{2-}-Cr^{3+} networks. The doping of Co at Mn site of $LaMnO_3$ was found to give similar type of result. Khalyavin *et al.* [290] have found the ferromagnetic and spin-glass like behaviour for $LaMn_{0.82}Co_{0.18}O_3$ and $LaMn_{0.46}Co_{0.54}O_3$ crystals, respectively. The spin-glass like state of $LaMn_{0.46}Co_{0.54}O_3$ crystal is addressed to a random distribution of cobalt and manganese ions in the B-site of the crystal lattice Unlike the Cu doping in CMR materials [218, 219], the Cu doping in the parent compound introduces DE-FM and then contributes for competing AFM and spin glass behavior.

4.4. Conclusions

The effect of Cu doping at Mn site of parent compound $LaMnO_3$, have been studied in this chapter. All the materials for $0.05 \leq y \leq 0.30$, in the series $LaMn_{1-y}Cu_yO_3$ exhibit PM-FM transition. The ferromagnetic transition temperature decreases with the Cu concentration. It reveals that, even though Cu doping increases the Mn^{4+} concentration, thereby increasing the Mn^{3+}- Mn^{4+} pairs, the Cu atoms exhibit a strong antiferromagnetic interactions with Mn ions. So the DE ferromagnetic interaction is weakened and the ferromagnetic T_c is reduced with doping.

Compounds for $y \geq 0.10$ exhibit paramagnetic to ferromagnetic transitions followed by sharp fall in susceptibility as the temperature is lowered. The analysis of dc magnetization, frequency dependence of linear susceptibility and temperature variation of non linear susceptibility shows that the present materials exhibit spin glass like behaviour at low temperature. From the analysis of third harmonic ac susceptibility, the critical exponent (γ) is found to be $\cong 3.2$.

Chapter 5: Hole Doped (Nd, Ag)-Mn-O Series

Nd-Mn-O series falls in the category of medium size e_g band width and hence the ionic size of doped materials plays a very sensitive and crucial role in tuning the electrical transport & magnetic properties in this system. Even though, there are several reports on divalent alkaline earth doped Nd-Mn-O series, the work on mono-valent doping in place of Nd is limited. Moreover, the ionic size of Ag^{1+} is greater than some of the alkaline earth and alkali ions. So, it would be interesting to study the doping of Ag in Nd-Mn-O series. In the present chapter, I have discussed $Nd_{1-x}Ag_xMnO_3$ compounds for x=0.05 to 0.20. I have studied their crystal structure, magnetic properties and electrical transport property.

5.1. Sample Preparation and Characterization

Polycrystalline samples of $Nd_{1-x}Ag_xMnO_3$ (x= 0.05, 0.10, 0.15, 0.20) were prepared by conventional solid state reaction method. Stoichiometric ratio of Nd_2O_3, $AgNO_3$ and manganese acetate with 99.9% purity were weighed and mixed thoroughly under acetone. The mixture was presintered at 300 ^{0}C, 400 ^{0}C, 500 ^{0}C, 600 ^{0}C and 700 ^{0}C for 5 hrs. at each temperature and at 800 ^{0}C for 36 hrs with intermediate grindings. The powdered samples were pressed into pellet and were sintered at 1000 ^{0}C for 40 h. The final sintering in pellet form was carried out at 1150 ^{0}C for 40 h.

The $Nd_{1-x}Ag_xMnO_3$ compounds for x = 0.05, 0.10, 0.15 and 0.20 are found to be in single phase form as per their XRD patterns. The XRD patterns for these samples are shown in Figure 5.1. The XRD patterns of all the samples could be indexed to *Pbnm* space group with orthorhombic structure. Typical XRD patterns along with Rietveld refinement are shown in Figure 5.2 for x = 0.05 & 0.15 samples. The room temperature lattice parameters, reliability factors (R_p, $R_{\omega p}$, R_{exp}, R_{Bragg}, R_F & χ^2) and unit cell volume values are listed in Table 5.1. The lattice parameters a and c are found to increase with doping up to x=0.15 due to the replacement of Nd^{3+} ion by larger Ag^{1+} ions. However the lattice parameter b is found to decrease with increase in doping. As a result of elongation of MnO_6 octahedra along a and c direction, there is a counter effect of contraction along b direction. The lattice parameters are comparable to those of Na doped, $Nd_{1-x}Na_xMnO_3$ compounds [252]. The $< r_A >$ value of present series is marginally higher than that of $Nd_{1-x}Na_xMnO_3$ series [252] for a particular doping concentration. The Mn-O bond lengths and ∠Mn-O-Mn bond angles are calculated from the refined atomic positions and lattice parameters and, these values are listed in Table 5.1. The Mn-O-Mn bond angle for x=0.10 is found to be highest followed by x=0.05 sample.

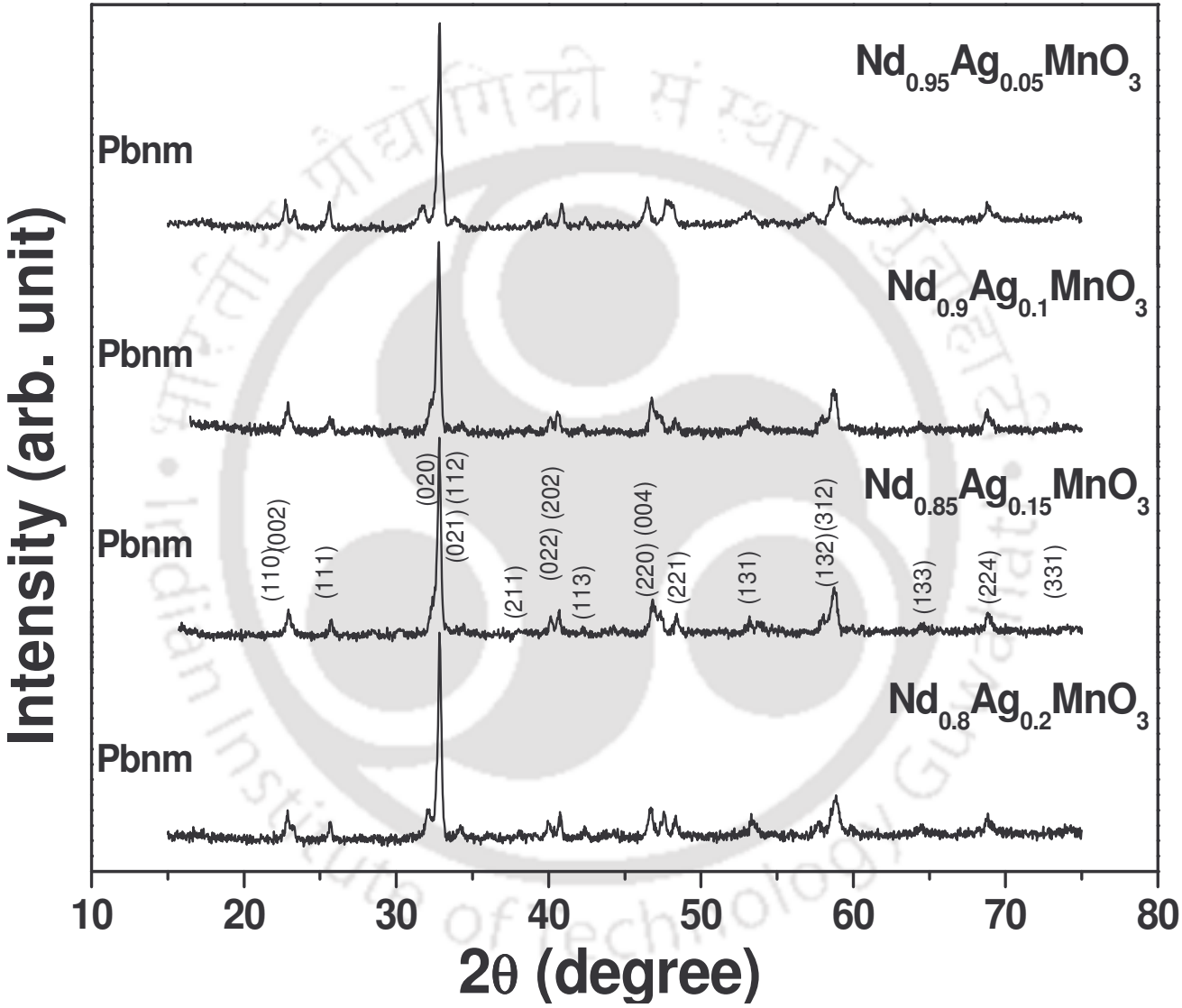

Figure 5.1: XRD patterns of the samples $Nd_{1-x}Ag_xMnO_3$ for x = 0.05-0.20.

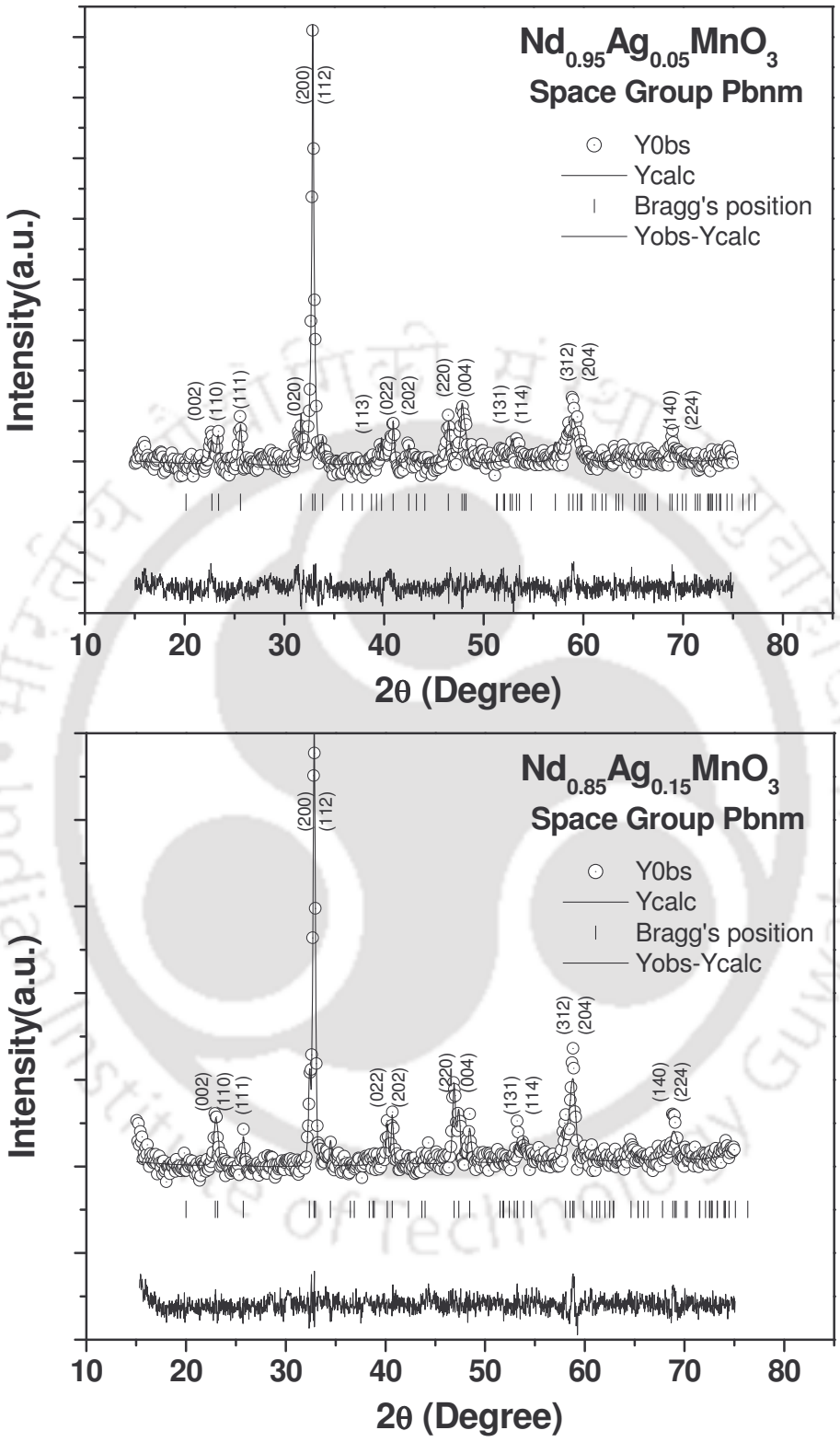

Figure5.2: XRD patterns for the x = 0.05 & 0.15 samples. The circles represent experimental points and solid line represents Rietveld refined data. The bottom line shows the difference between experimental & refined data. The marked 2θ positions are the allowed Bragg peaks.

Table 5.1: Parameters obtained from the Rietveld analysis of XRD patterns of $Nd_{1-x}Ag_xMnO_3$ (x= 0.05, 0.10, 0.15, 0.20). The numbers in brackets are estimated errors.

Sample/ Parameters	x = 0.05	x = 0.10	x = 0.15	x= 0.20
Space Group	Pbnm	Pbnm	Pbnm	Pbnm
a=b (Å)	5.4091 (0.0016)	5.4271 (0.0018)	5.4292 (0.0016)	5.4205 (5.4205)
b (Å)	5.6276 (0.0016)	5.5295 (0.0020)	5.5252 (0.0018)	5.5638 (0.0017)
c (Å)	7.6045 (0.0024)	7.6675 (0.0028)	7.6728 (0.0026)	7.6344 (0.0024)
Volume(Å^3)	231.5 (0.1)	230.1 (0.1)	230.2 (0.1)	230.2 (0.1)
χ^2 (%)	1.56	2.59	2.64	2.53
R_p (%)	3.14	5.75	5.33	4.24
R_{wp} (%)	4.05	7.25	6.75	5.34
R_{exp} (%)	3.25	4.51	4.16	3.35
R_f (%)	10.6	13.0	8.85	8.54
R_{Bragg} (%)	12.4	14.6	11.1	9.67
<Mn-O_1>(Å)	2.009	1.991	2.012	2.024
<Mn-O_2>(Å)	2.007	1.967	1.981	1.990
∠ Mn-O_1-Mn (°)	142.3	148.7	144.9	141.1
∠ Mn-O_2-Mn (°)	152.9	159.8	155.7	154.6
< r_A > (Å)	1.169	1.175	1.180	1.186
Mn Valency	3.14	3.25	3.32	3.38

The average valency of Mn ions determined from the chemical titration is given in Table 5.1. The systematic increase in Mn valency with Ag doping depicts the formation of Mn^{3+}/Mn^{4+} mixture with increase in Mn^{4+} concentration.

Typical SEM micrograph for $Nd_{0.85}Ag_{0.15}MnO_3$ is shown in Figure 5.3. The microstructure morphology of the samples are found to be uniform with average particle size in the order of 1-2 μm. Typical EDS spectrum for y = 0.20 sample is shown in Figure 5.4.

The chemical compositions determined from EDS analysis are found to be comparable to the nominal starting composition. The cationic ratio for all the samples is given in Table 5.2.

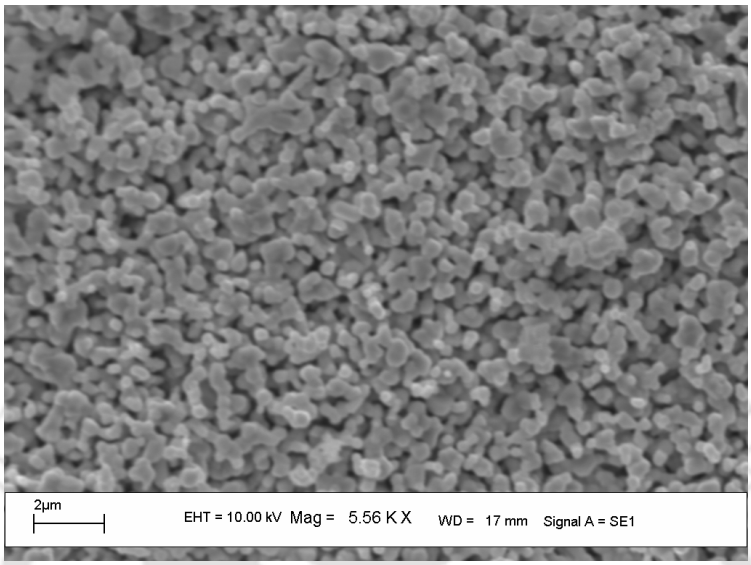

Figure 5.3: SEM image (magnification 55600) of $Nd_{0.85}Ag_{0.15}MnO_3$ sample.

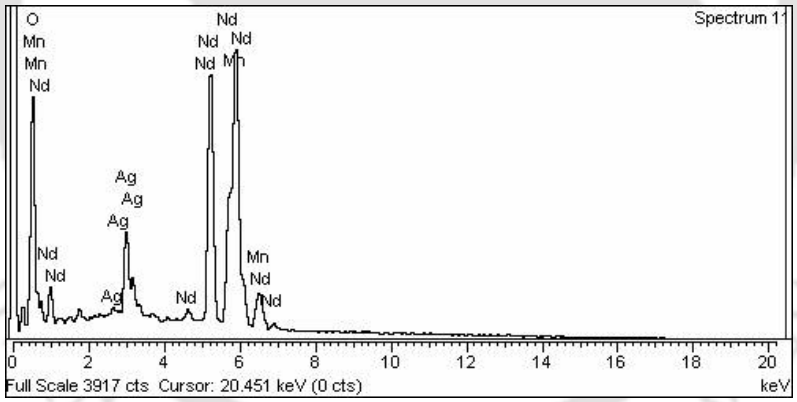

Figure 5.4: Typical EDS spectrum for x=0.20 sample.

Table 5.2: The cationic ratio determined from EDS analysis for $Nd_{0.85}Ag_{0.15}MnO_3$ samples.

Sample	Calculated Cationic Ratio from EDS		
	Nd	Ag	Mn
x=0.05	0.95	0.04	1.01
x=0.10	0.88	0.11	1.01
x=0.15	0.86	0.15	0.99
x=0.20	0.79	0.20	1.01

5.2 Study of Magnetic Property using dc Magnetization

The temperature variations of magnetization for x=0.05, 0.10, 0.15, 0.20 samples in zero field cooled (ZFC) and field cooled (FC) conditions are shown in Figure 5.5 & Figure 5.6. Sharp rise in magnetization at ~80 K has been observed for x=0.05 and the complete transition could not be seen because of low temperature limitation in the present set up. The above transition temperature is comparable to the transition observed in the parent compound, $NdMnO_3$ reported in the literature [248, 249]. On the other hand, for the doping concentrations, x≥0.10, FM transitions are observed with T_c around 120 K. For x=0.10 and 0.15, the T_c values are comparable and there is a bifurcation of ZFC and FC curves and such behavior could not be seen for x= 0.2 sample because of slightly lower transition temperature.

The dc susceptibility χ_{dc} in the paramagnetic region was analyzed by using Curie-Weiss law (equation 1.10). The Curie-temperature (θ_C) for all the four samples are found to be positive and indicating the FM interaction. Thus the Ag doping gives rise to generation of Mn^{3+}/Mn^{4+} mixture and the Zener double exchange FM interaction. Typical plots of $1/\chi_{dc}$ versus temperature for x=0.10 and 0.15 samples are shown in Figure 5.7 along with Curie-Weiss law fitting. The FM transition temperature obtained from M versus T curve and θ_C are given in Table 5.3. The difference between T_C and θ_C are mainly due to the observed broad magnetic transition. The FM T_c observed in the present series is comparable to that reported for $Nd_{1-x}Na_xMnO_3$ series [252]. However unlike (Nd, Na)-Mn-O series, we have not observed any charge ordering type of transitions. It may be noted that the $<r_A>$ values of the present series of materials are marginally greater than that of (Nd, Na)-Mn-O series.

The effective magnetic moment, μ_{eff} was determined from the fitted curie constant C and are given in Table 5.3. It is found to decrease systematically with increase in Ag doping as a result of oxidation of some of Mn^{3+} ions into Mn^{4+} state. The above μ_{eff} values obtained from the analysis of experimental data can be compared with the theoretical effective magnetic moment μ_{th}. By taking into account magnetic moment contribution from Nd^{3+}, Mn^{3+} and Mn^{4+} ions, μ_{th} can be calculated as follows.

$$\mu^2_{th} = x_1 \mu^2_1 + x_2 \mu^2_2 + x_3 \mu^2_3 \qquad \text{----------} \qquad (5.1)$$

Here, x_1, x_2 & x_3 are the fractional concentration of Nd^{3+}, Mn^{3+} & Mn^{4+} ions per formula unit. μ_1, μ_2 μ_3 are the theoretical magnetic moments of Nd^{3+}, Mn^{3+} & Mn^{4+} ions and their values due to spin only contribution are 3.62 μ_B, 4.9 μ_B and 3.87 μ_B respectively. The μ_{th} values are tabulated in Table 5.3 and they are comparable to μ_{eff} values and the minor difference

between them could be mainly due to error in the estimation of concentration of Mn^{3+} and Mn^{4+} ions.

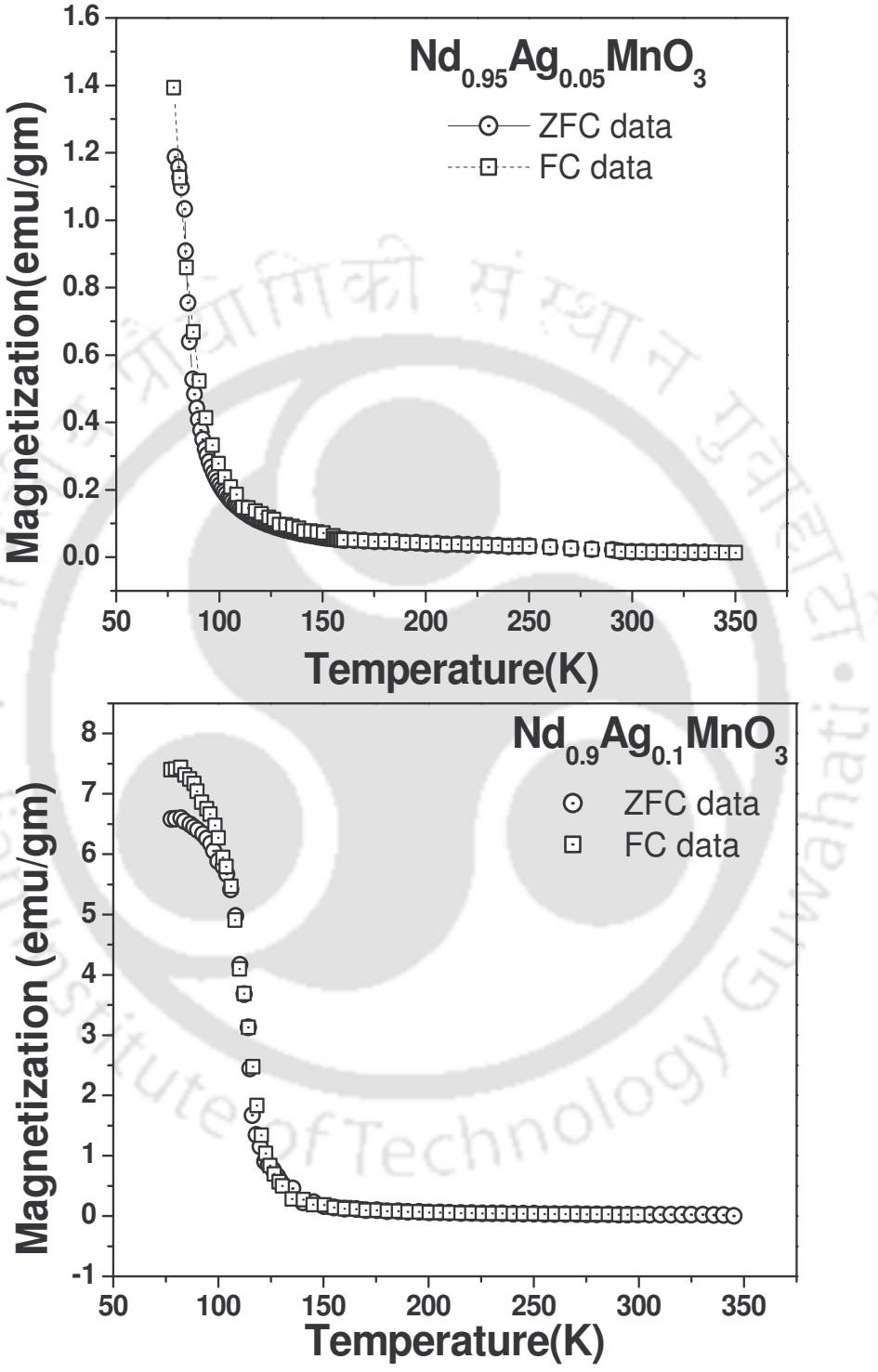

Figure 5.5: The temperature variation of (ZFC) zero field cooled (Circles) and (FC) field cooled (square) magnetization curves for x=0.05 & 0.10 samples.

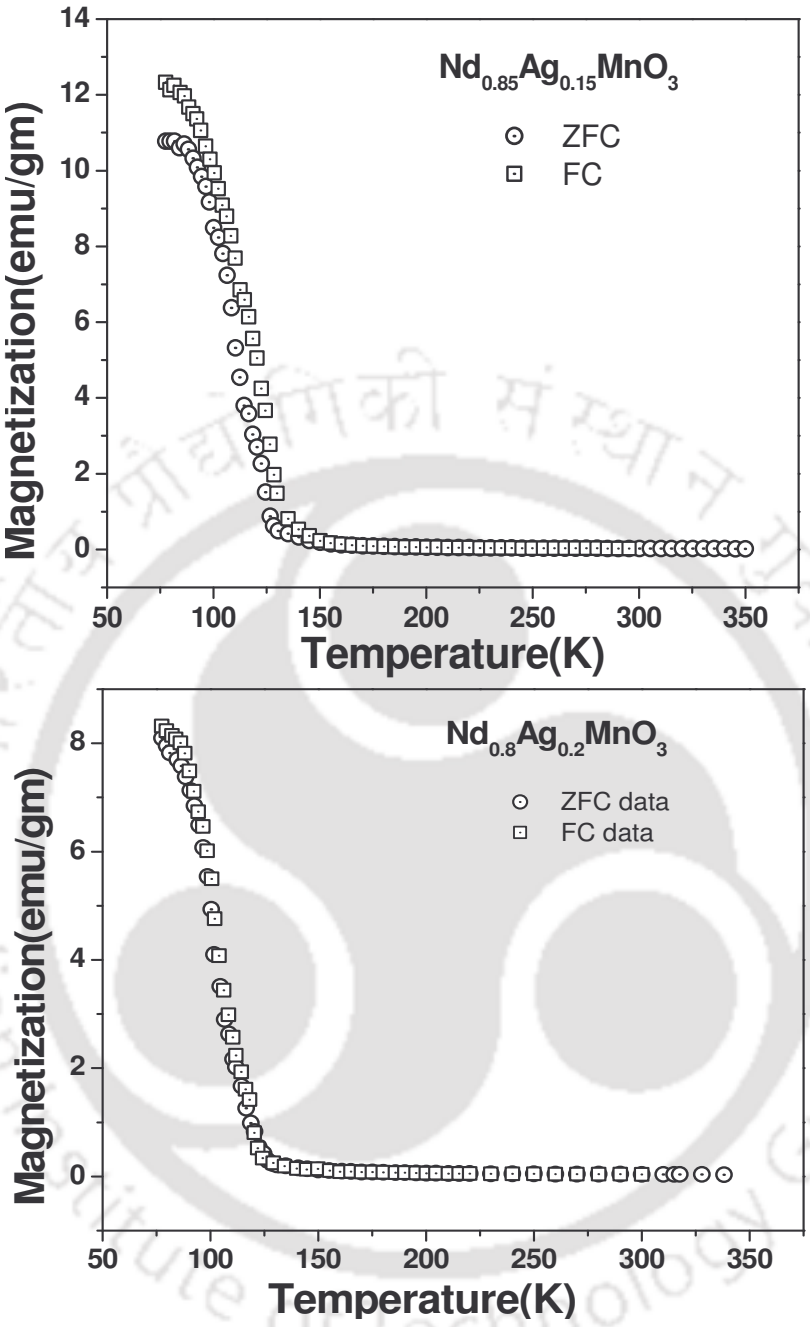

Figure 5.6: The temperature variation of (ZFC) zero field cooled (Circles) and (FC) field cooled (square) magnetization curves for x=0.15 & 0.20 samples.

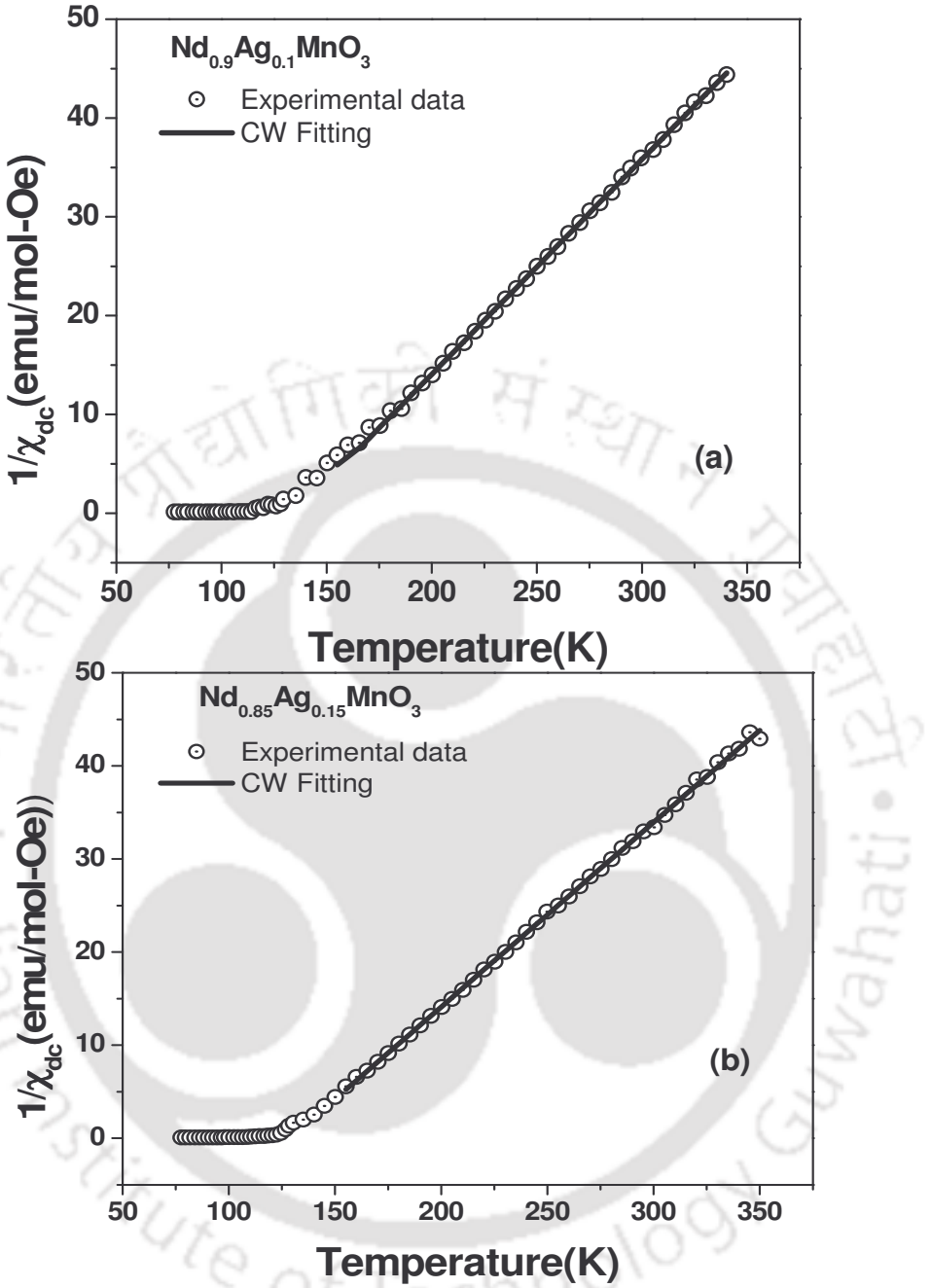

Figure 5.7: $1/\chi_{dc}$ versus temperature for the samples (a) $Nd_{0.90}Ag_{0.10}MnO_3$ and (b) $Nd_{0.85}Ag_{0.15}MnO_3$. Solid lines represent fit to the Curie-Weiss law.

Table 5.3: Parameters obtained from the measurement and analysis of magnetization of $Nd_{1-x}Ag_x MnO_3$.

Sample/Parameters	x = 0.05	x = 0.10	x = 0.15	x = 0.20
T_C(K)	84.0	114.0	113.0	102.0
θ_C (K)	74.6	135.3	128.4	114.6
C	4.90	4.60	5.05	4.22
μ_{eff} (μ_B)	6.30	6.06	6.35	5.81
μ_{eff}^{th}(μ_B)	5.96	5.83	5.69	5.60

The magnetization loops measured at 78 K for B= ± 2 T are shown in Figure 5.8. There is a large increase in magnetization as the doping concentration increases from 5% to 10%. The magnitude of magnetization for x=0.10 and 0.15 are comparable and it decreases for x =0.20 sample. For x=0.05 sample, even though there is a minor ferromagnetic contribution, the magnetization is found to increase almost linearly with increase in magnetic field and it indicates the presence of considerable AFM/paramagnetic contribution. The M_s value after subtracting the linear contribution is found to be 0.34 μ_B per formula unit. Even though, the magnetization of higher doped materials has increased appreciably, their magnetization is less than the expected spin only contribution of Mn ions and there was no saturation of M. The saturation magnetization, M_S was determined by extrapolating the M-H curve to H=0 and they are given in Table 5.4 for all the samples. The lack of hysteresis loss indicates the soft magnetic properties of the materials.

By following, the neutron diffraction results of Yu. *et. al.* [248] and Munoz *et. al.* [249] in $NdMnO_3$ parent compound and by assuming the canting of magnetic spins of Mn ions with its FM component parallel to c-axis and AFM component within the ab plane, the canting angle β with respect to c axis can be estimated by determining the effective magnetic spin S_{eff}, which contributes ferromagnetic interaction.

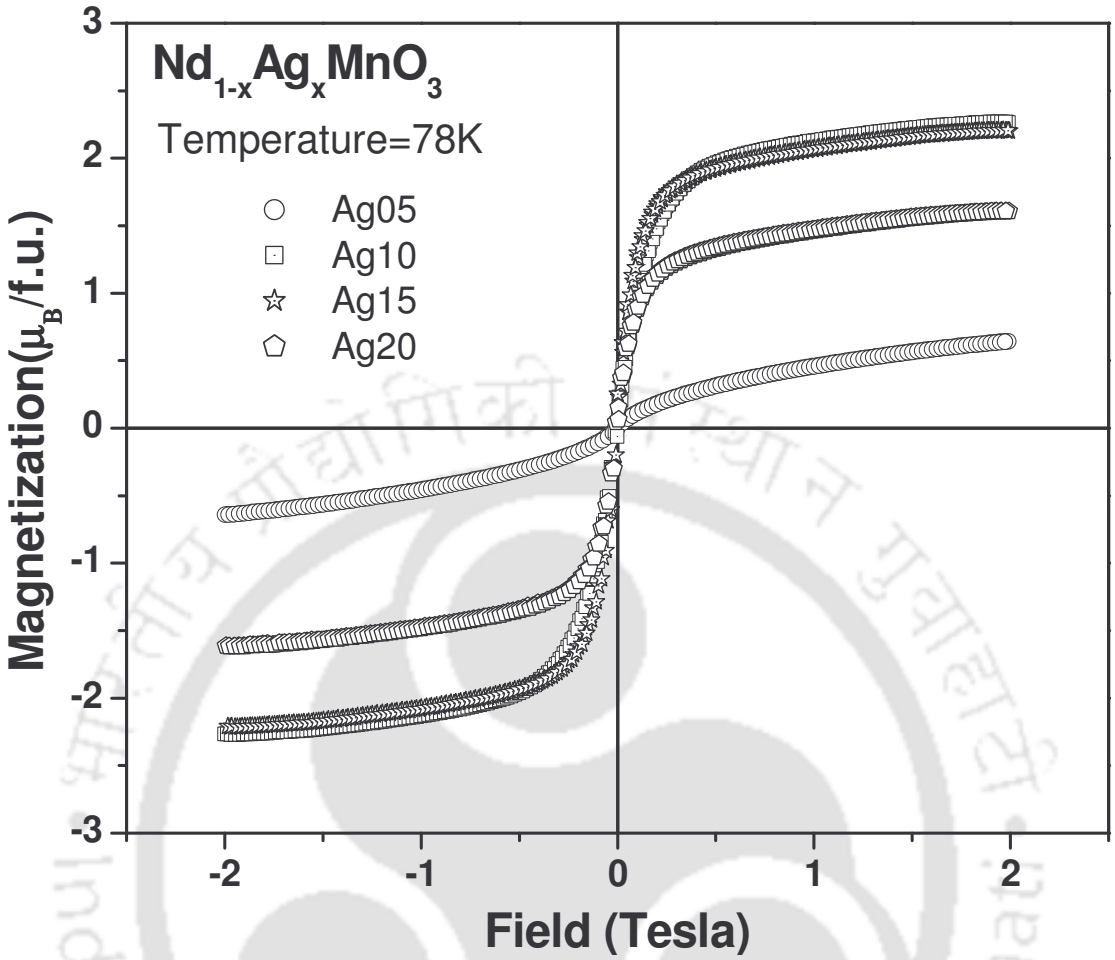

Figure 5.8: Magnetization versus magnetic field plots for x=0.05, 0.10, 0.15 and 0.20 samples.

The field variation of magnetization after subtracting the linear contribution was fitted to the relation,

$$M = M_0 B_S(x) \qquad \text{---------- (5.2)}$$

Where $$B_S(x) = \frac{1}{|S_{eff}|}\left[\left(S_{eff} + \frac{1}{2}\right) Coth x\left(S_{eff} + \frac{1}{2}\right) - \frac{1}{2} Coth \frac{x}{2}\right] \qquad \text{---------- (5..3)}$$

Here, $M_0 = Ng\mu_B |S_{eff}|$, $x = \frac{g\mu_B}{kT} B$, and $B = B_a + \lambda M$. λ is the Weiss molecular field constant for ferromagnetic interaction. We have carried out the fit by assuming the λ values determined from the FM T_c and Curie constant C ($T_c = \lambda C / \mu_0$) for different samples. The magnetization fit for x=0.10, 0.15 & 0.20 samples are shown in the Figure 5.9. However the magnetization data for x=0.05 sample could not be fitted well. We can see that the fitted data closely follow the experimental data. The fitted values of S_{eff} are given in Table 5.4. The canting angle $\beta = Cos^{-1}(S_{eff} / S)$ has been calculated. Here S is the expected value of spin for a particular

sample corresponding to their Mn valency. The values of β for x= 0.10, 0.15 & 0.20 samples are given in Table 5.4. Theses values are comparable to value reported for $NdMnO_3$ compound [248].

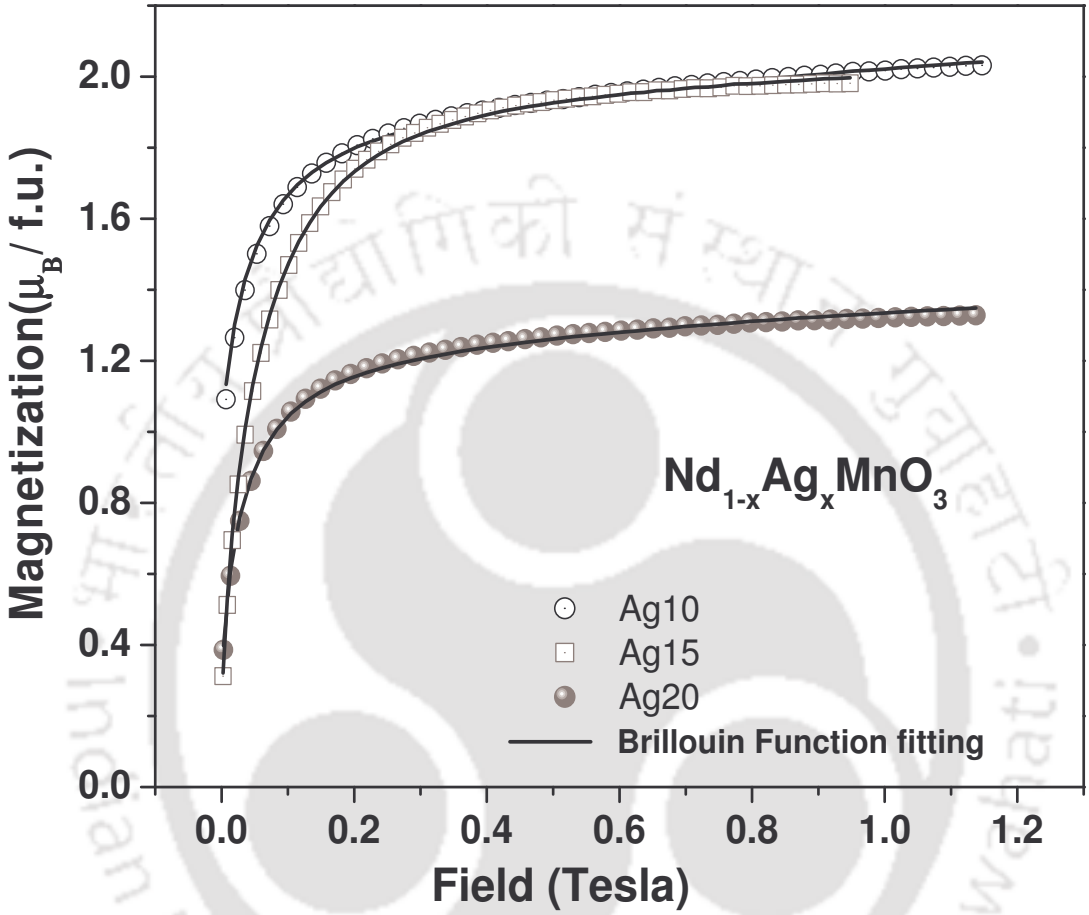

Figure 5.9: Brillouin function fitting to magnetization data (after subtracting the linear part) for x= 0.10, 0.15 & 0.20 samples.

Table 5.4: Parameters obtained from Brillouin function fitting to magnetization data of $Nd_{1-x}Ag_xMnO_3$. S_{eff} is the effective spin contribution towards FM interaction. β is spin canting angle. M_s is the experimental saturation magnetization.

Sample/ Parameters	x= 0.10	x= 0.15	x= 0.20
S_{eff}	1.40	1.40	1.31
β (°)	42	39	40
r m s (%)	0.51	0.55	0.52
M_S (μ_B /f.u.)	1.98	1.85	1.31

5.3. ac Susceptibility Study

The temperature variations of in-phase linear ac susceptibility (χ'_1) are shown in Figure 5.10 for x=0.05, 0.10, 0.15 and 0.20 samples. A magnetic transition with peak effect has been observed for x= 0.05 sample. It coincides with the transition observed from magnetization measurement and AFM transition reported in literature [249] for the parent $NdMnO_3$ compound. So, it is basically a FM transition with AFM component or vice versa due to spin canting. For further increase in doping concentration, i.e. $x \geq 0.10$, we can see the double exchange FM transition at around 115 K. In addition to that, low temperature hump has also been observed and is comparable to the AFM transition observed in x=0.05 sample. For x=0.2 samples, FM T_c is found to reduce due to increase in Mn^{4+} concentration beyond the optimum value and this transition merges with low temperature hump.

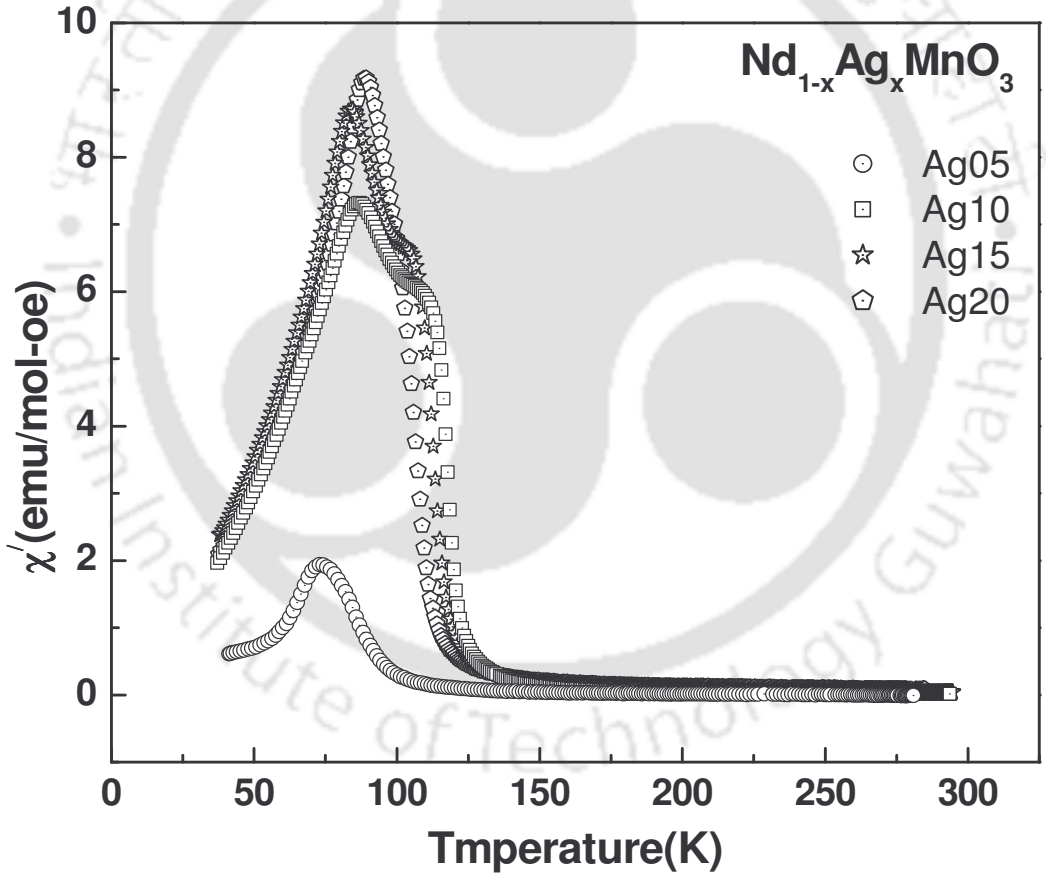

Figure 5.10: Temperature variation of linear ac susceptibility (χ_1') of samples $Nd_{1-x}Ag_xMnO_3$ (x=0.05, 0.10, 0.15 and 0.20).

The temperature variations of out of phase susceptibility ($\chi^{//}_1$) also depict the similar double peak effect as shown in Figure 5.11. As the doping concentration increases, there are two effects namely; increase in concentration of Mn^{4+} ions and average A-site ionic size. The increase in ionic size leads to the increase in ∠Mn-O-Mn bond angle. The increase in ∠Mn-O-Mn bond angle along with Mn^{3+}/Mn^{4+} pairs have a role on the strength of double exchange ferromagnetic interaction. Thus for low level of doping, there is a dominant AFM interaction with weak FM due to spin canting. When the doping concentration is increased to 10 or 15%, appreciable FM has been observed, however still there is a presence of AFM interaction due to spin canting. This is mainly due to difficulty in getting the optimum Mn-O-Mn bond angle in Nd-series because of its low ionic size compared to La-series. Thus in this system, there is a competition between FM and AFM for a wide range of Ag doping concentration. Thus from the magnetization and ac susceptibility results we can infer that these materials exhibit FM transition along with the presence of competing AFM interaction.

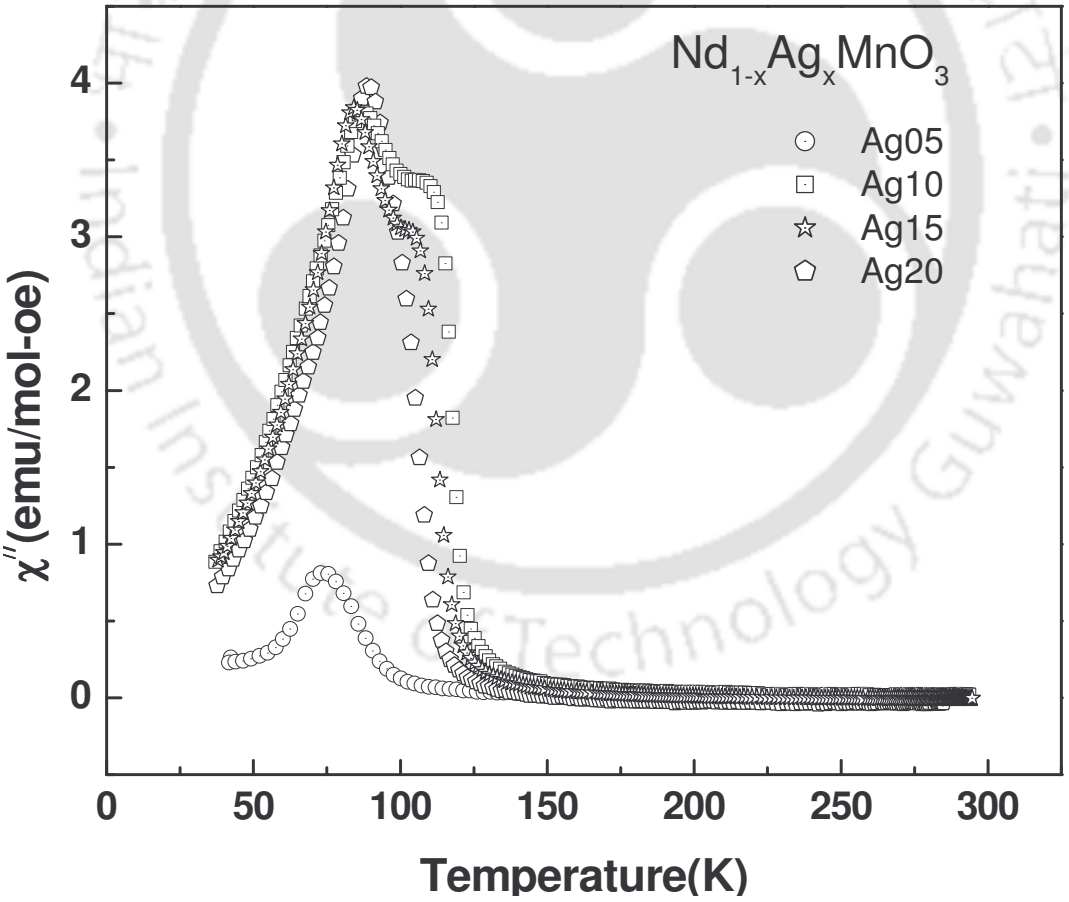

Figure 5.11: Temperature variation of linear ac susceptibility ($\chi_1^{//}$) of samples $Nd_{1-x}Ag_xMnO_3$ (x=0.05, 0.10, 0.15 and 0.20).

To further explore the magnetic behavior we have carried out the frequency variation of ac susceptibility for x=0.10 & 0.15 samples. Typical plots of χ'_1 versus temperature for x=0.15 sample are shown in Figure 5.12 and they exhibit double peaks. The low temperature peak is found to shift towards higher temperature with increase in frequency as a result of spin glass (SG) like behavior. The low temperature peak is taken as the spin glass freezing temperature T_f. The variation of T_f is shown in the inset of Figure 5.13. Unlike the Mn site doped CMR materials [203], where a strong frequency dependence of T_f has been observed, we observe relatively weak frequency dependence. However there is a clear shift in T_f , as can be seen from the Figure 5.13. The observed shift in T_f is comparable to that reported by Cao *et al.* [291] in $(Nd, Sm)_{0.5}Ca_{0.05}MnO_3$ samples. Thus there is a weak spin glass like behavior in the present series. Similar behavior was found for x=0.10 sample.

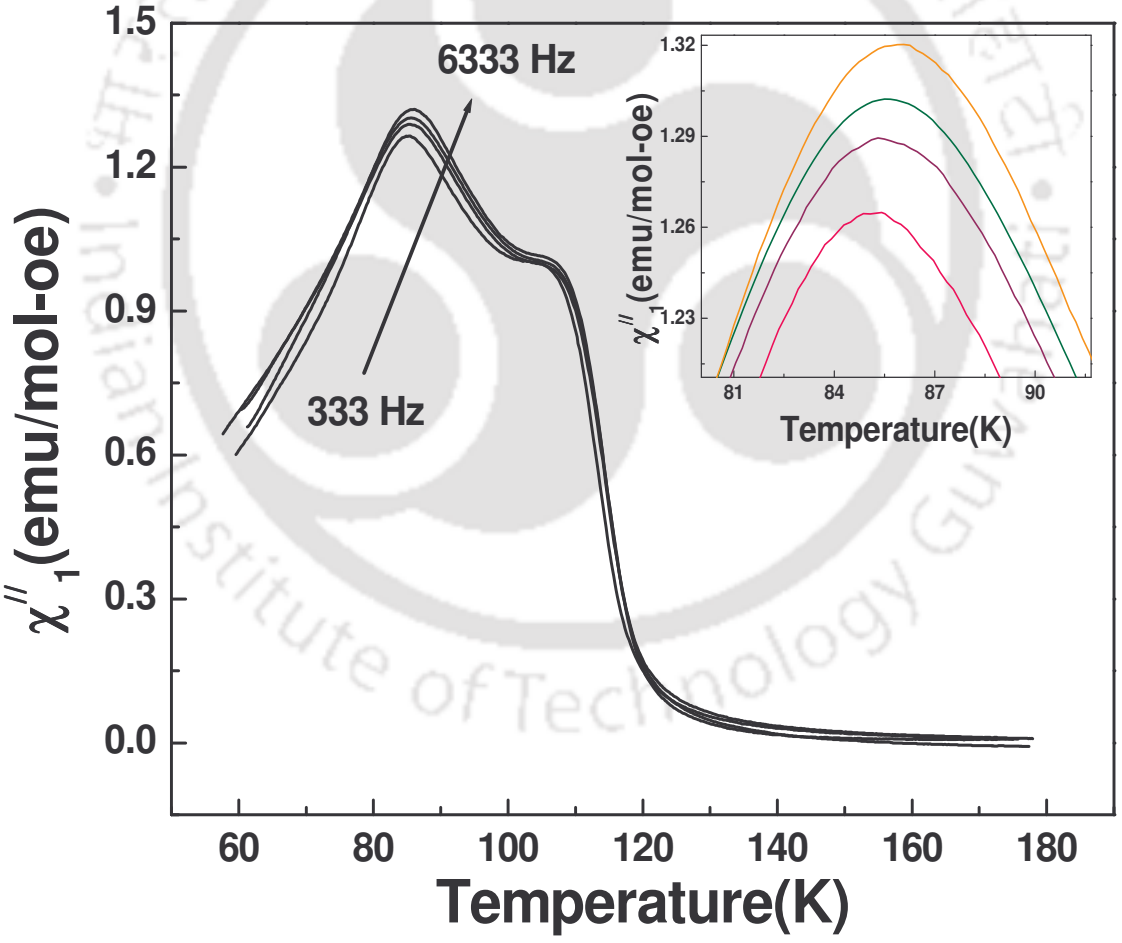

Figure 5.12: χ'_1 versus temperature (T) measured at frequencies f = 333 Hz, 1333 Hz, 3333 Hz and 6333 Hz for the x= 0.10 sample. Inset shows the magnified part of low temperature peak.

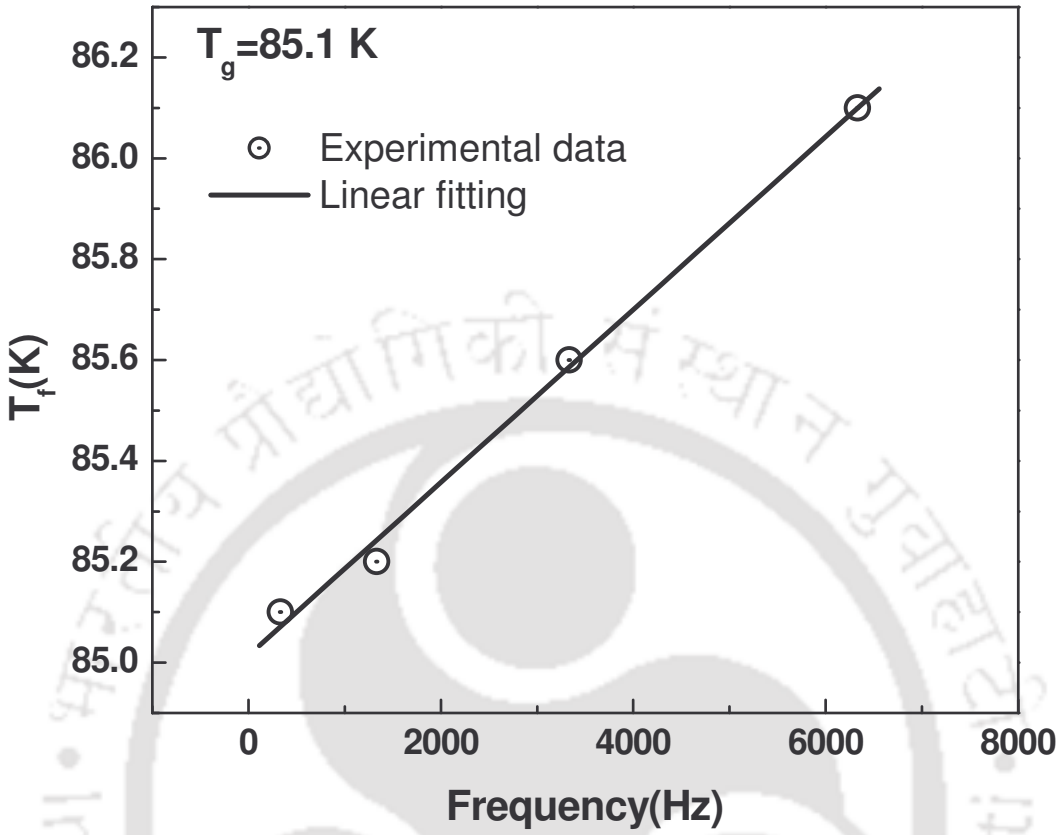

Figure 5.13: Variation of freezing temperature with frequency for x=0.15 sample

The dynamic property of spin glasses was analyzed based on conventional power law model (equation 3.5). The T_g values for x=0.10 and 0.15 samples were determined by extrapolating the plot of T_f versus frequency to f=0 and they are found to be 86.9 and 85.1 K respectively. Typical plot of $\ln(\tau)$ versus $\ln[(T_f - T_g)/T_g]$ is shown in Figure 5.14, for x=0.10 & 0.15 samples. These data were fitted to equation 3.11 by varying the parameters τ_0 and $z\nu$ and, the fitted data are shown as solid line. The values of τ_0 are found to be 6.18×10^{-8} s & 37.12×10^{-8} s for x= 0.10 & 0.15 samples respectively.

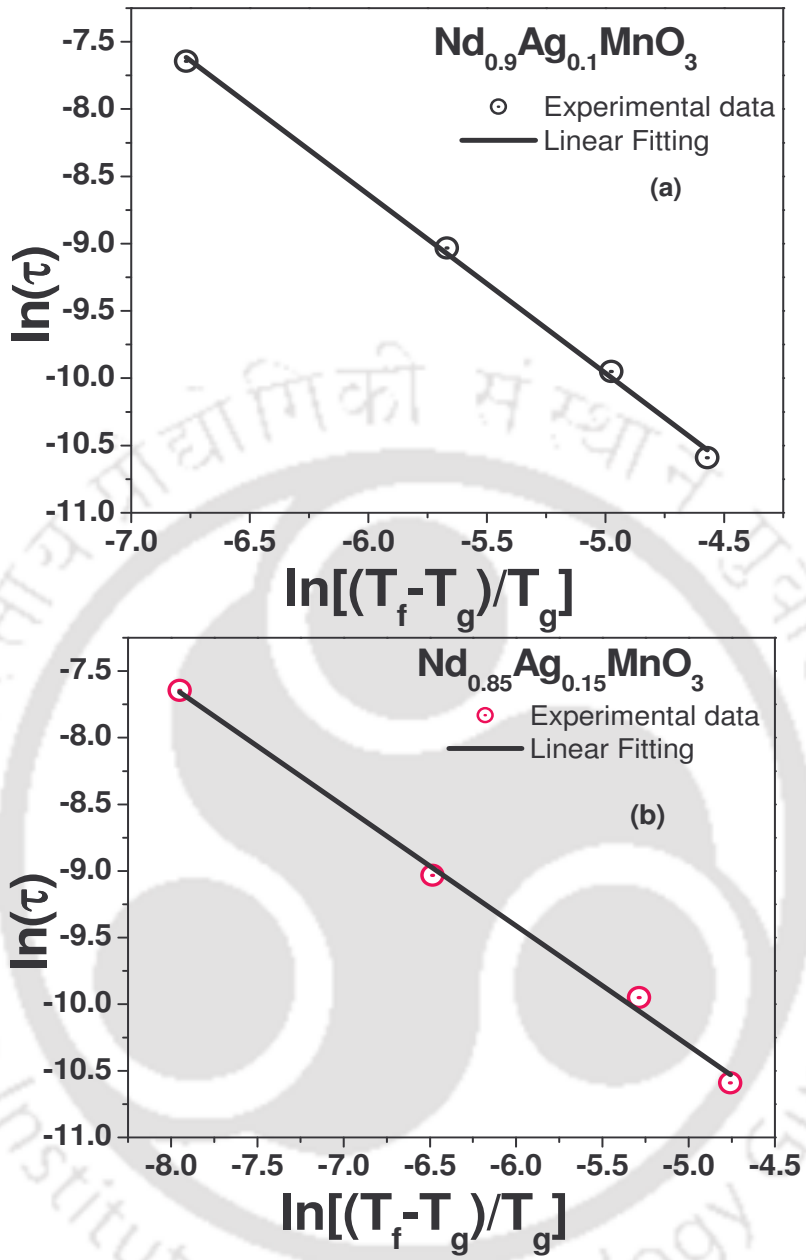

Figure 5.14: Plots of ln(τ) versus $\ln[(T_f-T_g)/T_g]$ for (a) $Nd_{0.9}Ag_{0.1}MnO_3$ (b) $Nd_{0.85}Ag_{0.15}MnO_3$ samples.

The observed frequency variation of fundamental harmonic susceptibility is not the unique property of spin glass behavior. Another interesting magnetic property i.e. super-paramagnetism also exhibits similar frequency variation of fundamental susceptibility. In order to ascertain unequivocally that the present low temperature transition is due to the spin glass like behavior, one has to carryout the measurement and analysis of harmonic susceptibility. The typical plot of temperature variation of third harmonic ac susceptibility, χ'_3 is shown in Figure 5.15 for 0.15 sample. It exhibits a sharp negative peak at 113 K and it coincides with ferromagnetic transition temperature. In addition to that, there is a low temperature peak at 84 K. The position of low temperature peak is closely comparable to that observed from χ_1'' vs. T plot (Figure 5.12) and is attributed to spin glass transition temperature. Thus the harmonic susceptibility clearly depicts the presence of FM and low temperature SG state. It is comparable to the harmonic susceptibility of ferromagnetic spin glass material $Fe_{1.5}Mn_{1.5}Si$ reported by Chakravarti *et al.* [282].

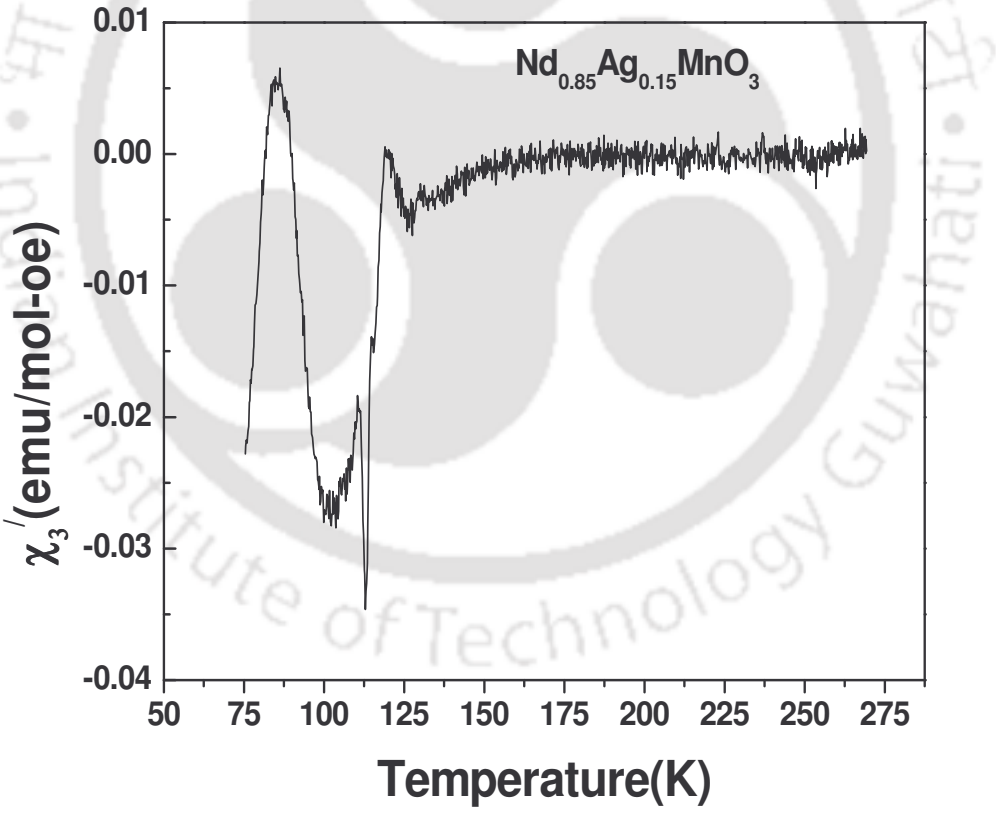

Figure 5.15: Third harmonic ac susceptibility (χ_3') versus T for the sample x=0.10 & 0.15 samples.

The unique property of spin glass material is that their χ_3 values follow the critical scaling relation $\chi'_3 \alpha \varepsilon^{-\gamma}$, [41]. Here, $\varepsilon = (T-T_g)/T_g$ and γ is the critical exponent of spin glass transition. The plot of $\ln|\chi'_3|$ versus $\ln(\varepsilon)$ is shown in the Figure 5.16 for the sample x = 0.15 and it exhibits a linear behavior. They were fitted to a linear equation by varying the parameter γ and the fitted data are shown as solid line. The value of γ is found to be 2.02±0.02 for x=0.15 sample. The present γ value is comparable to γ=2.3±0.2, reported for AgMn spin glass system [55] and γ=2.2±0.2 reported for PdMn spin glass material [56]. However it differs considerably from the values reported for other spin glass system [57] and manganites [289]. According to Mathieu *et al.* [289], the critical exponent corresponding to three dimensional Heisenberg like model is 2.3 and the critical exponent of present material can be compared to this model. Thus the low temperature transition observed in the linear and non-linear ac susceptibility measurements originates from spin glass like behavior.

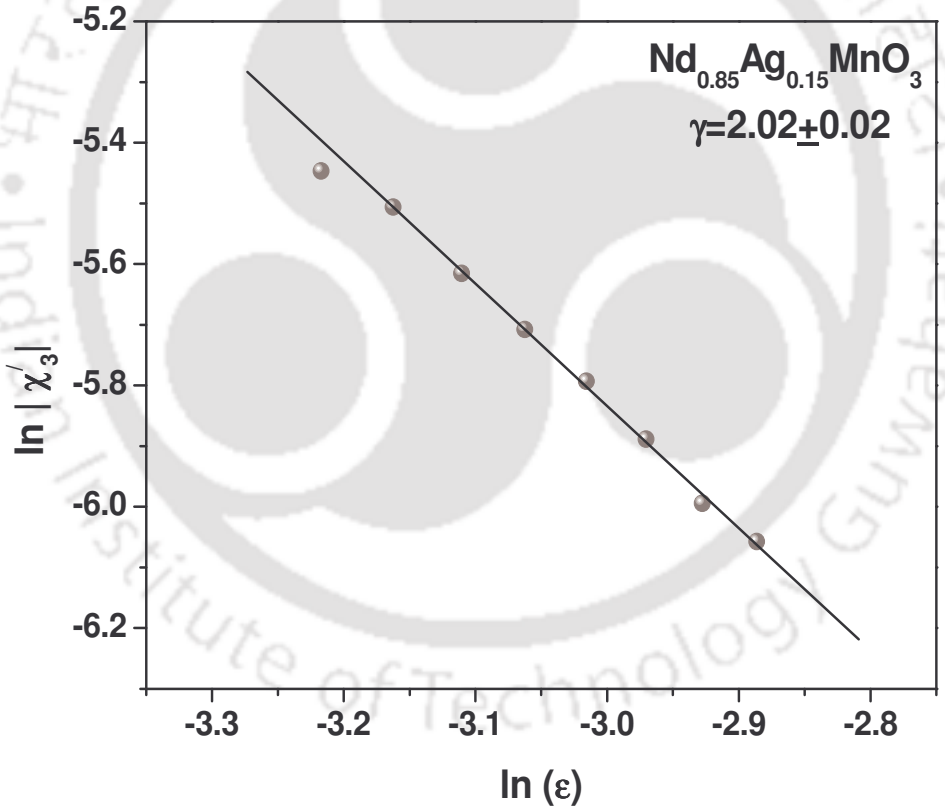

Figure 5.16: Plot of $\ln|\chi'_3|$ versus $\ln(\varepsilon)$, with $\varepsilon = (T-T_g)/T_g$.

5.4. Electrical Resistivity study

The temperature variations of dc electrical resistivity for x = 0.05, 0.10, 0.15 and 0.15 & 20 samples are shown in Figure 5.17. For the sake of clarity and for easy comparison, the resistivity data are shown in logarithmic scale. Even though the materials show ferromagnetism transition, no M-I transition is observed and it reveals that the ferromagnetic phase is below the threshold value.

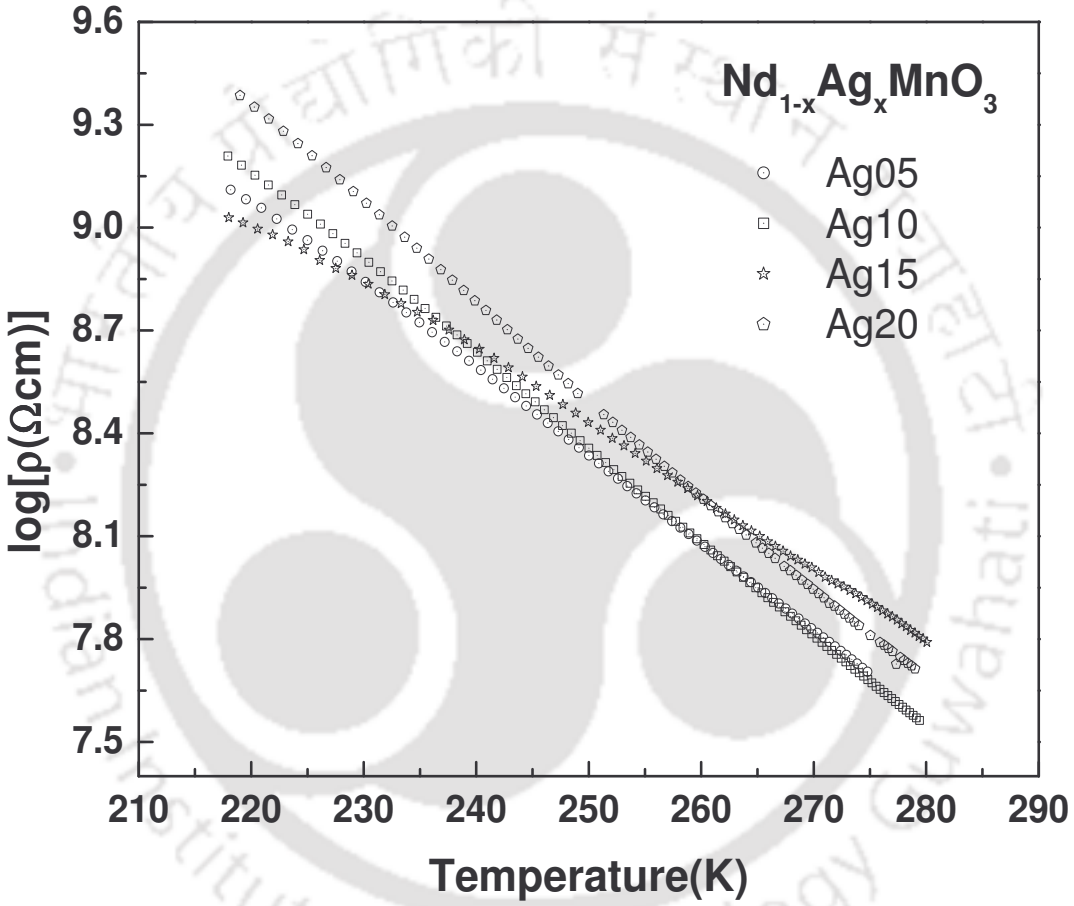

Figure 5.17: Temperature variation of electrical resistivity of samples $Nd_{1-x}Ag_xMnO_3$ (x=0.05, 0.10, 0.15 and 0.20).

The resistivity data of above samples have been analyzed using Mott variable range hopping (Mott-VRH), Efros-Shklovskii VRH (ES-VRH), and Adiabadic small polaron hopping (ASPH) models. We have found that the experimental data could be fitted well to ES-VRH model. Typical plots of ln(ρ) versus $T^{-1/2}$ are shown in Figures 5.18 (a) & (b) for x = 0.05 and 0.15 samples respectively. The experimental data (open circles) closely follow the fitted data shown as solid line. From the ES-VRH fitted values of T_{os}, dielectric constant ε_r,

hopping distance $R_{hs}(T) = (1/4)a(T_{os}/T)^{1/2}$ and hopping energy $E_{hs}(T) = (1/2)k_BT(T_{os}/T)^{1/2}$ were estimated and they are tabulated in Table 5.5.

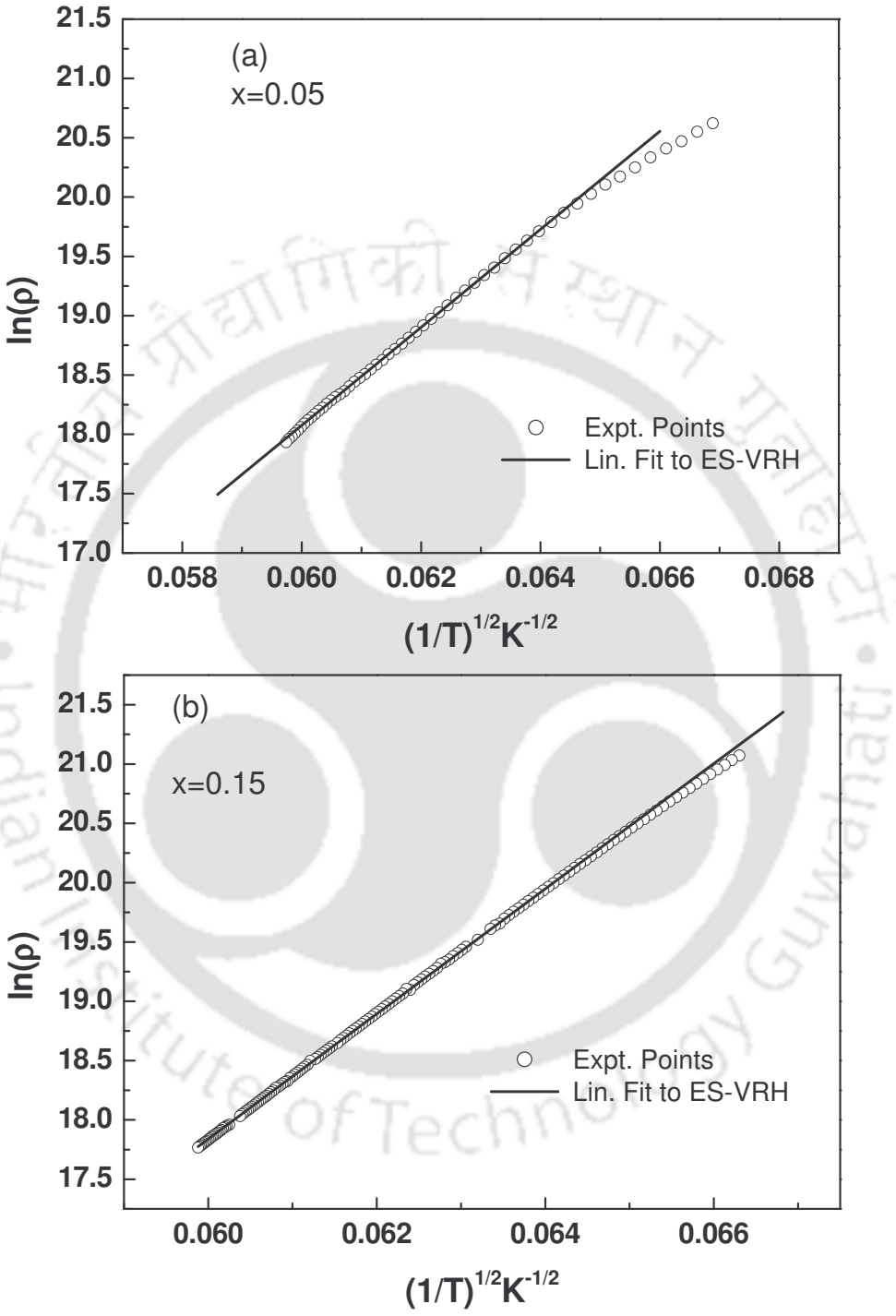

Figure 5.18: Plot of ln(ρ) as a function of $T^{(-1/2)}$ for (a) x=0.05 and (b) x=0.15 samples. Solid lines are fit to ES-VRH model.

Table 5.5: Results obtained from resistivity analysis. Here, ρ_{0s} is the ES residual resistivity and T_{0s} is the ES characteristic temperature ε_r is the dielectric constant.

Sample Parameters	**x = 0.05**	**x = 0.10**	**x = 0.15**	**x =0.20**
rmsd (ES – VRH)(%)	0.91	1.41	0.44	1.3
ρ_{os} (10^{-6}mΩcm)	8.22	1.08	1217.90	1.01
T_{os}(10^4K)	23.87	27.17	17.07	27.81
R_{hs}(300 K) (Å)	31.73	33.86	26.83	34.25
E_{hs}(300 K) (meV)	1035.6	1178.8	740.3	1206.5
ε_r	0.434	0.382	0.608	0.373

5.6. Conclusions

Polycrystalline samples of $Nd_{1-x}Ag_xMnO_3$ (x=0.05, 0.10, 0.15, 0.20) have been prepared for x = 0 to 0.20. All the samples are found to be in single phase form. X- ray diffraction patterns could be refined by using Pbnm space group. The lattice parameters a & c are found to increase with Ag doping. Temperature variation of magnetization measurement shows that these materials exhibit paramagnetic –ferromagnetic transition with the signature of presence of competing antiferromagnetic transition. The paramagnetic susceptibility could be analyzed by using Curie-Weiss law and the estimated μ_{eff} was comparable to the theoretical magnetic moments due to Mn^{3+}/ Mn^{4+} and Nd^{3+} ions. The field variation of magnetization could be fitted to Brillouin function relation by considering the FM interaction. The measured magnetization was explained on the basis of spin canting. The frequency variation of ac susceptibility and third harmonic susceptibility data indicate the presence of spin glass like behavior for x=0.10 &0.15 samples. All the materials exhibit semiconducting behavior. The semiconducting behavior could be understood by ES-VRH model.

Chapter6: Electron Doped (Y, Ce)-Mn-O Series

As reviewed in the introduction, the electron doping in perovskite manganites by substituting tetravalent elements in place of La has been studied by a few groups. They ended with impurity phase or hole doping. The main problem was ionic size mismatch. Typically, the ionic radius of tetravalent ions is less than that of the trivalent rare earth ions that form the perovskite structure. Therefore, there is a problem of segregation of CeO_2 impurity in Ce doped $LaMnO_3$. Nevertheless, tetravalent doping would be very significant because it is expected to lead the mixed valence of Mn^{2+}/ Mn^{3+} ions. The higher spin value of Mn^{2+} could lead to higher magnetic ordering temperatures, while preserving the strong electron phonon interaction of the Jahn-Teller active Mn^{3+} ions.

The ionic size of Y is comparable to the tetravalent Ce ion, so it would be possible to prepare single phase electron doped $Y_{1-x}Ce_xMnO_3$ compounds in bulk and it would be interesting to study their physical properties. However one would end up with hexagonal structure because of similar size of Y. This chapter deals with the study of crystal structure, and magnetic properties of electron doped $Y_{1-x}Ce_xMnO_3$ compounds.

6.1. Sample Preparation and Characterization

$Y_{1-x}Ce_xMnO_3$ (x=0, 0.05, 0.10 and 0.15) compounds have been prepared by solid state route. Stoichiometric ratio of Y_2O_3, CeO_2 and Mn metal powder with 99.9% purity were weighed and grinded under acetone. The mixture was presintered in powder form at 860ºC for 36 h with intermediate grindings. The presintered powder was pressed into cylindrical pellet form and was annealed at 1050°C for 24 h. The final sintering was carried out at 1250º C for over 50 h under oxygen atmosphere with several intermediate grindings. These samples were annealed again in a Hot Press Furnace by applying a load of 8Ton/cm^2 at 950°C for 2 h to improve the microstructures.

The XRD patterns recorded for all samples are shown in Figure 6.1. The materials could be prepared in single phase form upto 15% of Ce doping. All the observed peaks could be indexed to *$P6_3cm$* space group and hence the samples are essentially in single phase form. Typical XRD patterns along with Rietveld refinement is shown in Figure 6.2 for x =0.05 and 0.10 samples. Here the experimental data are shown as crosses (+) and the calculated intensities are shown as solid lines. The bottom line represents the difference between measured and calculated intensities.

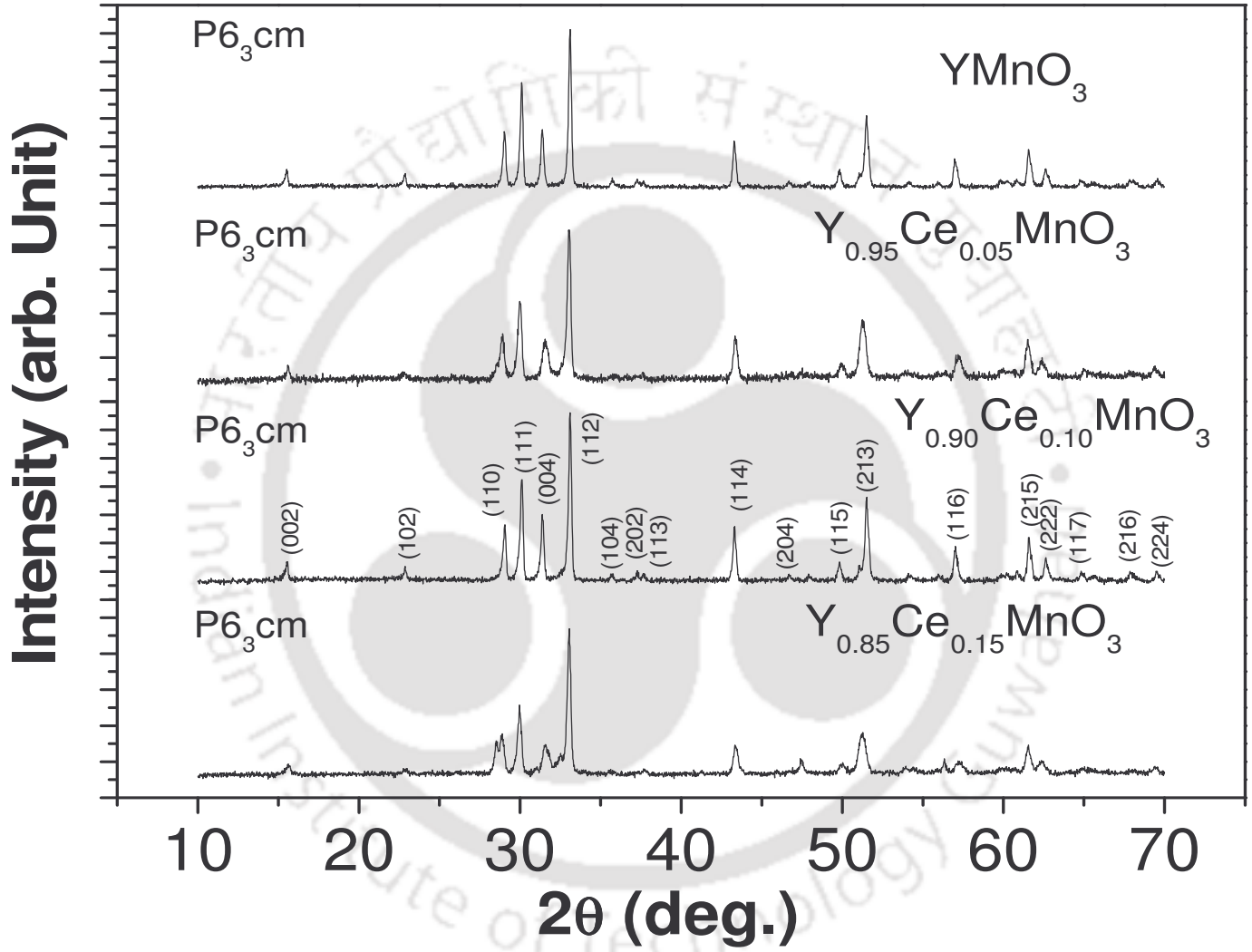

Figure 6.1: XRD patterns of the samples $Y_{1-x}Ce_xMnO_3$ for x = 0, 0.05, 0.10 and 0.15.

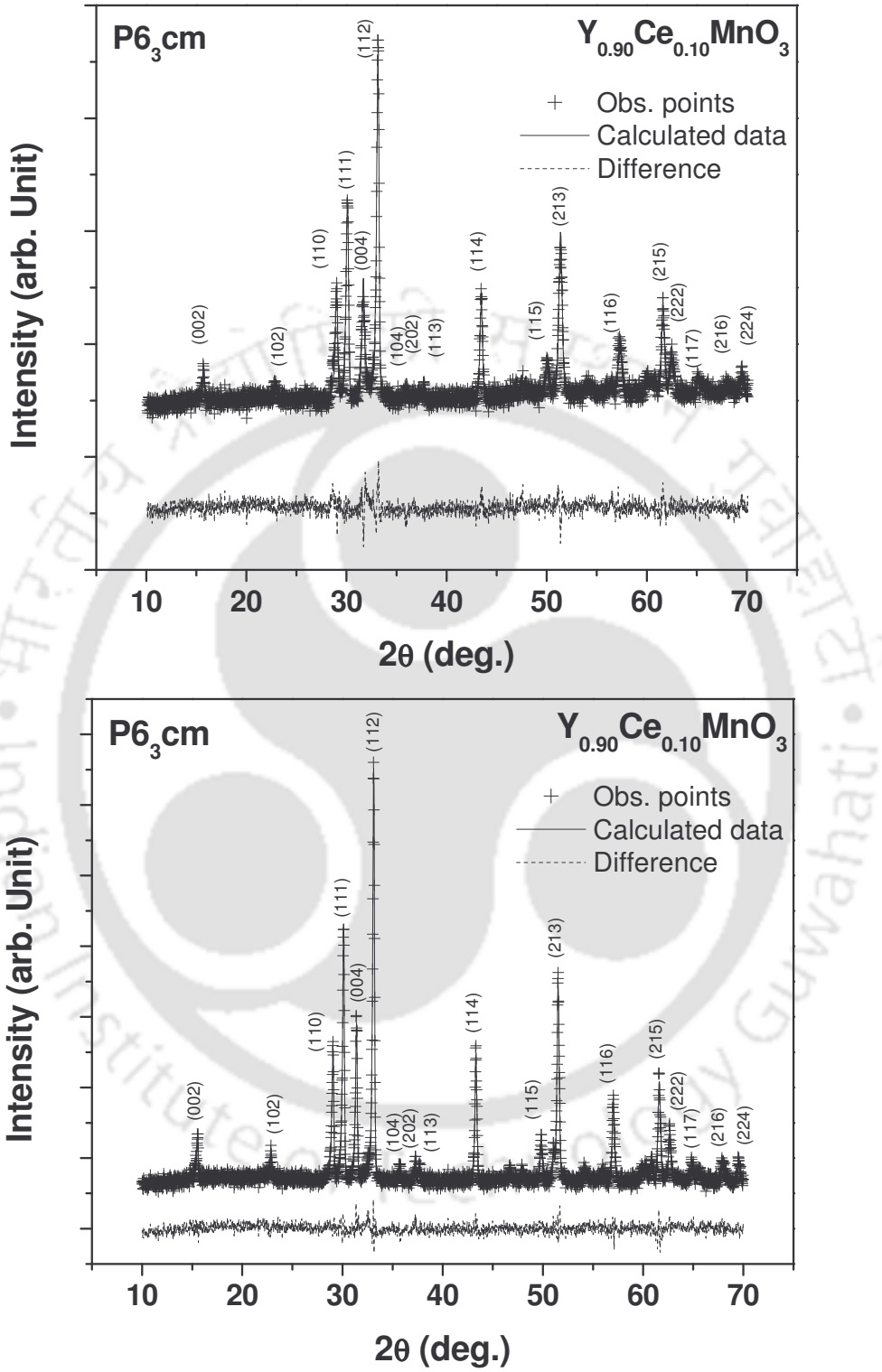

Figure 6.2: XRD patterns for x=0.05 and 0.10 samples. The + signs represent experimental data and solid line represents Rietveld refined data. The dotted lines show the difference between experimental and refined data.

The lattice parameters, reliability factors and unit cell volumes are tabulated in Table 6.1. The typical lattice parameters are found to be a = b = 6.132 Å and c = 11.368 Å for $YMnO_3$. These values are comparable to those reported for $YMnO_3$ by Vega *et. al.* [22]. No appreciable variation in lattice parameters and unit cell volume has been observed. For the present series, average crystallite size (S_C) has been calculated using the Scherrer's formula [262]. The values are listed in Table 6.1. The crystallite sizes are found to decrease systematically with increase in Ce doping.

The grains are generally formed due to the agglomeration of several crystals and as a result, the size of grains is higher than that of crystals or crystallite size. The typical SEM micrographs for x = 0.0 and x= 0.10 samples with the magnification of 7000 are shown in Figures 6.3 and 6.4 respectively. We can see that the morphology of the samples is uniform and it suggests the monophasic nature of the sample. The average grain size for all samples is found to be in the order of 1 micron. The grain size is found to decrease with increase in Ce concentration and it is in correlation with the trend of decrease in crystallite size.

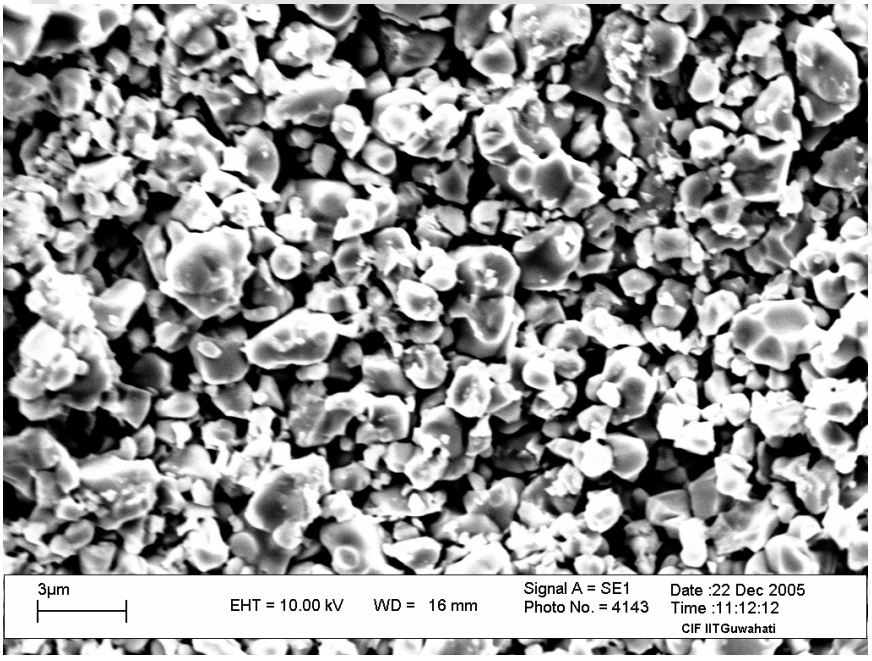

Figure 6.3: SEM photograph (magnification 7000) of the $YMnO_3$ sample.

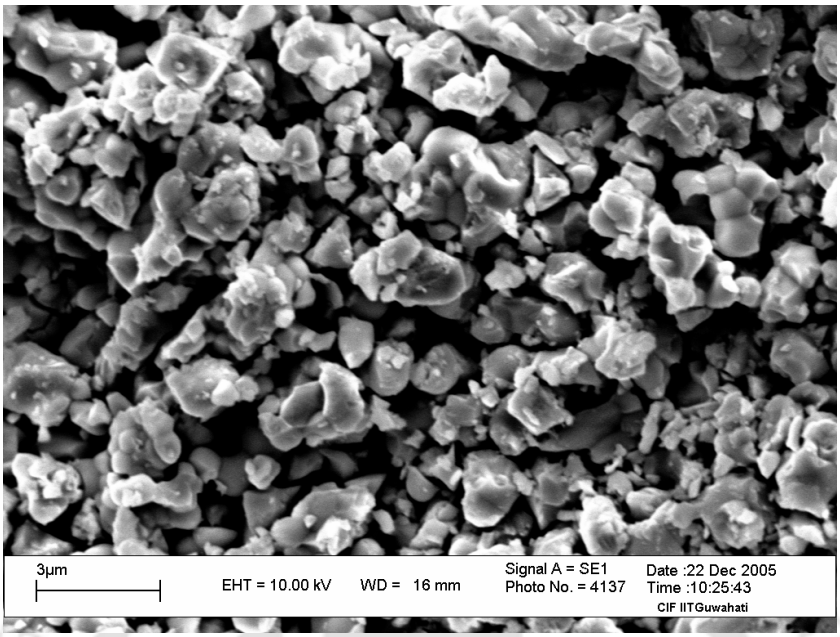

Figure 6.4.SEM photograph (magnification 7000) of the $Y_{0.9}Ce_{0.1}MnO_3$ sample.

Typical SEM EDS spectrum for x = 0.10 sample is shown in Figure 6.5. One can see that all the elements are present and their composition ratio is comparable to the nominal starting composition. The cationic ratio calculated from EDS is as given in Table 6.2.

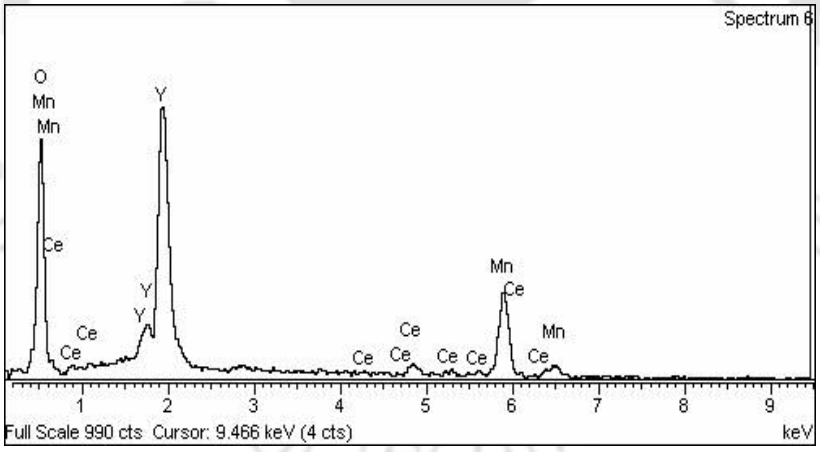

Figure 6.5: Typical SEM-EDS spectrum for x=0.10 sample.

The average Mn valency determined from chemical titration suggests the presence of mixture of Mn^{2+} and Mn^{3+} ions. These values are given in Table-6.1 and there is a systematic decrease in Mn valency with Ce doping, as expected. Thus, doping of Ce in $YMnO_3$ results in Mn^{2+}/Mn^{3+} ratio.

Table 6.1: Parameters obtained from the XRD analysis of the samples $Y_{1-x}Ce_xMnO_3$ (x = 0.0, 0.05, 0.10 and 0.15). R_p, $R_{\omega p}$, R_{exp}, R_{Bragg}, R_F and χ^2 are the reliability factors. S_C is the crystallite size.

Samples Parameters	**x = 0.00**	**x = 0.05**	**x = 0.10**	**x = 0.15**
Space Group	$P6_3cm$	$P6_3cm$	$P6_3cm$	$P6_3cm$
a=b (Å)	6.1324 (0.0003)	6.1562 (0.0002)	6.1316 (0.0008)	6.1575 (0.0022)
c (Å)	11.3679 (0.0006)	11.2940 (0.0003)	11.3661 (0.0015)	11.2734 (0.0042)
Volume(Å^3)	370.23 (0.028)	370.62 (0.182)	370.07 (0.085)	370.17 (0.235)
χ^2 (%)	5.70	4.81	4.45	6.35
R_p (%)	6.76	6.92	5.63	8.73
R_{wp} (%)	8.74	8.71	7.23	3.58
R_{exp} (%)	3.66	3.97	3.43	5.94
R_f (%)	6.47	8.63	5.75	12.8
R_{Brag} (%)	8.07	10.8	7.26	14.8
<Mn-O_1> (Å)	1.937	1.925	1.907	1.929
<Mn-O_2> (Å)	1.778	1.766	1.803	1.741
<Mn-O_4> (Å)	2.016	2.022	2.006	2.024
Mn-O_4-Mn (°)	118.4	118.3	119.3	118.4
Crystallite size, S_c (nm)	55.6	53.5	50.3	48.5
Mn Valency	2.95	2.92	2.90	2.88

Table 6.2: The cationic ratio determined from EDS analysis for $Y_{1-x}Ce_xMnO_3$ samples.

Sample	Calculated Cationic Ratio from EDS		
	Y	Ce	Mn
x=0.00	1.01	0.00	0.99
x=0.05	0.94	0.05	1.01
x=0.10	0.90	0.11	0.99
x=0.15	0.85	0.14	1.01

6.2. ac Susceptibility Study

In this series, I would like to discuss the ac susceptibility result first rather than starting with dc magnetization for the ease of explaining the magnetic property. AC susceptibility as a function of temperature was measured for all the samples at an ac field amplitude of 6 Oe with a frequency of 333Hz. Figure 6.6 shows the inphase ac susceptibility, χ' versus temperature (T) for the samples x =0.0, 0.05, 0.10 and 0.15. The x = 0.0 sample exhibits antiferromagnetic transition with a Neel temperature (T_N) at 42K and it is comparable to the value reported by Iliev *et al.* [257]. The Ce doped samples exhibit ferromagnetic (FM) transition at low temperature. We can see that the samples exhibit upturn in susceptibility with onset temperature around 100K followed by sharp peak in susceptibility at low temperature at 24 K, 28 K and 29K for x=0.05, x=0.10 and 0.15 samples respectively. The susceptibility value increases with the Ce doping and it could be due to increase in ferromagnetic interactions as a result of generation of Mn^{2+} and Mn^{3+} pairs and the presence of bound magnetic polaron in the material (discussed later from M-H curve). It is clear from the above observation that Ce plays the role of electron doping by creating a mixture of Mn^{2+} and Mn^{3+} ions.

The Hall Effect experiment was performed to find out the nature of charge carrier and nature of doping in samples. The Hall co-efficient (R_H) was measured on parallelepiped shaped samples by using a Walker electromagnet, Keithley constant current source and Keithley nano-voltmeter. The experiment was performed in both positive and negative direction of current. Four hall voltages were recorded at room temperature in both positive and negative direction of current and in two opposite directions of magnetic field, for all the samples. The magnitude of applied field was 1T. The typical value of Hall coefficient and charge density at room temperature was calculated by using the relation: $R_H = \left(\frac{V_H\ d}{I\ B}\right)$ and charge density=$1/(q\ R_H)$. From the measurement, the Hall coefficients are found to be negative and the typical values for x=0.10 and 0.15 samples are found to be -2.52 and -0.14$\times 10^4$ m^3/C as given in Table 6.3. The Hall coefficients suggest that there is an increase in charge concentration with doping. The negative values of R_H suggest that intended electron doping has been achieved in the present series.

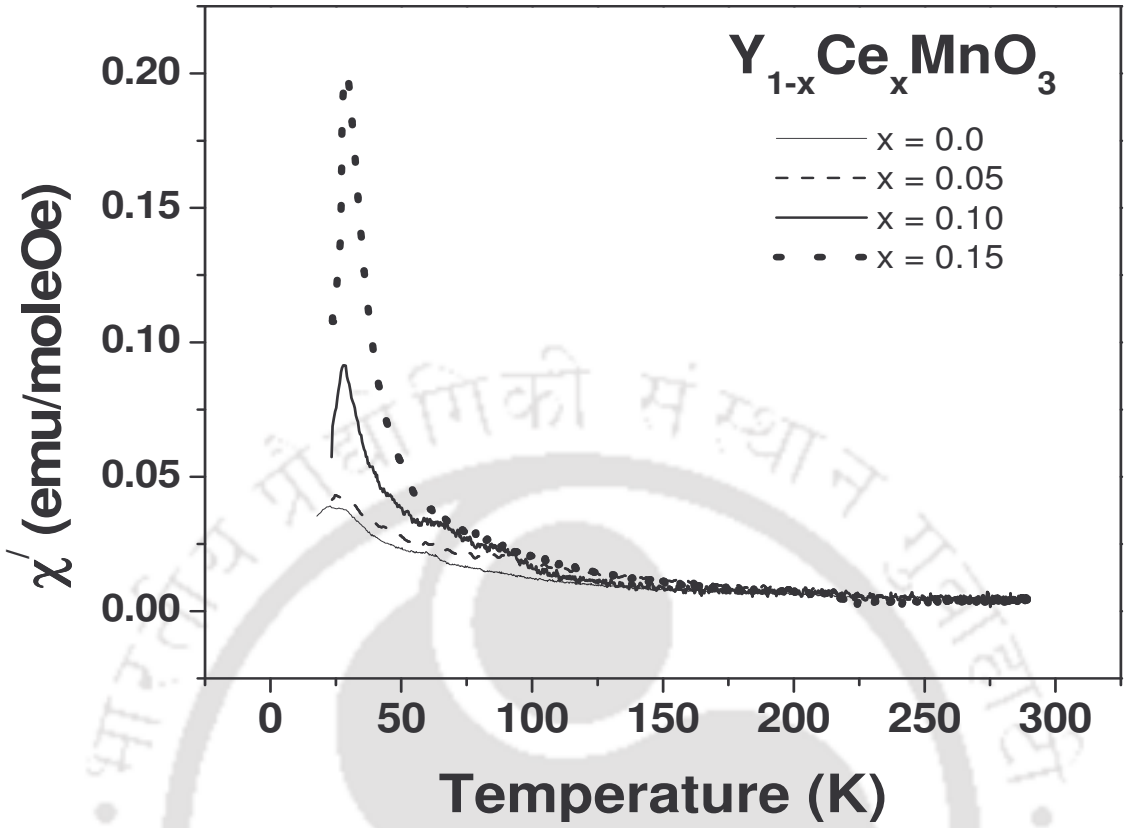

Figure 6.6: Temperature variation of in-phase ac susceptibility (χ') of $Y_{1-x}Ce_xMnO_3$ samples for x =0.0, 0.05, 0.10 and 0.15.

Table 6.3: Parameters obtained from ac susceptibility measurement and Hall-effect measurement.

Samples → / Parameters ↓	x = 0.0	x = 0.05	x = 0.10	x = 0.15
T_c(K)	---	26.0	28.0	33.0
χ'_S (emu/ mol-Oe)	0.04	0.05	0.09	0.20
Hall Coefficient R_H (10^4 m^3/C)	---	---	-2.52	-0.14
Charge Density (10^{14} m^{-3})	---	---	2.47	44.58

6.3. DC magnetization

The temperature variation of dc magnetization at an applied field of 100 Oe was measured using Quantum Design MPMS5 SQUID magnetometer at Bhabha Atomic Research Centre, Mumbai both in ZFC and FC conditions. The temperature variation of zero field cooled (ZFC) and field cooled (FC) magnetization curves are shown in Figure-6.7 for x=0.05, 0.10 and 0.15 samples. All the Ce doped samples exhibits PM to short range FM transition. The FM transition temperature is comparable to that observed from ac susceptibility measurement and it is given in Table 6.4. The ZFC magnetization data show peak effect in the vicinity of transition temperature that is similar to ac susceptibility measurement and such behaviour has been reported in literature for weak ferromagnetic material [260]. The rather low value of magnetization at low temperatures suggests that there is a weak FM interaction in Mn^{2+}-O^{2-}-Mn^{3+} networks. The FC data show a large increase in magnetization compared to ZFC data as a result of enhanced ferromagnetism due to better alignment of spin of core electrons. This feature can also be explained on the basis of presence of competing magnetic interaction. The temperature (T) variation of dc susceptibility (χ_{dc}) was fitted to Curie-Weiss law, $\chi_{dc}=C/ (T-\theta_c)$, by varying the Curie constant, C and Curie temperature, θ_C. The plots of $1/\chi_{dc}$ versus T for x = 0.05 and x = 0.10 samples are shown in Figure 6.8 along with fitted data as solid lines. They exhibit linear behaviour in the paramagnetic region. The θ_C values for Ce doped compounds are found to be positive, thereby indicating the presence of ferromagnetic interactions in the material. The θ_C values for Ce doped compounds are given in Table 6.4. The effective paramagnetic moment, μ_{eff} calculated from Curie constant for x = 0.05, 0.10 and 0.15 samples are given in the Table 6.4. Even though, these values are less than that expected for a given average Mn valency, they show increase in magnitude with doping.

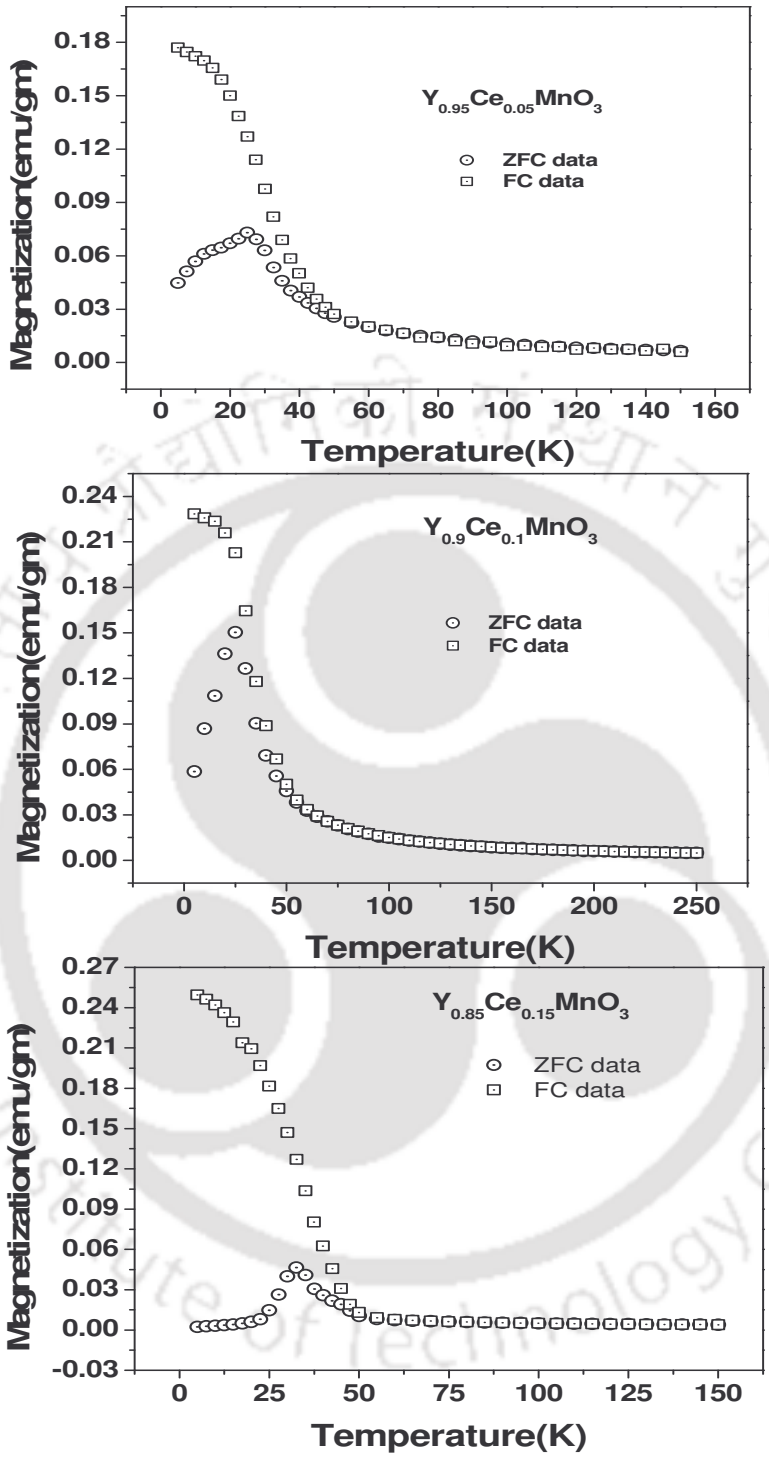

Figure 6.7: The temperature variations of ZFC- zero field cooled (circles) and FC- field cooled (squares) magnetization curves for x=0.05, 0.10 and 0.15 samples at 10mT magnetic field.

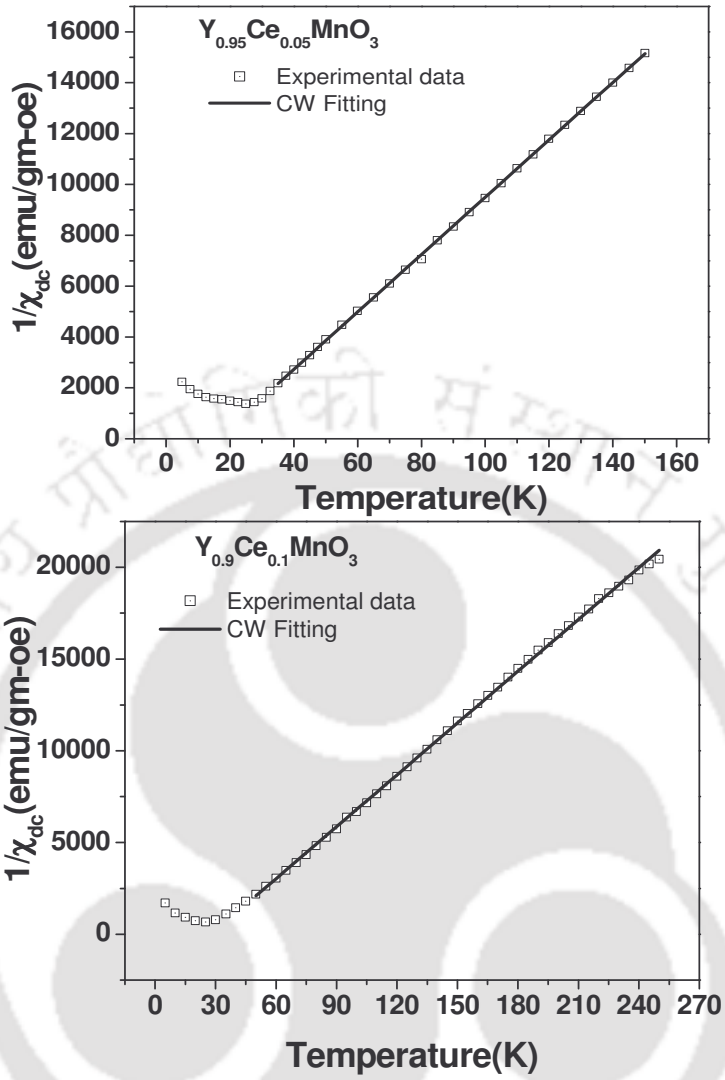

Figure 6.8: Temperature variations of inverse susceptibility ($1/\chi_{dc}$) along with Curie-Weiss law fits are shown in the inset.

Table 6.4: Parameters obtained from magnetization measurement of $Y_{1-x}Ce_x MnO_3$. T_C is the ferromagnetic transition temperature calculated from dM/dT. θ_C (Curie temperature), C (Curie constant), μ_{eff} (μ_B) have been found from the fit of dc susceptibility to Curie-Weiss law.

Sample/Parameters	x = 0.05	x = 0.10	x = 0.15
T_C(K)	32.0	34.7	36.3
θ_C (K)	15.7	28.0	34.0
C	1.7	2.09	2.25
μ_{eff} (μ_B)	3.73	4.09	4.23

The plot of magnetization as a function of magnetic field (M-H loop) measured at 5K is shown in Figure 6.9 for x=0.05 and 0.10 samples. It exhibits hysteresis behaviour and the magnitude of magnetization was found to increase with doping. They indicate the presence of weak ferromagnetic interaction due to double exchange interaction in Mn^{2+}-Mn^{3+} networks. The magnetization could not be saturated upto a field of 5T and indicates the presence of competing magnetic interaction. Even though the mixed valent manganite with Mn^{2+} and Mn^{3+} ions are prepared, we have not observed any long range FM behaviour. One of the reasons could be due to the localization of charge carriers as a result of narrow e_g band width in smaller rare earth ion based manganites. The other possibility is that the concentration of Mn^{2+} -Mn^{3+} pairs are not adequate enough to set up a long range ferromagnetic ordering.

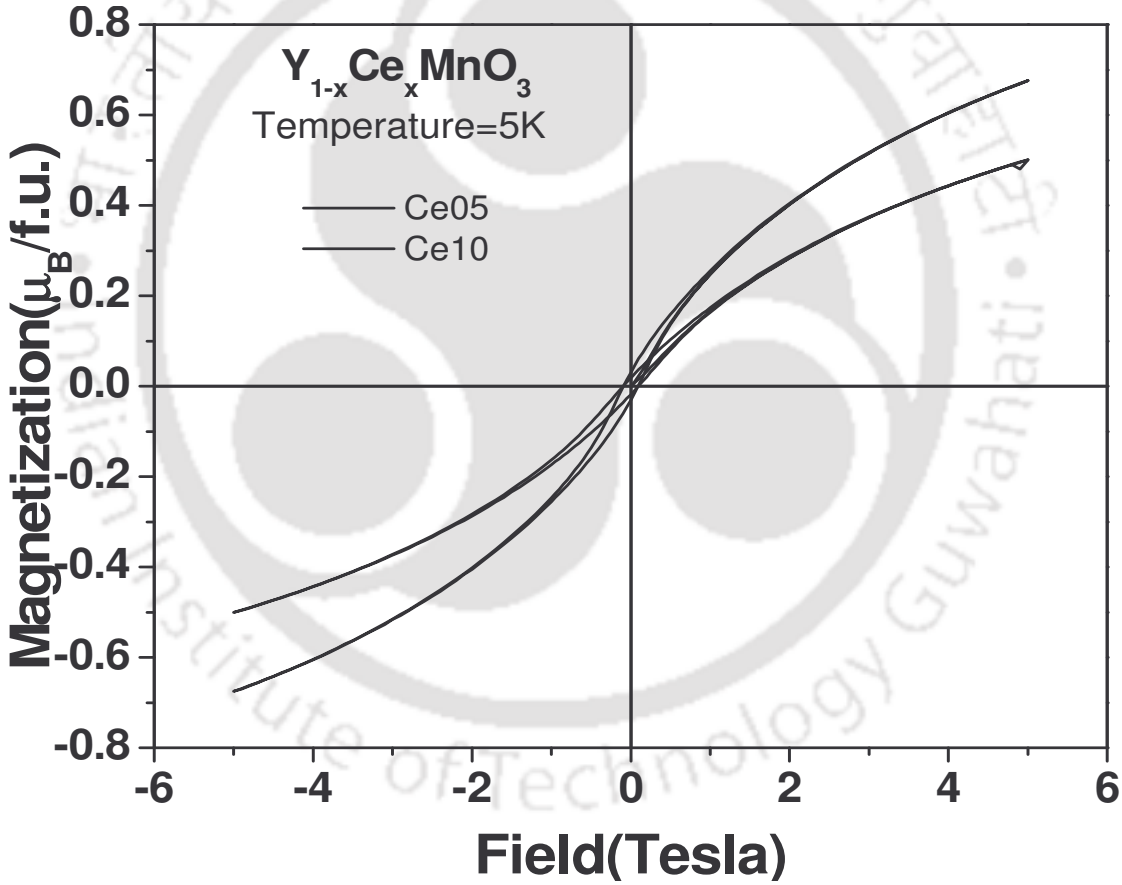

Figure 6.9: Magnetization versus field (M-H loop) at 5K for x= 0.05 and 0.10 samples.

To understand the nature of magnetic interaction, we have fitted the M versus H data to the bound magnetic polaron (BPM) model by following Chiorescu *et al.* [292]. According to BMP model, the measured magnetization can be fitted to the relation [69, 70].

$$M = M_0' L(x) + \chi_m H \text{ ----------(6.1)}$$

where the first term is from BMP contribution and the second term is due to paramagnetic matrix contribution. Here M_0' = Nm_s, N is the number of BMPs involved and m_s is the effective spontaneous moment per BMP. $L(x) = \coth x - 1/x$ is the Langevin function with $x = m_{eff} H /(k_B T)$, where m_{eff} is the true spontaneous moment per BMP and at higher temperature it can be approximated to m_s=m_{eff}. χ_m is the susceptibility of the matrix. We have analysed the M-H curve by using equation 6.1. The parameters M_0', m_{eff} and χ_m were varied during the fit. The experimental data along with fitted data are shown in Figure 6.10 for the x=0.05 and 0.10 samples at 5 K. We can see that the theoretical curve closely follows the experimental data. The fitted parameters are tabulated in Table 6.5. The total BMP magnetization M_0' values are found to in the order of 10 emu/gm. The χ_m value is found to be comparable to those reported for $Cu_2FeGeSe_4$ alloy [70]. By assuming m_s=m_{eff}, we have estimated the concentration of BMP and was found to be in the order of 10^{20} cm^{-3}.

Table 6.5: Parameters obtained from analysis of M- H curve employing Bound Magnetic Polaron (BMP) model. M_0' is the spontaneous magnetization, χ_m is the susceptibility of the matrix and m_{eff} is effective spontaneous moments per BMP. N is number of BMPs.

Sample/ Parameter	x=0.05	x=0.10
M_0' (emu/gm)	9.19	10.80
χ_m (10^{-4} emu/gmOe)	1.35	2.00
m_{eff} (10^{-20} emu)	8.33	11.00
N (10^{20} cm^{-3})	5.76	5.02

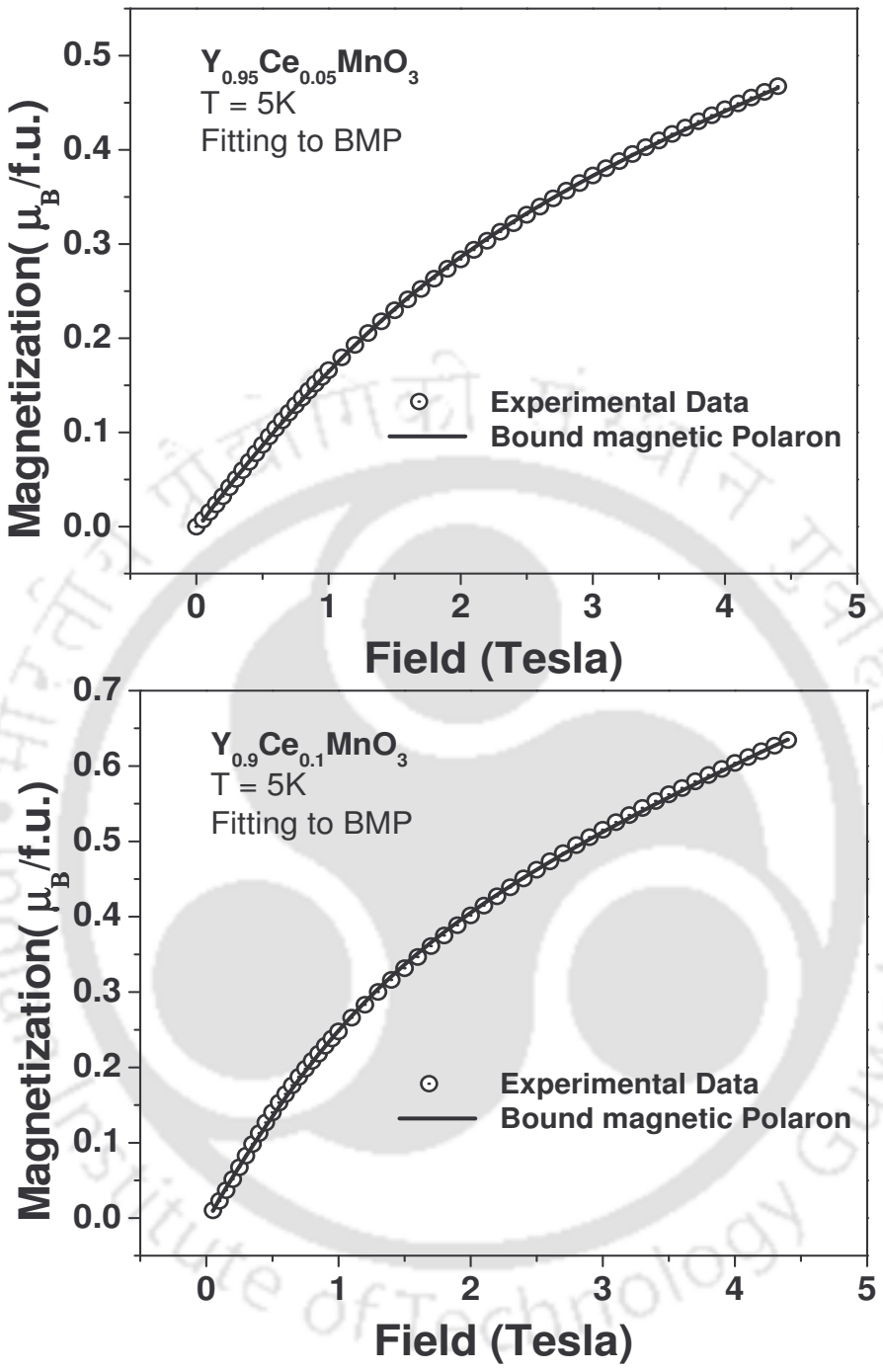

Figure 6.10: Magnetization versus field (M-H loop) at 5K for x=0.05 and 0.10 samples. The solid line represents fit to BMP model.

6.4. Conclusions

Electron doped, $Y_{1-x}Ce_xMnO_3$ compounds have been prepared by solid state route in single phase form for x = 0 to 0.15. The samples are found to be crystallized in hexagonal structure and the all observed peaks could be indexed to $P6_3cm$ space group. It has been shown that the doped samples exhibit ferromagnetic transition with increase in Curie temperature. The observed FM transition can be explained on the basis of double exchange interaction between Mn^{2+}- Mn^{3+} pairs. The experimental M-H curves could be analysed based on bound magnetic polaron model and its typical concentration is found to be in the order of 10^{20} per cm^3. Thus unlike in $LaMnO_3$ series, the bulk electron doped $YMnO_3$ series could be prepared in single phase form by using Ce substitution.

Chapter 7: Conclusions

In this chapter, the conclusions drawn from the various physical measurements and analyses of Mn site substituted $(La_{0.85}Ag_{0.15})MnO_3$ series, Cu substituted $LaMnO_3$, (Nd, Ag)MnO_3 and electron doped (Y, Ce)MnO_3 are summarized as below.

Co doped $(La_{0.85}Ag_{0.15})MnO_3$ series, i.e. $(La_{0.85}Ag_{0.15})Mn_{1-y}Co_yO_3$ compounds could be prepared in single phase form upto y=0.50. Structural transition from rhombohedral to orthorhombic symmetry has been observed with increase in doping. Both Cr and Al doped samples $(La_{0.85}Ag_{0.15})Mn_{1-y}M_yO_3$ (M= Cr, Al) could be prepared in single phase form upto 20 at% of doping. They both are found to crystallize in rhombohedral structure.

In Co doping, lattice parameters are found to increase with doping upto y=0.20, then it decreases. It is explained on the basis of some of Mn^{3+} ions being replaced by Co^{2+} ions having larger ionic size. On the other hand, the decrease in lattice parameters for y> 0.20 could be due to the transition of Co ions from high spin state to low spin state. However the presence of some of the Co ions in higher valence state can not be ruled out.

In Cr and Al doped samples, the lattice parameters are found to decrease with doping as a result of Cr^{3+} and Al^{3+} ions replacing some of Mn^{3+} ions. The ionic radius of Cr^{3+} and Al^{3+} are smaller than that of Mn^{3+} ions.

In Co doped samples, the FM T_C is found to decrease from 292 K for y=0 to 198 K for y=0.20 and the T_C was found to increase for further increase in doping. The doping concentration dependence of magnetization irreversibility, remnant magnetization and coercive field at 78 K and FM T_C show two distinct behaviours; one for y≤ 0.2 and the other for y>0.2. They are explained on the basis of possible Co-O-Co networks for y>0.20. The measured magnetization is explained on the basis of FM interactions in Mn^{3+}-O-Mn^{4+}, Co^{2+}-O-Mn^{4+}, Co^{3+}-O-Mn^{4+} networks and simultaneous AFM interactions in Mn^{4+}-O-Mn^{4+}, Co^{2+}-O-Mn^{3+} networks for the composition y=0.05 to 0.20. For y≥0.30, in addition to the above magnetic interactions, there is a probability of FM interaction in Co^{2+}-O-Co^{3+} and Co^{3+}-O-Co^{4+} networks, which is expected to play a role for increase in FM T_C for y≥0.30.

In Cr doped samples, the FM T_C is found to decrease systematically with increase in doping to the value of 220 K for y=0.20 and the rate of decrease in T_C is quite small compared to Co-doped samples. The experimental effective paramagnetic moment, μ_{eff} is comparable to the theoretical moment, μ_{th} which was determined by assuming that Cr^{3+} ions replace the Mn^{3+} ions. The measured saturation magnetization was explained by assuming

that the doped Cr^{3+} ions exhibit antiferromagnetic interactions in Mn^{3+} and Mn^{4+} ions and there is also antiferromagnetic interaction in Mn^{4+}-O-Mn^{4+} networks. The above AFM competes with the existing double exchange FM interaction in Mn^{3+}-O-Mn^{4+} networks.

In Al doped samples, the decrease in T_C with doping is found to be quite small compared to the doping of magnetic elements such as Co and Cr. The T_C was found to decrease from 292 K for y=0 to 273 K for y=0.20. The measured magnetization could be explained by simply assuming that the doped Al ions play a role of magnetic dilution, without contributing any other competing magnetic interaction.

The field variations of magnetization of all the above three series could be analysed by fitting to Brillouin function model and by taking into account the FM interaction. From the above analysis, the effective spin contribution, S_{eff} to FM interaction due to Co, Cr, and Al doping has been estimated. In all the three cases of doping, S_{eff} is found to decrease with doping, however for Co doped samples S_{eff} is found to increase for y≥0.3 due to FM in Co-O-Co networks.

Temperature variations of ac susceptibility have been measured in all the above three series. They basically reflect the similar type of magnetic transitions observed from their dc counter part. For Co and Cr doped samples, detailed frequency variation of fundamental susceptibility and variation of third harmonic susceptibility have been measured. From the analysis, it was found that the Co doped samples in the composition range y=0.10 to 0.20 and Cr doped samples in the composition range y=0.05 to 0.20 exhibit reentrant spin glass (RSG) like behaviour with typical spin flipping time τ_0 in the order of 10^{-6} s and the critical exponent $z\upsilon$= 0.8 to 1.20. The above values are comparable to RSG observed in other manganites, however τ_0 is quite large compared to conventional spin glass system. They highlight the absence of atomic scale spin glass behaviour in the present manganite systems.

Metal-Insulator transitions and colossal magneto-resistivity have been observed upto 10% of Co doping. All other samples show semiconducting behaviour. All Cr doped samples show semiconducting behaviour along with colossal magneto-resistivity. However, metal-insulator transition is found to be retained in all the Al doped samples. The electrical conductivity in the metallic region of Al doped samples could be explained by electron-magnon scattering. The magneto-resistivity at low temperature is found to increase with Al concentration. The order of magnetoresistivity in the vicinity of FM T_C was found to be 20%, 25% and 15% for the Co, Cr and Al doped series respectively.

The phase diagrams of Co, Cr and Al doped materials are shown in Figure 7.1, figure 7.2 & Figure 7.3 respectively. From the phase diagram of Co doped materials we can see that several interesting results. We can see the structural transition from rhombohedral to orthorhombic with increase of Co doping. These materials exhibit multiple magnetic transitions such as PMI-FMI/FMM, and low temperature spin glass (SG) states. The phase diagram also depicts the metallic behavior of Co doped compound up to 10 % of Co doping.

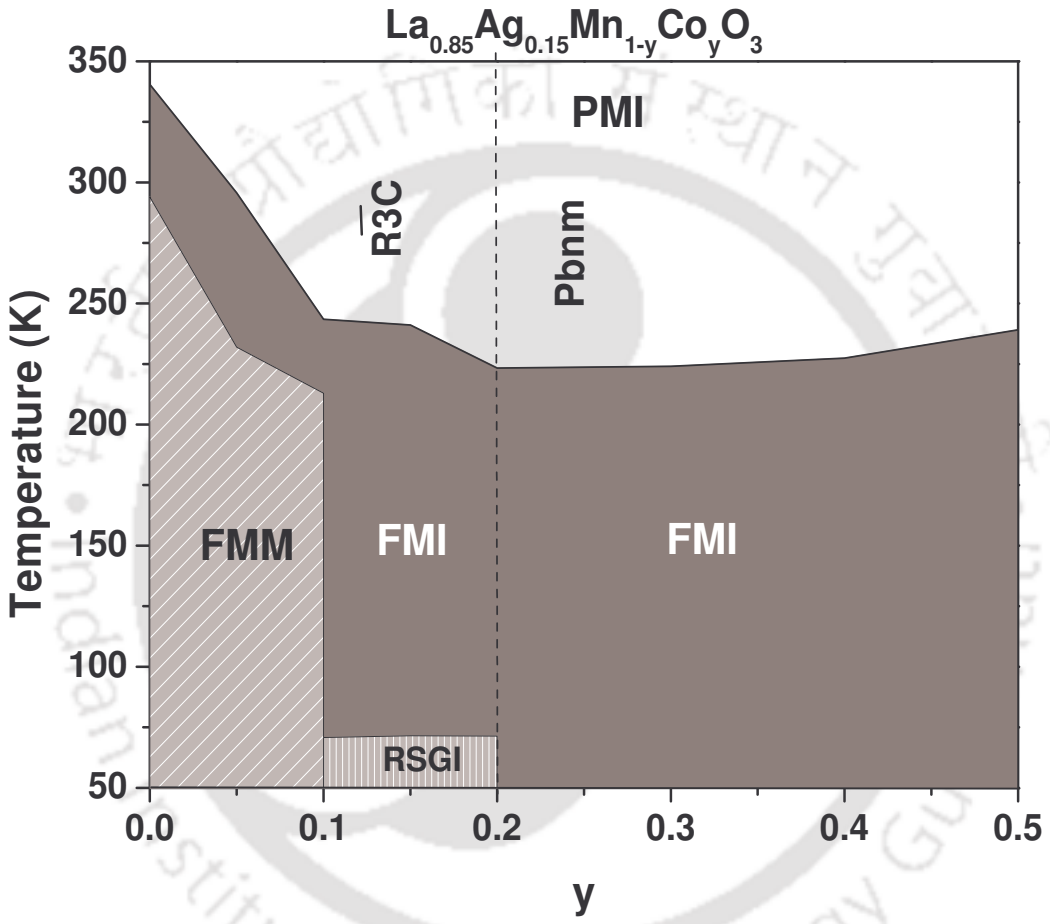

Figure 7.1: Phase diagram for $La_{0.85}Ag_{0.15}Mn_{1-y}Co_yO_3$ (y= 0-0.50).

However from the phase diagram of Cr doped materials as shown in Figure 7.2, we can see that all Cr doped materials exhibit magnetic transitions from PMI-FMI. Low temperature reentrant spin glass (RSG) state has been also observed.

The phase diagram of Al doped materials as shown in Figure 7.3 depicts that all Al doped materials exhibit transitions from PMI-FMI-FMM state. The doping of Al does not destroy the metallic behavior of parent compound and all samples show Metallic behavior.

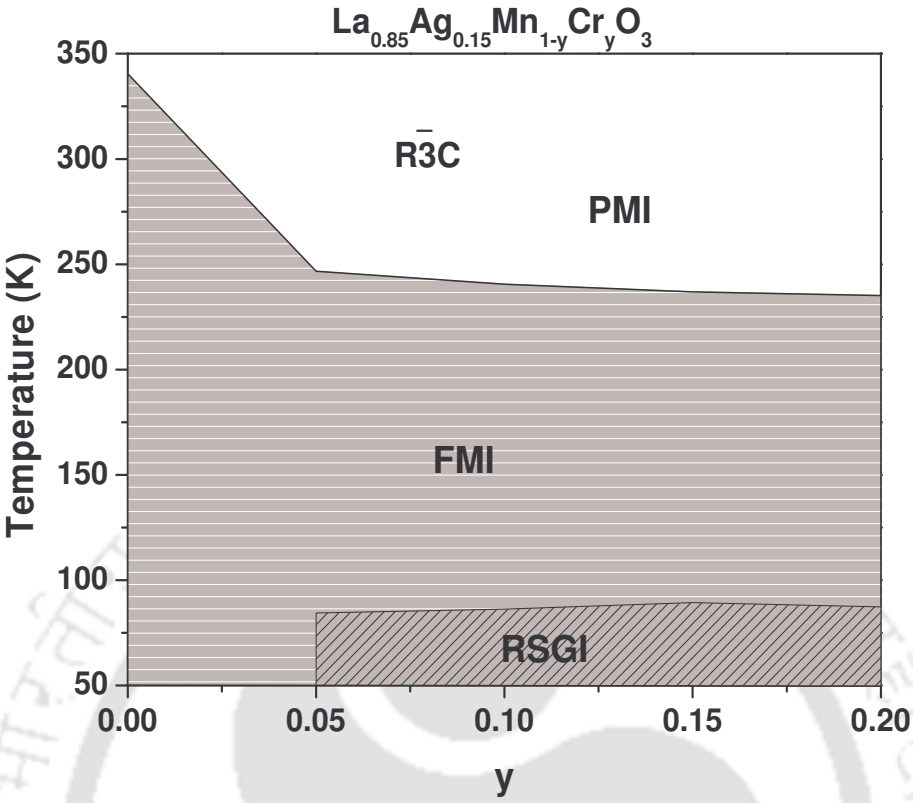

Figure 7.2: Phase diagram for $La_{0.85}Ag_{0.15}Mn_{1-y}Cr_yO_3$ (y= 0-0.20).

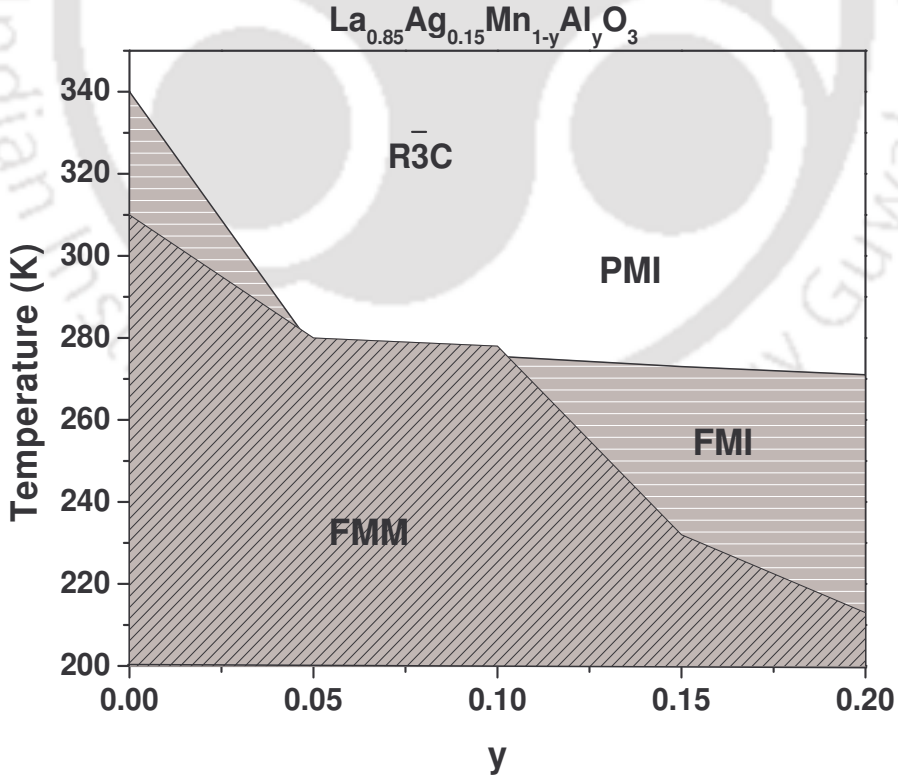

Figure 7.3: Phase diagram for $La_{0.85}Ag_{0.15}Mn_{1-y}Al_yO_3$ (y= 0-0.20)

The effect of Cu doping at Mn site of parent compound $LaMnO_3$, has been studied in this chapter. All the materials for $0.05 \leq y \leq 0.30$, in the series $LaMn_{1-y}Cu_yO_3$ exhibit PM-FM transition. The ferromagnetic transition temperature decreases with the Cu concentration. It reveals that, even though Cu doping increases the Mn^{4+} concentration, thereby increasing the Mn^{3+}- Mn^{4+} pairs, the Cu atoms exhibit a strong antiferromagnetic interactions with Mn ions. So the DE ferromagnetic interaction is weakened and the ferromagnetic T_c is reduced with doping. Compounds for $y \geq 0.10$ exhibit paramagnetic to ferromagnetic transitions followed by sharp fall in susceptibility as the temperature is lowered. The analyses of dc magnetization, frequency dependence of linear susceptibility and temperature variation of non linear susceptibility show that the present materials exhibit spin glass like behaviour at low temperature. From the analysis of third harmonic ac susceptibility, the critical exponent (γ) is found to be $\cong 3.2$.

The phase diagram of Cu doped ($LaMn_{1-x}Cu_xO_3$) materials is shown in Figure 7.4. The materials exhibit transition from FMI to PMI with the increase of temperature. FMM state is observed for $y \leq 0.10$ compounds at low temperature region. For $y \geq 0.10$ compounds, spin glass like behavior has been observed at low temperature.

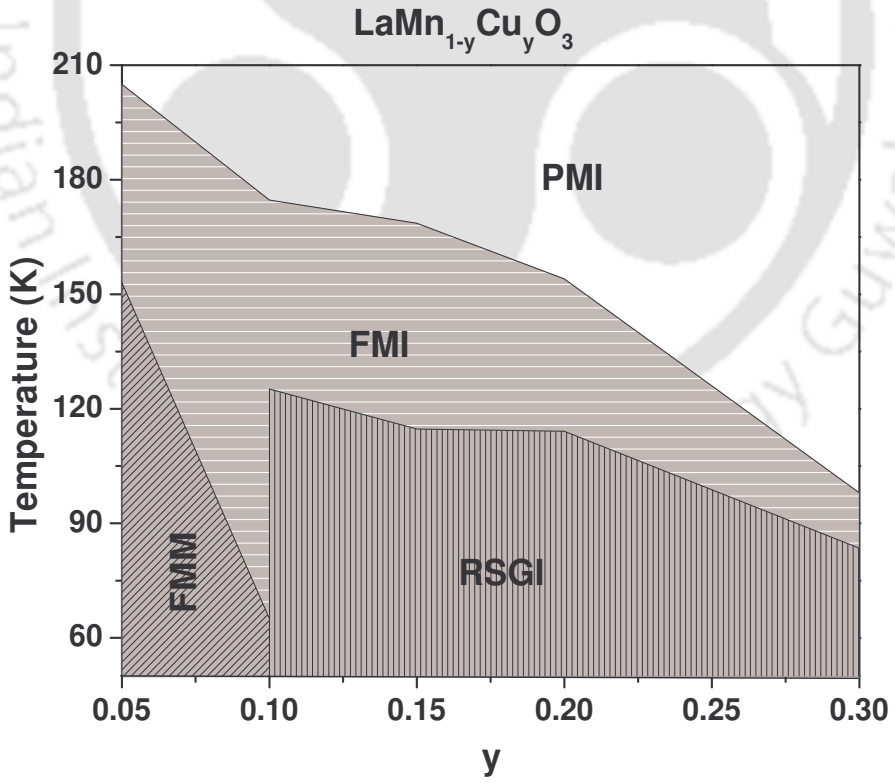

Figure 7.4: Phase diagrams for $LaMn_{1-y}Cu_yO_3$ (y= 0-0.20).

Polycrystalline samples of $Nd_{1-x}Ag_xMnO_3$ (x=0.05, 0.10, 0.15, 0.20) have been prepared for x = 0 to 0.20. All the samples are found to be in single phase form. X- ray diffraction patterns could be refined by using Pbnm space group. The lattice parameters a & c are found to increase with Ag doping. Temperature variation of magnetization measurement shows that these materials exhibit paramagnetic–ferromagnetic transition with a signature of presence of competing antiferromagnetic transition. The paramagnetic susceptibility could be analyzed by using Curie-Weiss law and the estimated μ_{eff} was comparable to the theoretical magnetic moments due to Mn^{3+}/ Mn^{4+} and Nd^{3+} ions. The field variation of magnetization could be fitted to Brillouin function relation by considering the FM interaction. From the analysis of magnetization in terms of Brillouin function model, effective spin contribution to FM, i.e. S_{eff} was determined. From S_{eff} and expected magnetic spin, S based on the concentration of Mn^{3+}/Mn^{4+} ions, the spin canting angle β with respect to a unique axis where there is a ferromagnetic component was determined. The β value could be compared with that reported in literature based on neutron diffraction results in Nd-Mn-O series. So, the measured magnetization could be explained on the basis of spin canting. The frequency variation of ac susceptibility and third harmonic susceptibility data indicate the presence of spin glass like behavior for x=0.10 &0.15 samples. The estimated spin flipping time, τ_0 is found to be in the order of 10^{-8} s, which is about two orders of magnitude less than that of Mn site doped samples. The electrical resistivity of all (Nd, Ag)-Mn-O materials exhibit semiconducting behavior and they could be understood by Efros-Shklovskii variable range hopping (ES- VRH) model.

The phase diagrams of hole doped $Nd_{1-x}Ag_xMnO_3$ materials are shown in Figure 7.5. One can see a smooth phase transition from PMI to FMI state as the temperature is lowered. Mostly the low temperature region is dominated by reentrant spin glass insulator (RSGI) state for y= 0.10 & 0.15 samples.

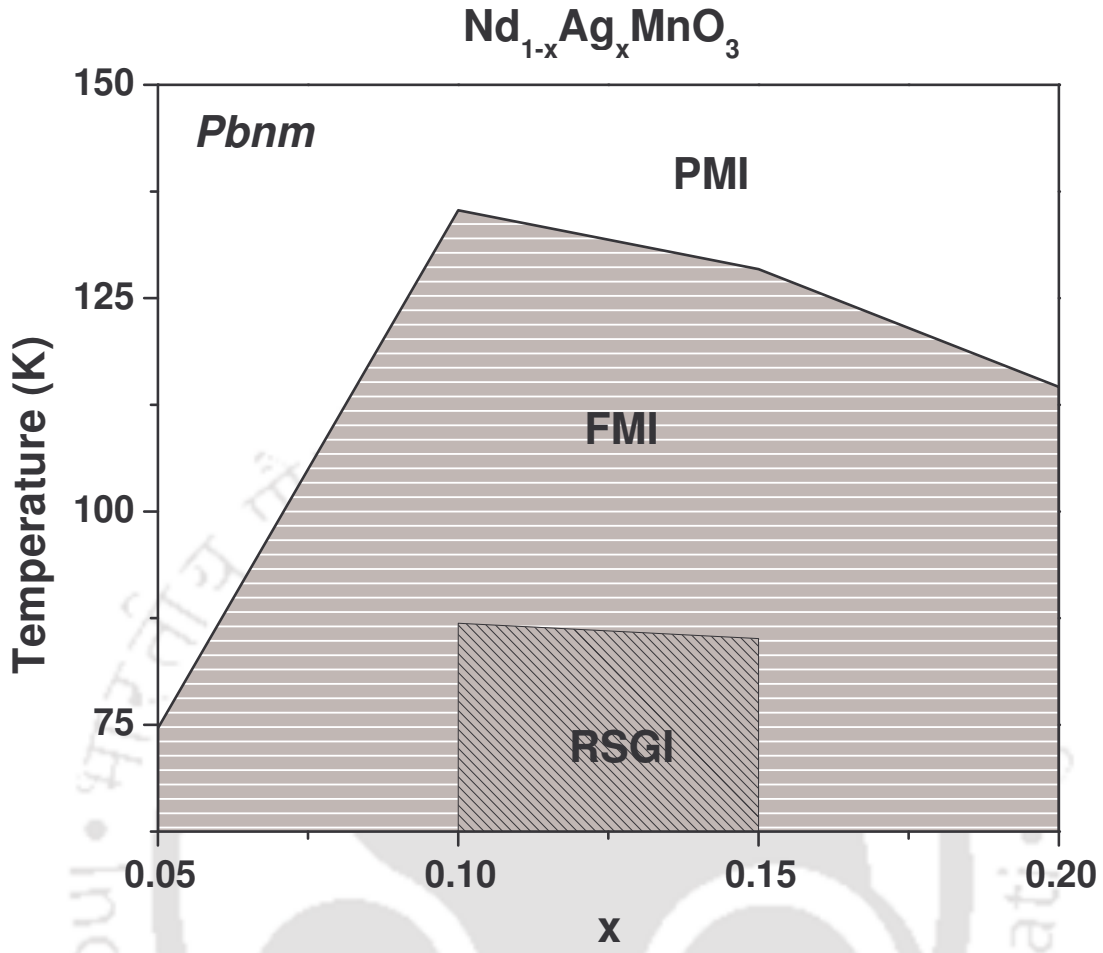

Figure 7.5: Phase diagram for $Nd_{1-x}Ag_xMnO_3$ (x= 0.05-0.20).

Electron doped, $Y_{1-x}Ce_xMnO_3$ compounds have been prepared by solid state route in single phase form for x = 0 to 0.15. The samples are found to be crystallized in hexagonal structure and the all observed peaks could be indexed to *P6₃cm* space group. It has been shown that the doped samples exhibit ferromagnetic transition with increase in Curie temperature. The observed FM transition can be explained on the basis of double exchange interaction between Mn^{2+}- Mn^{3+} pairs. The experimental M-H curves could be analysed based on bound magnetic polaron model and its typical concentration is found to be in the order of 10^{20} per cm^3. Thus unlike in $LaMnO_3$ series, the bulk electron doped $YMnO_3$ series could be prepared in single phase form by using Ce substitution.

In our knowledge, this is the very first report with an electron doping that gives rise to mixture of Mn^{2+}/Mn^{3+}. We have observed very first time the evidence of bound magnetic polarons in electron doped manganites.

The phase diagrams of electron doped $Y_{1-x}Ce_xMnO_3$ materials are shown in Figure 7.6. One can see a smooth phase transition from PMI to FMI state as the temperature is lowered. The parent compound is found to exhibit antiferromagnetic transition at 42 K.

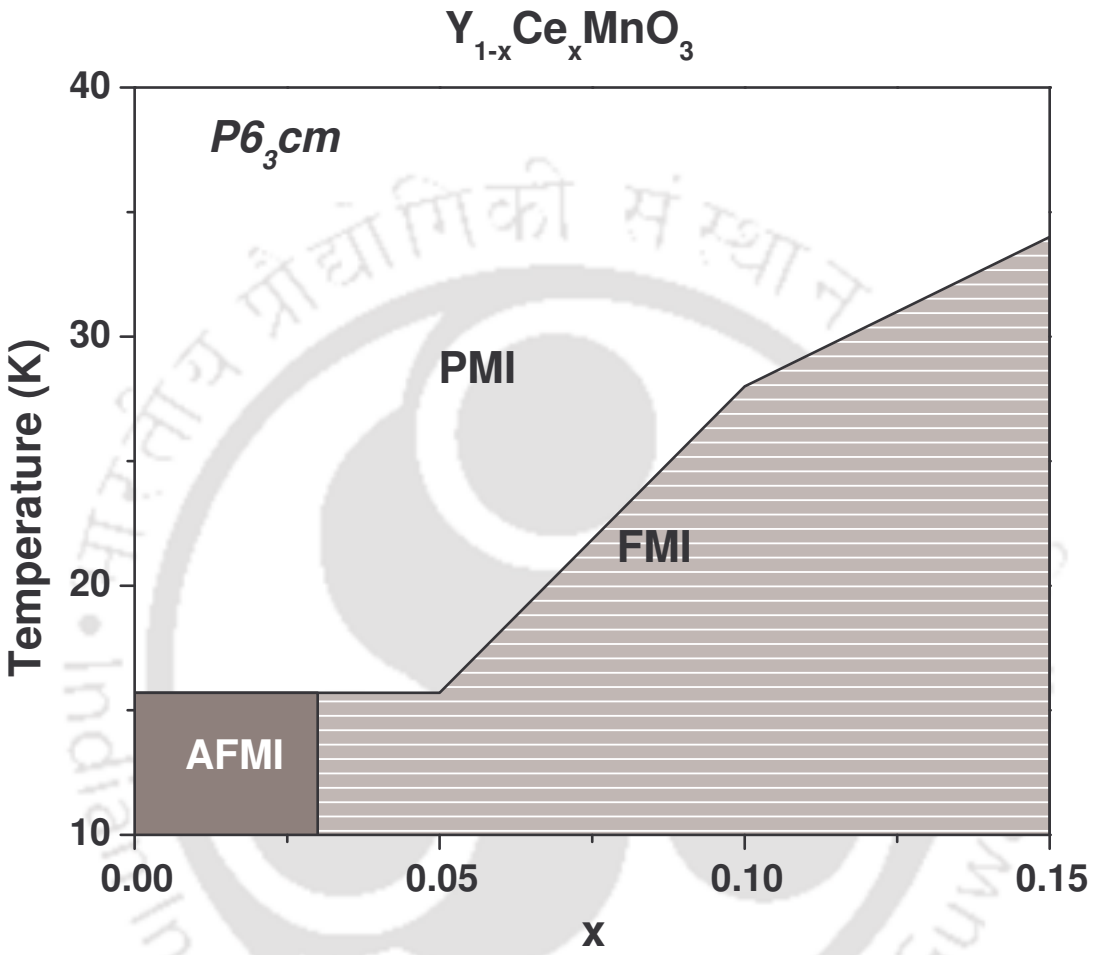

Figure 7.6: Phase diagrams for $Y_{1-x}Ce_xMnO_3$ (x= 0.0-0.15).

Papers Published / Communicated in International Journals:

(1) Ferromagnetic Insulating and Spin Glass Behavior in Cr substituted $La_{0.85}Ag_{0.15}MnO_3$ Compounds
S. K. Srivastava, Manoranjan Kar and S. Ravi, Journal of Physics: Condensed Matter 20 (2008) 235201-235207.

(2) Ferromagnetism in electron doped $Y_{1-x}Ce_xMnO_3$ compounds
S. K. Srivastava, Manoranjan Kar and S. Ravi, Journal of Magnetism & Magnetic Materials 320 (2008) 2382-2386

(3) Effect of Co Doping on the Magnetic Properties of $La_{0.85}Ag_{0.15}(Mn_{1-y}Co_y)O_3$
S. K. Srivastava, Manoranjan Kar and S. Ravi, Journal of Magnetism & Magnetic Materials 320 (2008) e107-e110

(4) Effect of Al Substitution on $La_{0.85}Ag_{0.15}MnO_3$ Double Exchange Ferromagnetic Compound
S. K. Srivastava, Manoranjan Kar and S. Ravi, Material Science & Engg. B 147 (2008) 84-89

(5) Linear and Non Linear ac Susceptibility studies in $La(Mn_{1-x}Cu_x)O_3$
S. K. Srivastava, Manoranjan Kar and S. Ravi, Journal of Magnetism & Magnetic Materials 307 (2006) 318-324

(6) Electrical Transport and Magnetic Properties on $La_{0.85}Ag_{0.15}(Mn_{1-y}Al_y)O_3$ Compound
S. K. Srivastava, Manoranjan Kar and S. Ravi, Indian Journal of Physics 82 (6) (2008) 147-154

(7) Preparation, Characterization and Magnetic Properties of Hexagonal $Y_{1-x}Ce_xMnO_3$
S. K. Srivastava, Manoranjan Kar and S. Ravi, Indian Journal of Physics 82 (2) (2008) 195-200

(8) Magnetic Properties of $Nd_{1-x}Ag_xMnO_3$ Compounds
S. K. Srivastava and S. Ravi (Communicated)

Papers Published in Refereed Conferences Proceedings and Presented in National /International Conferences:

(1) Study of effective ferromagnetic spin contribution in Cr and Al doped $La_{0.85}Ag_{0.15}MnO_3$ compound.
S. K. Srivastava, B. Samantaray and S. Ravi, Accepted in DAE Solid State Physics Symposium, Dec. 2008

(2) Neutron Powder Diffraction Studies in $LaMn_{1-x}Cu_xO_3$ (x=0.05 and 0.10)
S. K. Srivastava, S. Ravi, I. Dhiman and A. Das, Presented in International Symposium on Neutron Scattering Mumbai, India, December 2007.

(3) Reentrant Spin Glass Behavior in $(La_{0.85}Ag_{0.15})(Mn_{0.85}M_{0.15})O_3$ (M = Co, Cr)
S. K. Srivastava, Manoranjan Kar and S. Ravi, Proc., DAE SSPS, 52 (2007) 1017-1018
Presented in DAE Solid State Physics Symposium, Dec. 2007, Mysore, India

(4) Effect of Co doping on the crystal structure, electrical transport and magnetic properties of $(La_{0.85}Ag_{0.15})(Mn_{1y}Co_y)O_3$
S. K. Srivastava, Manoranjan Kar and S. Ravi, Presented in Latin-American Workshop on Magnetism and Magnetic Materials, Aug. 2007, Rio de Janeiro, Brazil

(5) Study of Crystal Structure and magnetic Properties of $(Y_{1-x}\ Nb_x)_2Mn_2O_7$ pyrochlore
S. K. Srivastava, B. Samantaray and S. Ravi, Presented in Condensed Matter Days, Aug. 2007, NIT Rourkela, India.

(6) Electrical Transport and Magnetic Properties on $La_{0.85}Ag_{0.15}(Mn_{1-y}Al_y)O_3$ Compound
S. K. Srivastava, Manoranjan Kar and S. Ravi, Presented in PANE, March 2007, Guwahati, India

(7) Crystal Structure Studies on $La_{0.85}Ag_{0.15}Mn_{1-y}Al_yO_3$ Compounds
S. K. Srivastava, Manoranjan Kar and S. Ravi, Presented in Crystallography Conference, March 2007, Chennai, India

(8) Effect of Co Substitution on Crystal Structure and Magnetic Property of $La_{0.85}Ag_{0.15}Mn_{1-y}Co_yO_3$ (y = 0 to 1) Compounds
S. K. Srivastava, Manoranjan Kar and S. Ravi, DAE SSPS, 51 (2006) 851-852
Presented in DAE Solid State Physics Symposium, Dec. 2006, Bhopal, India

(9) Study of Electrical Transport, Magnetic Properties of $La_{0.85}Ag_{0.15}Mn_{1-x}T_xO_3$(T=Co,Al)
S. K. Srivastava, Manoranjan Kar and S. Ravi, Presented in INSA-HAS Workshop, Dec. 2006 Univ. of Hyderabad, India

(10) Crystal Structure and Magnetic Properties of hexagonal $Y_{1-x}Ce_xMnO_3$
S. K. Srivastava and S. Ravi, Presented in Condensed Matter Days, Aug. 2006, Univ. of Tezpur, India

(11) Spin glass behavior in $La(Mn_{1-x}Cu_x)O_3$ compounds
S. K. Srivastava, Manoranjan Kar and S. Ravi, DAE SSPS, 50 (2005) 825-826
Presented in DAE Solid State Physics Symposium, Dec. 2005, BARC Mumbai, India